AD-A095 420 LEHIGH UNIV BETHLEHEM PA CENTER FOR SURFACE AND COA--ETC F/G 11/3
CORROSION CONTROL THROUGH A BETTER UNDERSTANDING OF THE METALLI--ETC(U)
DEC 80 H LEIDHEISER, M S EL-AASSER N00014-79-C-0731

UNCLASSIFIED NL

1 OF 3
AD
A095420

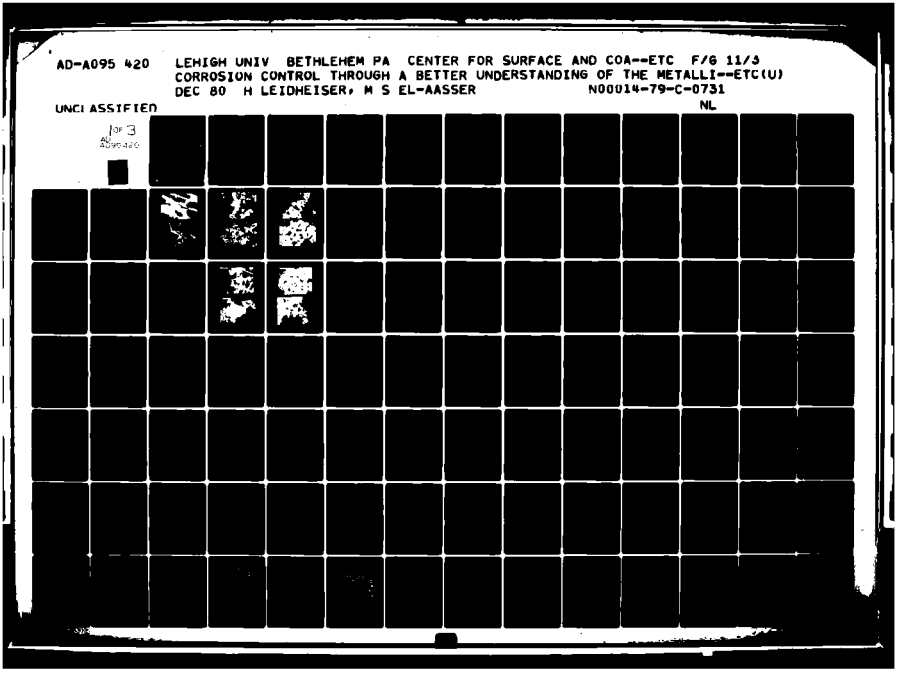

CORROSION CONTROL THROUGH A BETTER UNDERSTANDING OF THE METALLIC SUBSTRATE/ORGANIC COATING/INTERFACE.

Agreement No. N00014-79-C-0731

First Annual Report

Covering the Period,

September 1, 1979-August 31, 1980

Sponsor: Office of Naval Research
Washington, D.C.

Annual rept. no. 1, 1 Sep 79-31 Aug 80,

Principal Investigator: Henry/Leidheiser, Jr.

Co-Investigators: Mohamed S./El-Aasser
Frederick M./Fowkes
Michael C./Hughes
John/Manson
Fortunato J. Micale
David A. Thomas
Gary W. Simmons
John W. Vanderhoff

1 Dec 80

404 103

Center for Surface and Coatings Research
Lehigh University
Bethlehem, Pa. 18015

December 1, 1980

TABLE OF CONTENTS

FOREWORD

This report represents the first summary of experimental results obtained in a coordinated approach to a better understanding of corrosion beneath protective organic coatings. Six sections deal with the substrate/coating interface, 3 deal with the properties of the coating, and one deals with the substrate/interface/coating system as a whole.

A summary of the research is provided at the beginning of the report and a list of public disclosures made during the period, September 1, 1979 - August 31, 1980 is given after the summary.

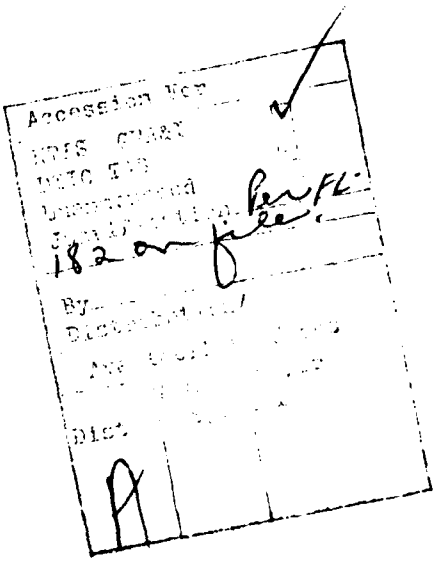

SUMMARY

Many different characteristics determine the protective qualities of organic coating/metal substrate systems exposed to a corrosive environment. This research focuses on the following properties: (a) the oxided surface to which a coating is applied; (b) the stability of the coating/substrate adhesion under adverse conditions; (c) solid/polymer adhesion in terms of the acid and base character of substrate, pigment, filler, and polymer; (d) chemical changes at the substrate/coating interface as a function of time; (e) film-forming mechanisms as they relate to protective properties; (f) morphological characteristics of organic coatings; (g) mechanical properties of organic coatings; (h) effect of pigments and fillers on film properties; and (i) electrical properties of organic coatings as they relate to corrosion behavior. Some of the studies represent direct attacks on understanding these properties and others represent preliminary stages.

SECTION 1

The goal of this research is the generation of information that may be useful in designing coating systems in which the coating may be applied to rusted steel surfaces after only minimal cleaning. The approach involves the preparation of high surface-area iron oxides by two techniques, precipitation from aqueous solution and grinding. Precipitated Fe_2O_3, Fe_3O_4, and FeOOH were prepared and partially characterized by electron microscopic and X-ray diffraction analysis. Fine particle dispersions of Fe_2O_3 and FeOOH were prepared by grinding. Partial characterization of particle size was obtained from settling times. Little success was achieved in reducing the particle size of Fe_3O_4.

SECTION 2

The objective of this work is to determine the solid/gas and solid/liquid interfacial properties of iron oxides that may exist as corrosion products on the surface of iron. Commercial oxides were utilized; products arising from Section 1 will be phased into the work later. Studies were carried out on Fe_3O_4, Fe_2O_3, and FeOOH whose surface areas were in the range of 6 to 20 m^2/g. Water adsorption measurements indicated that Fe_3O_4 has a surface which is 100% hydrophilic, whereas α-Fe_2O_3 is only 80% hydrophilic. The latter material becomes hydrophobic upon heat treatment at 100°. The electrophoretic mobility as a function of pH indicated that the zero point of charge is approximately at pH 4 for both α-Fe_2O_3 and Fe_3O_4. Changes in the surface properties after treatment with hexamethyldisilazane were also determined.

SECTION 3

Coating/substrate interactions and the stability of the adhesion are being studied by damaging a coating with a pin prick and noting the extent of delamination during cathodic treatment in an electrolyte. This research has application to the development of accelerated tests for determining the protective qualities of a coating/substrate system. The rate of delamination of polybutadiene and epoxy-polyamide coatings from steel and galvanized steel substrates during cathodic treatment in an electrolyte decreases in the order CsCl > KCl > NaCl > LiCl. The rate of cathodic delamination of the epoxy-polyamide coatings is a function of the curing procedure used. Under conditions of air saturation of the electrolyte, the rate controlling step in the delamination process is the rate of cation diffusion through the coating. Pretreatment of zinc in $CoCl_2$ solution results in a decreased rate of delamination. This latter effect is attributed to a decrease in the catalytic activity of the zinc oxide at the zinc/organic coating interface for the reaction, $H_2O + 1/2O_2 + 2e^- = 2OH^-$.

SECTION 4

The adhesive forces which govern the bonding of protective polymers to steel surfaces are acid-base interactions, best characterized by the heat of adsorption, ΔH_{ads}. In this work the proposal is tested that the heat of adsorption is equal to the heat of acid-base interaction, ΔH_{ab}, predictable by the Drago equation:

$$-\Delta H_{ab} = C_A C_B + E_A E_B$$

The values of C_A and E_A are being determined for the acidic sites on iron oxide surfaces, measurable by heats of adsorption of model bases of known C_B and E_B. Initial results obtained with iron oxide powders indicate values of C_A of 1.0 and E_A of 2.0 predict heats of adsorption of any base of known C_B and E_B. These findings suggest that the acid sites of iron oxide surfaces are "soft" acids, nearly as soft as iodine, and of slightly stronger acid strength. It is suggested that primers for iron oxide surfaces should feature very soft basic groups. Although most of the heats of adsorption were determined from the temperature-coefficients of adsorption isotherms, a few heats of adsorption were also determined calorimetrically, using a new flow micro-calorimeter; results for pyridine adsorption agreed within 1% of the previously determined values.

SECTION 5

The goal of this phase of research is to characterize those types of surfaces to which coatings are normally applied. The emphasis is on the acid/base character of iron surfaces as a function of pretreatment. Present efforts are focused on development of the technique. The hypothesis is being tested that the ion exchange properties of the surface with calcium ions in solution is a measure of the acid/base character of the surface. The amount of calcium on the surface and the type of surface hydroxyls were quantified by the use of Auger Electron Spectroscopy and X-Ray Photoelectron Spectroscopy. Calcium uptake by an iron surface increased dramatically above pH 11 and by titanium above a pH of 9.

SECTION 6

Mössbauer spectroscopy will be applied to (a) the characterization of iron oxide corrosion products, (b) the determination of chemical changes occurring at the iron/coating interface as a function of time of exposure to a corrosive environment, and (c) the characterization of the chemical bond between substrate and organic inhibitor molecules. The research to date has focused on the development of improved methods for computer analysis of spectral data. A method has been developed and has been written up in very detailed fashion. The present report includes a summary of the philosophy adopted and an outline of the critical steps. Copies of the full report will be provided to those interested.

SECTION 7

The mechanism by which an organic coating is formed may influence greatly its protective properties. Emphasis in the present studies is on the mechanism of cathodic electrocoating and the mechanism of drying of coatings. Epoxy-polyamide coatings were cathodically electrodeposited on steel substrates from an emulsion in an aqueous solution. Thick, smooth coatings were obtained that did not crack on drying and showed adherence to the steel substrate. Data are summarized relating to the morphology of the coating and the coulombic efficiency of the process. A two-stage linear relationship between mass deposited and deposition time was observed. Film growth at the beginning was fast, unimpeded and strongly dependent on the applied voltage. At a later stage, consolidation and compaction began and the film growth slowed to a common rate for all voltages. Distinct

differences in drying behavior were observed between a latex system and a conventional solvent-based system. The solvent-based system exhibited a falling drying rate after the constant rate region. A final rising rate was observed for the latex systems. An aqueous-based, solubilized polymer resin system exhibited a drying behavior intermediate between these two extreme cases.

SECTION 8

Preliminary experiments have been initiated to characterize the morphology of polymer coatings by means of electron microscope studies. Efforts will be made later to relate morphological observations to electrical measurements on the same region of a coating. Initial efforts have been made to determine the penetration of cations and anions into the organic coating.

SECTION 9

Zinc-filled epoxy systems were characterized by (a) drying time, (b) differential scanning calorimetry, (c) sea water permeation, and (d) dynamic mechanical tests. Data are summarized for coatings containing epoxy/polyamide ratios of 0.8 to 1.3 and zinc contents of 0, 77 and 93%. Coatings were also studied in which 50% of the zinc was replaced by ferrophos.

SECTION 10

Corrosion of polymer-coated metals exposed to electrolytes often occurs in a localized manner. An alternating current probe technique has been developed to determine the electrical properties while the coated metal is exposed to an electrolyte. Representative figures are given to show the probe response to purposely-introduced defects in the coating.

PUBLIC DISCLOSURE OF RESULTS MADE DURING THE FIRST CONTRACT YEAR, SEPTEMBER 1, 1979 - AUGUST 31, 1980.

Published Papers

(1) "Appraising the Corrosion Protective Properties of Organic Coatings by Electrical Measurements", H. Leidheiser, Jr., W. Wang, and J. V. Standish, Polymer News 6, 208-14 (1980).

Papers Accepted for Publication

(1) "De-Adhesion at the Organic Coating/Metal Interface in Aqueous Media", H. Leidheiser, Jr., Croatica Chemica Acta, in press.

(2) "Some Substrate and Environmental Influences on the Cathodic Delamination of Organic Coatings", H. Leidheiser, Jr., and W. Wang, Journal of Coatings Technology, scheduled for December 1980 issue.

(3) "Rate Controlling Steps in the Cathodic Delamination of 10-40 Micron Thick Polybutadiene and Epoxy-Polyamide Coatings from Metallic Substrates", H. Leidheiser, Jr. and W. Wang, to appear in book on Proceedings of International Conference on Corrosion Control by Organic Coatings, National Association of Corrosion Engineers.

(4) "An AC Impedance Probe as an Indicator of Corrosion and Defects in Polymer/Metal Substrate Systems", M. C. Hughes and J. M. Parks, to appear in book on Proceedings of International Conference on Corrosion Control by Organic Coatings", National Association of Corrosion Engineers.

(5) "Enhancing Polymer Adhesion by Acid-Base Interactions", F. M. Fowkes, to appear in book on Proceedings of International Conference on Corrosion Control by Organic Coatings, National Association of Corrosion Engineers.

(6) "Some Aspects of Cathodic Electrodeposition of Epoxy Latexes as Corrosion-Resistant Coatings", C. C. Ho, A. Humayun, M. S. El-Aasser and J. W. Vanderhoff, to appear in book on Proceedings of International Conference on Corrosion Control by Organic Coatings, National Association of Corrosion Engineers.

Talks at Professional Meetings

(1) "Enhancement of Mechanical Properties of Filler-Matrix Systems by HSAB Interactions", John A. Manson, American Chemical Society Meeting, San Francisco, August 29, 1980.

(2) "Adsorption Sites of Inorganic Surfaces Characterized by HSAB Interactions", F. M. Fowkes, C.-Y. Sun, S. T. Rubin, and L. A. Casper, American Chemical Society Meeting, San Francisco, August 29, 1980.

(3) "Rate Controlling Steps in the Cathodic Delamination of 10-40 Micron Thick Polybutadiene and Epoxy-Polyamide Coatings from Metallic Substrates", H. Leidheiser, Jr. and W. Wang, International Conference on Corrosion Control by Organic Coatings, Bethlehem, Pa., sponsored by NACE, August 10-15, 1980.

(4) "An AC Impedance Probe as an Indicator of Corrosion and Defects in Polymer/Metal Substrate Systems", M. C. Hughes and J. M. Parks, International Conference on Corrosion Control by Organic Coatings, Bethlehem, Pa., sponsored by NACE, August 10-15, 1980.

(5) "Enhancing Polymer Adhesion by Acid-Base Interactions", F. M. Fowkes, International Conference on Corrosion Control by Organic Coatings, Bethlehem, Pa., sponsored by NACE, August 10-15, 1980.

(6) "Some Aspects of Cathodic Electrodeposition of Epoxy Latexes as Corrosion-Resistant Coatings", C. C. Ho, A. Humayun, M. S. El-Aasser, and J. W. Vanderhoff, to appear in book on Proceedings of International Conference on Corrosion Control by Organic Coatings, Bethlehem, Pa., sponsored by NACE, August 10-15, 1980.

(7) "Characterization of Acidic Sites on Fe_3O_4 Powders", F. M. Fowkes, C.-Y. Sun, and S. Rubin, Adhesion Society Meeting Savannah, Ga., February 12, 1980.

SECTION 1

Objective: An Understanding of the Principles Related to the Application of Paints to Corroded Steel Surfaces with Little or No Surface Preparation

Title: Preparation of Colloidal Iron Sols by (a) Aqueous Precipitation and (b) by Dispersion

Senior Investigator: John W. Vanderhoff

Associates: M. J. Cantow, Visiting Scientist
K. A. Earhart, Research Associate
L. Bennetch, Consultant
M. H. Kang, Graduate Student
D. W. Timmons, Graduate Student

INTRODUCTION

This program has as its goal the generation of information that may be useful in designing coating systems in which the organic coating (paint) may be applied to rusted steel surfaces after only minimal cleaning, i.e., removal only of the loose surface rust. The following approach is being used: (i) preparation of the various corrosion products of iron in colloidal form to give a large surface area for characterization studies; (ii) characterization of the surface of these colloidal particles by gas adsorption, solution adsorption, electrophoresis, surface titration, electron microscopy, acid-base interaction, and other available analytical methods; (iii) determination of the wetting characteristics of various coating systems on these colloidal particles; (iv) correlation with tests on rusted panels. The preparation in colloidal form is being used in order to give a very large surface area for characterization studies, as compared with the small surface areas of rusted steel panels. Different characterization studies can be carried out on the same sample because the relatively small amounts prepared furnish a large surface area. The wetting characteristics of various coating systems, e.g., epoxy resins, can also be determined on samples of large surface areas. Finally, the behavior of the colloidal iron corrosion products will be correlated with the results obtained with rusted steel panels.

The first year's work comprised the development of methods to prepare colloidal sols of the various iron corrosion products. The colloidal sols were prepared using two approaches: (i) aqueous phase precipitation reactions; (ii) dispersion of dried powdered iron compounds.

Preparation of Colloidal Iron Sols by Aqueous Precipitation (M. H. Kang)

Introduction

The proposed approach comprises preventing further corrosion by applying coatings to a rusted steel surface with only minimal cleaning, e.g., wire brushing to remove loose surface matter, but not removing all corrosion products down to uncorroded metal. To minimize corrosion, the coatings system must wet the iron corrosion products thoroughly, filling any voids or interstices in oxide films, to solidify the surface and inhibit further corrosion. To develop such coatings systems requires an understanding of the interactions between the polymers and solvents used in coatings and the corrosion products found on rusted steel surfaces. A colloidal dispersion offers interfacial areas in the order of a square mile, and enhances the

chance of determining interactions between dispersed particles and components of the liquid medium.

Iron corrosion products (1) such as α-FeOOH, β-FeOOH, γ-FeOOH, α-Fe_2O_3, and Fe_3O_4 were chosen to be synthesized as colloidal particles of uniform size and shape in aqueous media. These particles were then to be transferred to organic media using the technique of serum replacement (2) and the interactions with coatings polymers were to be determined using the method of Manson and Fowkes (3,4) in which, by using Drago's equation (4,5) the acid-base interaction between adsorbate and adsorbent can be interpreted quantitatively as well as qualitatively. The conclusions based on the adsorption isotherms were then expected to provide a guideline for the formulation of coatings systems useful for repainting of corroded surface with minimal cleaning.

Experimental Details

The glasswares were cleaned with concentrated HCl followed by chromic acid cleaning solution, and were then thoroughly rinsed with distilled, deionized water.

The sols were prepared using the general method described by Matijević et al. in which the syntheses of iron oxides and hydrous oxides by precipitation were modified by careful adjustment of the relative counter ion concentrations and the premixed iron salt solutions were aged in a closed system at elevated temperatures for a controlled period of time.

The stock solutions of iron(III) chloride were prepared by dissolving about 100g $FeCl_3$ to make up 250 ml solution. After filtration through a 0.2 μm Nucleopore filter, this solution was titrated with standardized $KMnO_4$ solution after reduction by tin(II) chloride. For example, the concentration of iron(III) ions in a stock solution with 103g of $FeCl_3$ was determined to be 2.40M.

Chemical-resistant borosilicate glass containers sealed with screw caps lined with Teflon film were used for these experiments. The aqueous solutions of starting materials were filtered through a 0.2 μm Nucleopore filter to remove any particulate material. The sealed containers were then aged at constant temperature in a preheated circulating-air oven.

X-ray diffractograms of commercial oxides were taken by packing the powder in the hollow space of an ordinary aluminum holder. X-ray diffractograms of the samples prepared in this study were measured from a powder film of sufficient thickness dried by deposition of the thickened sol onto clean glass plates. Several cycles of sol deposition and drying were necessary to build up the sample size owing to the low solids contents of the sols. Before measurement, the samples were dried for at least

24 hrs in a vacuum desiccator. A Siemens diffractometer with $CuK\alpha$ lines (40 KV), Ni filter, and scanning rate of 2°/min was used.

Samples for transmission electron microscopy (TEM) were prepared by applying the diluted sol to a metal grid and drying in air at ambient temperature with protection from dust.

Experimental Results and Discussion

The stock solutions of $FeCl_3$ (e.g., 2.40M) were of high enough concentration so that hydrolysis at ambient temperature was considered not to occur. Several sols were prepared in preliminary experiments with the concentrations of the reactants in the ranges reported by Matijević et al. (6) to give β-FeOOH and α-Fe_2O_3 sols. The details of the preparation and the procedure of cleaning before examination by TEM are listed in Tables I and II. It is shown by TEM that the particles were well-defined, and in some cases both the size and shape were observed to be very uniform. For example, Figure 1 shows that the particles of K-41-1, a yellow sol, were long needles about 3 μm in length, and Figure 2 shows that the particles of K-47-3, a red sol, were uniform and spherical of about 0.1 μm diameter. The electron micrographs of these particles before and after cleaning by serum replacement are shown for comparison.

Figure 3 shows the particles of K-51-1 and K-51-2. The particles of the former are uniform and very similar to those of K-47-3 in both size and shape. The particles of K-51-2 are not quite as uniform in size or shape. Both of these sols, which were prepared with aging period of one week and two weeks, respectively, showed deeper red color than that of K-47-3. SEM is expected to give more information on the morphology of these particles.

The effectiveness of the serum replacement cleaning process as shown in Figure 1 and Figure 2 indicates that this technique can also be used to clean these iron oxide and hydrous oxide sols.

Since the particles generated in K-47-3 (Figure 2) and in K-51-1 (Figure 3,a) were shown by TEM to be nearly monodisperse, these preparations were scaled up with a little modification. The details of the four sols prepared are listed in Table III.

The values of the d-spacings are compared with those of the standard and commercial products in Table IV. It was decided that the preparation of K-129-11 would be adopted as the standard procedure for α-Fe_2O_3 synthesis in the future, provided that TEM and SEM show satisfactory morphology of particles.

Table V gives details for the scale-up of K-41-1 and K-49-1.

Figure 1: TEM of particles in the yellow sol K-41-1: (a) before cleaning; (b) after cleaning.

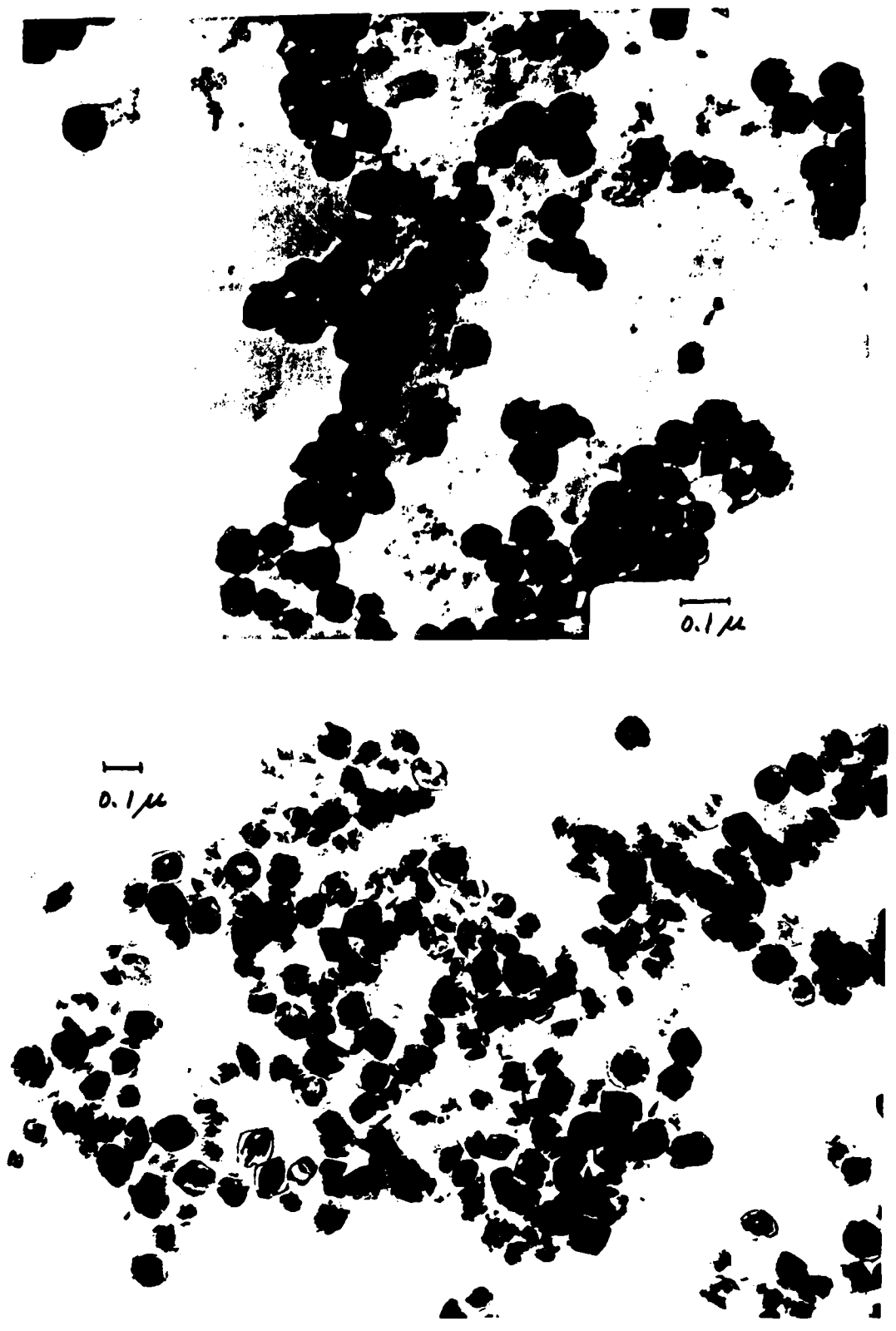

Figure 2: TEM of particles in the red sol K-47-3: (a) before cleaning; (b) after cleaning.

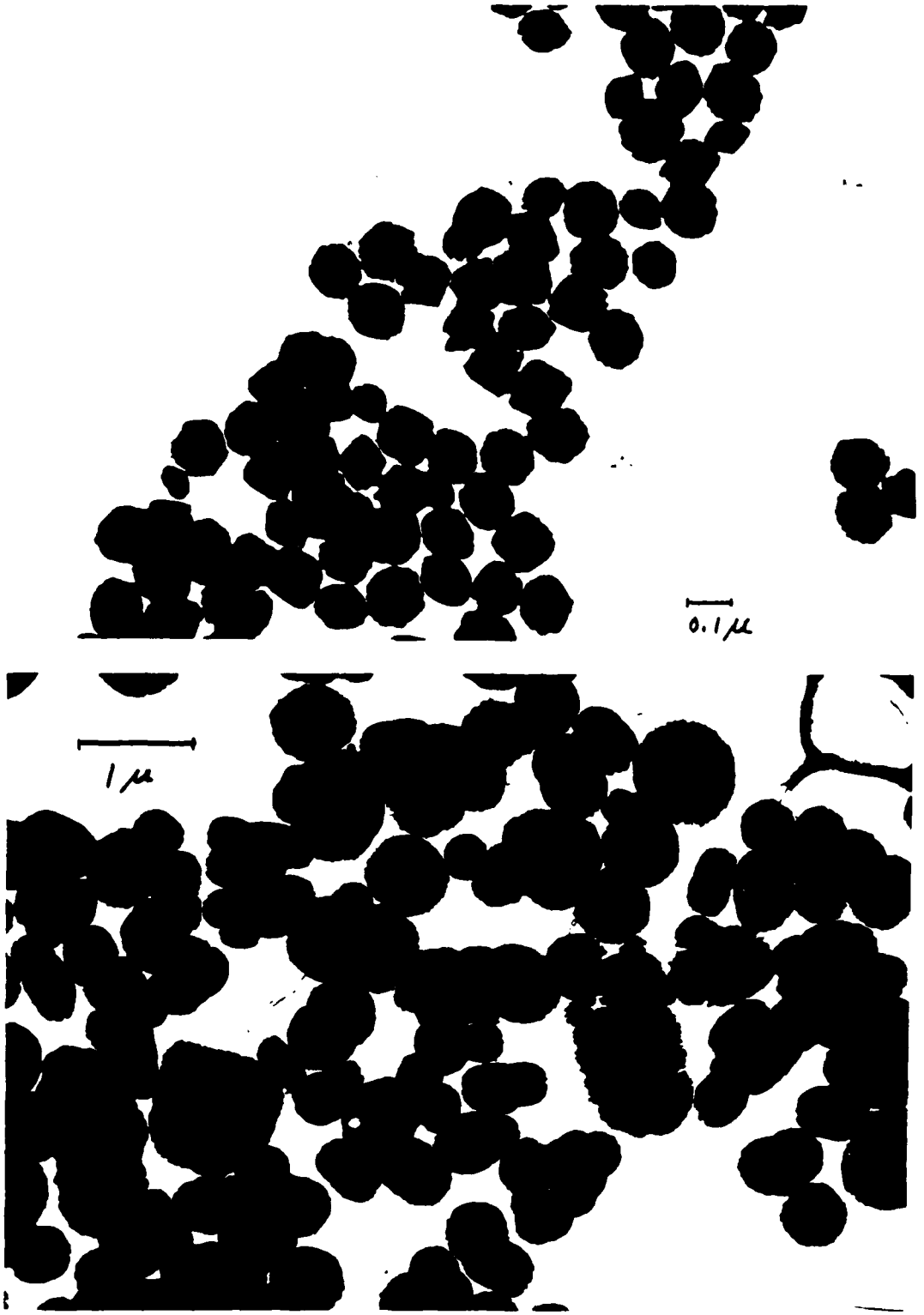

Figure 3: TEM of particles in the red sols K-51-1, (a) and K-51-2, (b), both were cleaned.

Table I

Preliminary Preparation of Sols with Concentrations of Starting Materials within the Ranges for β-FeOOH in the Literature (6)

	K-41-1	K-43-1	K-47-3	K-49-1
[$FeCl_3$], M	0.48	0.019	0.013	0.013
[HCl], M	0.083	0.0010	0.013	0.013
Total Vol.	18 ml	15 ml	15 ml	180 ml
100°C for	24 hr	24 hr	24 hr	24 hr
Cleaning for TEM	collected and rinsed on 0.1 μm nucleopore filter	gentle washing of the dried grid in water at room temperature for 4 min	gentle washing of the dried grid in 60° water for 4 min	gentle washing of the dried grid in water at room temperature for 2 min

Table II

Preliminary Preparation of Sols with Concentrations of Starting Materials Falling in the Ranges (6) for α-Fe_2O_3

	K-51-1	K-51-2
$[FeCl_3]$, M	0.018	0.032
[HCl], M	0.052	0.0052
Total Vol.	20 ml	20 ml
100°C for	1 wk	2 wk
Cleaning for TEM	gentle washing of the dried grid in water at room temperature for 2 min	gentle washing of the dried grid in water at room temperature for 2 min

Table III

Modification and Scaling Up of Some Sol Preparations Aiming at α-Fe_2O_3

	K-129-1	K-129-11	K-129-2	K-129-21
[$FeCl_3$], M	0.018	0.018	0.018	0.018
[HCl], M	0.010	0.010	0.040	0.040
Total Vol.	500 ml	500 ml	500 ml	500 ml
100°C for	24 hr	1 wk	24 hr	1 wk

Table IV

Comparison of the d-Spacings of the Commercial and Synthesized α-Fe_2O_3 to the Standard

α-Fe_2O_3 standard	R-2199 commercial	K-129-11
3.686	3.675	3.631
2.703	2.696	2.665
2.519	2.513	2.493
2.208	2.204	2.189
1.843	1.839	1.829
1.697	1.694	1.685
1.601	1.602	1.592
1.487	1.487	1.483
1.454	1.454	1.445

Table V

Modification and Scaling Up of Sol Preparations
Aiming at β-FeOOH

	K-115-1	K-115-2
[$FeCl_3$], M	0.45	0.012
[HCl], M	0.082	0.013
Total Vol.	500 ml	500 ml
100°C for	24 hr	24 hr

It is of interest that the cleaned particles of the red sol K-115-2 showed broad diffraction peaks with values corresponding to those of R-2199, the commercial α-Fe_2O_3, even though the concentrations of reagents were in the range for β-FeOOH according to Matijević et al. The cleaned particles of K-115-1 were measured using both the aluminum holder and the glass plate. While no conclusions can be drawn by comparison of diffraction pattern from the aluminum holder with the standard (Ref. 7), the values (Table VI) obtained by diffraction from the glass plate did match satisfactorily with the standard.

A suspension of Fe_3O_4, K-79-1, was prepared by a conventional method (Ref. 8) involving heating to boiling of a solution of $FeSO_4$ and $NaNO_3$ after addition of aqueous NaOH. The reaction is believed to be:

$$12\ FeSO_4 + NaNO_3 + 23\ NaOH \longrightarrow 4\ Fe_3O_4 + 12\ Na_2SO_4 + NH_3 + 10\ H_2O. \qquad (1)$$

Another sol of Fe_3O_4, K-107-1, was prepared using a method described by Matijević et al. (Ref. 9) which is actually a modification of the foregoing traditional method. The relative amounts of reagents used are compared in Table VII. Since K-107-1 was prepared by aging (90°C, 4 hr) the premixed reagent solution in a closed system, a much higher quantity of NO_3^-, the oxidant, was required.

X-ray diffraction of cleaned particles of K-107-1 also showed a satisfactory match with the standard. This comparison is shown in Table VIII. The diffraction data for the commercial product, BK-5000, are also listed for comparison.

The commercial γ-Fe_2O_3, MO-2228, and α-FeOOH, YLO-2288D, were measured, and the results are shown in Table IX.

Preparation of Colloidal Iron Sols by Dispersion (D. W. Timmons)

Introduction

The objective of this approach was to obtain commercially manufactured iron oxides known to be components of steel corrosion and disperse these compounds in suitable, coating-related solvents, followed by characterization of the surface properties

Table VI

Comparison of the d-Spacings of the Synthesized β-FeOOH to the Standard

β-FeOOH standard	K-115-1
7.40	7.36
5.25	5.21
3.31	3.31
2.62	2.61
2.54	2.54
1.75	1.75
1.64	1.64

Table VII

Relative Concentrations of Reagents Used in Two Different Preparations of Colloidal Fe_3O_4 Particles; Actual $[Fe^{2+}]$ in K-107-1 : 0.030 M

	K-79-1	K-107-1
$[Fe^{2+}]$	100	100
$[OH^-]$	200	160
$[NO_3^-]$	8.5	660

Table VIII

Comparison of the d-Spacings of the Commercial and Synthesized Fe_3O_4

Fe_3O_4 standard	BK-5000 commercial	K-107-1
4.850	4.790	4.980
2.967	2.948	3.015
2.532	2.513	2.568
2.099	2.083	2.120
1.715	1.705	1.726
1.616	1.609	1.630
1.485	1.478	1.495

Table IX

Comparisons of the d-Spacings of the Commercial γ-Fe_2O_3, (a), and α-FeOOH, (b), to the Standard

(a) γ-Fe_2O_3 standard	MO-2228 commercial	(b) α-FeOOH standard	YLO-2288D commercial
5.90	5.94	4.98	4.98
2.95	2.95	4.18	4.15
2.52	2.52	3.38	3.37
2.08	2.08	2.69	2.68
1.61	1.60	2.45	2.44
1.48	1.47		

of the oxides. Finally, the adsorption of various coating systems on these oxide surfaces are to be studied, to determine which have the best adsorptivity.

When the project was initiated, the eight compounds identified as known corrosion products included α-, β-, and γ-FeOOH, α- and γ-Fe_2O_3, Fe_3O_4, and $FeCO_3$. Various chemical companies were contacted to determine which were capable of supplying these compounds. Pfizer Chemical (Easton, Pennsylvania) was the only company contacted which could supply oxides in sufficiently pure form required for these studies. Of the eight compounds sought, only α-FeOOH, α- and γ-Fe_2O_3, and Fe_3O_4 were obtained. The crystalline shapes of these compounds are well documented in the literature and electron microscopy was employed to check on the claims of high purity. One finding was that the α-FeOOH had a visibly different outer edge than the central portion of the crystal. Through subsequent discussion with Pfizer, it was determined that the outer layer was the result of treatment of the oxide with a protective sulfate solution. Since this layer could not be removed without altering the surface properties of the oxide, an alternative source of the material was required. Therefore, samples of the seed material and also the production product prior to the treatment step were obtained.

While the process of locating and acquiring these compounds proceeded, an exhaustive literature search was conducted. This search emphasized the compounds which it seemed were most likely to being obtained. One product of the search was a number of solubility parameters. It was initially thought that these might prove useful in reducing the particle size of the oxides and thus facilitate their dispersion, but the chemistry of the crystalline lattice binding forces and the fear of sample contamination made this approach infeasible.

Experimental Results and Discussion

Because the surface of these oxides should not be altered during the dispersion process, the conventional methods employing surfactants or wetting agents were rejected. Earlier work showed that the technique of ball-milling had promise of dispersing various oxides. Care was taken in the selection of the grinding material and the milling bottles to ensure that there would be little or no interaction between them and the oxides during the milling process.

The final choice for the system was polypropylene "animal feed" bottles and ceramic milling cylinders (Fisher Chemical). The dispersing medium was distilled, deionized water, since it was desired that ions not be present in the medium. All glassware which contacted the oxides was washed thoroughly with tap

water, wiped with paper towels, and then rinsed at least three times with distilled, deionized water. The reason for use of the towelling step was that the oxides have a tendency to coat the glassware, possibly resulting in contamination of the samples. In addition, all bottles and cylinders were thoroughly rinsed in distilled, deionized water to remove any dust associated with their manufacture or storage. At the same time that samples were dispersed by ball-milling, similar dispersions were made using The Red Devil Paint Shaker with glass beads. The purpose of this effort was to correlate the effectiveness of the two methods in wetting the oxide. It was found that Red Devil Paint Shaker was more effective. This result was expected since the shaker action is more violent. The amount of oxide in each sample was fixed at 1g.

The two parameters which were varied in the initial studies were the amount of grinding material (number of milling cylinders) and the milling time. It was found that the effect of milling ball number on the stability of the dispersion was slight in the range of 25-40 studied. Since the volume of the bottles was fixed at about 200 ml, large numbers of balls meant a decrease in the water content of the bottle and the amount available to wet the oxide; therefore, the minimum number of balls was used. Subsequently, all later experiments used 25 milling cylinders. For the milling time variations, each of the six oxides was milled for 24,72, and 120 hours. After milling, dispersions were transferred to glass bottles of similar volume, and the settling times were noted and recorded.

The results of these observations are presented in tabular form in Table X. Figure 4 shows schematically the settling patterns of the oxides. Table X shows that the Fe_3O_4 was relatively insensitive to increased milling time. The α-FeOOH seed showed the greatest sensitivity to the milling process, and the other four samples had comparable sensitivity. Figures 5 and 6 show TEM photographs of ball milled products. The numbers given in the table are representative of the settling times noted. Moreover, the settling times of the samples shaken for 30 minutes on the Red Devil Paint Shaker correlated well with those of the 24-hour milled samples. The numbers in parentheses represent one experiment in which the settling times differed drastically from the normally observed values. The numbers resulted from a repeat check of the samples after aging for 60 days. These two oxides are the only ones in which the settling time changed appreciably in that time period. Other samples checked before and after that particular experiment failed to show this effect. For that reason, possible variations between this system and the others will be conducted using X-ray diffraction and Auger Spectroscopy to determine if the compound changed structure during the aging process. Aside from their unusually long settling times, the pattern of settling was also different. No sharp definition of the larger particles was noted, as in the other settling patterns (see Figure 4). Instead, the consistency

Table X

Oxide Settling Times
(Hrs)

milling time (hrs) / compounds	24	72	120
α-Fe_2O_3	2.5 (78)	4	6.5
γ-Fe_2O_3	0.33	0.5	0.75
Fe_3O_4	1	1	1.5
α-FeOOH	1.75 (97)	3	4.75
α-FeOOH seed	0.5	3.25	10.5
α-FeOOH untreated	3	1.5	4.75

TYPICAL:

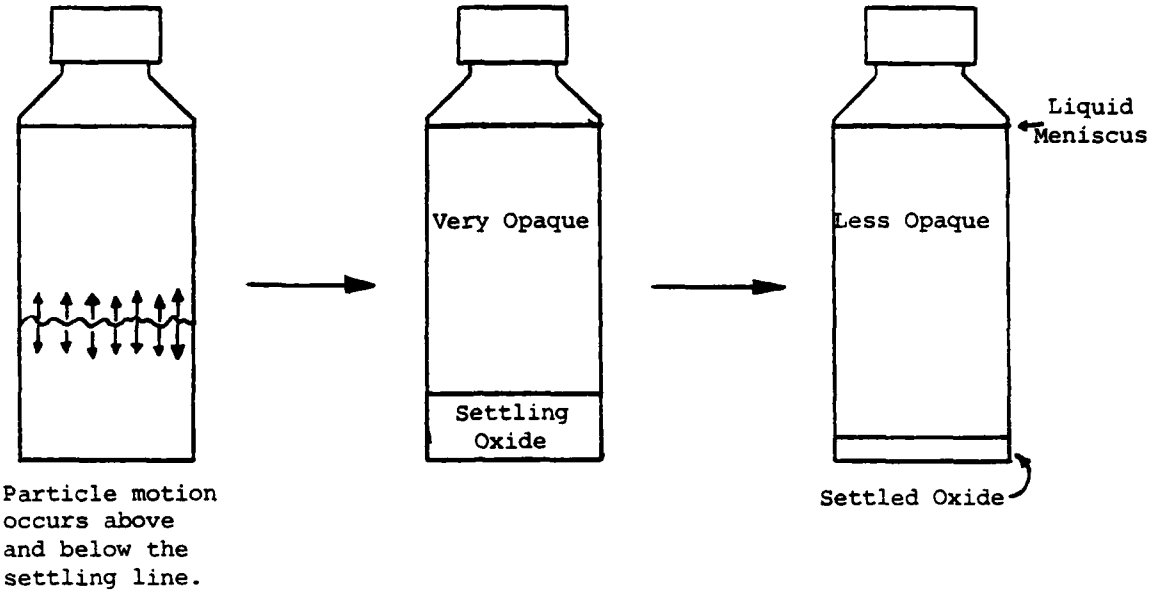

SPECIAL CASE:

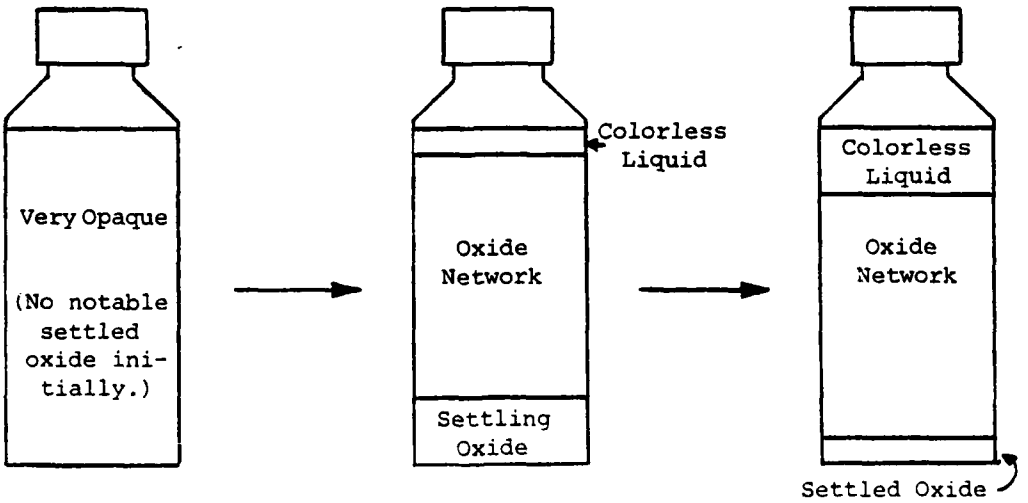

Figure 4. Settling Patterns of Oxides

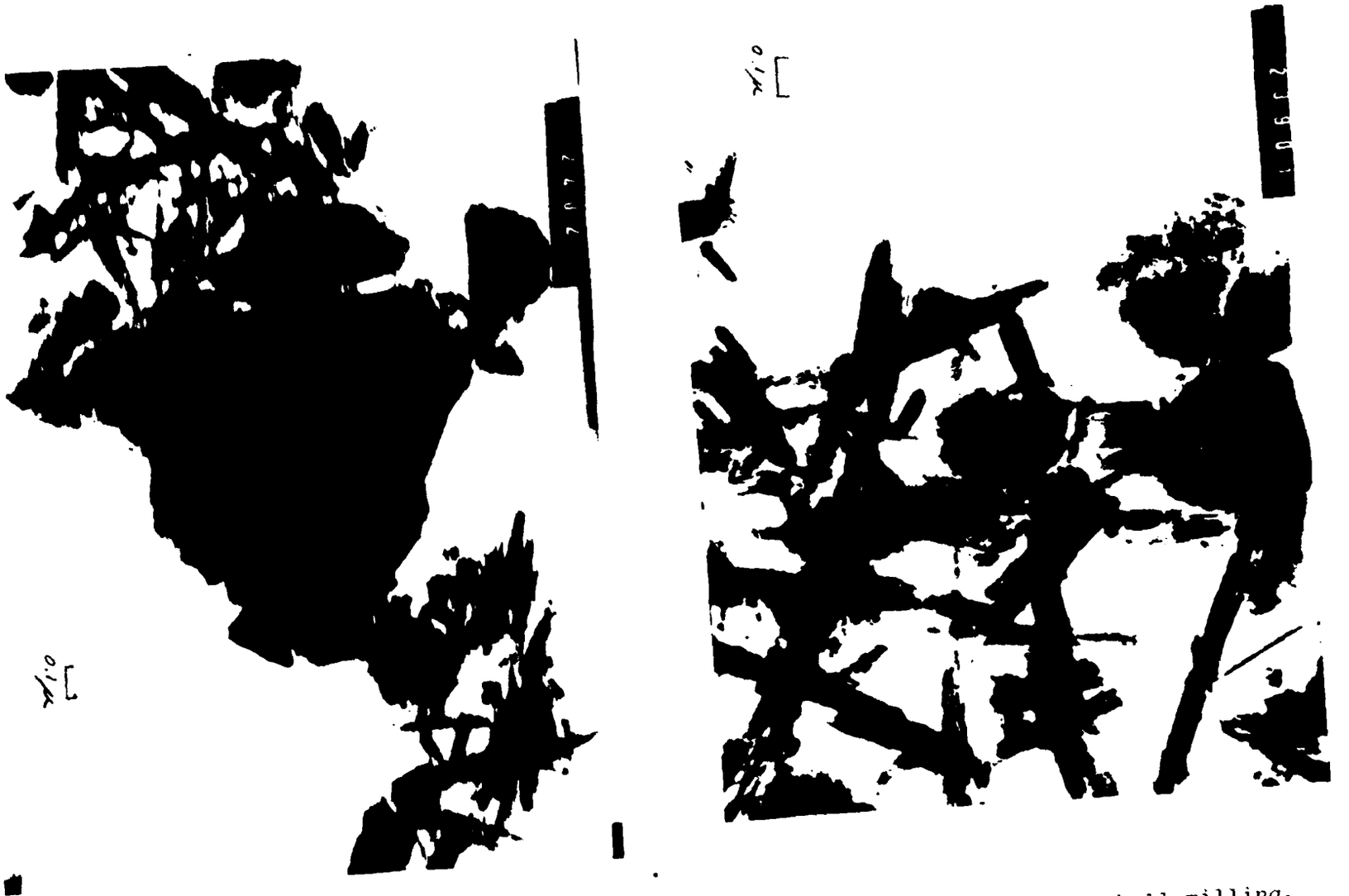

Figure 5. TEM of α-$Fe(OH)_3$ seed particles after 24 hours (a) and 120 hours (b) bail-milling.

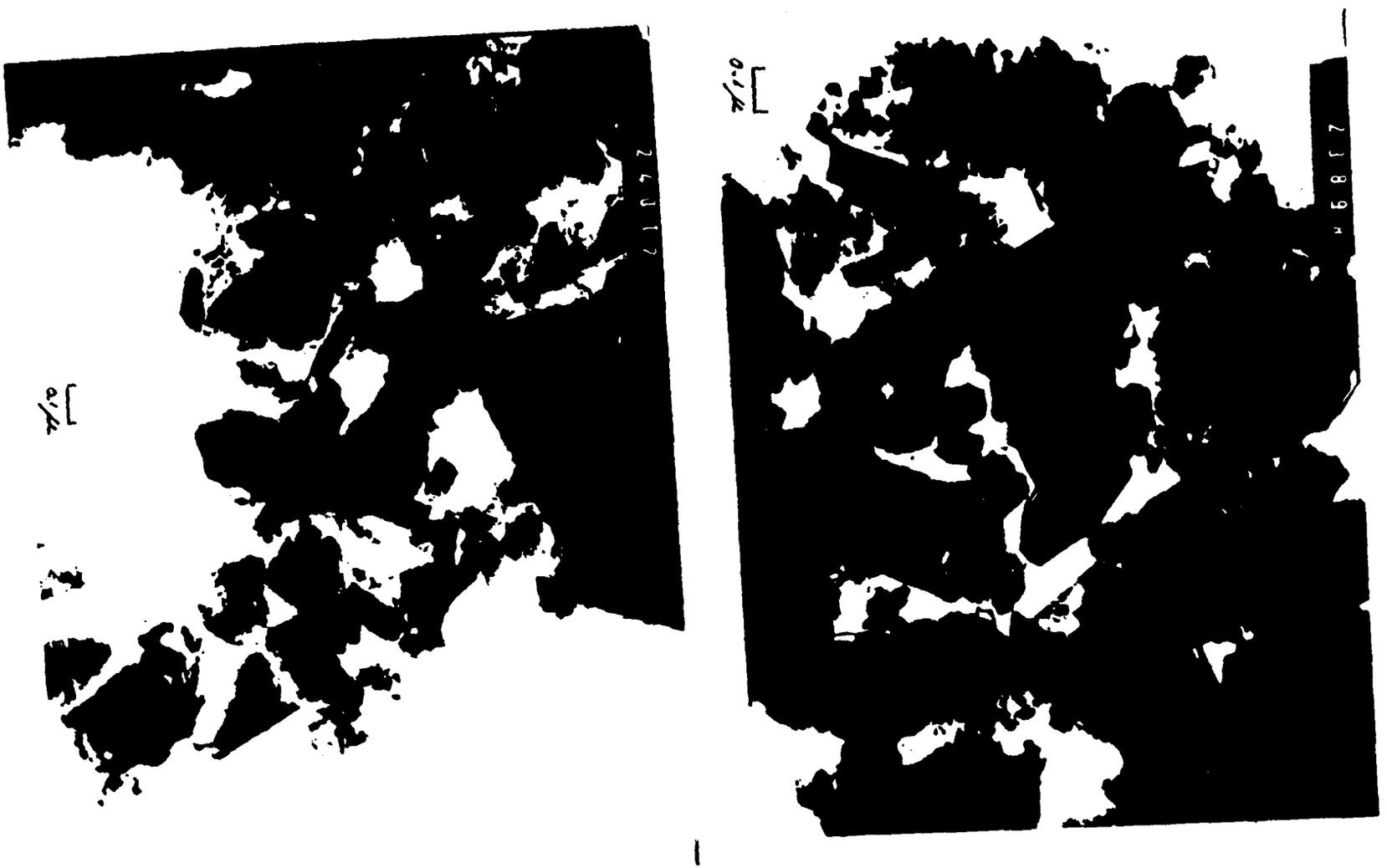

Figure 6. TEM of Fe_3O_4 particles after 24 hours (a) and 120 hours (b) ball-milling.

appeared to be uniform, and some network appeared to hold the dispersions, although it was not thick or gelatinous. Some of the oxide particles settled out initially, as in all other cases, but then the solution cleared at the top and settled out as an opaque region. In the other cases, the dispersions gradually cleared at the top as oxide particles continually settled out from all regions.

The reason that such emphasis has been placed on these two samples is that their 3.0-3.5 day stability lends itself to the preferred method of polymer adsorption study, serum replacement. Thus, these experiments will be repeated. If the X-ray diffractograms show that these oxides are as reported, and if the parameters required to achieve these suspension times can be determined, the polymer adsorption studies will be initiated. Work will also be continuing on the other oxides to determine if similar parameters can be determined.

SECTION 2

Objective: To Characterize the Surface Properties of Iron Oxide and Hydroxide Corrosion Products

Title: Characterization of the Surface of Iron Oxide Corrosion Products

Senior Investigator: F. J. Micale

Associates: T. Vital
C.-C. Yu

Introduction

The development of protective coatings for metallic substrates requires a knowledge not only of the physical properties of the coating, but also the nature of the interaction of the coating with the substrate. Corrosion products on the substrate of interest in this program are iron oxide, iron hydroxide, and iron carbonate. Since the coating can be expected to interact with the corrosion products present on the surface, identification of the corrosion products as a function of the corrosion environment, and a knowledge of the surface properties of the corrosion products are necessary in order to enhance both the adhesion and interfacial protective features of the coating.

The objectives of this phase of the program are to determine the solid/gas and solid/liquid interfacial properties of different corrosion products and to determine the change in surface properties as a function of pretreatment conditions. The pretreatment conditions which have been investigated thus far are high temperature (up to 300°C), outgassing under high vacuum, and chemical treatment of the surface with hexamethyldisilizane, HMDS, which interacts quantitatively with surface hydroxyl groups. The reason for this approach is to determine what conditions are necessary to render the iron oxide surfaces hydrophobic, and to what extent this can be accomplished irreversibly.

Experimental

The iron oxide samples used in this study were obtained from Pfizer Inc. and were designated: black, Fe_3O_4; magnetic, γ-Fe_2O_3; red, α-Fe_2O_3; and yellow, FeOOH. Both the magnetic, γ-Fe_2O_3 and yellow, FeOOH were found, according to specifications obtained from Pfizer, to contain surface impurities and thus were not investigated intensively. Much of the future work is expected to be carried out on iron oxide samples prepared in our laboratory. See Section 1.

The argon gas adsorption isotherms for specific area determination were obtained at liquid nitrogen temperatures using a classical BET volumetric vacuum rig. The residual pressure of 10^{-6} Torr was monitored by an ion gauge. A capacitive electronic manometer equipped with a 1000 Torr differential pressure transducer (Datametrics, Inc.) was used to measure the argon gas pressure with a sensitivity of 10^{-3} Torr. Specific areas were calculated for argon molecular cross-section of 17 $Å^2$. The water adsorption isotherms were measured on a quartz spring (Worden Quartz Co) balance with a sensitivity of 10 µg/g of sample. The equilibrium water vapor pressure was measured with a 100 Torr capacitive differential manometer (Datametrics,Inc.).

The iron oxide samples were prepared for electrophoretic mobility measurements by ultrasonic dispersion in the medium of interest. Three electrophoresis systems were used in this study: Rank Brothers Mark II, Pen Kem Model 500, and Pen Kem Model 3000. The latter instrument, currently on loan from the Pen Kem Co., is completely automated and requires less than 5 minutes to complete a measurement, as opposed to about 30 minutes for the other instruments. This feature allows the electrophoretic mobility to be measured as a function of time.

Results

Water Adsorption

Argon adsorption isotherms were measured on the four available iron oxide samples. The results, Table XI, show that all four samples have sufficient surface area for carrying out gas adsorption measurements. The high BET C values, which are a relative measure of the average energy of adsorption as an exponential function of C, were high for all the samples with the possible exception of yellow, FeOOH. These results indicate that the surfaces are generally homogeneous and hence crystalline in nature. A comparative analysis of the shapes of the isotherms with isotherms of known materials indicates that the samples were nonporous.

Table XI

Argon Adsorption Results on Iron Oxides

Sample	Specific Surface Area, M^2/g	BET C Value
Black, Fe_3O_4	5.72	
Magnetic, γ-Fe_2O_3	19.80	1158
Red, α-Fe_2O_3	9.96	3589
Yellow, FeOOH	10.66	445

Water adsorption isotherms were measured on red, α-Fe_2O_3 at 0 and 25°C for the sample activated at 25°C. The isotherms were essentially reversible with a b-point monolayer value of 8 molecules/100 $Å^2$, indicating that the surface is about 80% hydrophilic. The isosteric heats of adsorption calculated from these isotherms are presented in Figure 7. The results show high heats of adsorption, indicative of strong physical adsorption, below 4 molecules/100 $Å^2$, which gradually decrease to close

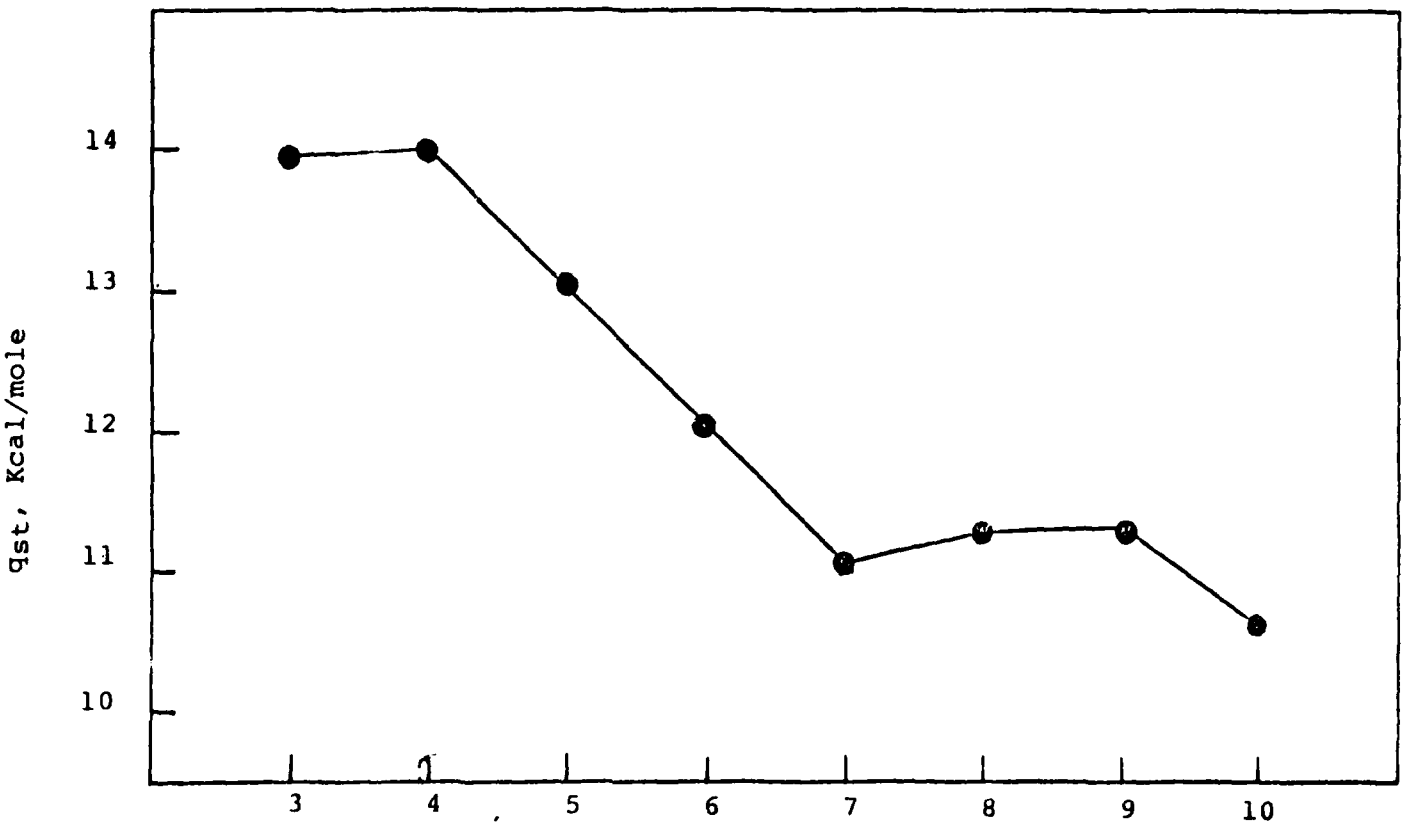

Figure 7. Isoteric Heats of Water Adsorption on α-Fe_2O_3 Activated at 25°C.

to the heat of vaporization of water (10.5 kcal/mole) at a surface coverage of 7 molecules/100 $Å^2$. The red α-Fe_2O_3 was also activated at 100°C prior to water adsorption isotherm measurements at 0°, 25°C and 50°C. The isotherms, however, were not reversible and hence the isosteric heats of adsorption could not be calculated from these data. Figure 8 shows an adsorption-desorption isotherm measured at 25°C with the sample activated at 100°C. The monolayer value for this adsorption isotherm was 7.7 molecules/100 $Å^2$ while a second isotherm measured on the same sample after 25°C activation yielded a monolayer value of 5.7 molecules/100 $Å^2$. The decrease in the monolayer value, which corresponds to the strong physically adsorbed water was 2.0 molecules/100 $Å^2$. The weight loss which occurred in the activation from 25 to 100°C also yielded a value of 2.0 molecules/100 $Å^2$.

Water adsorption isotherms were also measured on black Fe_3O_4 according to the following procedure. The sample was activated at 25°, 100°, 200°, and 300°C. Water adsorption isotherms were measured at 25°C following each activation, followed by a second isotherm after 25°C activation. Figure 9 summarizes the monolayer results for both Fe_3O_4 and α-Fe_2O_3. The results for the first isotherm show that the water monolayer increases with increasing activation temperature up to 200°C followed by a decrease at 300°C. The second isotherm results show only a small linear decrease in the monolayer value with increasing activation temperature. Furthermore, the differences between the first and second monolayer values, which is indicative of the degree of chemisorbed or strong physically adsorbed water, decreases dramatically after 300°C activation. The indication is that the water which is desorbed, primarily in the range of 200° to 300°C, is not readsorbed at 25°C. The weight loss results over this temperature range are shown in Figure 10 and compared to the cumulative irreversible water adsorption, i.e., the difference in monolayer values between the first and second isotherms. These results show that for both Fe_3O_4 and α-Fe_2O_3 strong physical adsorption of water is involved up to an activation temperature of 100°C due to the fact that whatever is removed at the elevated temperature can be readsorbed at 25°C. This is not true at higher temperatures where the surface is altered irreversibly.

Although the results are not yet complete, especially for the α-Fe_2O_3, there are some interesting comparisons to be made between the two iron oxides. Fe_3O_4 is essentially 100% hydrophilic after 25°C activation as compared with 80% for α-Fe_2O_3. After activation at 100°C α-Fe_2O_3 becomes more hydrophobic indicating, even at this temperature, an irreversible change in surface properties. These results, however, are not yet conclusive due to the limited data available.

Electrical Double Layer Properties of Iron Oxide

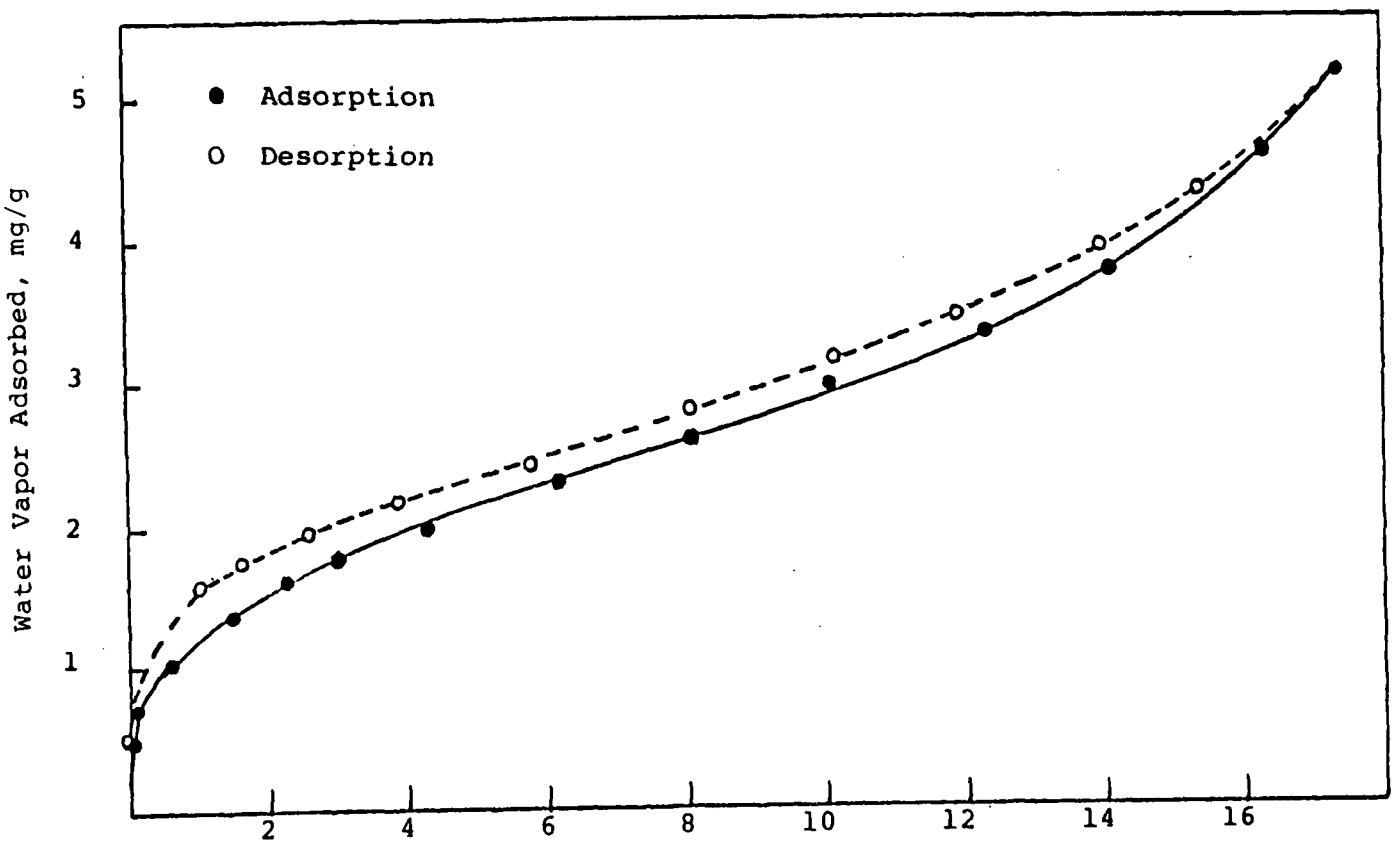

Figure 8. Water Adsorption-Desorption Isotherm at 25°C on α-Fe_2O_3 Activated at 100°C.

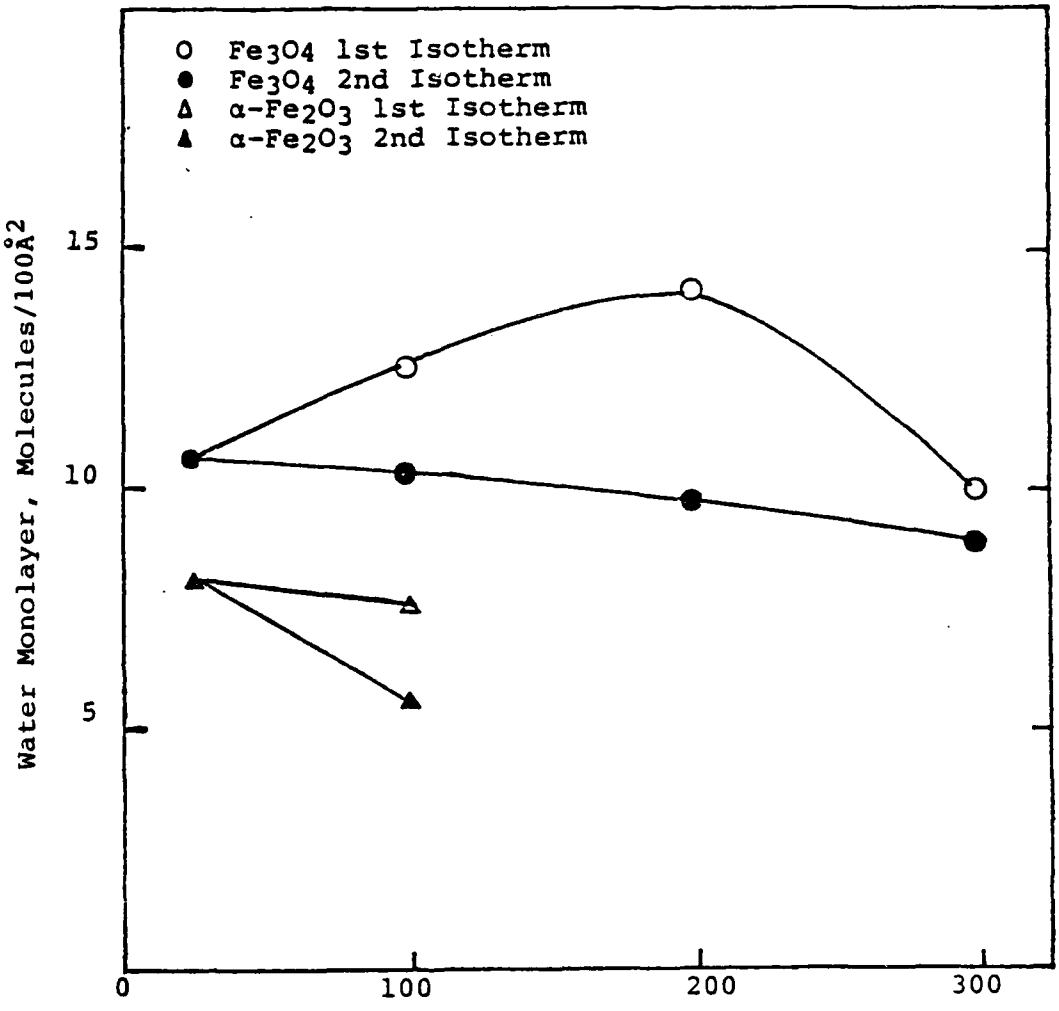

Figure 9. Water Monolayer Results on Iron Oxides Obtained from Water Adsorption Isotherms at 25°C after Activation at the Indicated Temperature (1st Isotherm) and after Subsequent Activation at 25°C (2nd Isotherm).

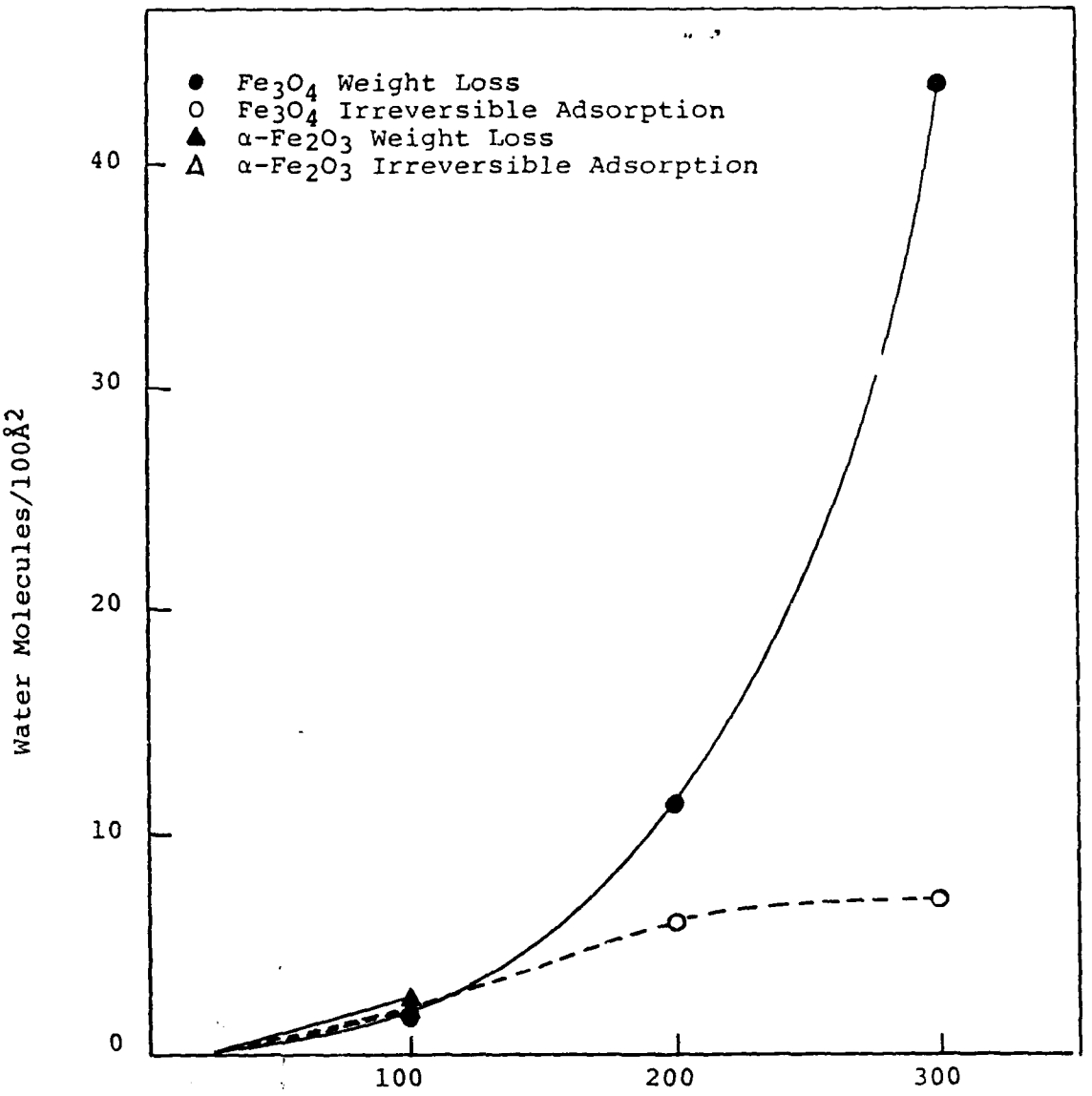

Figure 10. Weight Loss and Cumulative Irreversible Adsorption of Water as a Function of Activation Temperature.

Electrophoretic mobility measurements were carried out for all four iron oxide samples, Table XI, in the pH range of 4 to 8. All the samples, with the exception of yellow FeOOH were negative over the entire range. The behavior of yellow FeOOH was attributed to its surface treatment which was designed to aid in dispersibility in aqueous systems. The results of these measurements were erratic both in terms of dispersion aging effects and reproducibility. An effort to find out the cause for this behavior was carried out with black Fe_3O_4 and red α-Fe_2O_3 dispersions by performing a large number of measurements, at least three for each run, on the automated Pen Kem electrophoresis apparatus. An additional sample which was investigated was black Fe_3O_4 treated with hexamethyldisilazane, HMDS, where the HMDS was designed to react with the surface hydroxyls resulting in a hydrophobic surface.

The iron oxide samples were prepared by carrying out the dispersion just prior to the measurements. This procedure allowed the electrophoretic mobility to be followed as a function of time where the first measurement was taken after aging for five minutes. Although equilibrium generally occurred within two hours, long range aging effects are still being investigated. Figure 11 summarizes the electrophoretic mobility results as a function of pH for α-Fe_2O_3, Fe_3O_4, and HMDS treated Fe_3O_4. The results show that both α-Fe_2O_3 and Fe_3O_4 exhibit similar behavior as a function of pH, with a zero point of charge at a pH close to 4. Although only limited results are currently available for the HMDS-treated Fe_3O_4, this sample exhibits a much stronger positive character which may be attributed to a blocking mechanism of the surface hydroxyl groups.

The electrophoretic mobility was also measured as a function of time with the first point being measured after five minutes of aging. The Fe_3O_4 sample did not show any significant change with time. The results for the α-Fe_2O_3, Figure 12, show that dramatic changes occur when the electrophoretic mobility is small, i.e. at pH values close to 4. Also, a concentrated dispersion at pH 4 exhibited essentially no change with time. Since the concentration of dispersion was not quantitative, but was primarily prepared only for convenience of measurement, more work will have to be carried out in order to verify these results.

Water adsorption isotherm measurements will be continued on both α-Fe_2O_3 and Fe_3O_4 for activation conditions up to 400°C. Work will also be initiated for both oxides treated with HMDS. The specific surface area will also be followed as a function of activation temperature and HMDS pretreatment. The electrophoretic mobility will be measured as a function of pH and time for the iron oxides which have undergone different activation temperatures and HMDS treatments. Also, the chemical treatment of the surface will not necessarily be limited to HMDS, but will be extended to other molecules such as silanes with different functional groups.

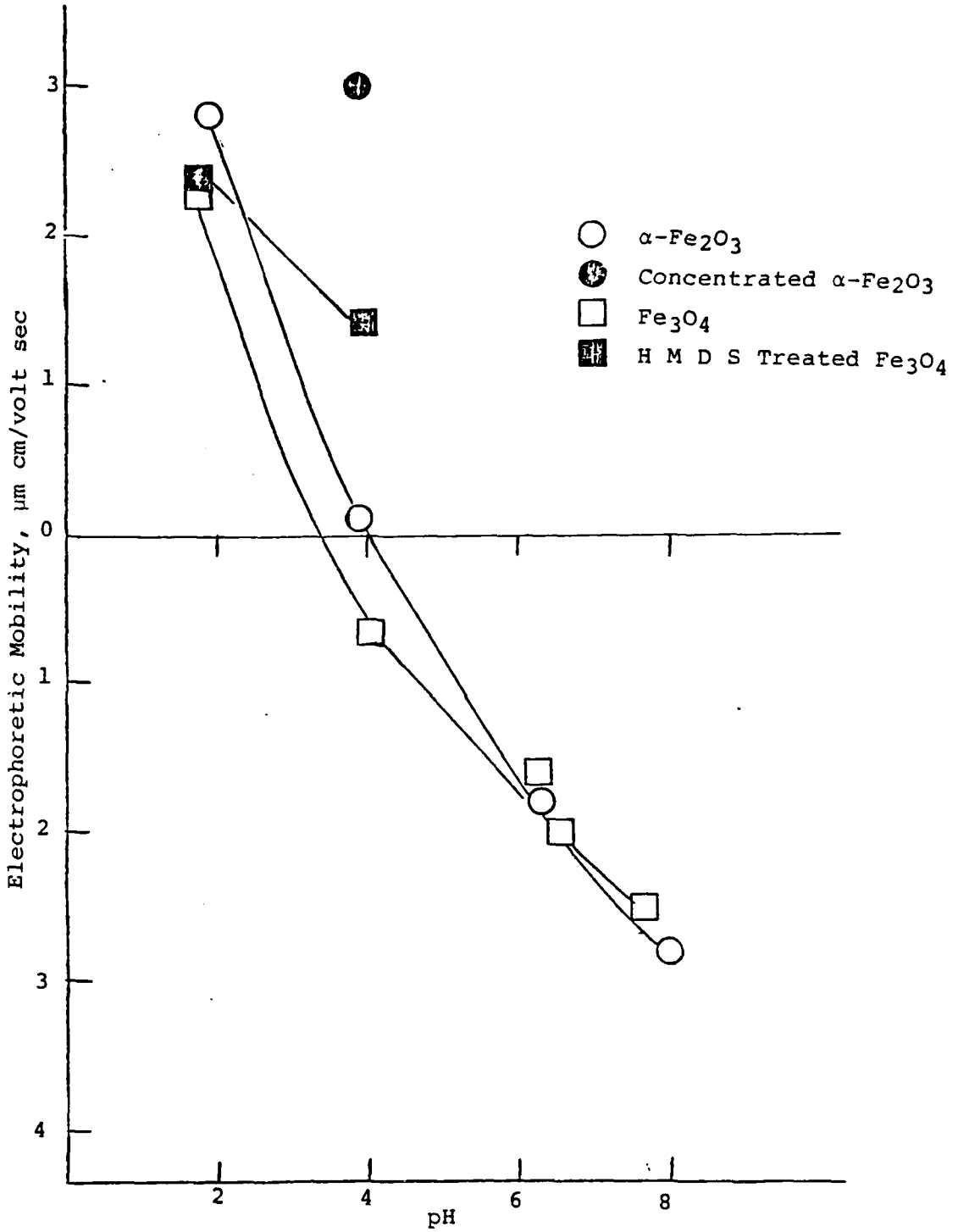

Figure 11. Electrophoretic Mobility of Fe_3O_4 and α-Fe_2O_3, after Aging for More Than One Hour, as a Function of pH.

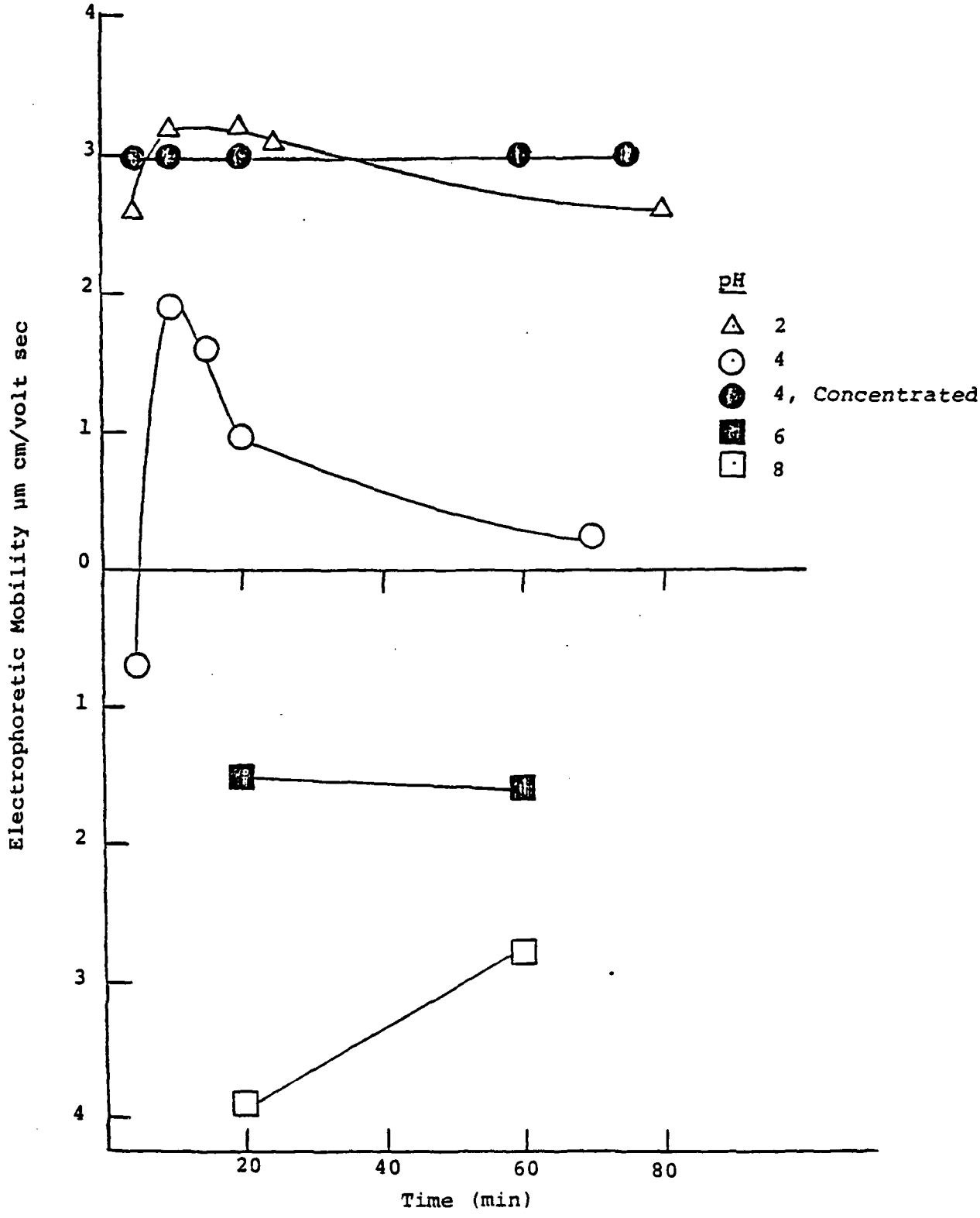

Figure 12. Electrophoretic Mobility of α-Fe_2O_3 as a Function of Time at Different pH Values.

SECTION 3

Objective: An Understanding of Those Factors that Control the De-Adhesion of an Organic Coating from a Metallic Substrate When Exposed to an Aggressive Environment

Title: Rate Controlling Steps in the Cathodic Delamination of 10-40 μm Thick Poly-Butadiene and Epoxy-Polyamide Coatings from Metallic Substrates

Senior Investigator: Henry Leidheiser, Jr.

Associate: Wendy Wang, Graduate Student

Introduction

The major function of an organic coating in providing corrosion protection to a metallic substrate is to serve as a barrier to reactants in the environment such as water, oxygen and other gases, and ions. Since all organic coatings are permeable to these species in some degree, the important consideration is whether or not the corrosion reaction occurs when the species are in the vicinity of the metal surface. If the reaction does occur, a natural consequence is localized delamination of the organic coating from the metallic substrate. Alternatively, the presence of a defect in the coating permits electrolyte to reach the metal surface and the protective value of the coat- is determined to a major extent by the ability to resist delamination laterally from the defect. In both the absence and presence of a defect the precursor to the loss of corrosion protection is delamination of the coating with consequent exposure of the metal to the corrosive environment. Studies of the delamination process are thus of relevance in understanding corrosion protection by an organic coating.

Delamination of an organic coating by a corrosion reaction is generally considered to result because of the separation of the cathodic half reaction, $H_2O + 1/2O_2 + 2e^- = 2OH^-$, which occurs under the coating, from the anodic half reaction, $Fe - 2e^- = Fe^{++}$, which occurs at a defect. The mechanism of the delamination process itself is poorly understood but it is thought to result from attack of the coating or the interfacial bond by the very alkaline conditions generated at the leading edge of the delaminating region (10). Acceptance of the above concepts implies that delamination should be accelerated under conditions where the metal is made the cathode in an aqueous medium. Cathodic treatment does indeed accelerate delamination and cathodic delamination is widely used as an accelerated test method for determining the quality of an organic coating/metal substrate system.

The study reported herein represents the second stage in efforts to understand better the corrosion phenomena involved in the delamination of organic coatings from metallic substrates when the metal is made the cathode while immersed in an electrolyte. The previous study (11) identified the following variables as important in the delamination phenomenon: oxygen in electrolyte, film thickness, substrate metal, pretreatment of the substrate, type of electrolyte, concentration of electrolyte, and temperature.

The purpose of this report is to utilize data obtained in the prior investigation of polybutadiene coatings and new information on epoxy-polyamide coatings in an effort to explain the cathodic delamination process in a more quantitative manner.

Experimental Procedure

Three different substrate materials were used with the epoxy-polyamide coatings: (1) a commercial cold rolled steel, 0.09 cm in thickness, obtained in the form of square panels, 30x30 cm, from Bethlehem Steel Co., (2) commercial galvanized steels in the form of panels, 10x30 cm and 0.05 cm in thickness, (3) aluminum 1100 panels, 30x30 cm and 0.035 cm in thickness, obtained from a commercial source.

Several surfacing procedures were used. Aluminum samples were used after degreasing in trichloroethylene. The term "polished" refers to samples that were degreased in trichloroethylene followed by abrasive polishing with metallographic paper. "Acid cleaned" samples were immersed for 5 min at 70-90°C in a 1:1 solution of concentrated HCl and water, rinsed in distilled water, and then immersed in a 1:1 solution of concentrated sulfuric and nitric acids at room temperature for 10 seconds. The panels were rinsed in distilled water, immersed for 5-10 min in 5% NaCN solution at room temperature, rinsed in distilled water, dried in acetone, and stored in acetone until ready for application of the coating. "Alkaline cleaned" panels were immersed for 5-10 min at 80°C in a 200 cm^3 solution containing 6 g NaOH, 4.8 g Na_2SiO_3, 0.6 g EDTA, 0.48 g Na_2CO_3, and small amounts of the wetting agent, hexadecyl trimethyl ammonium bromide. The panels were thoroughly rinsed in distilled water, dried in acetone, and stored in acetone until ready for the application of the coating.

Information on the polybutadiene coatings has been given previously (11). Coatings were prepared from Epon 1001 obtained from Shell Development Company and Polyamine Emerez 1511 obtained from Emery Industries Inc. Both components were dissolved separately in a solvent consisting of 65 wt % butyl cellusolve and 35 wt % xylene. The coating formulation was a 2:1 mixture of the epoxy and polyamide solutions. The mixture was stirred for one hr before applying to the metal surface using a standard applicator technique. Three different curing techniques were used. The one used in the majority of the experiments consisted simply of curing in air at room temperature for one week. A second procedure involved heating in air at 100°C for one hr before curing at room temperature for a week and the third procedure involved curing in air for one week followed by heating in air at 100°C for one hr. Unless otherwise stated, the delamination process was studied on samples that had been cured at room temperature.

Coated samples, 7.5x10 cm, were cut into pieces, approximately 2x6 cm, and the edges and backside were protected from the electrolyte with a thick coating of a commercial pigmented epoxy-polyamine applied with a brush. Just before the experiment was initiated, the center of the sample was damaged by

pressing a pointed instrument into the surface. The exposed metal was approximately 0.001 cm^2 in area.

The experimental procedure has been described previously (11). The cathode potential was sensed with a capillary tube filled with the electrolyte which was connected by means of a "U" tube to a vessel holding the reference electrode, a saturated calomel electrode (SCE). All potentials are given with respect to SCE. The cathode potential was held constant during the experiment by means of a potentiostat and the current flowing through the cathode/electrolyte interface was monitored continuously during the experiment.

The cathode potential used with each metal was selected early in the study on the basis that a current of approximately 10 μamp flowed shortly after the experiment was initiated. Unless otherwise noted in the text, the following cathode potentials were used:

Aluminum	-1.39 v
Steel	-0.95 v
Zinc (galvanized steel)	-1.35 v

It will be noted that these potentials are slightly different from those used in the previous study with polybutadiene coatings. The measured cathode potential was not critically sensitive to the location of the capillary tip so long as the tip was within a mm of the defect and did not cover the defect.

The delaminated area was determined after the completion of the experiment by removing the delaminated coating with adhesive tape and measuring by microscopic examination the area that was removed. No coating was removed if the adhesive tape was applied to the defect before exposure to the electrolyte.

The term "delamination parameter" used in the text is defined as the area (in cm^2) delaminated divided by the number of coulombs passed through the interface. The term "delamination rate" is defined as the area delaminated divided by the time (in min).

Results

The area delaminated as a function of the number of coulombs passing through the interface was reproducible for a standard set of conditions and was essentially linear over the range used in the experiments. Representative data for a series of halides are given in Table XII. Delamination rates for polybutadiene and epoxy-polyamide coatings on a polished steel substrate immersed in CsCl, KCl, NaCl, and LiCl electrolytes are given in

Table XII

The Delamination Parameters of 25 μm Thick Epoxy-Polyamide Coatings on Steel Surfaced in Different Ways

Pretreatment	Electrolyte	Concentration	Delamination Parameter
Polished	LiCl	0.125M	1.8 cm^2/coulomb
Acid Cleaned	LiCl	0.125M	1.3
Polished	LiCl	0.5M	1.4
Acid Cleaned	LiCl	0.5M	1.0
Polished	NaCl	0.125M	4.4
Acid Cleaned	NaCl	0.125M	3.5
Polished	NaCl	0.5M	3.1
Alkaline Cleaned	NaCl	0.5M	2.5
Acid Cleaned	NaCl	0.5M	2.0
Polished	NaCl	1.0M	1.6
Polished	KCl	0.125M	7.0
Acid Cleaned	KCl	0.125M	5.0
Polished	KCl	0.5M	5.0
Alkaline Cleaned	KCl	0.5M	4.5
Acid Cleaned	KCl	0.5M	3.5
Polished	CsCl	0.125M	14
Acid Cleaned	CsCl	0.125M	6.2
Polished	CsCl	0.5M	9.6
Acid Cleaned	CsCl	0.5M	4.5
Polished	NH_4Cl	0.5M	2.0
Acid Cleaned	NH_4Cl	0.5M	0.45
Polished	KF	0.5M	5.8
Alkaline Cleaned	KF	0.5M	4.8
Acid Cleaned	KF	0.5M	3.9

Figure 13. For both systems it will be noted that the rate of delamination decreased in the order of CsCl > KCl > NaCl > LiCl. Thus, the rate of cathodic delamination, as well as the delamination parameter, is strongly a function of the electrolyte in which the substrate is immersed. A similar order of delamination efficiency was observed when the substrate was galvanized steel. Delamination was negligible, relative to steel and galvanized steel, in all electrolytes when aluminum was used as the substrate.

Although the delamination parameter was a function of the method of surfacing the substrate before application of the coating, the delamination rate for the epoxy-polyamide coating was not obviously a function of surface preparation, or even electrolyte concentration, as shown by the data in Figures 14-17. This lack of sensitivity to surface preparation method contrasts sharply with the behavior of polybutadiene coatings in which the rate of delamination was very strongly a function of surface preparation method as shown in Figure 18.

No extensive investigation was made of the method of cure and its influence on the tendency of the epoxy-polyamide coatings to delaminate during cathodic treatment. However, three different cure methods were used as described earlier. Data are given in Figure 19 for the delamination as a function of coulombs passing through the interface and in Figure 20 in terms of delamination rate. It will be noted that the samples cured at room temperature had the largest delamination parameter and the lowest rate of delamination.

The effect of cathode potential on the delamination parameter of epoxy-polyamide coatings on a polished steel substrate in 0.5M NaCl is shown in Figure 21 where it will be noted that the delamination parameter increases as the cathode potential is made less negative. The rate of delamination apparently is independent of the applied potential as shown by the data collected in Figure 22.

An insufficient number of experiments was done to determine quantitatively the effect of coating thickness on delamination rate. The data in Figures 14-17 do show that the rate of delamination was slower when the coating thickness was 40 μm than when it was 25 μm. Previous work with polybutadiene coatings showed that the delamination decreased as the coating thickness increased over a range of 10-20 μm.

Work in this laboratory has shown that dipping galvanized steel in 0.1M $CoCl_2$ solution decreases the ability of the surface to catalyze the cathodic reaction, $H_2O + 1/2O_2 + 2e^- = 2OH^-$. Several galvanized steel substrates were used for polybutadiene coatings (Figure 23) and a single substrate (Code E-12) was used with the epoxy-polyamide coating (Figure 24). In all cases the pretreatment in $CoCl_2$ solution reduced appreciably the rate of

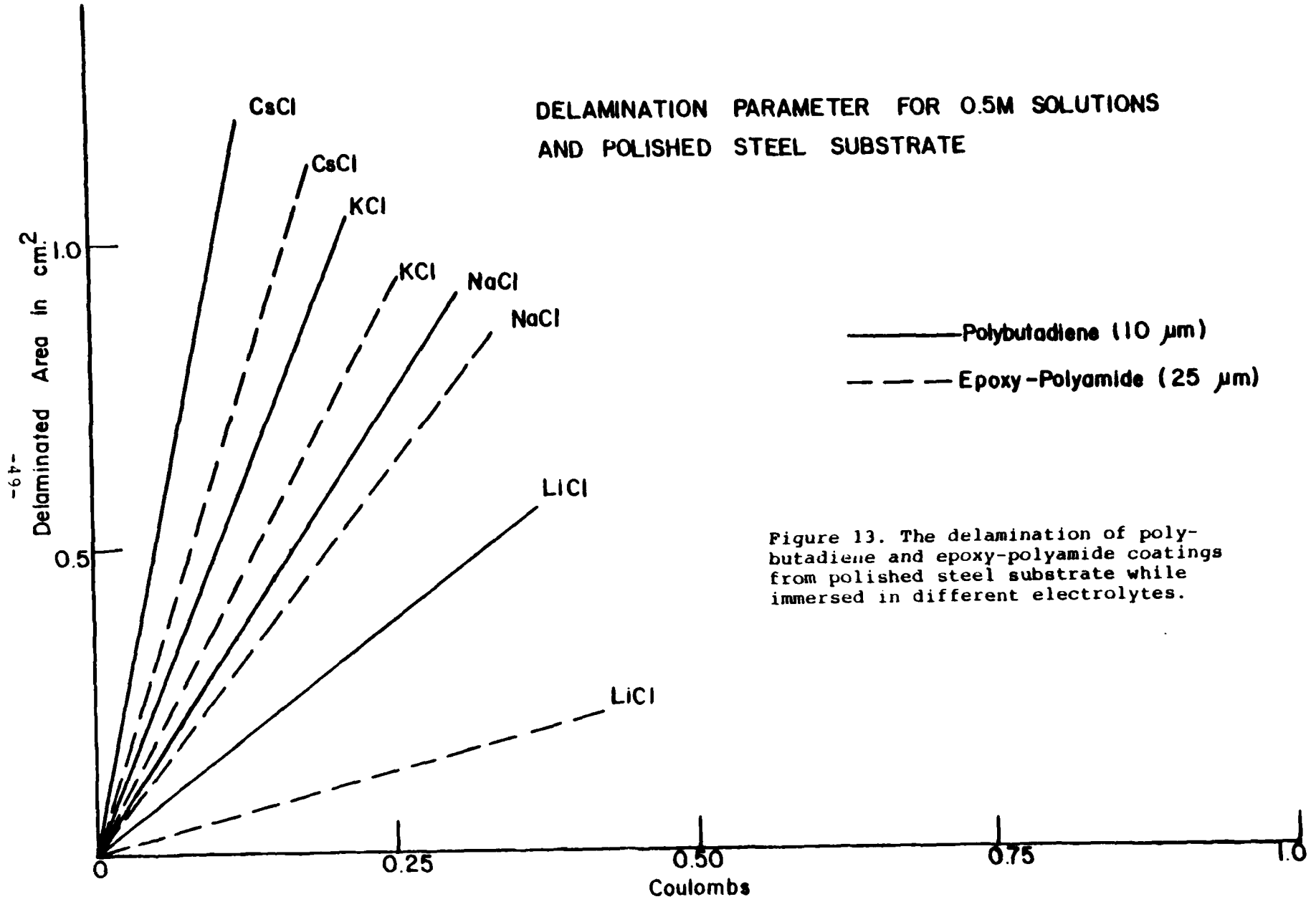

Figure 13. The delamination of polybutadiene and epoxy-polyamide coatings from polished steel substrate while immersed in different electrolytes.

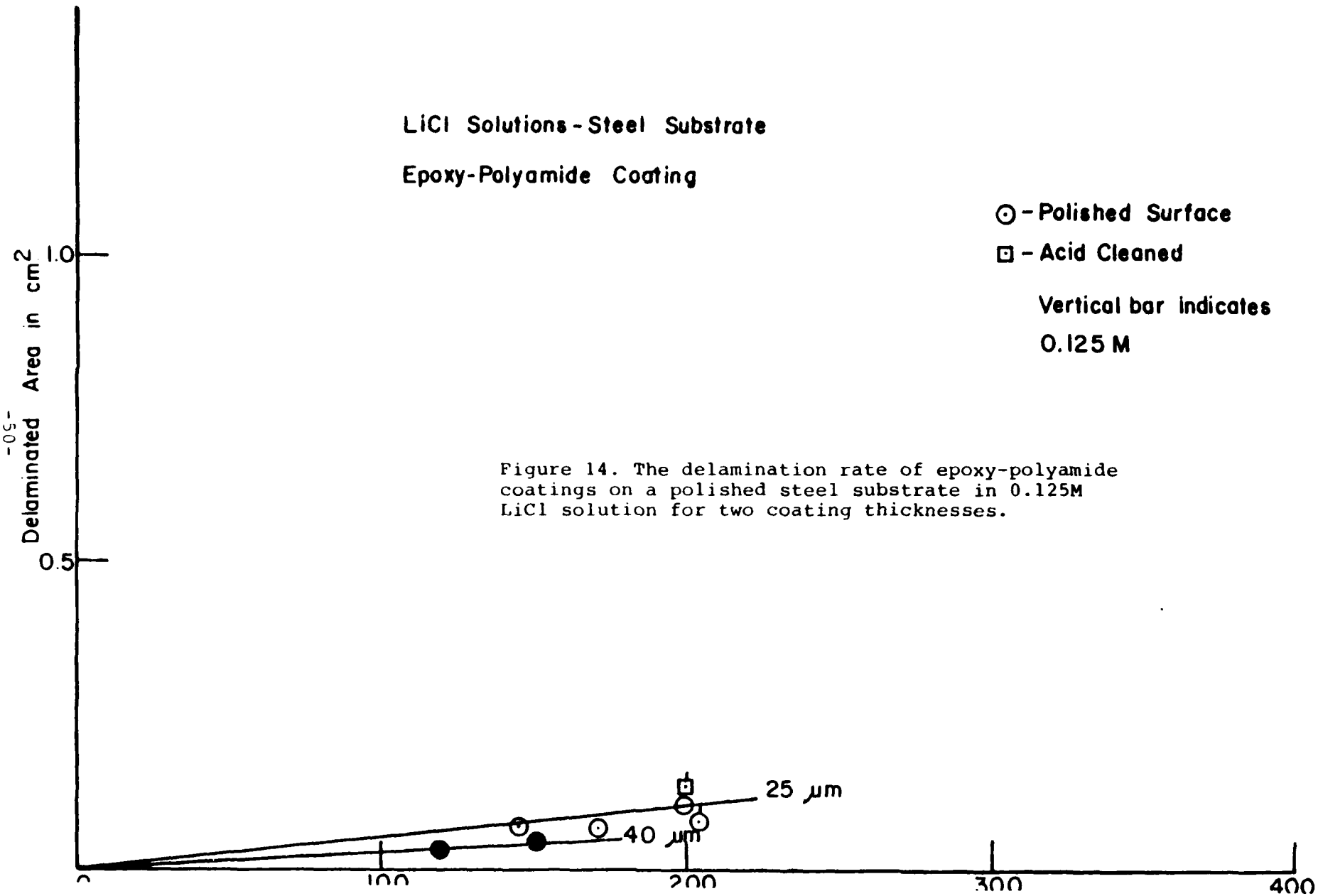

Figure 14. The delamination rate of epoxy-polyamide coatings on a polished steel substrate in 0.125M LiCl solution for two coating thicknesses.

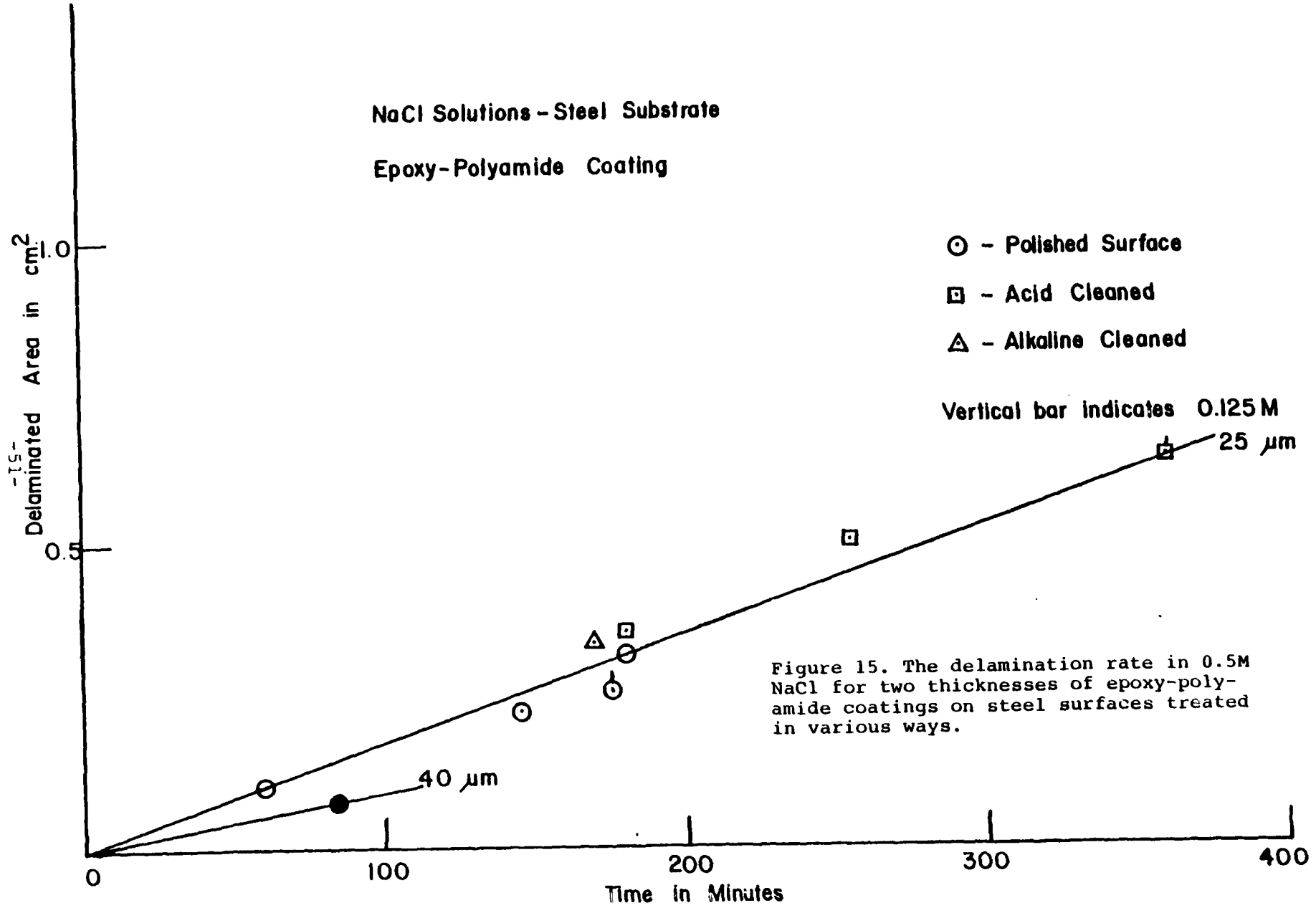

Figure 15. The delamination rate in 0.5M NaCl for two thicknesses of epoxy-polyamide coatings on steel surfaces treated in various ways.

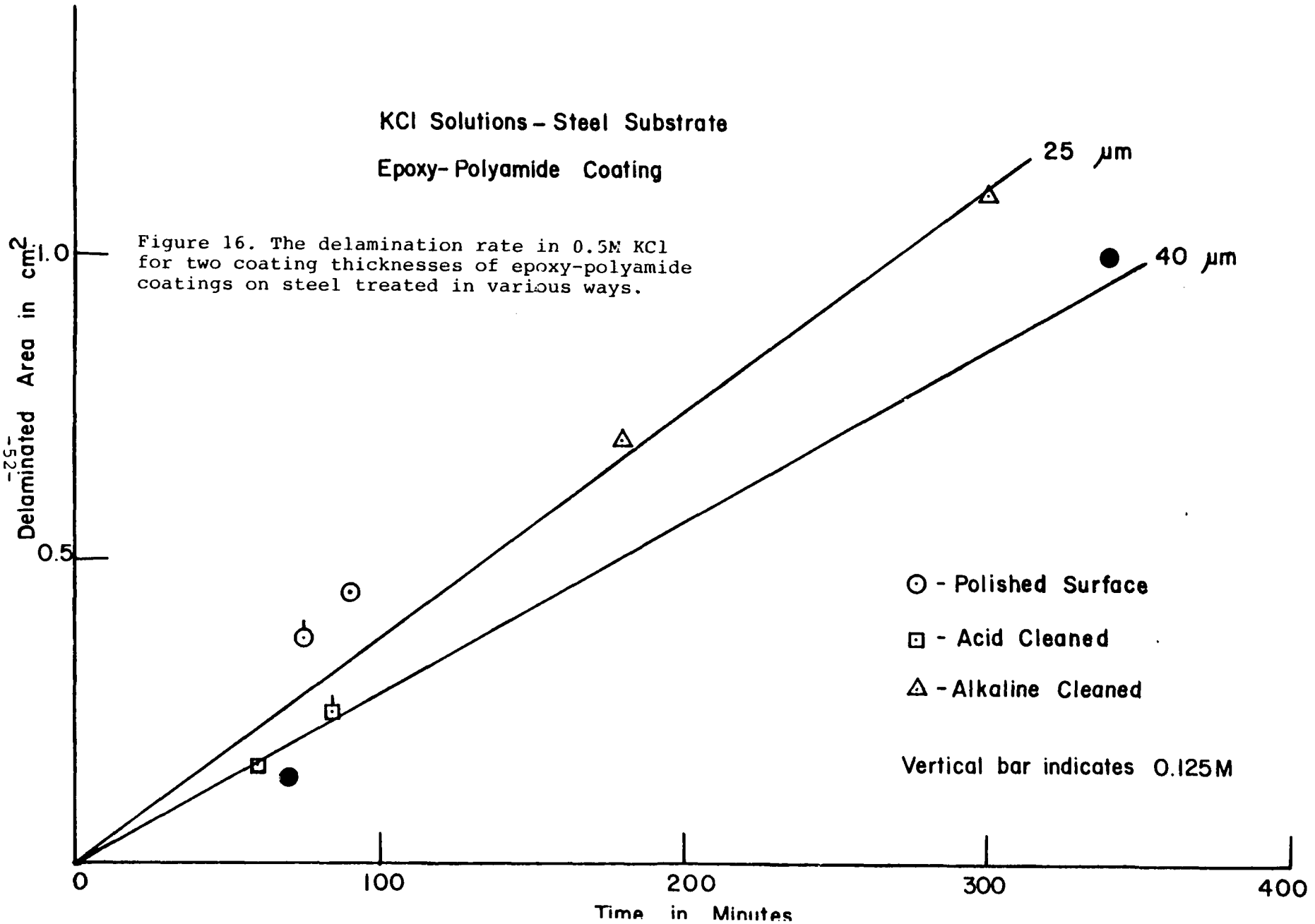

Figure 16. The delamination rate in 0.5M KCl for two coating thicknesses of epoxy-polyamide coatings on steel treated in various ways.

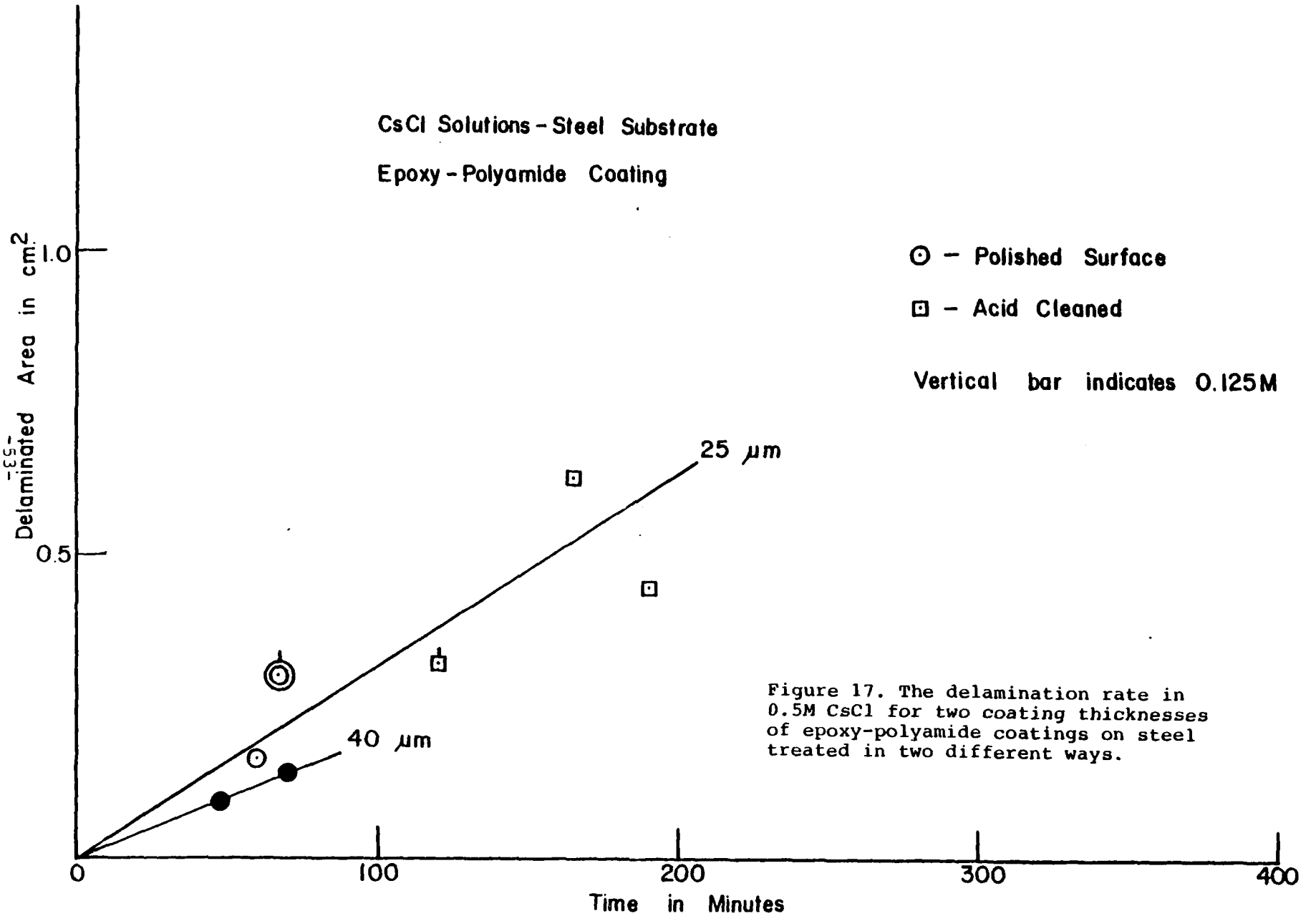

Figure 17. The delamination rate in 0.5M CsCl for two coating thicknesses of epoxy-polyamide coatings on steel treated in two different ways.

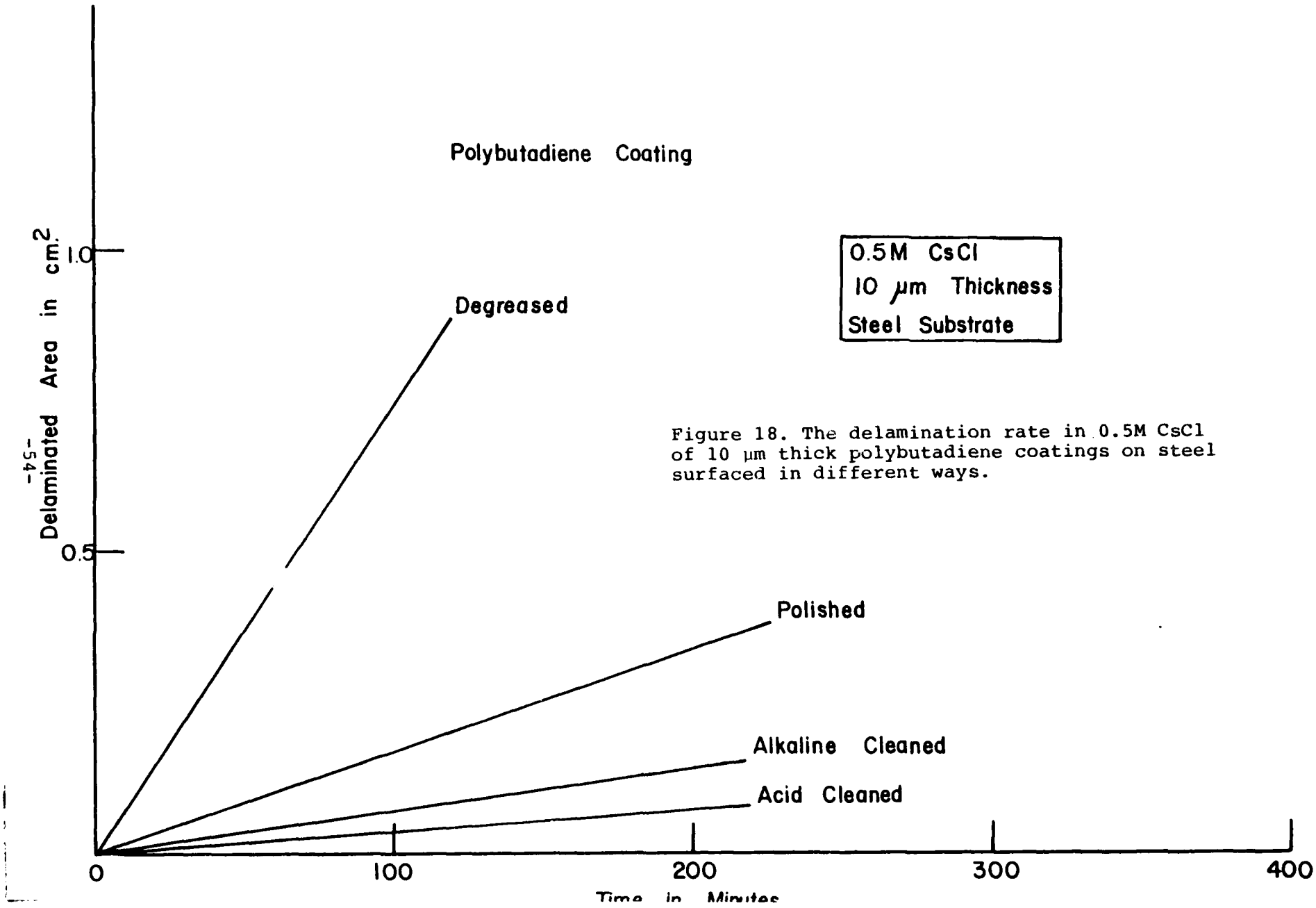

Figure 18. The delamination rate in 0.5M CsCl of 10 μm thick polybutadiene coatings on steel surfaced in different ways.

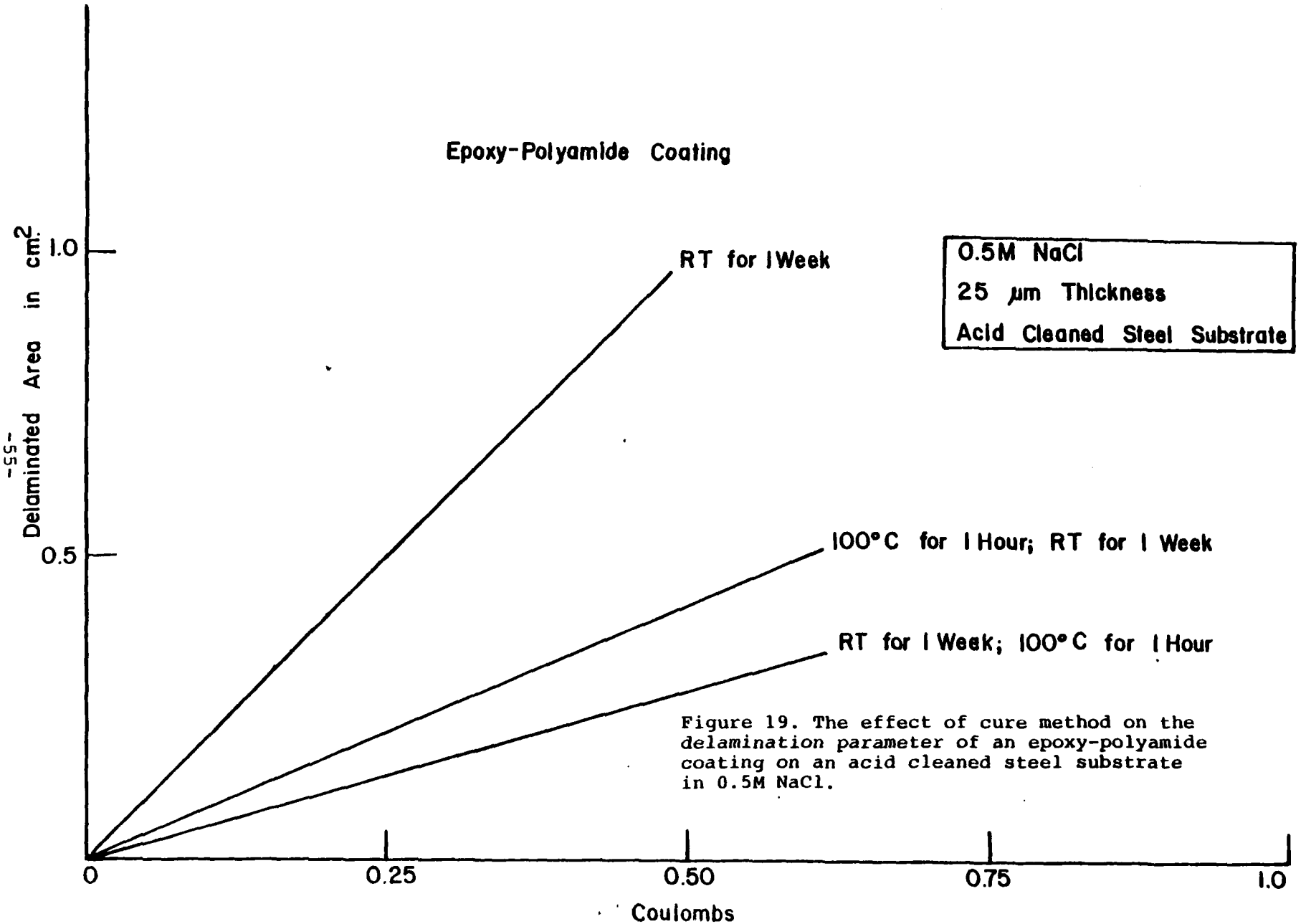

Figure 19. The effect of cure method on the *delamination* parameter of an epoxy-polyamide coating on an acid cleaned steel substrate in 0.5M NaCl.

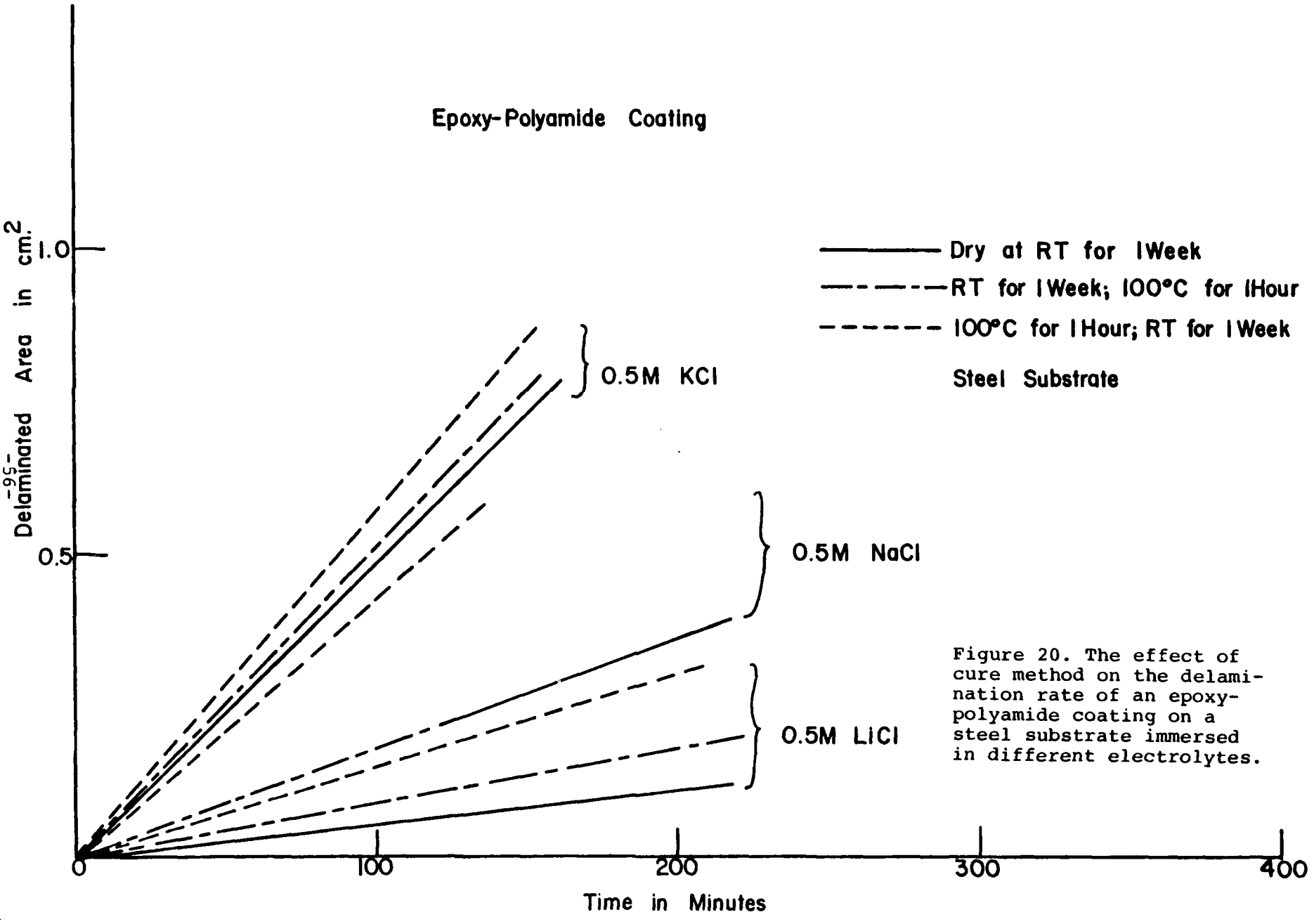

Figure 20. The effect of cure method on the delamination rate of an epoxy-polyamide coating on a steel substrate immersed in different electrolytes.

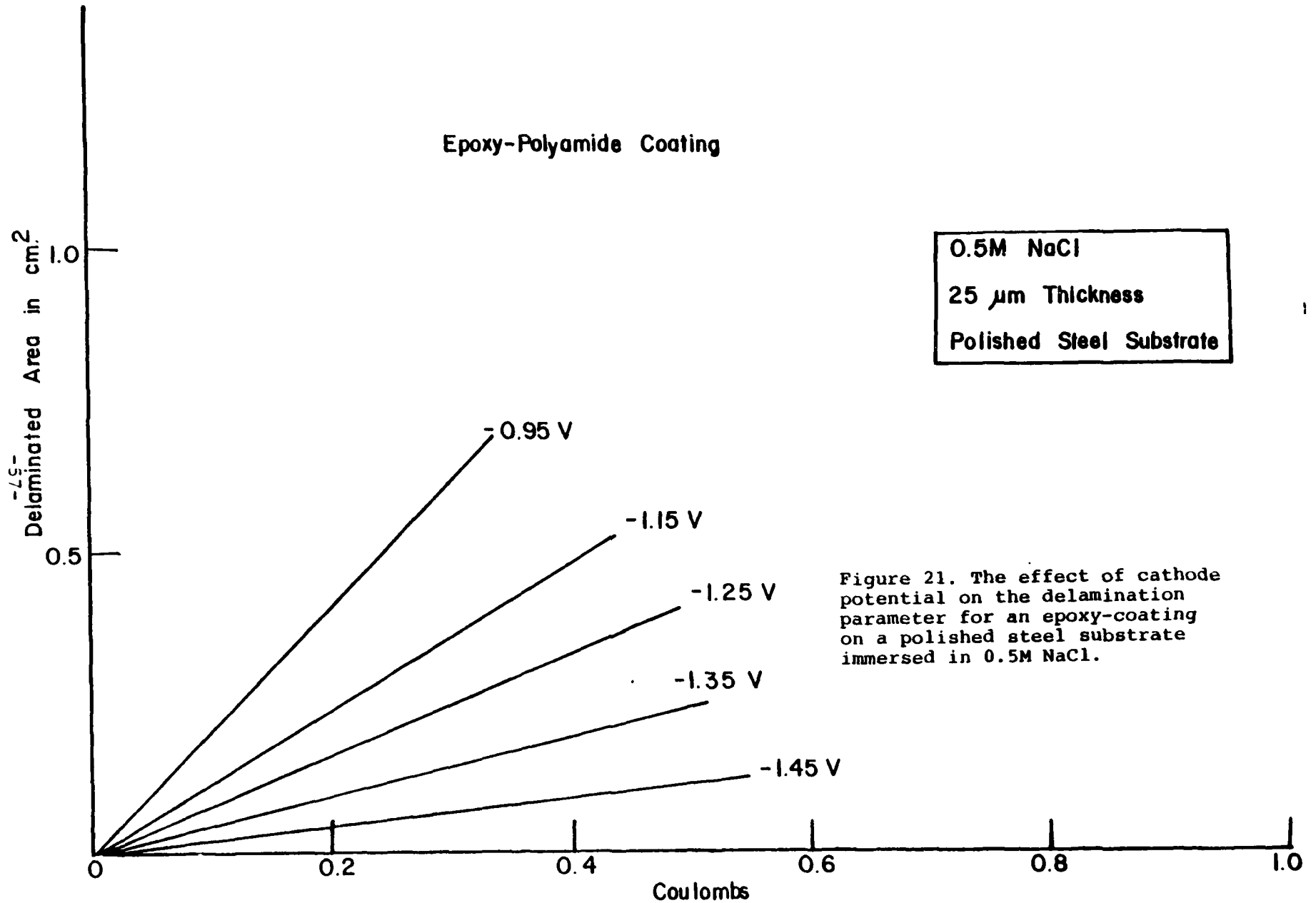

Figure 21. The effect of cathode potential on the delamination parameter for an epoxy-coating on a polished steel substrate immersed in 0.5M NaCl.

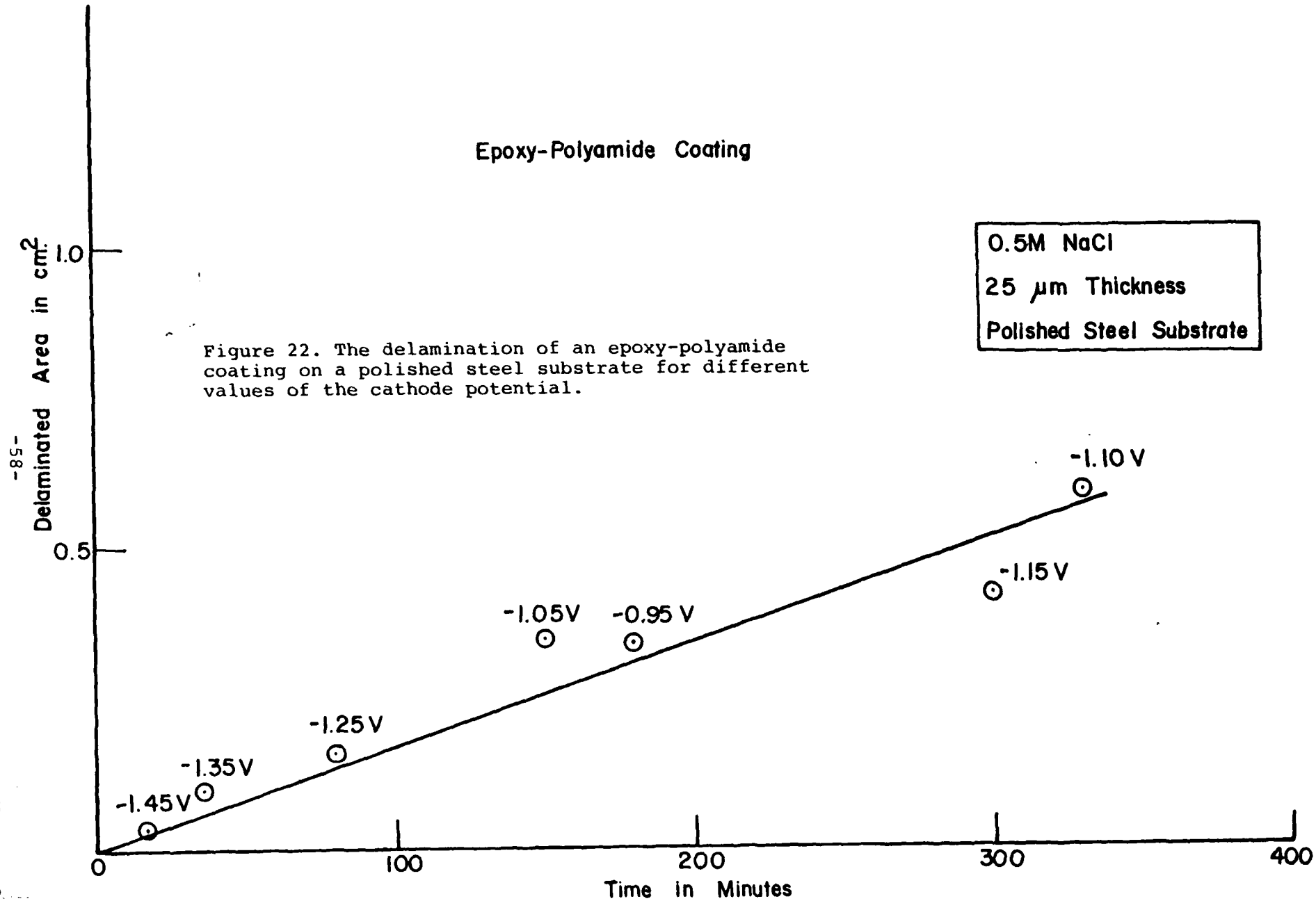

Figure 22. The delamination of an epoxy-polyamide coating on a polished steel substrate for different values of the cathode potential.

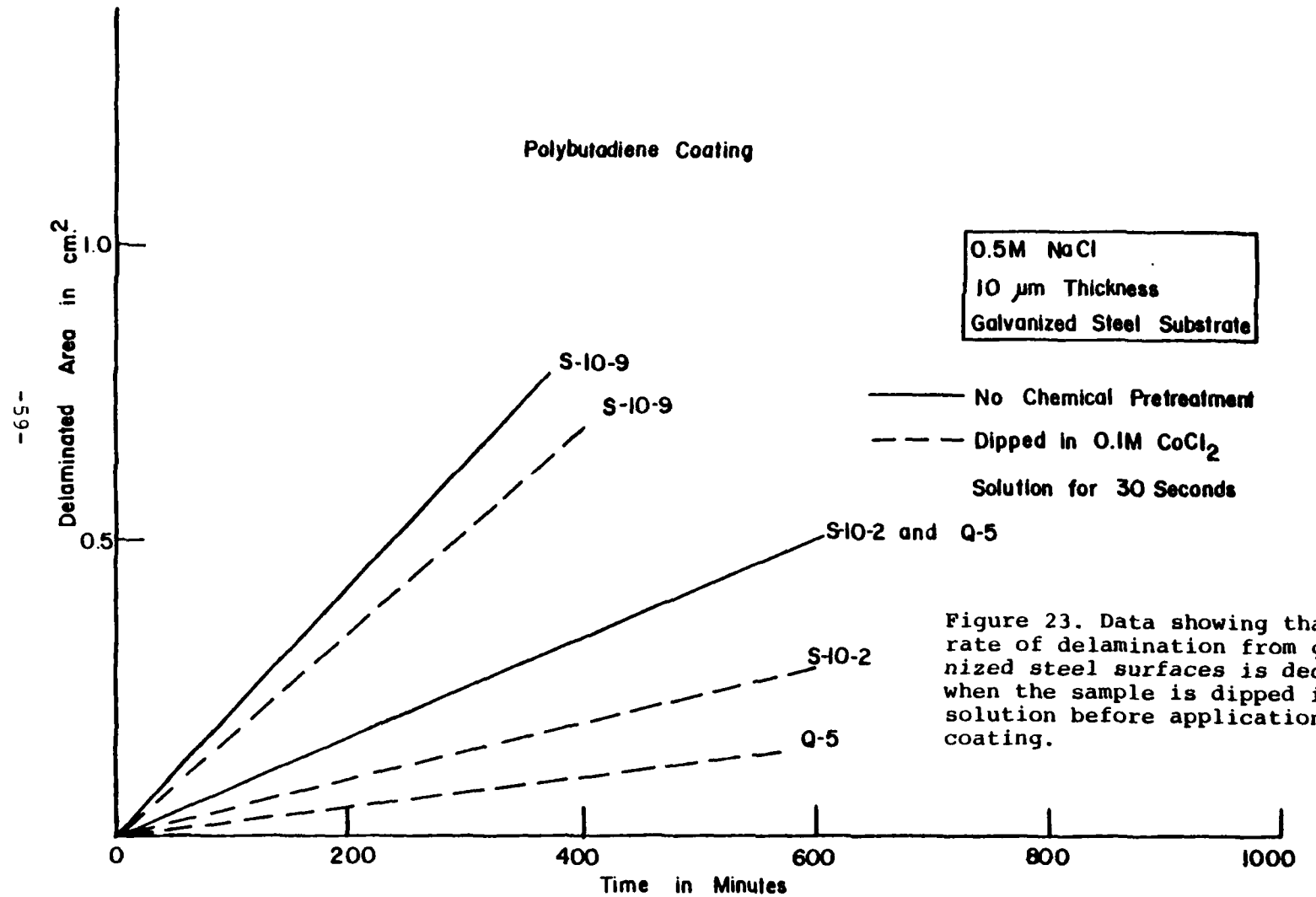

Figure 23. Data showing that the rate of delamination from galvanized steel surfaces is decreased when the sample is dipped in $CoCl_2$ solution before application of the coating.

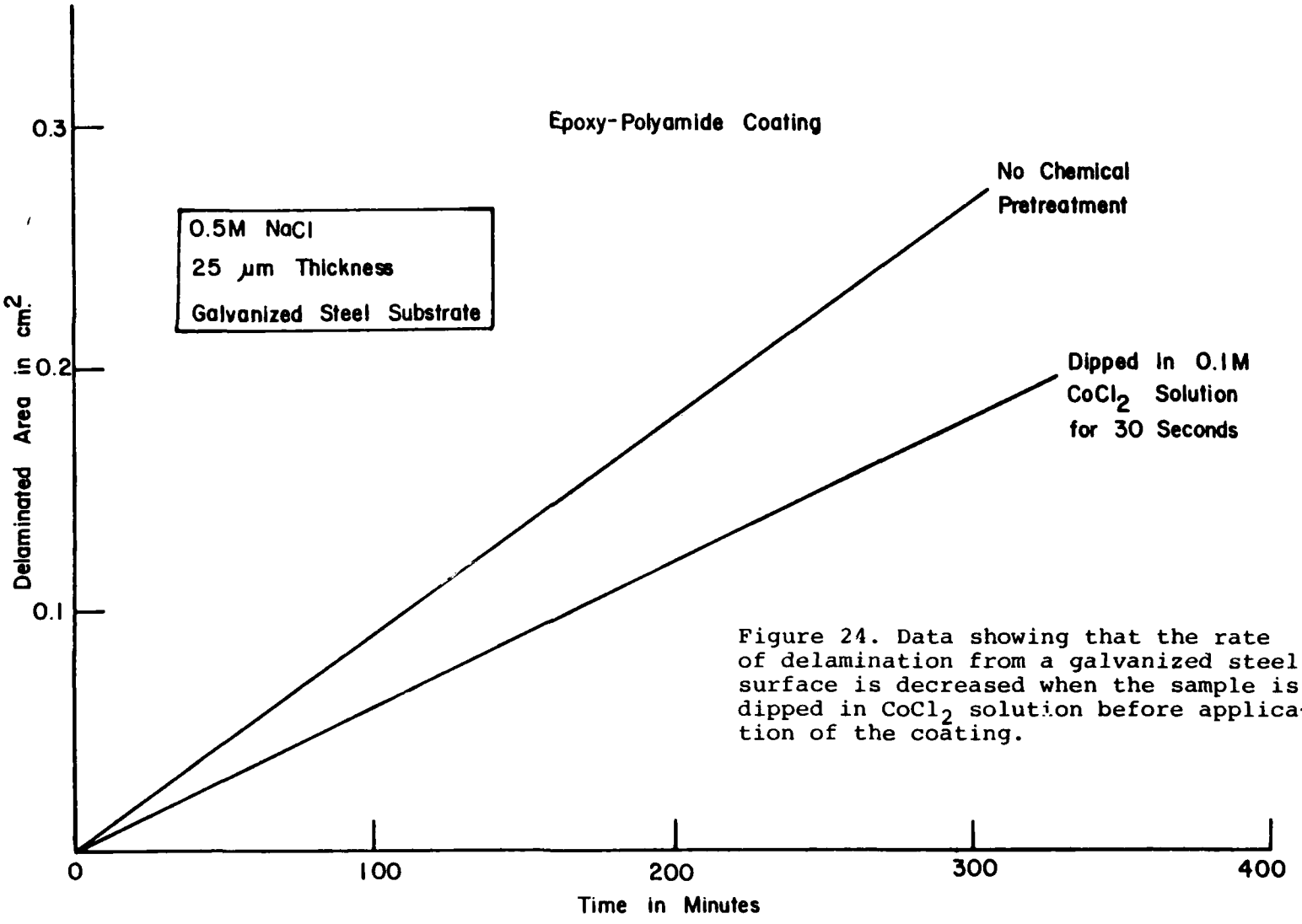

Figure 24. Data showing that the rate of delamination from a galvanized steel surface is decreased when the sample is dipped in $CoCl_2$ solution before application of the coating.

delamination on cathodic treatment.

Discussion

The data presented herein and those reported previously are supportive of the following hypothesis for the mechanism of cathodic delamination in neutral halide solutions of polybutadiene and epoxy-polyamide coatings from steel and galvanized steel substrates which contain a defect that exposes a small area of substrate metal.

The current that flows across the interface is the sum of two components: the current for the cathodic reaction, largely $2H^+ + 2e^- = H_2$, which occurs at the defect; and the current for the reaction, $H_2O + 1/2O_2 + 2e^- = 2OH^-$, which occurs under the coating and adjacent to the delaminating region. The second reaction may also occur at the defect because the concentration of dissolved oxygen (2.3×10^{-4}M) is of the same order as the H^+ ion concentration assuming that hydrolysis of Fe^{++} ions occurs in the vicinity of the defect. The appearance of visible gas bubbles at the defect is evidence that the $2H^+ + 2e^- = H_2$ reaction is an important consumer of electrons at the defect. The delamination parameter measures the relative activity as a cathode of the region exposed at the defect and the area under the coating, and the delamination rate is determined by the rate at which the reaction, $H_2O + 1/2O_2 + 2e^- = 2OH^-$, occurs under the coating. The rate of cathodic delamination in the presence of sufficient oxygen is determined largely by the rate at which cations reach the metal interface to serve as counterions for the OH^- generated. Under conditions where the substrate is inactive for the cathodic reaction under the coating, the rate of reaction may be limited by the catalytic properties of the oxide on the surface of the substrate metal. The comments that follow will provide support for the above hypothesis.

There is overwhelming evidence that the predominant delamination reaction under the coating is $H_2O + 1/2O_2 + 2e^- = 2OH^-$. The pH is known to become very high under the coating both in our studies (12) and those of many other workers (11). No evidence for hydrogen evolution under the coating has been observed in our work so we discard the reaction, $2H^+ + 2e^- = H_2$, as an important reaction under the coating in the delaminating region. At the defect, on the other hand, the hydrogen evolution reaction is the important reaction as indicated by the evolution of gas bubbles during the cathodic treatment. The important role of oxygen in the delamination process is shown by the fact that the rate of delamination is negligibly low when the electrolyte is freed of dissolved oxygen (11).

The most important variable in determining the delamination

rate under cathodic treatment in oxygen-containing solutions is the nature of the cation. In all systems studied, the rate of delamination decreases in the order CsCl > KCl > NaCl > LiCl, although under some conditions the rate of delamination in KCl solutions tended to approach those in CsCl solutions. A rough parallelism exists between the rate of delamination and the diffusion coefficient of the cation in aqueous solutions of these four electrolytes. This parallelism is supportive of the concept that diffusion of the cation through the coating is rate limiting.

Information is available to calculate the rate of oxygen transmittal through polybutadiene coatings. The permeability of oxygen through polybutadiene is 19.2×10^{-10} cm^3-cm/sec cm^2-cm Hg (13) and the solubility of oxygen in 0.125M CsCl solution at 25°C is 5.67 cm^3/l (14). If it is assumed that the concentration of oxygen at the coating/electrolyte interface is 5.67 cm^3/l and the concentration at the coating/substrate interface is zero, the rate of oxygen passage through a 10 μm thick coating may be calculated to be 3.4×10^{-11} mole/cm^2-sec. If the assumption is made that oxygen is consumed at the interface by the reaction, $H_2O + 1/2O_2 + 2e^- = 2OH^-$, this amount of oxygen will consume 8.2×10^{13} electrons/cm^2-sec equivalent to a current flow of 1.3×10^{-5} amp/cm^2. This rate of oxygen passage through the film may be compared with the fastest rate of delamination observed in CsCl solutions, namely 2.2×10^{-4} cm^2/sec, by making the assumption that there are approximately 10^{15} coating/substrate bonds per cm^2 of substrate surface and that each electron flowing through the interface leads to rupture of one coating/substrate bond. Under such assumptions the current flow is equivalent to 0.0035×10^{-5} amp/cm^2, a value approximately 1/400 that obtainable if all oxygen molecules participated in the electrode reaction. Thus, these very crude calculations show that there is sufficient oxygen transmission through polybutadiene coatings, 10 μm in thickness, to support the most rapid delamination rate observed. The calculations also suggest that the rate of oxygen transmittal through the coating is not the rate controlling step in the delamination process.

The above calculations also allow a separate determination as to whether the oxygen concentration is sufficient to support the $H_2O + 1/2O_2 + 2e^- = 2OH^-$ reaction at the rate at which it proceeds in the absence of a coating. Information is available from another study (15) to make such a calculation. Galvanized steel immersed in 3% NaCl (pH = 6.4) at room temperature under quiescent conditions exhibits a cathodic polarization curve that indicates that the reaction occurs at a rate equivalent to approximately 20×10^{-6} amp/cm^2. This reaction rate should be compared with a delamination current of 0.0037×10^{-6} amp/cm^2, calculated as above on the basis of a delamination rate of 2.3×10^{-5} cm^2/sec observed with galvanized steel immersed in NaCl solutions. It is clear that the reaction rate itself is not limiting.

The data summarized in Figure 20 show that the method of curing the epoxy-polyamide coating has an effect on the rate of delamination. The slowest rate of delamination in LiCl, NaCl, and KCl solutions was obtained on coatings that were cured at room temperature and the most rapid rate of delamination was obtained on coatings that were heated at 100°C for 1 hr before curing at room temperature. Coatings that were cured at room temperature for a week followed by heating at 100°C for 1 hr had delamination properties not greatly different from coatings that were cured at room temperature. The tentative interpretation of these data is that the higher temperature treatment leads to a larger number of pathways of easy diffusion through the coating.

Two studies carried out in this laboratory indicate that water uptake by polybutadiene coatings and epoxy-polyamide coatings is very rapid. Capacitance measurements (16) have yielded information on the rate of water uptake by polybutadiene coatings and John Standish (17) has shown by quartz microbalance studies that epoxy-polyamide coatings on aluminum take up water rapidly. These data, unfortunately, do now allow calculation of the rate of water transmission but they do indicate that water uptake is rapid. Rapid water uptake suggests rapid movement of water through the coating.

The very low rate of delamination of polybutadiene and epoxy-polyamide coatings from aluminum is in accord with service experience that indicates that epoxy-polyamide coatings are very adherent to aluminum substrates under adverse environmental conditions. Our interpretation of the behavior of aluminum is as follows. Aluminum is a very reactive metal and exposure to the atmosphere or to an aqueous medium, prior to application of the coating, results in the formation of a thin layer of aluminum oxide on the aluminum surface. This aluminum oxide is the surface that is in contact with the organic coating and it is the surface on which any cathodic reaction must occur. The cathodic reaction requires three components: water, oxygen and electrons. As shown previously, oxygen readily passes through the polybutadiene coating and presumably it readily passes through the epoxy-polyamide coating as well. Information summarized above proves that water transmittal through the ocating is very rapid. The rate limiting constituent appears to be the electrons. The normal potential drop across the surface oxide during anodization of aluminum is of the order of 10^7 v/cm. If the oxide film on aluminum is 3×10^{-7} cm in thickness, it is apparent that a significant voltage is required to overcome the effective resistance of the aluminum oxide. Since electrons may flow through two parallel paths, one at the defect and the other underneath the coating adjacent to the defect, it is obvious that the electrons will follow the path of least resistance and will flow largely through the defect where the aluminum surface does not have a continuous oxide film, since aluminum pitted at the defect during the experiment.

The experimental information and calculations summarized above suggest that the rate of the cathodic delamination reaction under polybutadiene and epoxy-polyamide coatings on steel and galvanized steel substrates is not limited by the availability of oxygen, water, and electrons, the three reactants in the cathodic reaction. Since the OH^- ions are being formed in a very confined volume at the delaminating edge, space charge effects would rapidly prevent additional reaction. The charges of the OH^- ions generated by the reaction can be balanced by the diffusion of cations through the film to the interface. The likely diffusing species is the alkali metal cation, rather than the H^+ because of the very large difference in concentration. The concentration of the cation in solution is 0.5M in a typical experiment, approximately 10^6 greater than the H^+ concentration. The high pH under the coating (12) also is indicative of the fact that the alkali metal cations, and not the H^+ ions, are the major diffusing species. It is thus hypothesized that the rate-limiting step in the cathodic delamination of both polybutadiene and epoxy-polyamide coatings from polished steel and galvanized steel substrates is the diffusion of alkali metal cations through the coating. It is recognized that metal cations can be supplied both through the coating and through the liquid that enters at the defect. The fact that the delamination rate decreases with increase in coating thickness in the case of both types of coatings is strongly suggestive that the cations are supplied through the coating and not from the liquid adjoining the delaminating region.

Data reported previously in a different form (11) allow the calculation of an activation energy for the delamination of polybutadiene coatings on galvanized steel substrates when cathodically treated in 0.5M NaCl. These data are given in Figure 25. The temperature range, 11-31°C, is very small but nine data points are available for estimating the activation energy. These data yield an activation energy for the delamination process of the order of 9,500 cals/mole, a reasonable value for a diffusion process.

Data reported in Figures 23 and 24 show that predipping galvanized steel in 0.1M $CoCl_2$ for 30 sec prior to application of the polybutadiene or epoxy-polyamide coatings results in a lower rate of cathodic delamination. These findings may be explained by a lower activity of the zinc oxide at the coating/substrate interface as a catalyst for the $H_2O + 1/2O_2 + 2e^- = 2OH^-$ reaction since it is known that the introduction of small amounts of cobalt into the oxide film on zinc lowers the activity of the surface for this cathodic reaction (18).

The delamination process has been studied in terms of two variables, time and the number of coulombs passing through the interface. In the case of the polybutadiene coatings on steel and galvanized steel, the relative behavior under different experimental conditions was the same whether the time or the

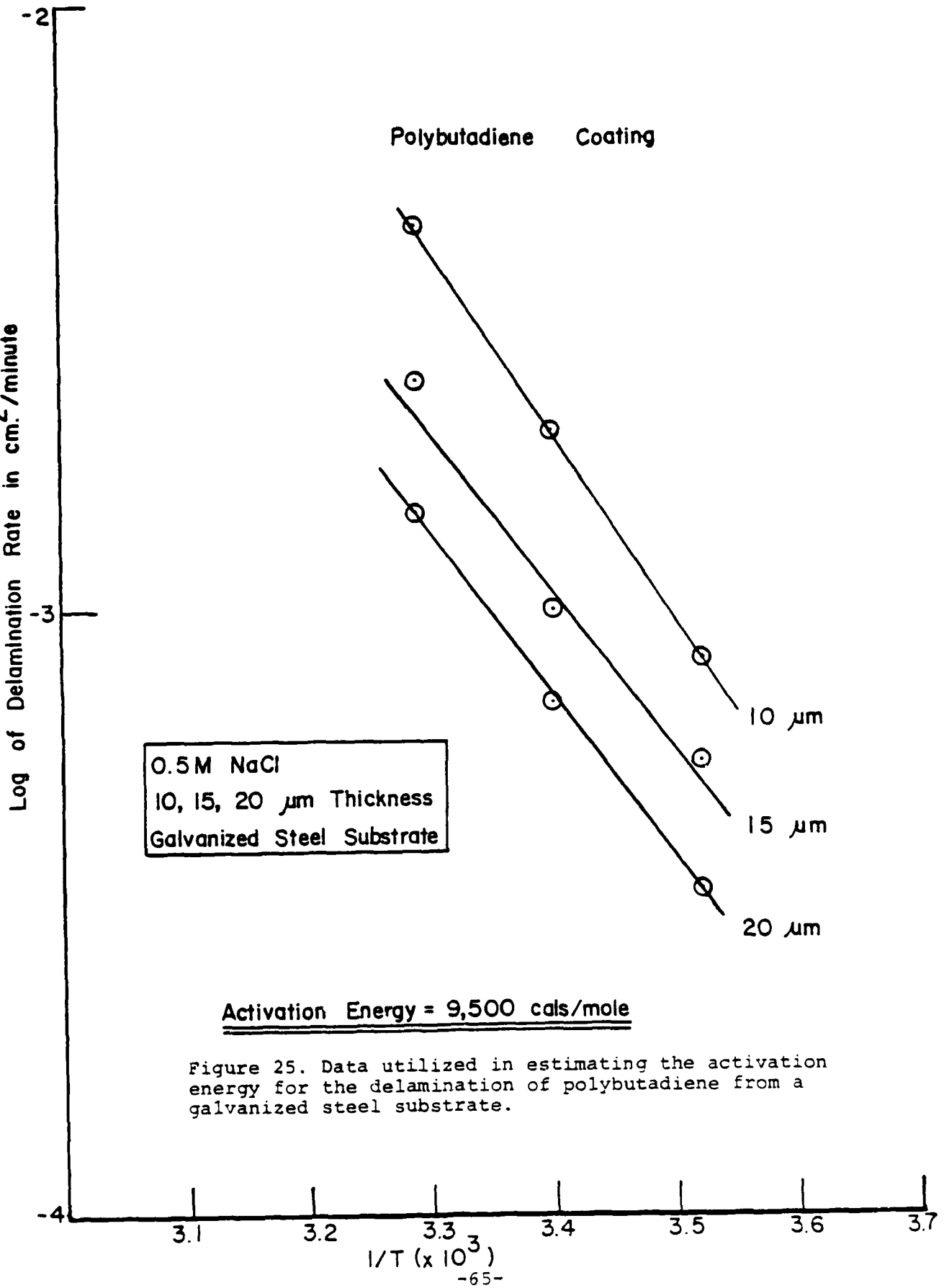

Figure 25. Data utilized in estimating the activation energy for the delamination of polybutadiene from a galvanized steel substrate.

number of coulombs passed was the variable. In some cases there was an approximately 1:1 relationship between these two variables, as shown for example in Figure 26. The behavior of the epoxy-polyamide coatings, however, was very different from polybutadiene coatings in that a 1:1 relationship did not exist between these two variables under those conditions in which the surface pretreatment was varied. Figure 27, for the epoxy-polyamide coatings should be compared with Figure 26. Our tentative interpretation of these two different behaviors is that the polybutadiene coating is very sensitive to the character of the oxided steel surface with which it is in contact and that bond cleavage is at the polymer/substrate interface. The lack of sensitivity to the surface character in the case of the epoxy-polyamide coatings is considered to be indicative of the fact that bond cleavage is within the polymer itself. Evidence for bond fracture within the polymer during the delamination process has been obtained by Hammond et al. (19).

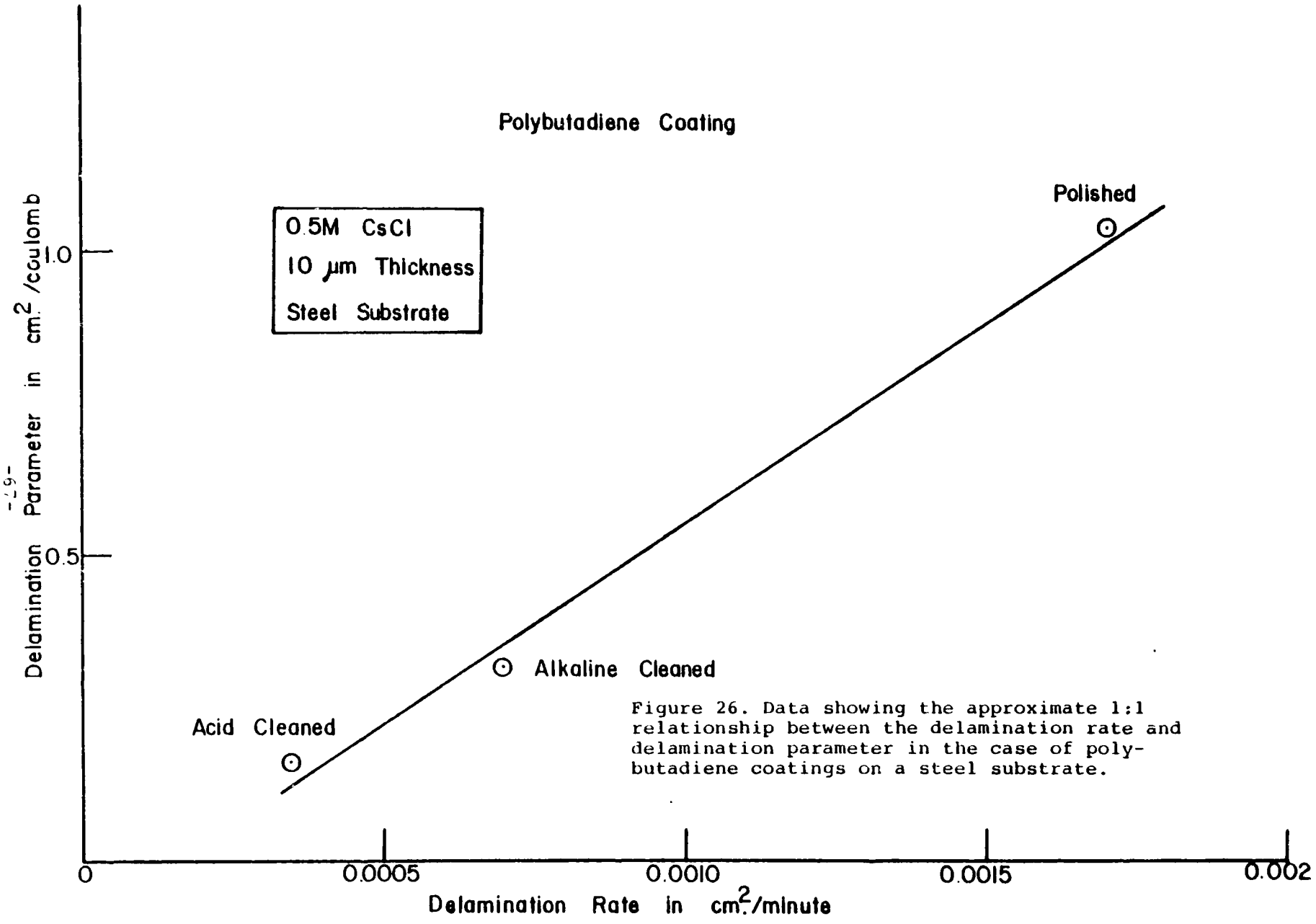

Figure 26. Data showing the approximate 1:1 relationship between the delamination rate and delamination parameter in the case of polybutadiene coatings on a steel substrate.

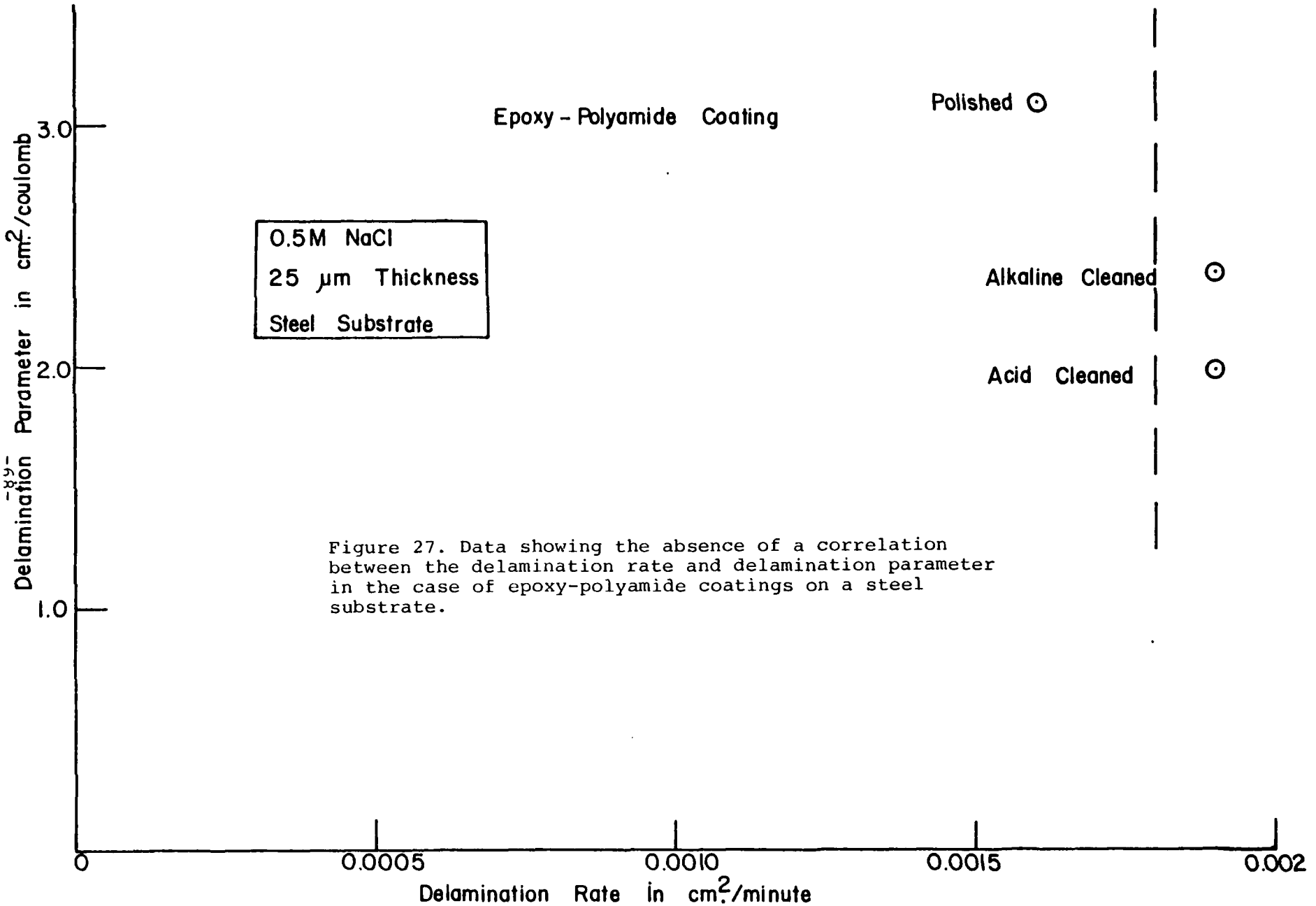

Figure 27. Data showing the absence of a correlation between the delamination rate and delamination parameter in the case of epoxy-polyamide coatings on a steel substrate.

SECTION 4

Objective: To Understand Adhesive Forces between Substrate and Polymeric Coating and and Pigments and Polymeric Coating in Terms of Acid/Base Interactions

Title: Acid-Base Properties of Iron Oxides

Senior Investigator: Frederick M. Fowkes

Associate: Sara Joslin
Graduate Student

Introduction

The adhesion of organic polymers to inorganic oxides such as those on steel surfaces has been shown earlier to result entirely from acid-base interactions between the polymer and the oxide (20). Hydrogen-bonds were shown to be a sub-set of acid-base interactions, and dipole-dipole interactions were shown to be so negligibly small that no experimental evidence for them has yet been found (21). It therefore becomes important to find a method of measuring and predicting acid-base interactions in the bonding of organic polymers to metal oxide surfaces, especially the oxide layers on steel.

In earlier studies use has been made of the "C and E" equation of Drago (20) for correlating and summarizing heats of acid-base interactions:

$$-\Delta H_{ab} = C_A C_B + E_A E_B \qquad (1)$$

in which the acidic strength of the acid is fully characterized by the constants C_A and E_A, and the basic strength of the base is fully characterized by the constants C_B and E_B. A hypothesis is now being tested that the heat of adsorption of bases on metal oxide powders is precisely equal to the heat of acid-base interaction of these bases with the acidic sites of the oxide and also that the acid strength of these oxide sites can be fully characterized by C_A and E_A parameters.

In this work the heats of adsorption will be determined from the temperature coefficient of adsorption isotherms. If the equilibrium surface concentration Γ of adsorbed base is determined at equilibrium bulk concentration C, these values are related by an equilibrium constant K for Langmuirian adsorption:

$$K \frac{\Theta}{(1-\Theta)C} = \frac{\Gamma}{(\Gamma_m - \Gamma)C} \qquad (2)$$

which can be re-arranged to give:

$$\frac{C}{\Gamma} = \frac{1}{\Gamma_m K} + \frac{C}{\Gamma_m} \qquad (3)$$

where Γ_m is the surface concentration for a complete monolayer. If the adsorbed molecules are not too tightly packed, equation (3) predicts a straight line plot of C/Γ vs. C, with intercept $1/\Gamma_m K$, from which the equilibrium constant K of equation (2) may be determined. If this equilibrium constant is determined for two or more temperatures the heat of adsorption may be calculated from:

$$\Delta H_{ads} = \frac{RT_1T_2}{T_2 - T_1} \ln \frac{(K \text{ at } T_2)}{(K \text{ at } T_1)} \qquad (4)$$

Experimental

Fe_3O_4 powder from Chas. Pfizer and Co. was used for most of these studies. Its surface area, determined by the BET method with argon gas at liquid nitrogen temperatures, was 6.0 m^2/g. Some Fe_2O_3 powder from the same source was also used; its surface was 12.0 m^2/g.

The powders were dried for 1 hr at 120°C in a vacuum oven at $1x10^{-4}$ Torr. This amount of drying is not believed to be enough to remove all of the adsorbed water. The powders were then stirred and tumbled with glass beads in cyclohexane solutions of the model bases.

The triethylamine and pyridine were obtained from Aldrich Chemical Company. The pyridine was 99+% Gold Label grade and triethylamine was 99% purity.

Heats of adsorption were largely determined from the temperature-dependence of adsorption isotherms, as described above. For each solute at least twelve adsorption measurements must be made, and the heat of adsorption is determined from differences in these measurements. A faster and more accurate method is to use microcalorimetry, for with this technique the heat is measured directly. A Microscal Flow Microcalorimeter is now being used. Initial studies indicate that both rapid and accurate results are obtained.

Discussion

Figure 28 shows the adsorption isotherms obtained with triethylamine, pyridine, ethyl ether, and ethyl sulfide. The amounts of pyridine adsorbed per unit area were about twice those of triethylamine, so for the pyridine curves the ordinates have been reduced by a factor of two to allow them to fit on the same graph. The ether and sulfide data are too inaccurate at this time to be reported in more detail, but the triethylamine and pyridine adsorption data were very reproducible and were Langmuirian in all details; the graphs of these data according to equation (3) are shown in Figures 29 and 30. The straightness of the lines indicates that the isotherms are indeed Langmuir isotherms; that is, the equilibrium constant K is constant at all surface concentrations, suggesting that all the acid sites are of equal strength and that the adsorbed bases are not tightly crowded together at full coverage.

Adsorption of triethylamine and of pyridine was checked on three different iron oxide samples and nearly identical results were obtained. The adsorption of pyridine was the same even on Fe_2O_3. Examination of the Fe_3O_4 showed that it was not pure

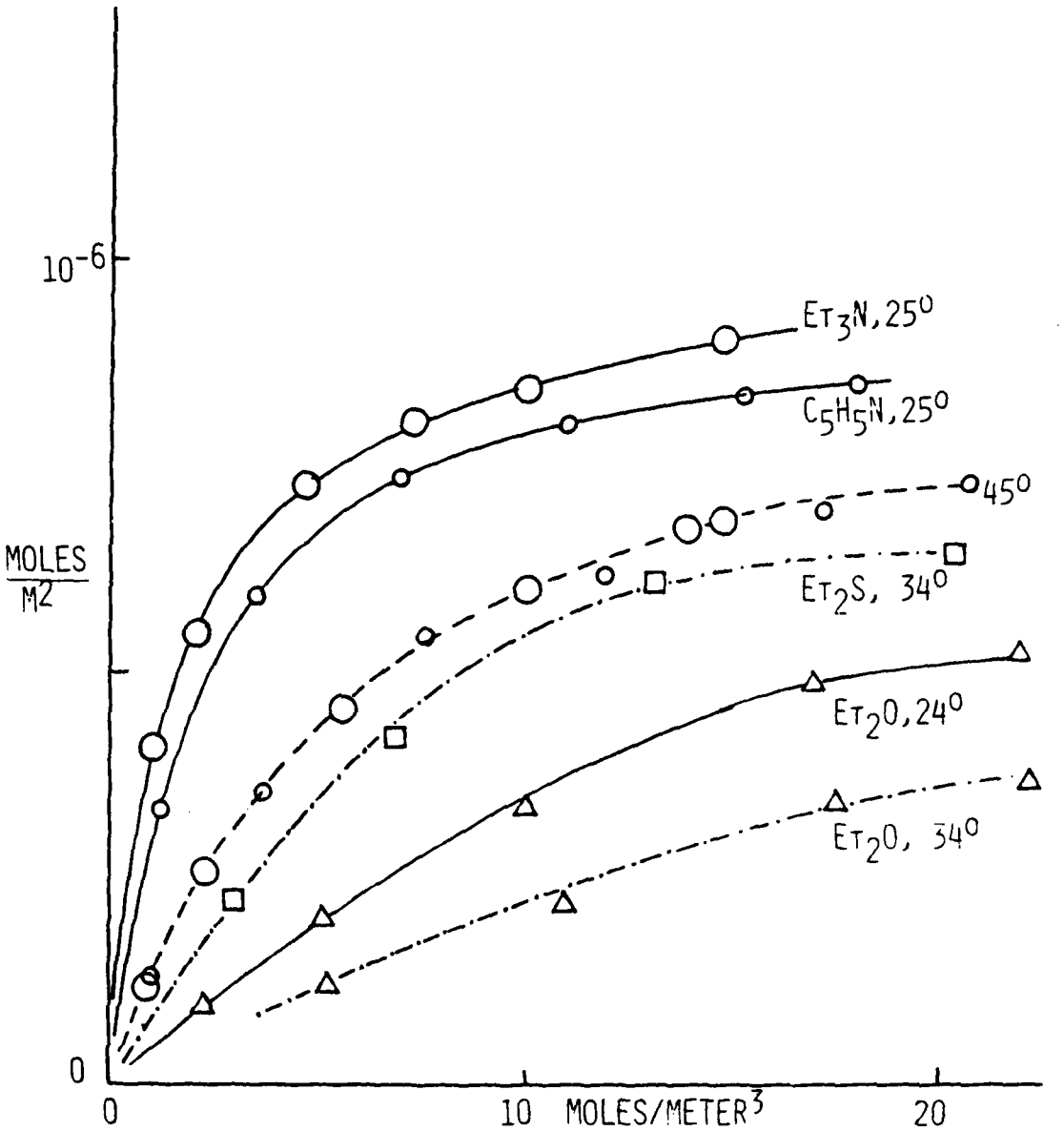

Figure 28. Adsorption isotherms for pryidine, triethylamine, ethyl sulfide and ethyl ether adsorbing from cyclohexane solutions on iron oxide powder (6 m^2/g).

Note: Adsorption values for pyridine should be multiplied by 2.

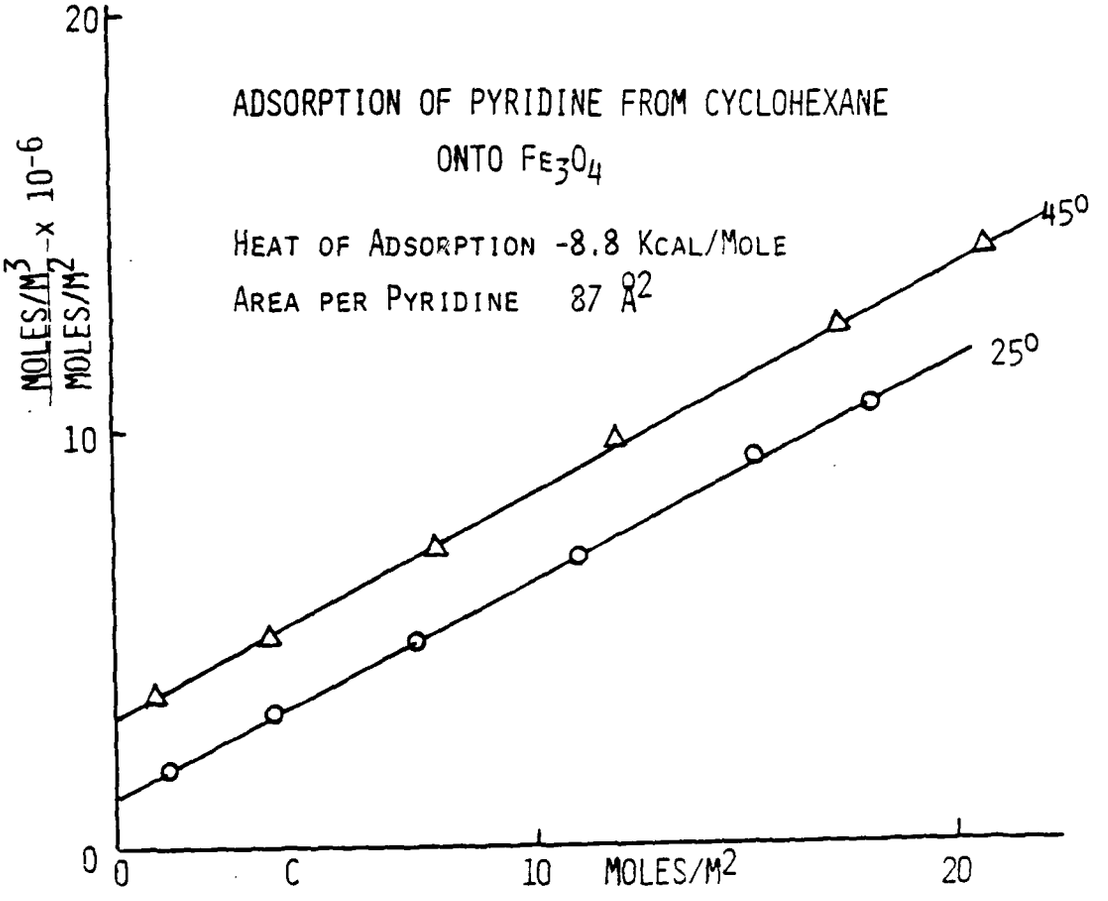

Figure 29. Langmuir isotherm for adsorption of triethylamine from cyclohexane onto iron oxide powder.

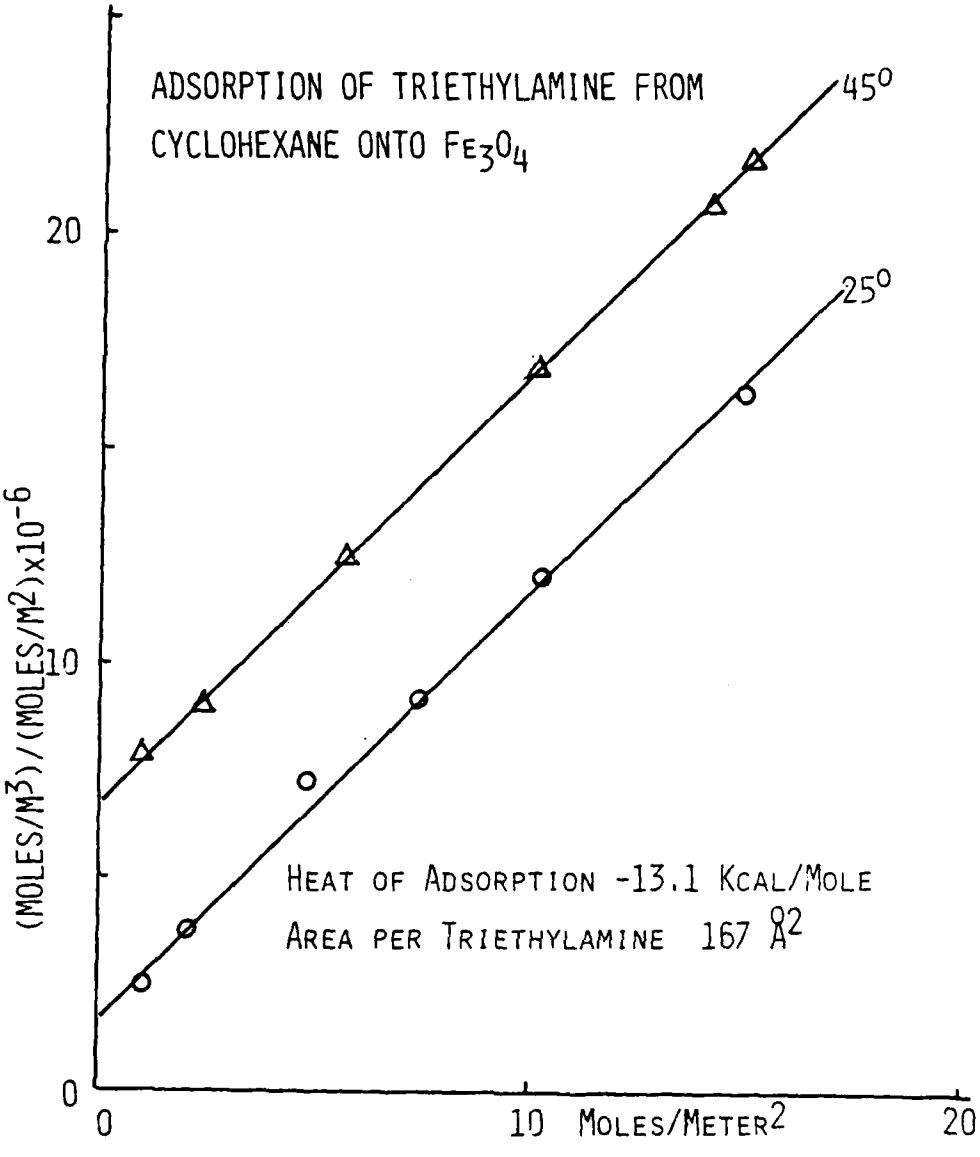

Figure 30. Langmuir isotherms for adsorption of pyridine from cyclohexane onto iron oxide powder.

Fe_3O_4 but was about 20% oxidized to Fe_2O_3, probably on the surface. Therefore our results really apply only to Fe_2O_3 surfaces.

The heats of adsorption were 13.1 ± 0.3 Kcal/mole for triethylamine and 8.8 ± 0.3 Kcal/mole for pyridine on Fe_2O_3 surfaces. These values are sufficient to determine the C_A and E_A values for the acidic sites of iron oxide. Since it is known that triethylamine has C_B = 11.09 and E_B = 0.99 the relation of C_A to E_A can be determined from:

$$C_A = (\Delta H_{ads} - E_A E_B)/C_B, \text{ or}$$

$$C_A = (13.1 - 11.09E_A)/0.99$$

Figure 31 shows a graph of C_A vs. E_A for the triethylamine and pyridine experiments. The two lines differ appreciably in slope and the values of C_A and E_A at the intersection are believed to be the correct values: C_A = 1.0, and E_A = 2.04. These values give a C/B ratio of 0.5, indicating that the acid sites on iron oxide are quite soft, though not as soft as iodine (which has a C/B ratio of unity). This evidence suggests the sites to be Fe^{3+} ions rather than FeOH acid sites, which would be expected to be much harder, and have a C/B ratio nearer to 0.1.

The softness of iron acid sites suggests that adhesives and coatings for iron and steel should feature basic groups (electron-donors) which are strong soft bases, for these might best withstand the incursion of water into the interface.

The Microscal Flow Microcalorimeter allows faster and potentially more accurate measurements of heats of adsorption. Figure 32 illustrates the measurements of the heat of adsorption of pyridine onto Fe_3O_4 powder at 23°C from a solution of 2×10^{-2} moles/L in cyclohexane; the area of the peak corresponds to 14.8×10^{-3} cal of heat released in 45 min from 140.8 mg of iron oxide, corresponding to 8.9 Kcal/mole. This value compares well with the 8.8 Kcal/mole determined from adsorption isotherms at two temperatures. This experiment can be done more rapidly at higher concentrations and temperatures.

Conclusions

A method of interpreting heats of adsorption as acid-base interactions predictable by the Drago equation is presented. It appears that the dominant acidic adsorption sites can be best characterized by their C_A and E_A values of 1.0 and 2.04, respectively. This information, plus the measured surface density of sites, should allow prediction of the adsorption of any bases at any temperature, and should predict the energy of adhesion of any basic coating to such surfaces. Further work is needed to verify these predictions.

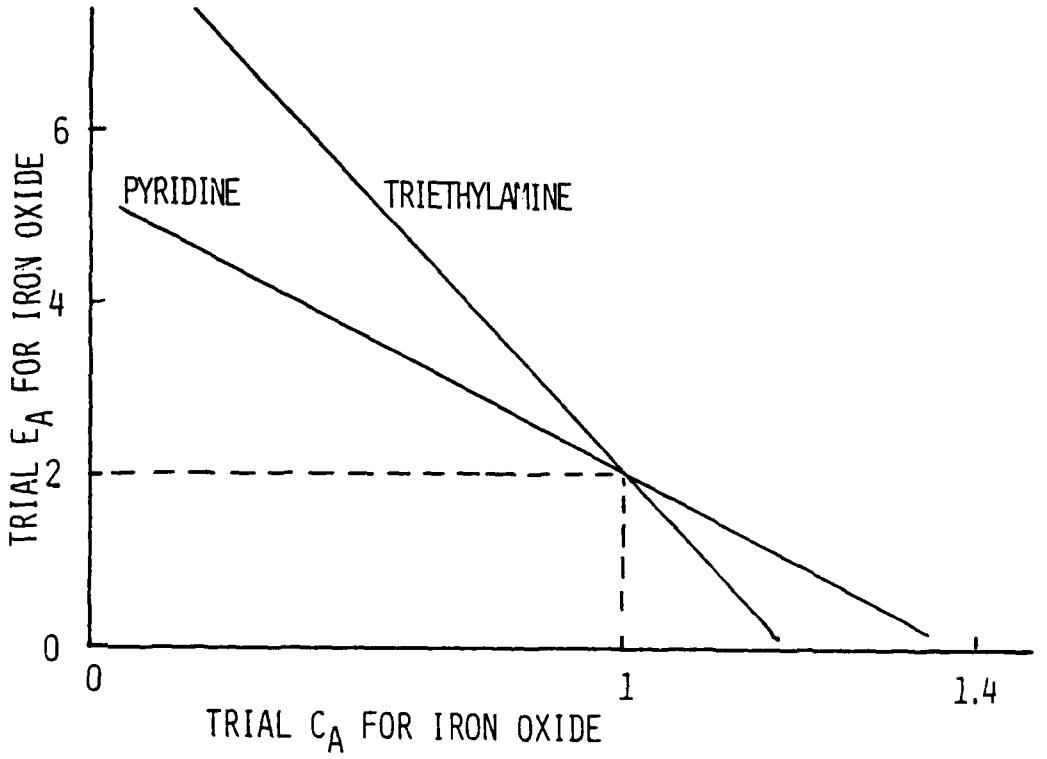

Figure 31. Trial plot of E_A vs C_A for iron oxide surfaces. See text for details.

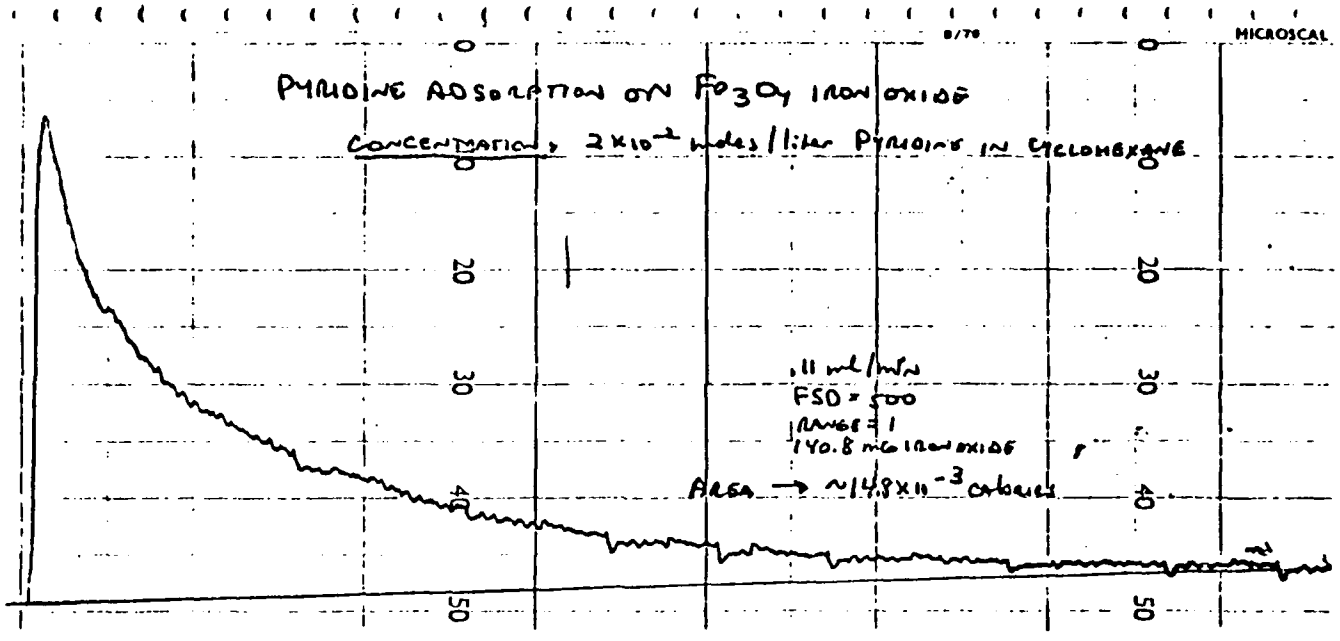

Figure 32. Micro-calorimetric determination of the heat of adsorption at 28°C of 20 x 30^{-3} moles/l of pryidine on 140.8 mg of Fe_3O_4 powder.

SECTION 5

Objective: To Utilize Auger Electron Spectroscopy and X-Ray Photoelectron Spectroscopy to Characterize the Acid/Base Character of Metal Substrates

Title: The Adsorption of Calcium Ions on Iron and Titanium Substrates as a Function of pH

Senior Investigator: Gary W. Simmons

Associate: Bruce C. Beard
Graduate Student

Introduction

A detailed knowledge of the interaction between polymers and metal substrates is fundamental in the development and evaluation of corrosion prevention by paint films. Realistically the surface of any metal surface to be protected by painting is covered with an oxide film, and the paint (polymer) thereby interacts with this oxide rather than directly with the metal. The intermolecular attractions that contribute to the adhesion of polymers to substrates include dispersion forces, dipole interactions and hydrogen-bonding. When the hydrogen bond is treated as an acid-base interaction (20), Fowkes (21) has shown that the strength of the adhesive bonds between a polymer and filler (an oxide such as silica) can be correlated with the relative acidic or basic strengths of the filler, polymer and solvent. For systems in which the filler and polymer are both basic or both acidic, adhesion is primarily via weak dispersion forces, while on the other hand, when one is basic and the other acidic the binding between filler and polymer is dominated by strong hydrogen bonds. The adhesion of polymer coatings to metal surfaces covered with an oxide may also be considered on the basis of acid-base interactions. It is the premise of this work that Auger electron spectroscopy (AES) and X-ray photoelectron spectroscopy (XPS) may be used (a) to determine the acidic or basic strength of oxide films on metal substrates, (b) to determine what factors influence this strength (such as adsorption of Ca and/or Mg ions and (c) to determine the strength of the interaction of different functional groups with oxide films.

Background

All metals exposed to ambient environments have an oxide film on their surfaces. Furthermore, the surface of this oxide is expected to be hydrated from either the moisture in the environment or from previous immersion in an aqueous environment (22,23). Metal surfaces can then be realistically considered in terms of an oxide film and its interaction with water as follows (23).

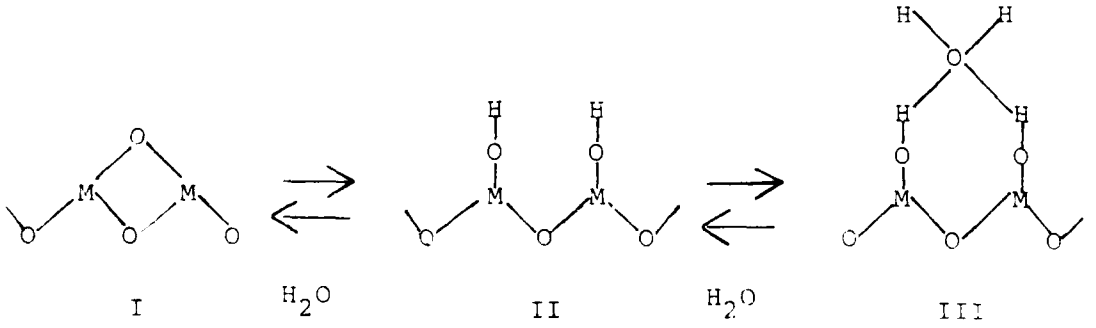

If most metal surfaces can be represented by structure II, then the acidic or basic strength of the surface is determined by the nature of the surface hydroxyl. When electrons are displaced more toward the metal ions than the -OH, the surface will act as an acid whereas when the electrons are displaced more toward the -OH than the metal ion, then the surface will act as a base. Differences in electron charge on the oxygen ions in the oxide lattice and the oxygen in the hydroxyl have been observed in XPS studies of metals oxidized in the presence of water (24,25). Two O_{1s} photoelectron lines are found in these cases and the line with the higher binding energy has been attributed to the hydroxyl. The binding energy of the O_{1s} electrons of hydroxyls may provide a means of measuring the acid/base strength of these groups. The O_{1s} binding energy would be expected to increase for increasing acid strength of the surface hydroxyls. Development of this idea would lead to a convenient means of monitoring the acidic or basic nature of metal surfaces which will be used in evaluating the relative adhesive strengths of different polymer coatings.

Because of the acidic or basic nature of structure II, the surface may readily adsorb significant amounts of ions such as calcium and magnesium from aqueous systems, even when the ion concentrations are quite low. The hydrated oxide can acquire a negative surface charge according to the following reaction:

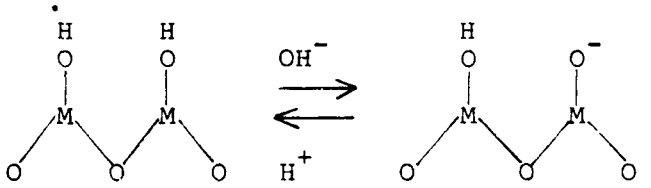

II IV

Cations may then be adsorbed on the oxide layer (26) in a hydrated form or in a form partly dehydrated, as for example in the following reaction:

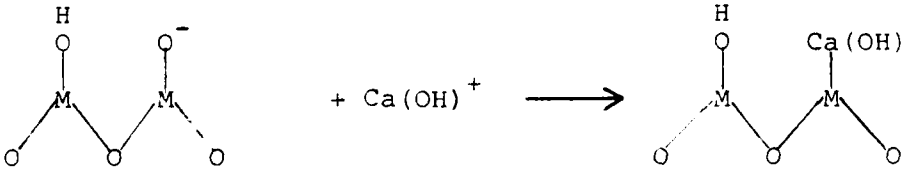

IV V

The extent of this reaction can be readily monitored by AES. Since the equilibrium concentration of calcium in structure V is a function of the surface pH of II, solution pH and calcium ion concentration, it may be possible to quantify the acidic or basic strength of II for different metals by determining the surface

coverage of calcium with AES as a function of pH and calcium ion concentration. The acid/base properties measured in this manner could then be correlated with the binding energies of the O_{1s} from the surface hydroxyls that are present before the adsorption of cations.

The net effect of the adsorption of hydrated or partially hydrated calcium ions is to neutralize the acidic properties of the original hydrated oxide layer. This change in the acidic strength could then alter subsequent adhesive bonding between a metal surface and polymer film. In the preparation of metal surfaces for coating, cation adsorption as well as other changes in the surface may occur. If the development of coatings for maximum adherence is to be developed on the basis of acid-base interactions, it is necessary to explore the possible sources of interference with these interactions that may be encountered in the application of coatings to real systems.

The XPS and AES spectroscopic techniques may also be used to study the interaction between organic functional groups and hydrated oxide surfaces that may be involved in the adhesion of polymer coatings to metals. XPS spectroscopy of organic molecules (containing acid or basic groups) that have been adsorbed onto the hydrated oxide surfaces of different metals may possibly provide information about the relative strengths of the acid base interactions. For example, if the adsorption of a molecule containing a basic amine group is adsorbed onto structure II, having a strong acid character, the decrease in charge on nitrogen may be detected by a shift in the energy of the N_{1s} photoelectron line. Since relative photoelectron peak positions are more precisely determined than absolute energy positions, the molecule should also contain a "reference" nitrogen such as NO_2 or NO_3 that would not participate in the acid-base interaction. The energy difference between these photoelectron peaks would then be a measure of the strength of the acid-base interaction for different metal surfaces and for different surface preparations.

Experimental Results

The objectives of the research are to use AES and XPS to measure the acid-base properties of metal surfaces that are typically coated by organic polymers for corrosion protection and to explore the possible mitigation of these acid-base interactions by adsorption of Ca and/or Mg ions.

(1) Measurements of the energy separation between the O_{1s} photoelectron peaks from lattice oxygen and "hydroxyl" oxygen in the hydrated oxide layers of apporpriately prepared metal substrates are proposed. The data will be evaluated in terms of possible correlations between these energy differences and the acid-base character of the different hydrated oxide layers.

(2) The adsorption of Ca and possibly Mg ions as a function of pH and ion concentration onto the hydrated oxide surfaces of different metal substrates will be studied with AES. The differences in pH at which adsorption occurs will be correlated with O_{1s} binding energy of the hydroxyls present before adsorption.

(3) XPS will be used to study the adsorption of simple organic molecules with different functional groups onto metal surfaces. Competitive adsorption of organic molecules monitored by XPS and/or AES from more aqueous sclutions will be used to establish a relative strength of interaction of different functional groups with metal surfaces.

Parts of tasks 1 and 2 outlined above have been accomplished. Work on task 3 has not yet been initiated. Details of the results obtained for 1 and 2 are described below.

Iron and titanium substrates were chosen for study. The hydrated oxides on these metals were expected to exhibit a relatively wide range of acid/base properties. To provide clean reproducible surfaces the following procedure was used for preparing specimens. Degreased 1.25 cm square specimens were mechanically polished with silicon carbide papers with a final polish with 0.05μ alumina. The specimens were rinsed in distilled, deionized water and absolute ethanol, and dried immediately after polishing. The specimens were heated in air at 180°C for 20 min to form a thin "passive" oxide and to remove carbonaceous contamination.

Exchanges of calcium ions with the surfaces of iron and titanium surfaces were carried out in 0.055M $Ca(NO_3)_2$ solutions. The solution pH was adjusted to the desired value by additions of either KOH (0.1M) or HNO_3 (0.1M). After immersion for two min, the specimens were rinsed in absolute ethanol, dried, and mounted in the AES/XPS spectrometer. AES was used to determine the relative concentration of Ca as a function of pH for each of the specimens and high resolution XPS spectra of metal O_{1s} and C_{1s} lines were obtained for selected specimens.

The most extensive studies have been carried out for iron substrates. Figure 33 shows the Ca/Fe Auger peak ratio as a function of pH for an iron substrate. The data points represent the average of several different experiments and the error bars represent the standard deviation in the averages. Although calcium was found to be present after exchange at all pH values, there is a significant increase in the amount of calcium on the surface in the pH range of 10-12. This result indicates that the hydrated oxide undergoes exchange with calcium ion or partially hydrated calcium ion as described earlier. Furthermore, the exchange occurs over a pH range that is characteristic of the acid strength of the surface hydroxyls.

To provide a contrast with the results obtained with calcium ion exchange with iron surfaces, similar experiments were con-

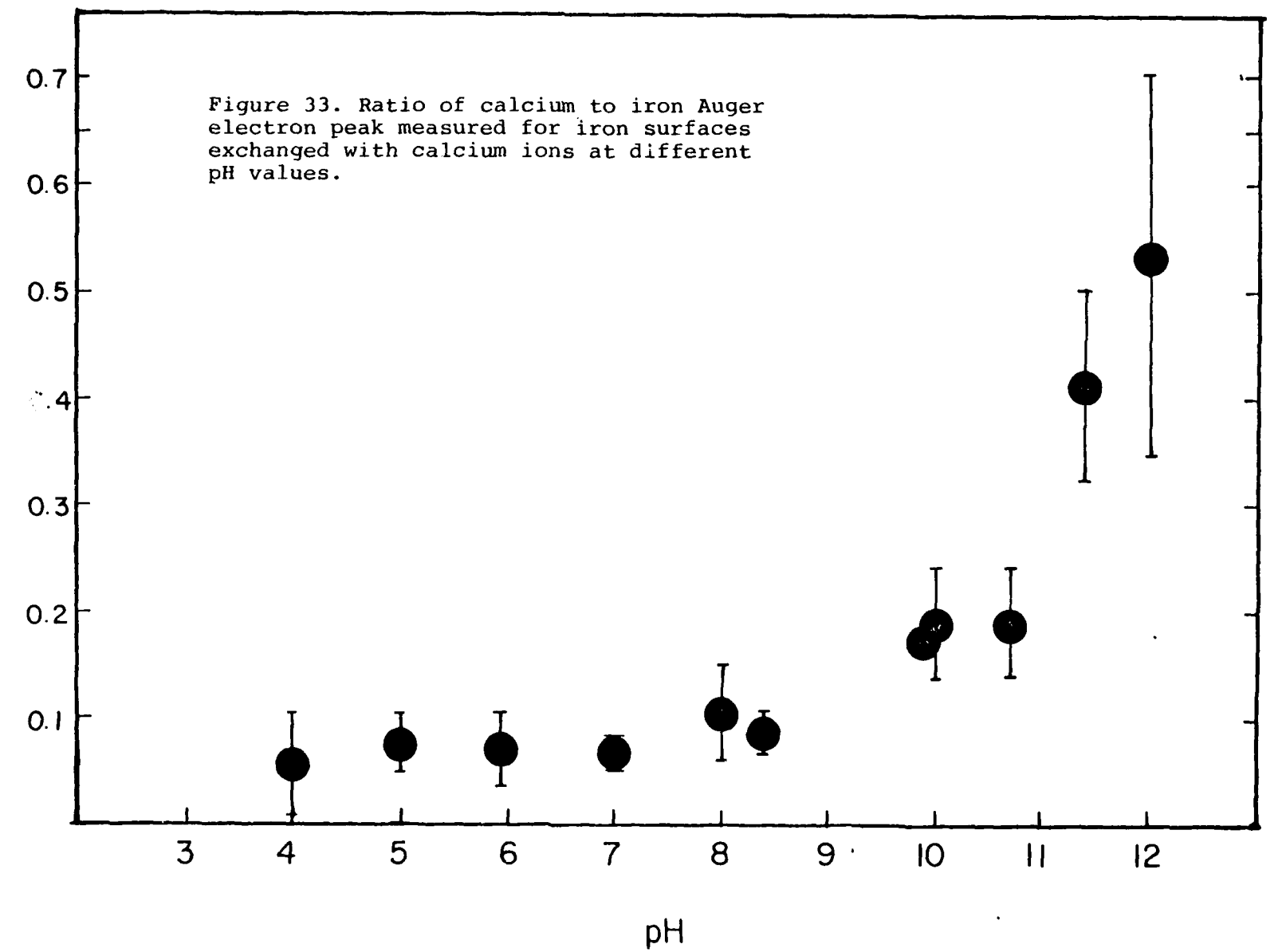

Figure 33. Ratio of calcium to iron Auger electron peak measured for iron surfaces exchanged with calcium ions at different pH values.

ducted with titanium surfaces which were expected to exhibit a relatively higher acid strength. The results for two exchange experiments are shown in Figure 34. Again, calcium was found for surfaces exposed to calcium solutions at all pH values. For titanium the increase in calcium ion exchange occurred in the pH range 9-10. This decrease in pH for exchange compared to that found for iron is consistent with the expected increase in acid strength for the hydrated oxide on titanium.

Oxygen 1s spectra from iron and titanium taken prior to calcium ion exchange are shown in Figures 35 and 36, respectively. These spectra were deconvoluted to resolve clearly the hydroxyl oxygen 1s peak. The relative intensity of the hydroxyl line with respect to the oxide oxygen 1s line can be used as a measure of the surface concentration of hydroxyl groups. After correcting the binding energy scale (based on the binding energy of C_{1s} peak for a small amount of carbon contamination present on each specimen) the oxygen 1s lines for the hydroxyl and oxide oxygen have nearly the same binding energies for both the iron and titanium substrates. A third component has been added to the deconvolution of the titanium O_{1s} spectrum to account for the broad high binding energy side. The identity of this component is uncertain. However, it appears to be present in all cases on titanium, but not iron. It is apparent, at least on the basis of these limited data, that differences in the acid strengths of surface hydroxyls will be difficult to determine from XPS.

The initial studies described above have produced encouraging results. Although there is some question that XPS can be used directly to determine relative acid/base strengths of hydrated oxides present on metal surfaces, the cation exchange monitored by AES is a promising approach. Furthermore, the XPS technique can be used for detection and quantification of surface hydroxyls.

It is proposed to continue along the lines of research developed here. Different surface preparations will be studied and exchange studies using different cations and anions will be considered. Initial experiments will be carried out as described in task 3.

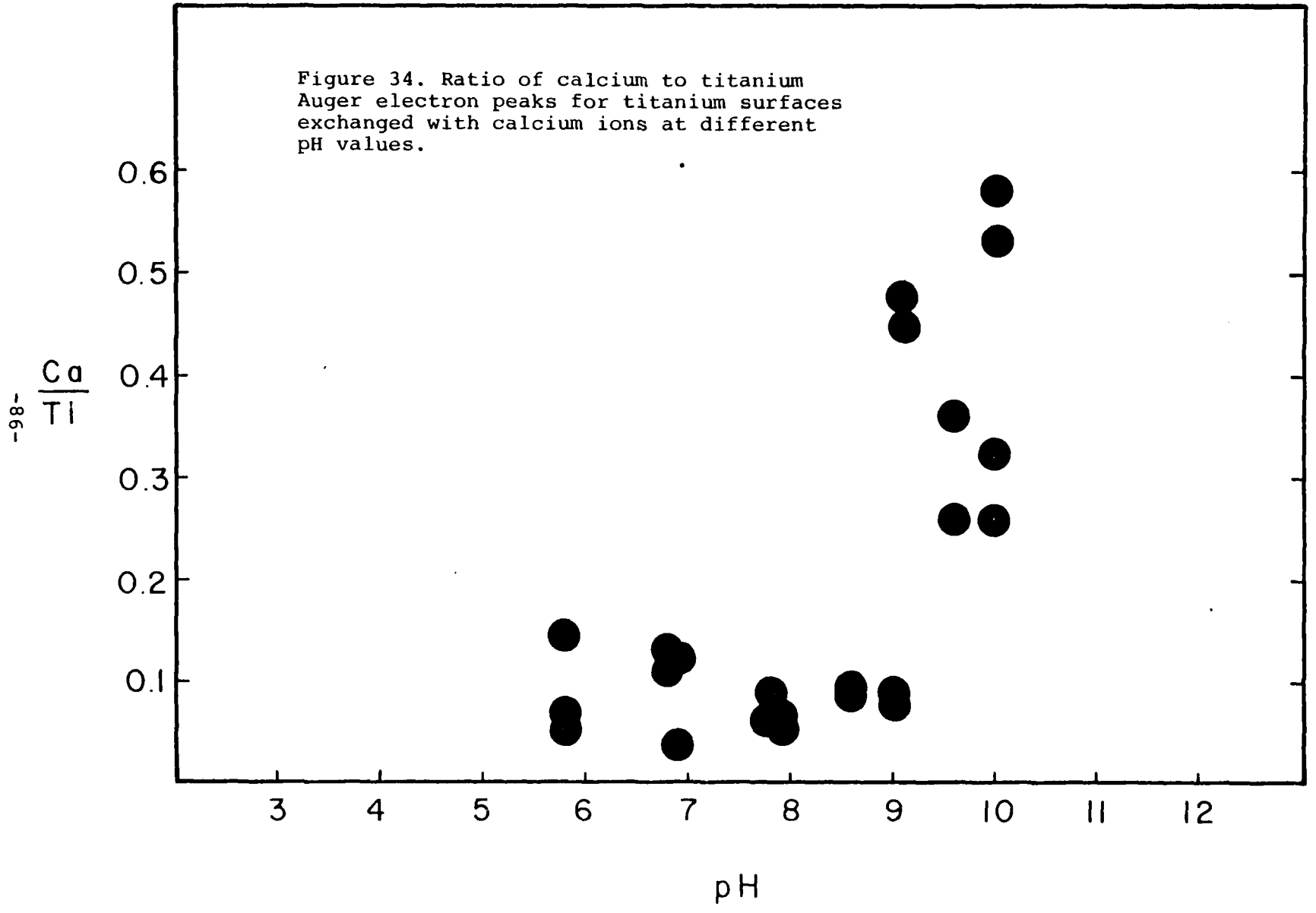

Figure 34. Ratio of calcium to titanium Auger electron peaks for titanium surfaces exchanged with calcium ions at different pH values.

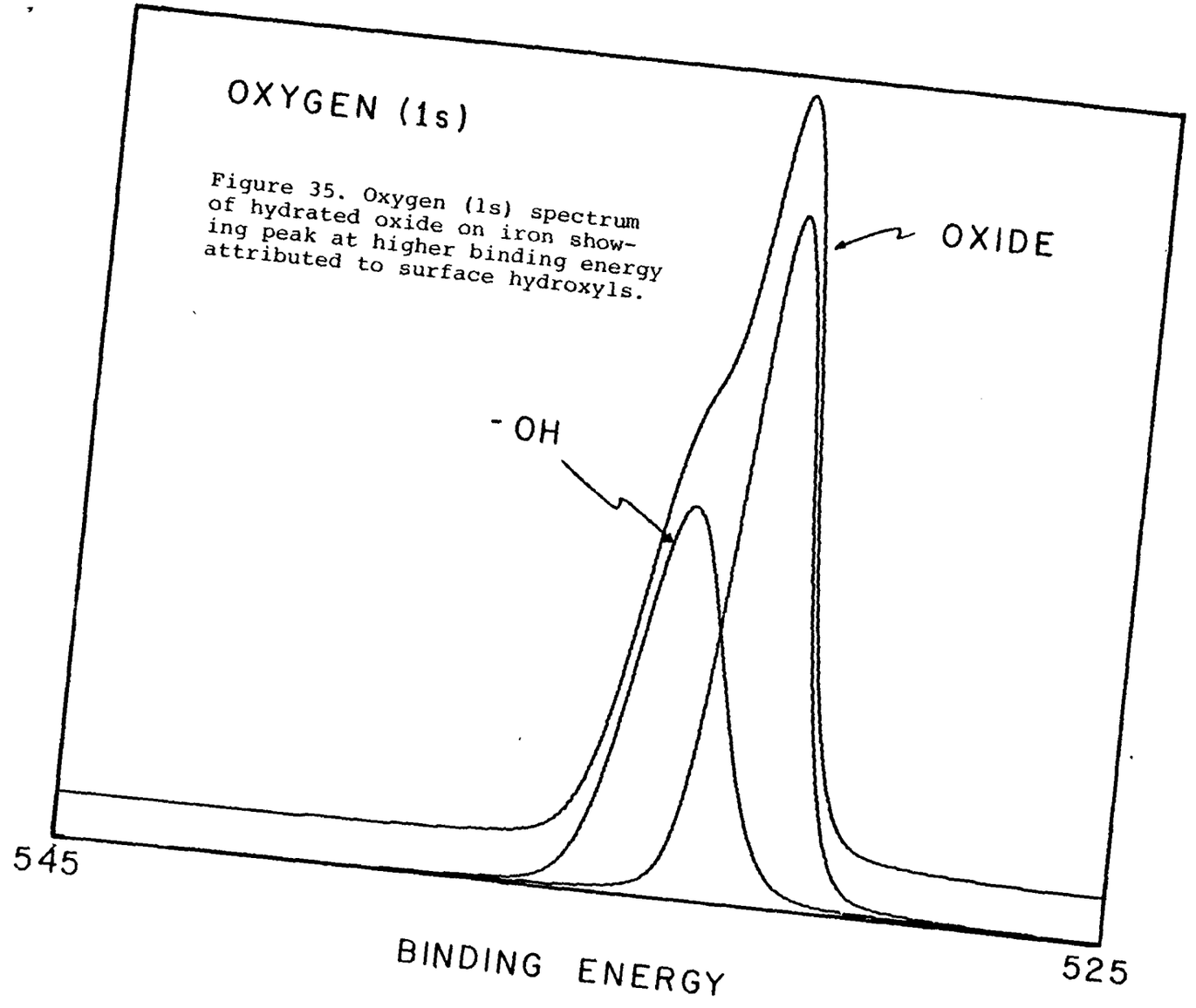

Figure 35. Oxygen (1s) spectrum of hydrated oxide on iron showing peak at higher binding energy attributed to surface hydroxyls.

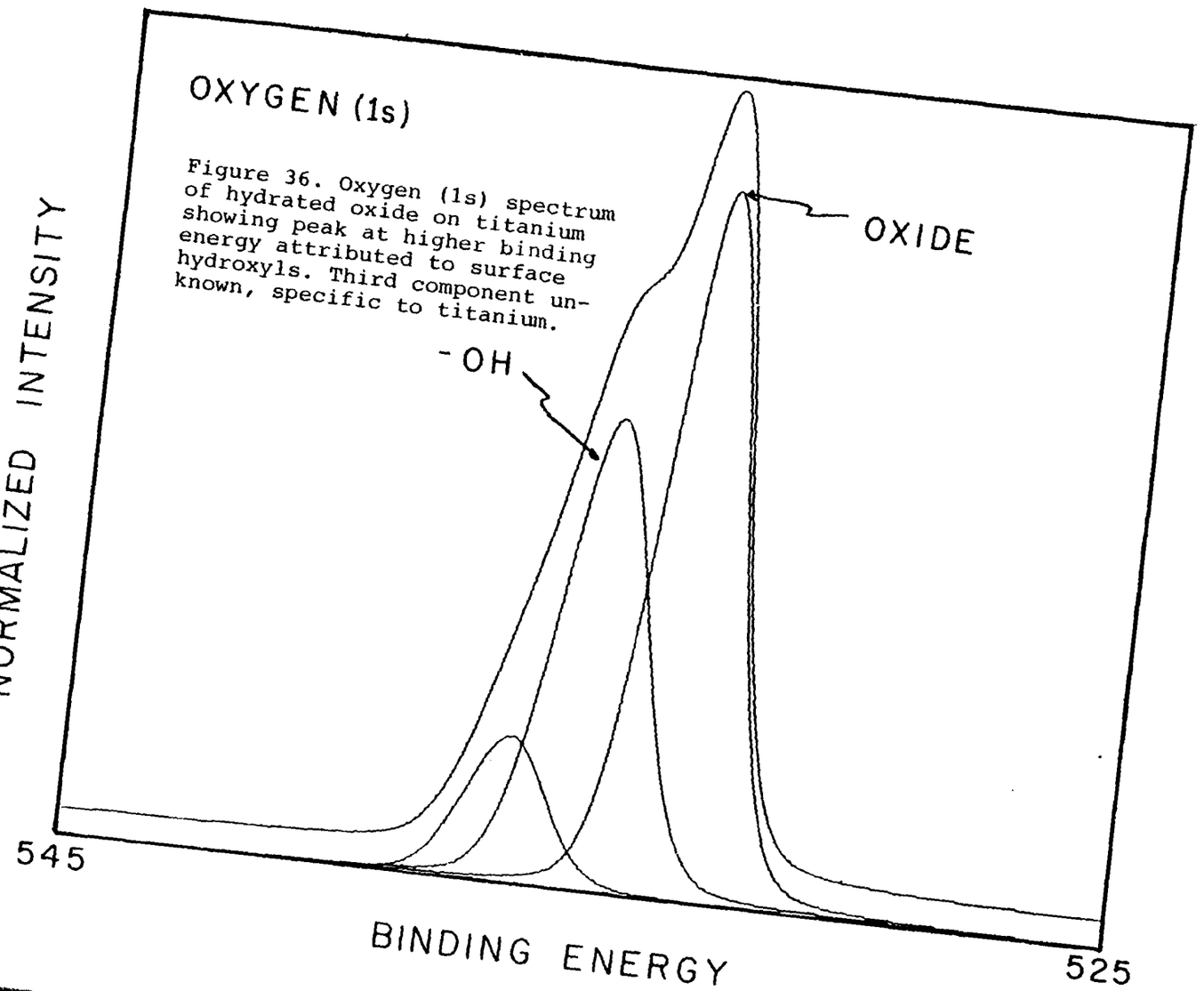

Figure 36. Oxygen (1s) spectrum of hydrated oxide on titanium showing peak at higher binding energy attributed to surface hydroxyls. Third component unknown, specific to titanium.

SECTION 6

Objective: To Characterize Iron Oxide Corrosion Products by Means of Mössbauer Spectroscopy

Title: The Development of a Detailed Computer Program Useful in Characterizing Mössbauer Spectra for Magnetic and Non-Magnetic Materials

Senior Investigator: Gary W. Simmons

Work Performed Largely by: Sandor I. Nagy, Visiting Scientist
Thomas Weir, Graduate Student

Introduction

The oxide corrosion products formed on iron and steel under atmospheric exposure have been studied by Graham and Cohen (1). These "fingerprint" spectra are very useful. However, companion studies in this program will utilize iron oxides prepared under carefully controlled conditions in the presence of different anions. It is expected that several hundred different iron oxides will be examined and minor differences in the Mössbauer spectra will be sought. In order to determine these minor differences, a modified computer analysis program has been developed based on one in use at the Central Physical Research Institute in Budapest, Hungary.

The program has been completely developed in a form that a new worker can immediately adopt to a specific application. The details of the program are too long for inclusion in the present report and the first ten pages of the detailed report only will be given here. Copies of the full program will be furnished to readers who might wish to examine its applicability to their research.

General Features of the SIRIUS Evaluating System

The SIRIUS system is designed for storing, handling, evaluating and plotting of Mössbauer spectra, or different kinds of nuclear spectra collected by multichannel analysers. The system is a modified version of the SIRIUS 40 system, the latter written in the Central Physical Research Institute, Budapest, Hungary.

The main constituents of the present system are shown in Figure 37. The core of the system consists of the SIRIUS Procedure File, the SIRIUS MT Program Library and the two volumes of the SIRIUS MT Spectrum Library. The flexibility of the SIRIUS procedure allows every user to have his own two volumes of spectrum library. The MT-s of the Program Library and the Spectrum Library are stored usually at the Computer Center. The SIRIUS Procedure which is a set of SCOPE control macros, is permanently stored in discs so that it is always available.

Typical cases of the use of the SIRIUS Procedure macros are shown in the flow diagram of Figure 38. The typical working day begins with a job controlled by the MORNing macro. This macro reads (R) the load module of the SIRIUS Program as well as both volumes of the Spectrum Library from the MT-s to disc. It also creates (C) a third disc data file called STORAGE. From a practical point of view, during the day, the SIRIUS Procedure file and the last four disc files can be regarded as "the SIRIUS System", since the program itself does not use the physical MT-s.

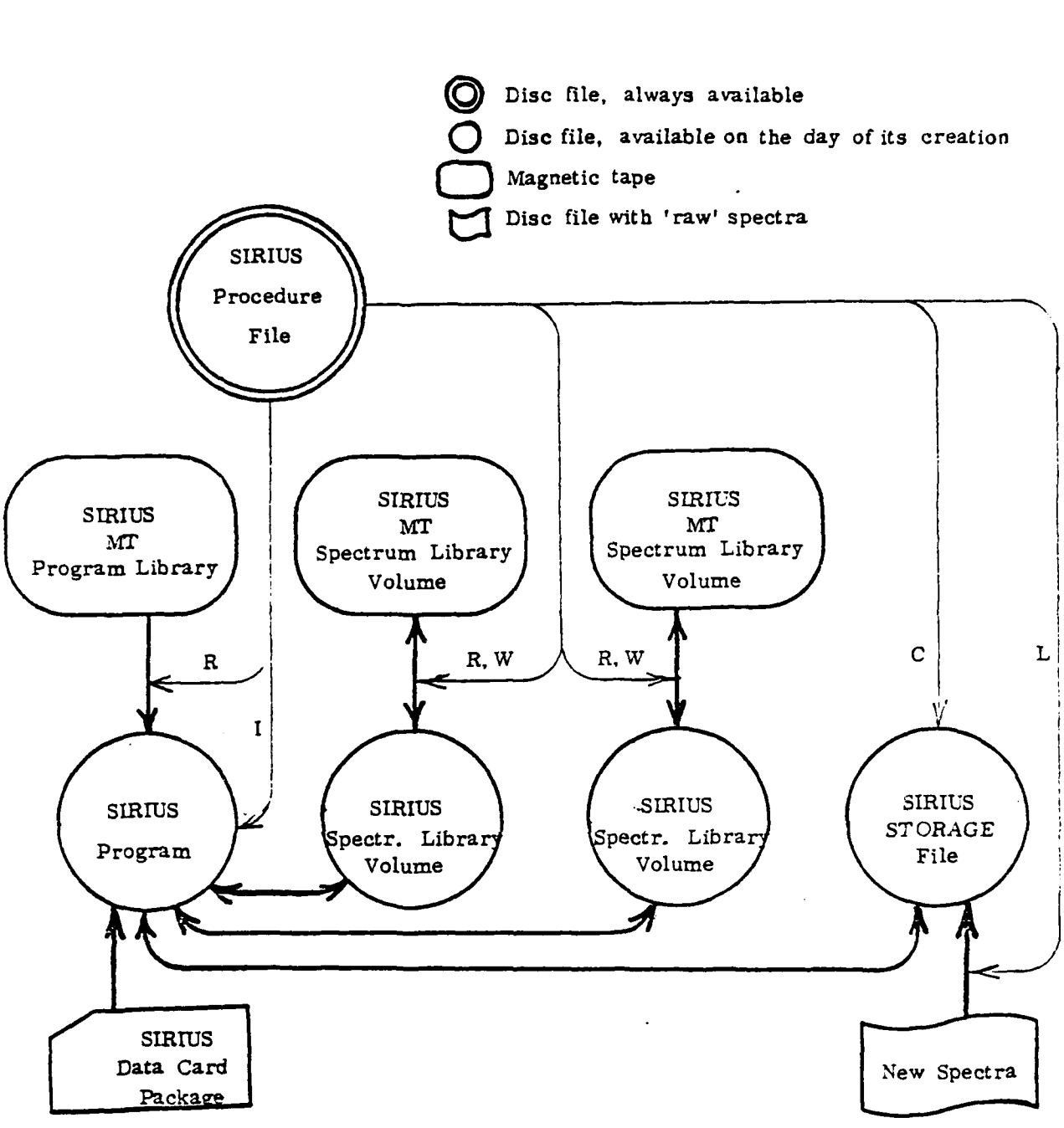

C= Create a disc file
I= Initiate the run of the SIRIUS program
L= Load the new ('raw') spectra into the STORAGE file
R= Read a file from manetic tape to disc
W= Write a file from disc to magnetic tape
The functions of the macros of the SIRIUS procedure are as follows:

MORN: R, C
DAILY: I
NEWSP: L, then I
EVE: W

Figure 37. The scheme of the SIRIUS system.

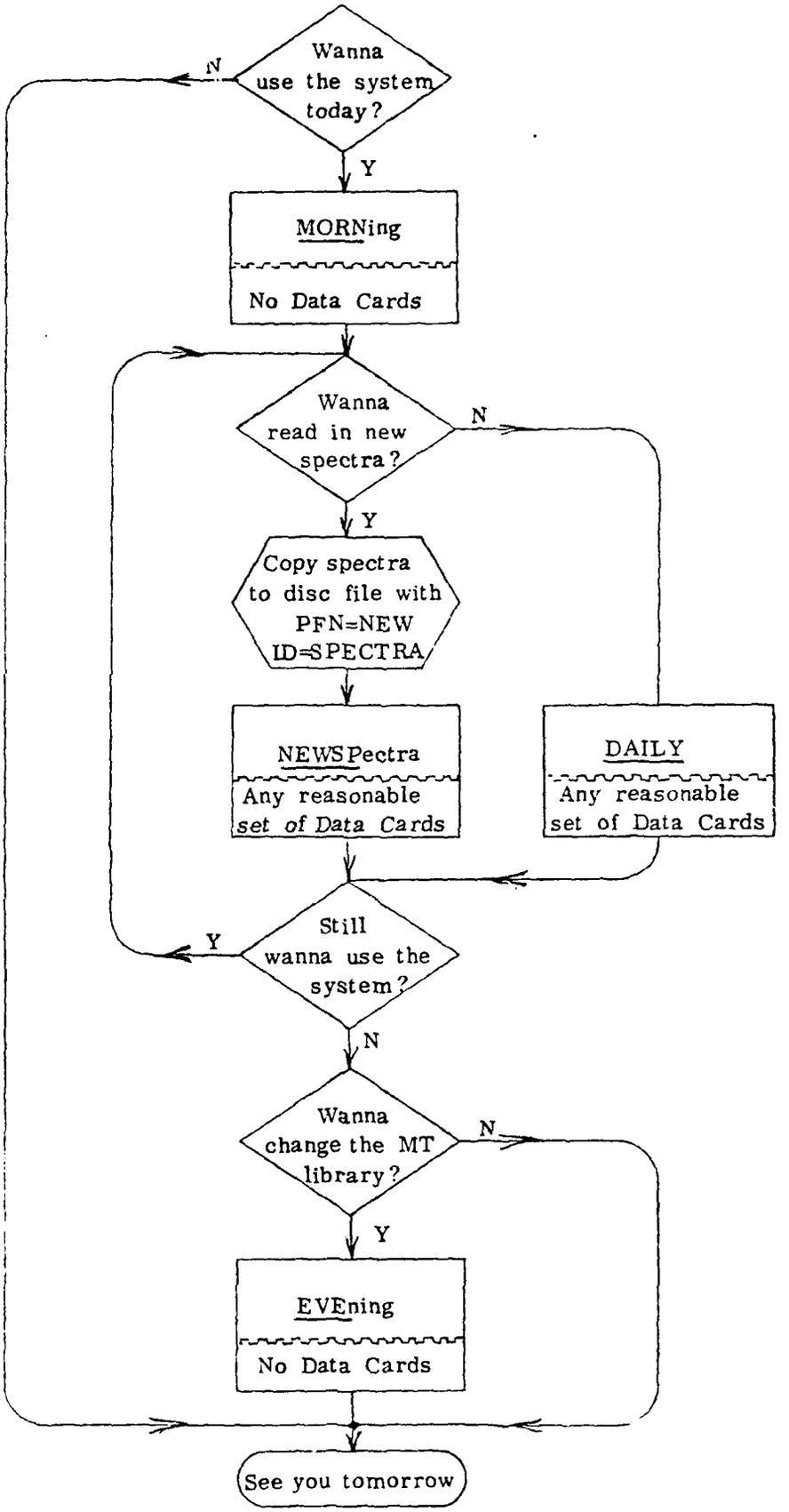

Figure 38. Typical sequence of jobs when working with the SIRIUS system.

During the day the DAILY and/or the NEWSP macros control the jobs. In each job either a NEWSP or a DAILY call is necessary, depending on one's desire to read or not to read in NEW SPectra to the Spectrum Library.

If during the day the user changed the disc copy of the Spectrum Library (e.g. by reading in new spectra) and wants to keep the new version, he must write (W) into the MT Spectrum Library. Since this has to be done at the latest in the evening of the same day, the macro doing this is called EVEning.

As Figure 39 shows the SIRIUS Program is actually a program system with a tree structure consisting of the main program (ROOT) and several subprograms (branches) with different functions. The subprograms can be activated in any order and at any time within the same job.

The activation and the control of the subprograms is managed by the SIRIUS Data Cards. Each activation of the XXXX Subprogram (XXXX=SAVE, LIBR, DISP, UNIV, SEXT, or ALLO) is associated with a certain group of DATA Cards which we call the XXXX Control Block. The first card of the Control Block is the

```
=XXXX
```

Routing Command, which actually activates the XXXX Subprogram. The last card of the Control Block is the

```
BACK
```

command, which returns control to the main program in order to read in and interpret the Routing Command of the next Control Block. The cards between the Routing Command and the BACK command we call Control Cards because their function is to control the activity of the subprogram. These cards have special syntax which will be explained later.

There is also a special Control Block, consisting of the sole

```
=STOP
```

Routing Command, the function of which is to stop the run of the program. Naturally this card must be the very last Data Card.

Figure 40 shows the general structure of a SIRIUS Data Card package.

One of the most important features of the SIRIUS System is that the spectra to be evaluated are stored in the SIRIUS Spectrum Library. The permanent Spectrum Library consists of two MT-s (volumes), but the SIRIUS Program itself uses their disc images.

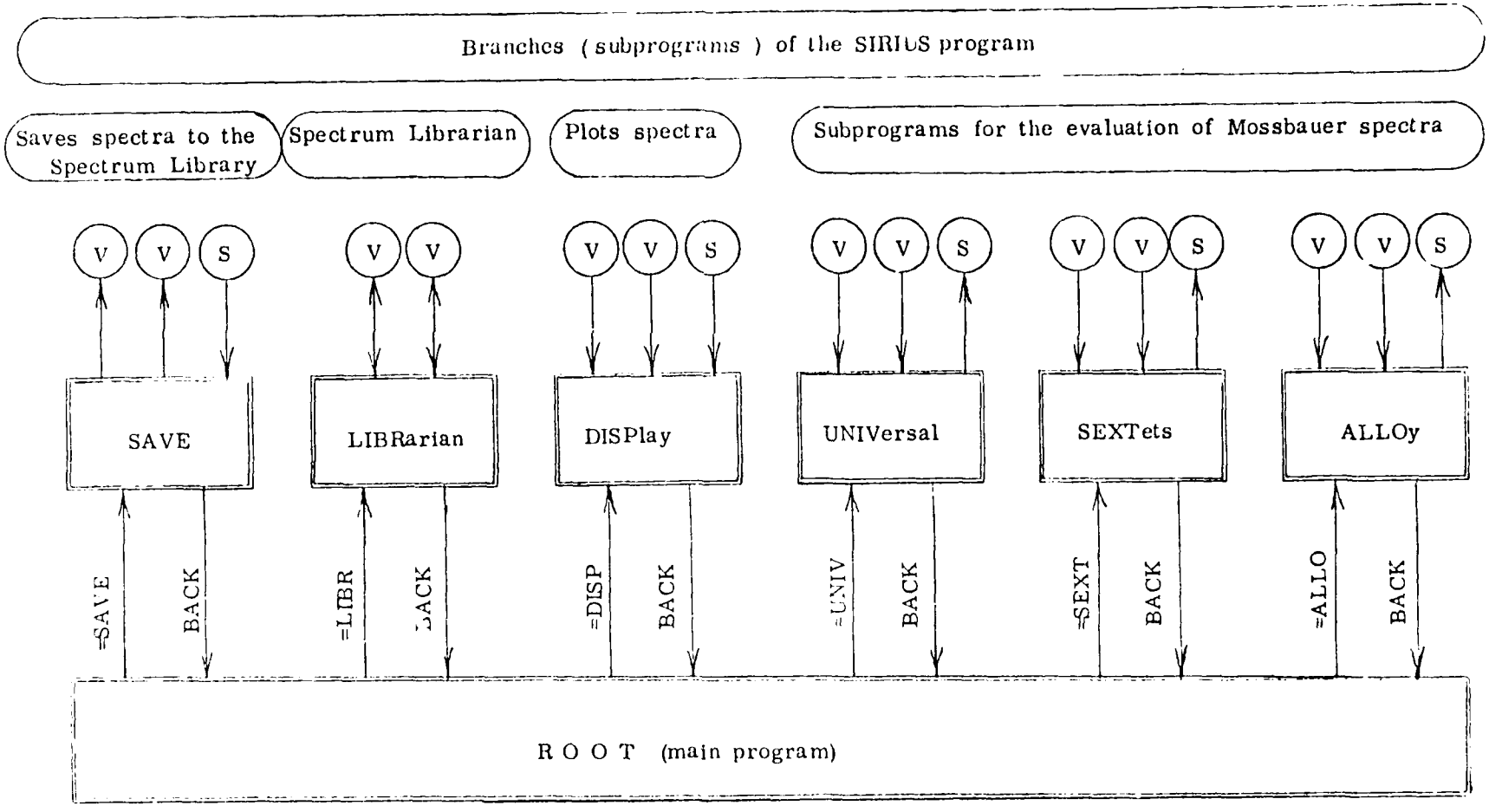

Figure 39. The tree structure of the SIRIUS program and its connection with the standard disc data files of the SIRIUS system. (V) = Volume of the Spectrum Library, (S) = STORAGE file.

AD-A095 420 LEHIGH UNIV BETHLEHEM PA CENTER FOR SURFACE AND COA--ETC F/G 11/3
CORROSION CONTROL THROUGH A BETTER UNDERSTANDING OF THE METALLI--ETC(U)
DEC 80 H LEIDHEISER, M S EL-AASSER N00014-79-C-0731

UNCLASSIFIED NL

2 OF 3
AD
A095420

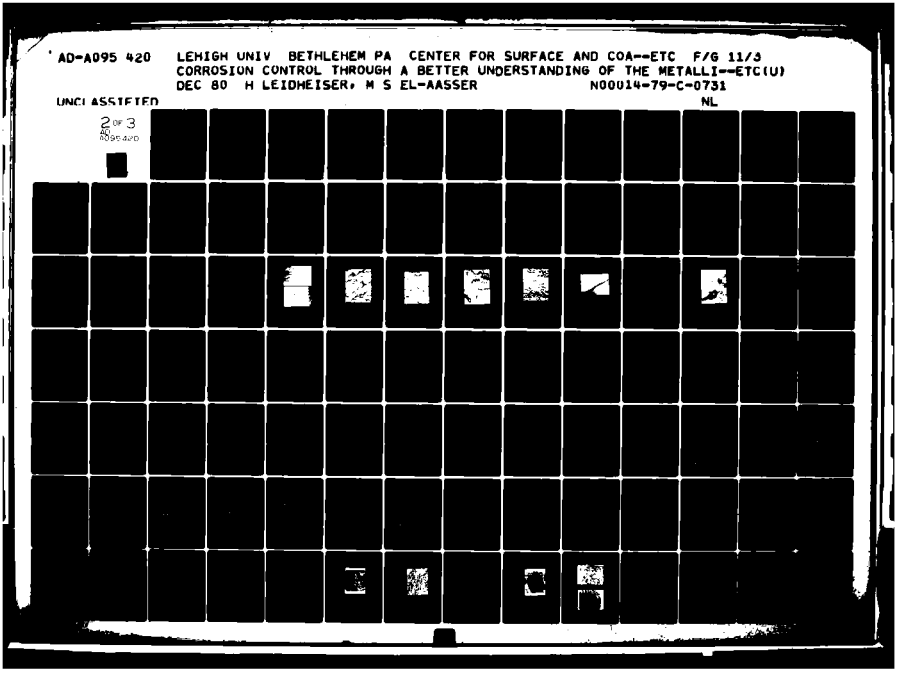

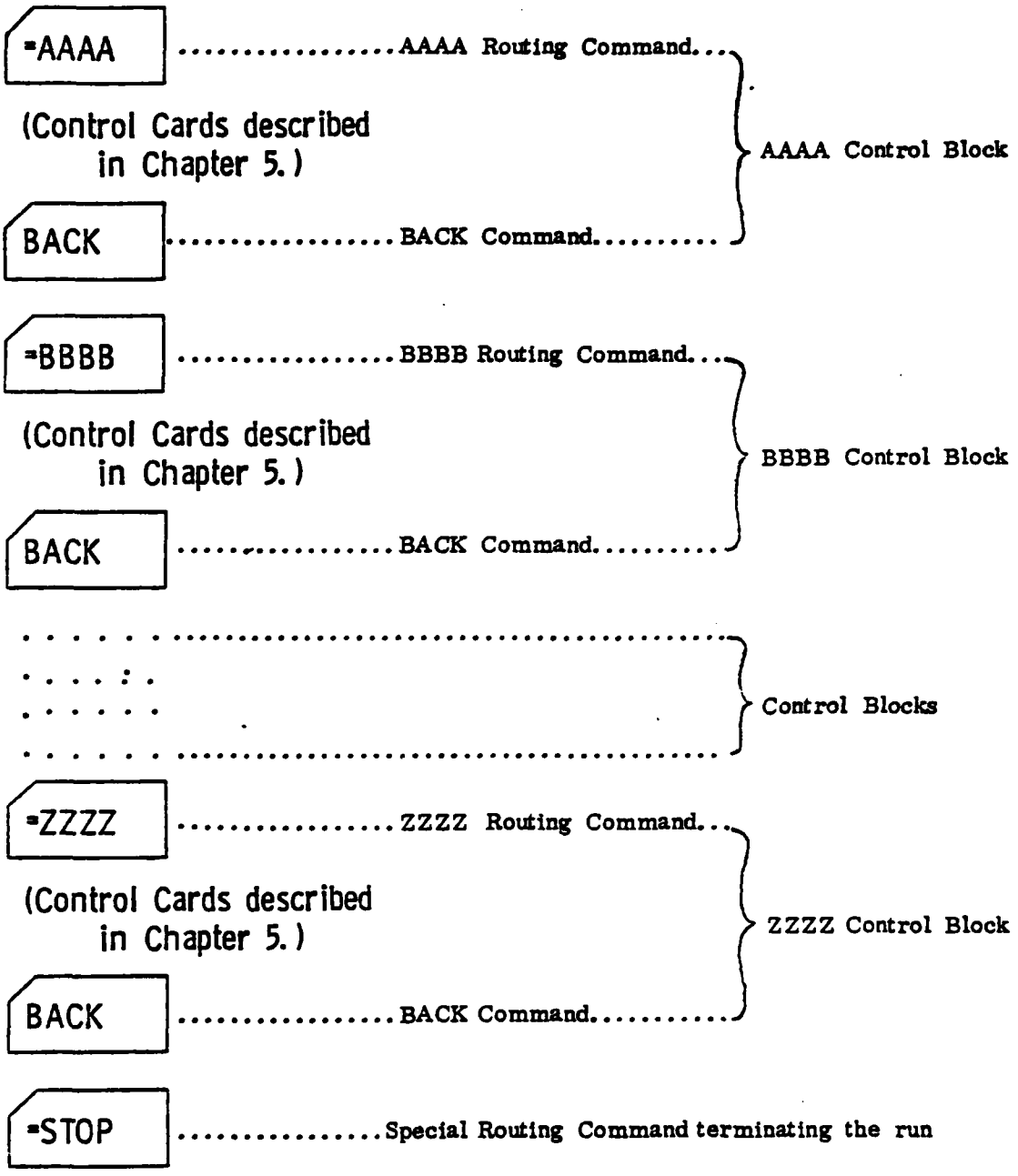

Figure 40. The structure of the SIRIUS Data Card Package. AAAA, BBBB, ... ZZZZ replace any of SAVE, LIBR, DISP, UNIV, SEXT, ALLO.

The advantage of the Spectrum Library concept is obvious: once the spectra are in the library, the punch tape or card package on which the spectra were recorded can be discarded and further the spectra are more easily available for plotting or evaluating by any of the fitting subprograms as many times as necessary. The advantage of the disc library to the MT Library is that the former is much faster, the disadvantage is that the rent of the disc space is much more expensive. That is why it was decided that the permanent storage of the Spectrum Library be magnetic tape, but during the working day the program would use the disc copy.

This kind of compromise resulted in another advantage. If the user should spoil the disc library, or make changes in it, which are not worth keeping there is nothing to worry about: the original library is intact and still available on the MT-s. It is important, therefore, to make sure that the new variant of the library on the disc is really better than the old one before over-writing the Library tapes. It is advisable to make a list of the Library by the LIBR subprogram after each change.

The volumes of the Spectrum Library are files with a special block structure. A Library file containing 'n' spectra contains n+2 blocks with serial numbers from 0 to n+1.

The 0-th block contains the Name of the Spectrum Library Volume. This name (up to 24 characters) is given by the user. The first 8 characters of the Volume Name is the ID of the Volume. Later on the user can refer to the volume by its ID. When referring to the volume, the last blank characters can be neglected. For example, these two ID-s are the same DATA-1$_{VV}$ or DATA-1. The Volume Name is given in the "creating" by the CREA Control Card of the LIBR subprogram.

The blocks numbered from 1 to n contain the n spectra with their individual spectrum titles (up to 120 characters each) and lengths. The user can refer to the spectra by these block numbers which we call the Spectrum Numbers. The related Spectrum Numbers and spectrum titles can be listed by the TLIS control card of the LIBR subprogram.

The (n+1)th block (filled with minus ones) is used as a special End Of Volume record for the spectrum searching part of the program, preventing the program from hitting the EOF mark when the user tries to read in a spectrum which is not in the Volume.

At present the program contains s' . subprograms (Figure 39). Their precise description is given in :hapter 5. Here, the most important functions only are summariz(i.

The LIBRarian subprogram is the spectrum Librarian of the System. This is the only subprogram which can "create" a new

Spectrum Library volume from an empty MT (or rather from an empty disc file). This function is very important, because the other branches cannot use a non-SIRIUS-like Spectrum Library volume. By LIBR, we can rearrange spectra in the Library, copy spectra from one volume to the other, delete spectra from the Library, fold and correct spectra, get contents of the volumes and get data lists of the desired spectra.

The SAVE is also a fundamental subprogram. This subprogram is the only branch which can transfer spectra from the STORAGE file to the Spectrum Library. This feature makes it possible to read in new spectra to the Spectrum Library and to save fitted spectra if desired. It can also erase the information in the STORAGE File.

The DISPlay is the plotter subprogram of the system. By DISP we can plot measured spectra from the Spectrum Library and visualize the results of spectrum fittings. The information required for the latter is deposited by the evaluating subprogram to the STORAGE File. After the DISP Control Block the STORAGE File is always rewound.

The UNIVersal, SEXTets and ALLOy subprograms can be used for fitting Mössbauer spectra. For general purposes the UNIV is the most suitable of the three, because of its flexibility in respect to constraining the fitted parameters. For Mössbauer spectra containing several sextets the SEXT subprogram can be recommended. The ALLO is a special subprogram for resolving spectra of ferromagnetic iron alloys with a few percent of alloying element concentration. After finishing the fitting of a spectrum, the evaluating subprograms write out a special display information block to the STORAGE File without ever rewinding it. The UNIV, SEXT and ALLO Control Blocks themselves cannot initiate the plotting of the results.

Blank

SECTION 7

Objective: To Obtain Fundamental Information about Film Formation Mechanisms

Title: Part A. Cathodic Electrodeposition of Epoxy Latexes and Morphological Studies of the Coating Films

Part B. Drying and Curing of Epoxy Films

Senior Investigator: M. S. El-Aasser

Associates: Babatunde E. Aremu, Graduate Student
Kenneth Earhart, Research Associate
C. C. Ho, Visiting Scientist
Arif Humayun, Graduate Student
John W. Vanderhoff, Faculty Member

Part A. Cathodic Electrodeposition of Epoxy Latexes and Morphological Studies of the Coating Films

Introduction

The process of electrodeposition of organic coating materials onto metal objects has been known since the early thirties. However, it was not until the beginning of the sixties that the process was widely adopted in the automotive and appliance industries to give prime and one-coat finishes to a variety of products. A wealth of information on the mechanism and development of this process has since been reported (27). However, most of the electrodeposition processes known hitherto are anodic. In contrast, development of the cathodic process has been relatively slow. This slow development is primarily due to the lack of resins and polymers suitable for the cathodic process. Apart from a handful of polymer systems designed to deposit at the cathode as described in some recent patents, very little basic information about cathodic systems for coating metallic substrates has been reported in the literature. Thus the present fundamental studies on the cathodic electrodeposition of epoxy latexes on steel substrates represent a natural extension of the extensive work done on conventional anodic systems. This paper describes factors affecting the deposition behavior of cationic latexes.

Cathodic Electrodeposition

The electrocoating process is based on the migration of macro-ions under the influence of an electric field and the subsequent discharge and deposition at the appropriate electrode which is the metal object to be coated. Cathodic electrodeposition involves immersing an electroconductive object in an aqueous dispersion of a polymeric material which contains cationic groups such as quaternary ammonium ions. An electric current is passed through the dispersion between the metallic object as the cathode and an inert anode. Deposition of the polymer on the cathode results under appropriate conditions.

Anodic electrodeposition is essentially the opposite of cathodic electrodeposition in that negatively charged polymers are deposited on the anode, but there are distinct performance differences between the two types of coatings. The anodic process is usually accompanied by electrochemical dissolution of the anodic workpiece, and the subsequent incorporation of this dissolved metal into the finished coating gives rise to reduced corrosion resistance and discoloration of the anodic coating. A variety of methods has since been developed and used in circumventing these shortcomings of the anodic process.

In contrast, cathodically deposited films are inherently corrosion-protective and devoid of staining and discoloration as a result of the alkaline nature of the cationic polymer and the passivity of the cathode. The inherent performance qualities of cationic films enable these coatings to surpass by far those properties obtained with anionic films, specifically, corrosion protection, detergent resistance, gloss retention and resistance to staining.

The electrodeposition process is an effective and proven technology capable of complete automation and easy control. The equipment required to operate a cathodic electrocoating system is not substantially different from that required to operate an anionic electrocoating system. With the incorporation of ultrafiltration technique in a closed loop rinsing system, the rinsed-off "drag out" materials can be recycled into the system, thus assuring nearly 100% utilization of polymer materials. Minimum pollution of the effluent water is maintained and the need for flocculating equipment is precluded. These factors, coupled with the utilization of aqueous systems containing minimal volatile additives, has enabled the electrodeposition process to become a virtually non-polluting coating process with the minimum adverse impact on the environment.

Most of the fundamental studies of electrodeposition have been carried out with polymer resins that are solubilized with acids or bases rather than with dispersed discrete particles such as latexes and dispersions. Solubilized polymer resins, when electrodeposited, coalesce easily to form a coherent film which is resistant to the passage of current. However, the process of film formation by electrodeposition of dispersions is more complex and may be the result of an entirely different mechanism. Recent work by Wessling et al (28) has demonstrated the use of tertiary sulfonium and quaternary ammonium salts to impart positive charges to latexes for cathodic electrodeposition. Cationic aqueous dispersions of epoxy resins have previously been prepared in this laboratory using a mixed emulsifier system such as hexadecyltrimethylammonium bromide and hexadecane (29); the particles of these dispersions are small and thus they are ideal for the studies of cathodic electrodeposition.

Materials and Experiments

The epoxy resin used for this work was Epon 1001 (a solid at room temperature with an epoxide equivalent of 450-550; Shell Chemical Co.) and the curing agent was Emerez 1511 (a highly viscous condensation product of a polyamine and a dibasic acid with an amine value of 230-246; Emery Industries Inc.). See details in appendix. Latexes were prepared from these resins by direct emulsification according to recipe and procedure given previously (29). Briefly, the method involved dissolving

the resin in a water-immiscible solvent, then mixing hexadecane with polymer solution, adding the solution to an aqueous solution of the emulsifier system (hexadecyltrimethylammonium bromide) to form a crude emulsion and homogenizing by using the Manton-Gaulin Submicron Disperser. The emulsions produced were stable when subjected to steam stripping under vacuum to remove the solvents.

The particle size distributions of the Epon 1001 and Emerez 1511 latexes were examined by transmission electron microscopy using the cold stage technique.

The substrate used was cold-rolled steel plates (Bethlehem Steel Corp.). These were first cleaned with soap solution, degreased according to ASTM method D609-73 using trichloroethylene, rinsed with deionized water followed by acetone, and then kept in a desiccator until use.

The electrodeposition was carried out at room temperature in a rectangular Plexiglas cell of dimension 2.7x3.8(h)x9 cm. Two equal-size carbon rods were used as anodes and these were positioned at the ends of the cell. An untreated cold-rolled steel plate of 2.2 cm width was used as the cathode, which could be raised or lowered into the cell midway between the anodes by a motor drive (at a speed of 3 ft/min) to ensure smooth entry. The experimental setup is illustrated schematically in Figure 41. A DC power supply capable of producing up to a maximum of 750 v and 10 amp was used. The circuit also included a strip chart recorder to plot current as a function of time. The area under the current-time curve was integrated using a Carl Zeiss MOP 3 analyzer to obtain the coulombs of charge passed. All depositions were conducted at constant applied voltage with live entry. Typically, the electrodeposition bath contained a 10% solids dispersion of pH 7.5-8.0 for epoxy latex and 9.3-9.7 for the mixture of latexes. Each plate was electrocoated for 60 sec. After deposition, the plate was dip-washed with deionized water, baked at 90°C for 4 hr, and weighed to determine the amount of polymer deposited.

To study the morphology of the surface films after deposition, the plates were not baked, but were allowed to air-dry followed by vacuum drying at room temperature. The coated portion of the plate was sectioned, vacuum-coated with a thin layer of palladium-gold alloy and examined in the scanning electron microscope.

Results and Discussion

Particle size analysis of the Epon 1001 latex indicated that 95% of the particles were smaller than 110 nm and the number average particle size of the dispersion was 65 nm, whereas that of the Emerez 1511 latex was 20-30 nm.

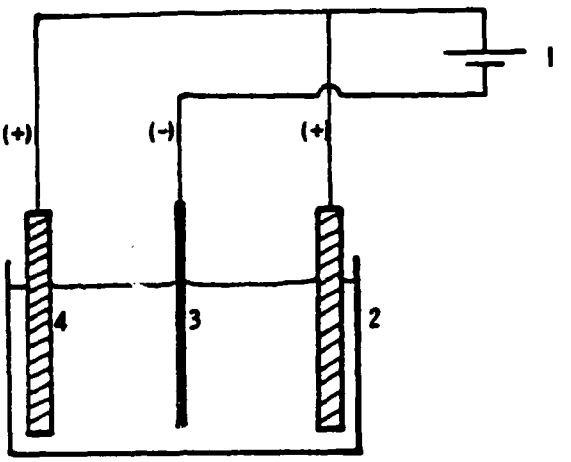

Figure 41. Schematic illustration of the electrodeposition cell: (1) 750 v, 10 amp DC power supply; (2) rectangular plexiglass cell; (3) cold-rolled steel cathode; (4) carbon anodes.

Preliminary investigations of the electrokinetic properties of the epoxy latex showed that:

i: electrophoretic mobility of the latex particles was constant down to a solids content of 10^{-3}% solids at pH 5.5-6.0 and then began to decrease on further dilution;

ii: at fixed solids content, the mobility varied from +3.5 μm cm v^{-1} sec^{-1} at pH 3.5 to ca +2.4 μm v^{-1} sec^{-1} at pH 10.7.

These results indicate that the emulsifier system used in the preparation of the epoxy dispersion can withstand dilution and variation in pH without any detrimental effect on the migration of the particles under the influence of an electric field.

Current-Time Voltage Relationship

Single-Component System: Epoxy Latex

Typical plots of the variation of current with time at various applied voltages are shown in Figure 42. The deposition time was 60 sec for each sample. The initial rapid rise in current within about one sec (up to point X) indicates the completion of the immersion of the plate. The behavior of the current-time curve beyond X depended on the magnitude of the applied voltage. At low voltage (Figure 42a) a conducting film was formed as evidenced by the increasing current with deposition. Similar observations (28) have been reported for a quaternary ammonium stabilized water-soluble polymer system deposited anodically at higher voltage of 200 v. At intermediate voltage (Figure 42b), the current-time curve was characterized by an initial rise in current followed by a slow current cutoff. The film still retained considerable conductivity at the finish. At high voltage (Figure 42c), the current fell off rapidly after reaching a maximum value (point Y) to a low residual amperage, showing that the film was becoming insulating. At still higher voltage (Figure 42d), an uncontrolled increase in current was observed after a rapid current cutoff. This behavior was taken to indicate that film rupture had occurred. The rupture occurred at shorter times as voltage was increased. For example, the abrupt increase in current occurred 42 sec after deposition started at 230 v, whereas it occurred after 33 sec at 268 v. The above results clearly show that an optimum voltage range is required for rapid current cutoff to give non-conducting films and that film rupture is dependent upon the current-voltage relationship of the deposited film.

An illustration is given in Figure 43 in which the residual amperage (in terms of mamp/cm^2) at the end of the deposition

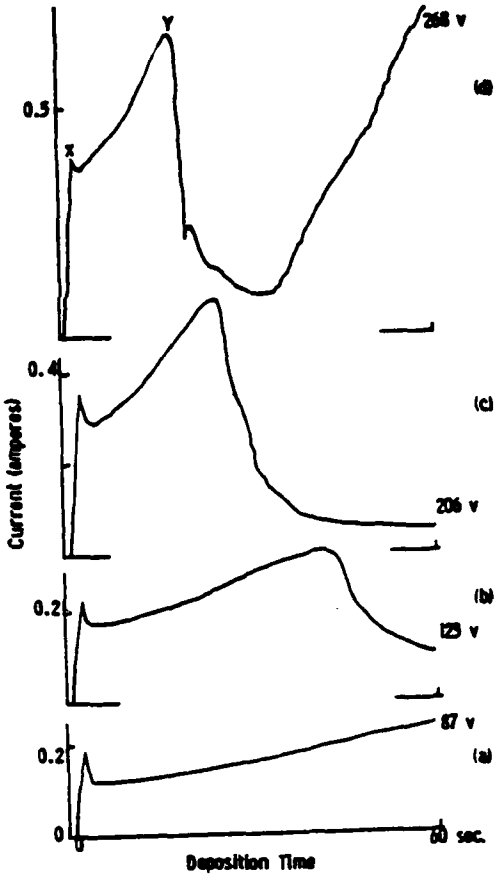

Figure 42. Current-time relationship for electrodeposition of Epon 1001 latex at various applied voltages.

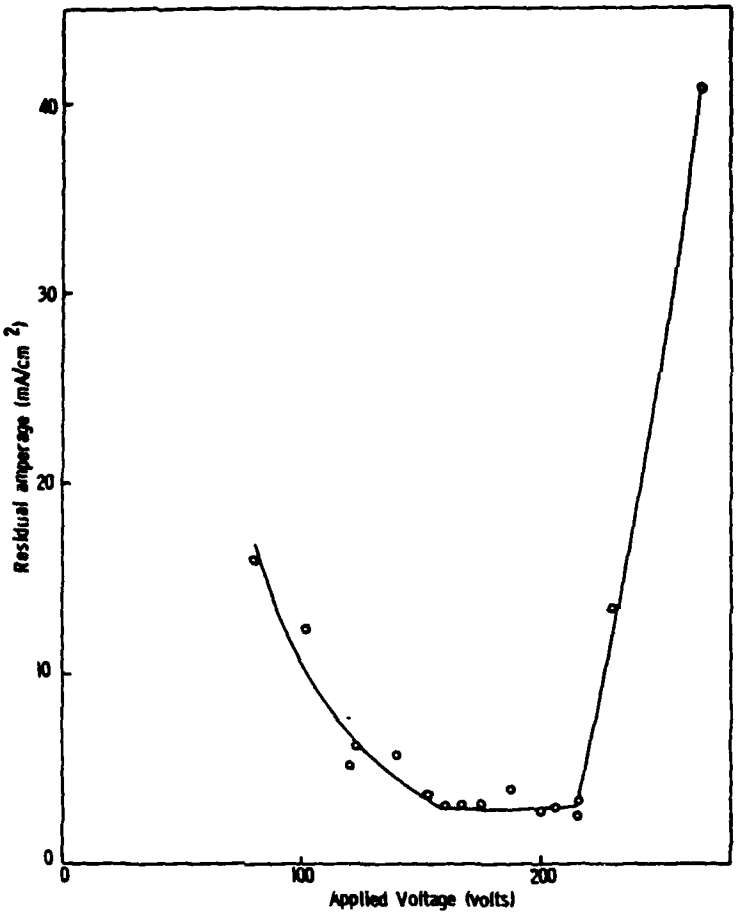

Figure 43. The effect of applied voltage on residual amperage for Epon 1001 latex.

period of 60 sec is shown as a function of applied voltage. It can be seen that the residual amperage was at its lowest value of ca 3.0 mamp/cm^2 over the voltage range of 150-216 v, beyond which a very steep increase of residual amperage with a small increment of voltage was observed. It was found that good non-conducting films were deposited within the above voltage range and film rupture became evident above 216 v. During film rupture, excessive bubbling was noted and the bath temperature went up to 58°C at 268 v. The appearance of excessive gassing was similar to boiling and eventually the boiling action (of water) within the film did 'blow' part of the film off the substrate as revealed by the morphology studies of the resulting deposited film and the lower film weight per cm^2.

The dependence of the deposition process on the applied voltage is further illustrated from a plot of film weight expressed as g/cm^2 against the applied voltage in Figure 44. The film weight increased rapidly with increasing voltage up to ca 140 volts when it reached a constant value of 60 mg/cm^2. It remained at this value with increasing voltage up to 216 v. With a further increase in the applied voltage, the film weight dropped abruptly. The drop is explained by the loss of part of the deposited film to the bath as a result of excessive bubble formation within the coating as outlined above. A decrease in film weight at the onset of film rupture has been reported previously by Mercouris et al (30) for anodic electrodeposition of polyacrylic resin on iron.

The coulombic efficiency defined as the weight deposited per coulomb passed was calculated for each applied voltage. The results are shown in Figure 45. Some scattering of data was noted, but the overall results suggest that the coulombic efficiency is essentially independent of applied voltage. An average value of 67.0 mg per coulomb for the coulombic efficiency was obtained with the omission of those two points for deposition at 230 and 268 volts. The coulombic efficiency could also be obtained by plotting film weight per cm^2 against the current passed (Figure 46). A straight line passing through the origin was obtained showing that the weight deposited is directly proportional to the coulombs of charge passed for each deposition. The slope of the line gives the coulomb efficiency which in this case is 66.5 mg per coulomb. Linearity of these data would be expected for a deposition mechanism by electrophoretic migration. Once again the points obtained for deposition at 230 and 268 v did not lie on the straight line. Lower film weights per cm^2 were obtained at these two applied voltages for the reasons already given above. Similar observations and deductions have been made by Rheineck et al (31) for an anionic system.

Further examination of the current-time curves reveals that the time at which the current reaches a maximum value (Y) before it falls off was strongly dependent upon the applied voltage.

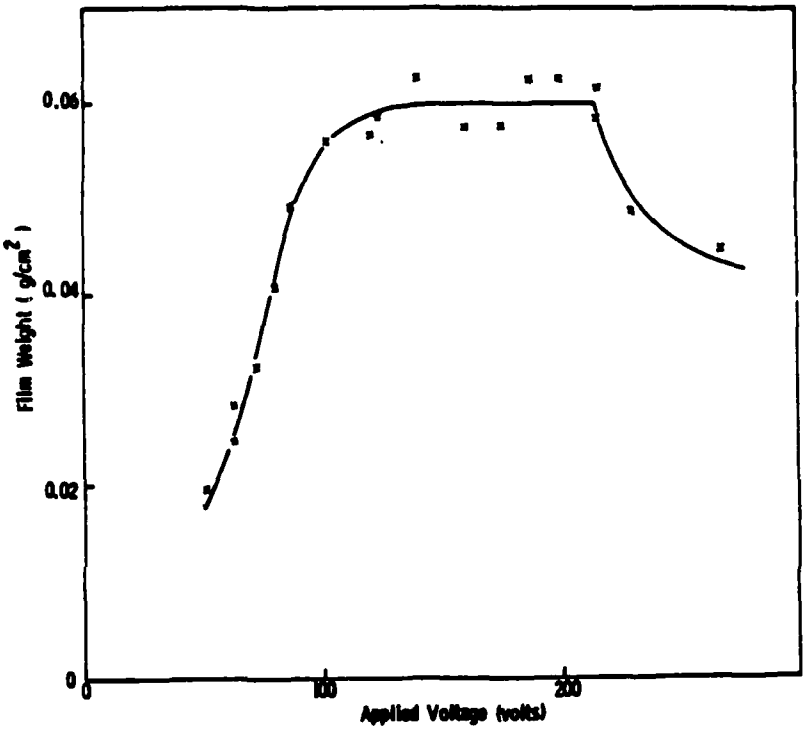

Figure 44. Variation of film weight with applied voltage for Epon 1001 latex.

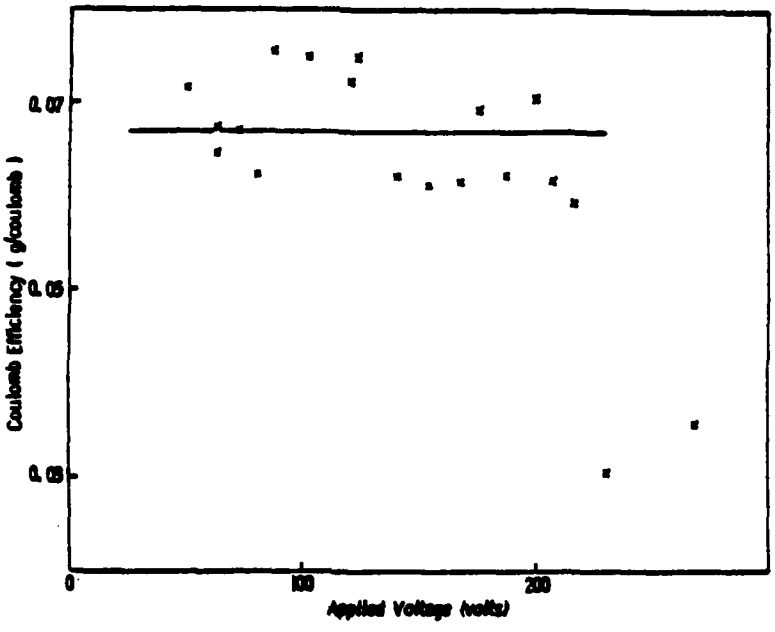

Figure 45. Coulombic efficiency vs applied voltage for Epon 1001 latex.

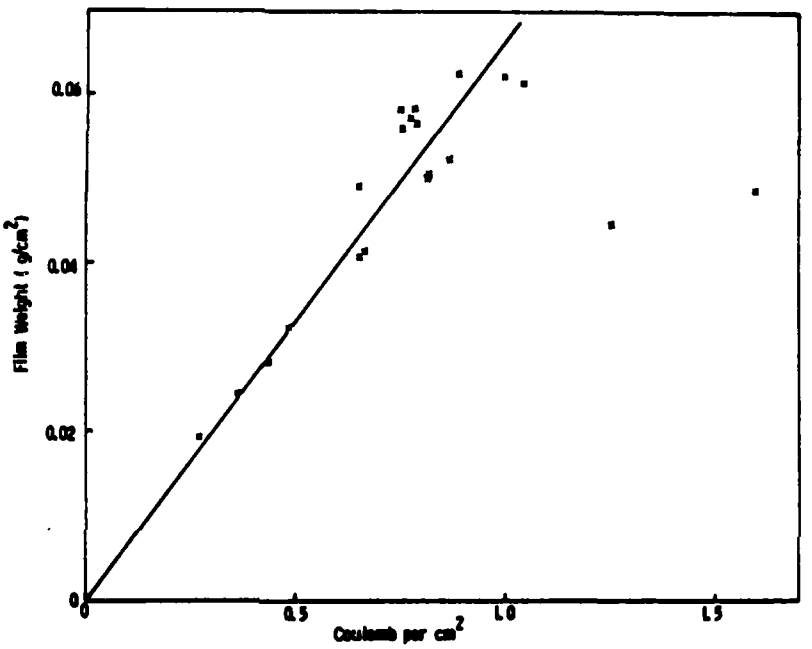

Figure 46. Film weight vs coulombs for deposition at various applied voltage for Epon 1001 latex.

At high voltage, the value of Y was large and was reached earlier, and the current fell off almost vertically, whereas at low voltage this maximum was never developed and the film was conducting. If the reciprocal of the time at maximum current is plotted against the voltage, a linear relationship is obtained as shown in Figure 47. According to this plot, for a maximum to develop in the current-time curve 60 sec after deposition begins, an applied voltage of about 90 v is required. This is indeed found experimentally: below 90 v, only conducting films were formed.

Two Component System: Epoxy Resin-Curing Agent Latex Mixtures

The current-time curves of the two-component reactive system were much different from those of the epoxy latex. The shape of the curve depended, not only on the applied voltage, but also on the composition and the time of aging of the mixture before electrodeposition. It is therefore imperative to determine an optimum aging time prior to studying the other effects on the electrodeposition. Figure 48 shows the current-time curves at various aging times for stoichiometric 2:1 mixtures of Epon 1001-Emerez 1511. Depositions at three different voltages for each aging time were determined. For samples aged for 1 hr before deposition, there was a fairly rapid current cut-off after the maximum current Y was reached; however, the current then increased on further deposition and the curve became 'wavy'. The same behavior was observed for all three deposition voltages used, viz 220, 250 and 280 v. Increasing the aging time to 2 hr decreased the 'waviness' of the curves beyond Y and also decreased the residual current. At 3 hr aging time, the current-time curves were smooth and the residual current was further reduced. However, a small 'peak' appeared after Y. This peak seemed to be more marked at low applied voltage than at high voltage. Generally, the best current-time curves were obtained for depositions at 280 v, i.e., rapid current cut-off with small residual amperage. Four hr aging time gave current-time curves completely different from those of the shorter aging times. A broad maximum as intense as the one at Y appeared on further deposition. However, the residual current was comparatively low. It is further noticed that, as the applied voltage increased, this second maximum was reduced in intensity and magnitude until at 280 v, only a small peak remained. The above series of experiments were repeated for latex mixtures having Epon 1001-Emerez 1511 weight ratios of 3:1 and 4:1. Increasing the Epon 1001 weight fraction to beyond stoichiometry with Emerez 1511 did not have any pronounced effect on the shape of the current-time curves: essentially the same coulombic curves were obtained as for the stoichiometric mixtures.

The effect of aging of the latex mixture was revealed more

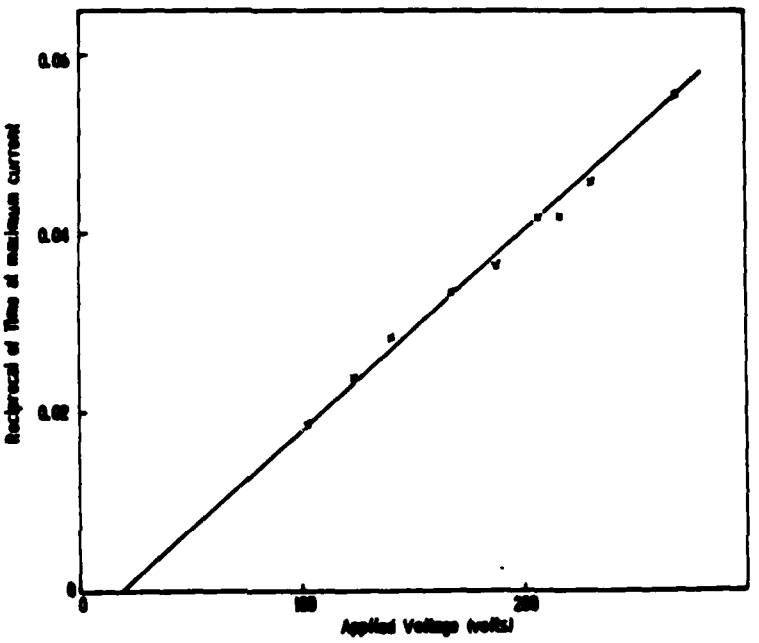

Figure 47. Reciprocal of time at maximum current vs applied voltage for Epon 1001 latex.

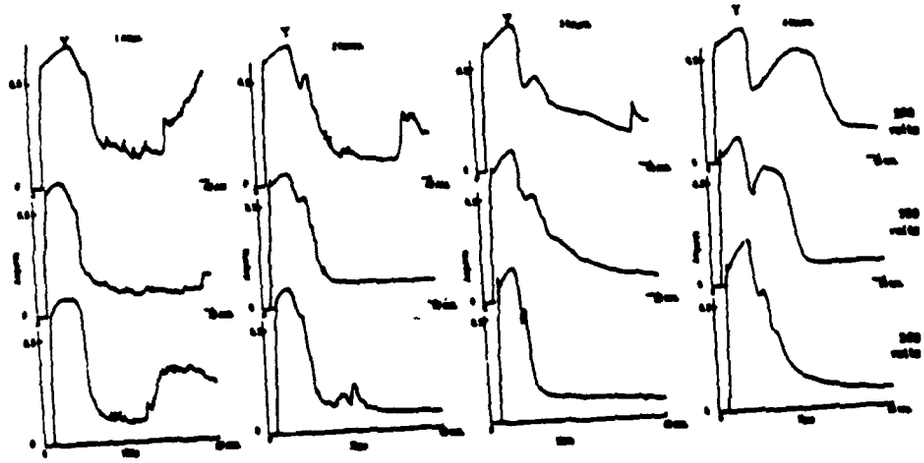

Figure 48. Current-time curves for stoichiometric mixtures of Epon 1001:Emerez 1511 (i.e. 2:1) aged for 1 hr, 2 hr, 3 hr and 4 hr at room temperature before deposition at 220, 250 and 280 v.

clearly when the variation of weight deposited per cm^2 and coulomb of charge passed per cm^2 were plotted against aging time. Figure 49 shows that the coulomb/cm^2 decreased initially with aging time until a minimum was reached after about 2 hr aging time and then increased again for longer aging times. An applied voltage of 280 v gave the lowest values of coulomb/cm^2 over the entire aging period. Higher values of coulomb/cm^2 were obtained at lower voltages. These conclusions are clearly illustrated in Figure 50, which shows that samples aged for 2 hr gave the lowest values of coulomb/cm^2 for all applied voltages. The film weight per cm^2 decreased with aging time for all applied voltages except for 220 v, where it decreased to a minimum and then increased again (Figure 51). In fact, an inverse relationship seems to exist between the weight deposited per cm^2 and the aging time for deposition at 280 v for different ratios of Epon 1001 and Emerez 1511 as shown in Figure 52.

Based on the above results, all subsequent electrodepositions were conducted using the stoichiometric mixtures of Epon 1001 and Emerez 1511 aged for 2 1/4 hr at room temperature before deposition. Figure 53 shows the current-time curves of such mixtures deposited at various voltages. At low voltage (100 v), the coating was conducting as indicated by a monotonic increase in current with deposition time. At intermediate voltage (100-200 v), a second broad maximum appeared after the first (Y) followed by a gradual decrease in current. At high voltage, a rapid current cut-off was observed. Gassing at the cathode was noted. However, the phenomenon of film rupture was not as obvious as it was in the case of the single-component system. From the above results, better-insulating films were formed only at the highest voltage used.

The coating weight increased almost linearly with increasing applied voltage (Figure 54) until a maximum value of about 0.125 g/cm^2 was reached; it then decreased gradually on further increase in applied voltage. The rate of weight increase with voltage was almost twice as fast as for the single-component system. The maximum weight deposited was also about double that of the single-component system. The weight per cm^2 was directly proportional to the coulombs of charge passed as indicated by a straight line passing through the origin shown in Figure 55. The slope of the line gives the coulombic efficiency of 103 mg per coulomb for this system.

The residual amperage for the mixture as a function of applied voltage is shown in Figure 56. In contrast to the single-component system, the residual amperage decreased continuously with increasing applied voltage up to 300 v. It is therefore not possible to tell from this plot whether film rupture had occurred. On the other hand, a similar reciprocal relationship between the time to reach maximum current at Y and the applied voltage exhibited by the single-component system was also observed for the two-component system as shown in Figure 57.

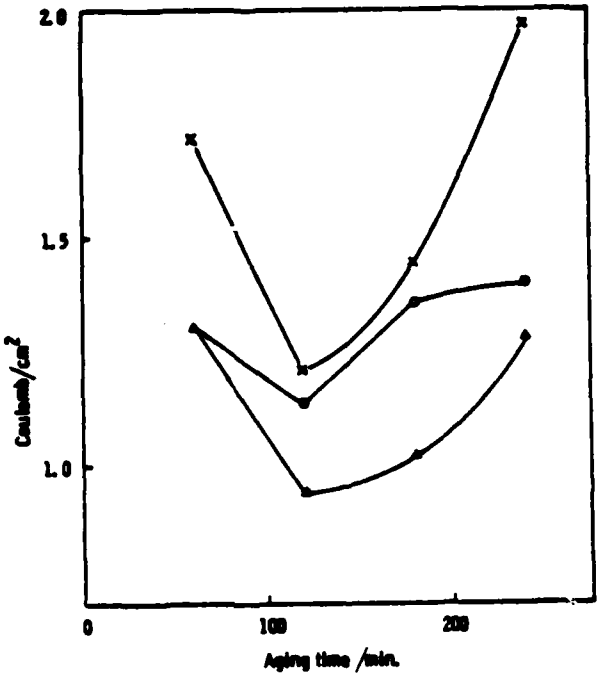

Figure 49. Variation of coulomb of charge passed as a function of aging time before electrodeposition for stoichiometric mixtures of Epon 1001: Emerez 1511. Deposition at (x) 220 v; (o) 250 v; and (Δ) 280 v.

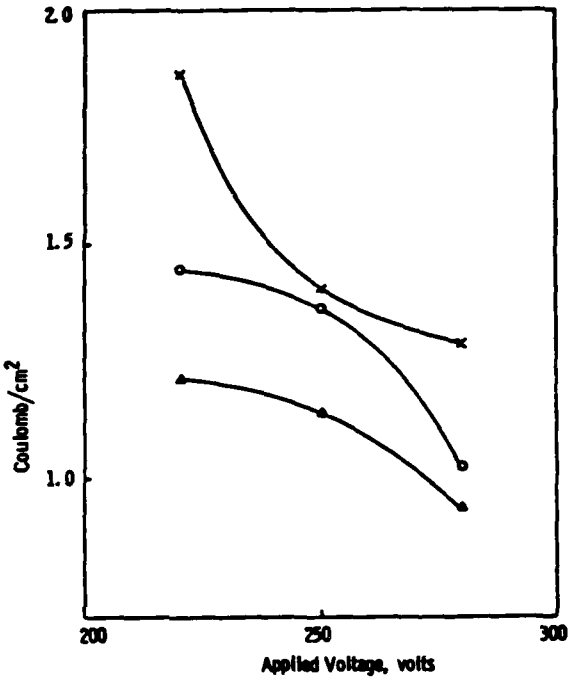

Figure 50. Effect of applied voltage on coulomb/cm^2 for stoichiometric mixtures of Epon 1001:Emerez 1511. Mixtures aged for (Δ) 2 hr; (o) 3 hr; and (x) 4 hr before deposition.

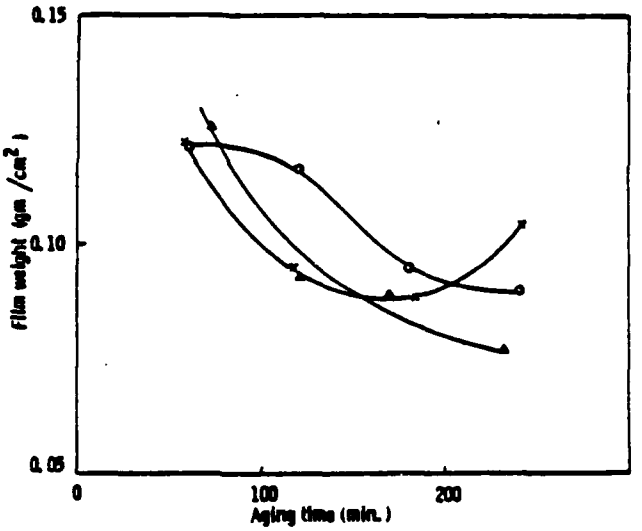

Figure 51. Variation of film weight as a function of aging time for stoichiometric mixtures (2:1) of Epon 1001:Emerez 1511. Deposition at (x) 220 v, (o) 250 v, and (Δ) 280 v.

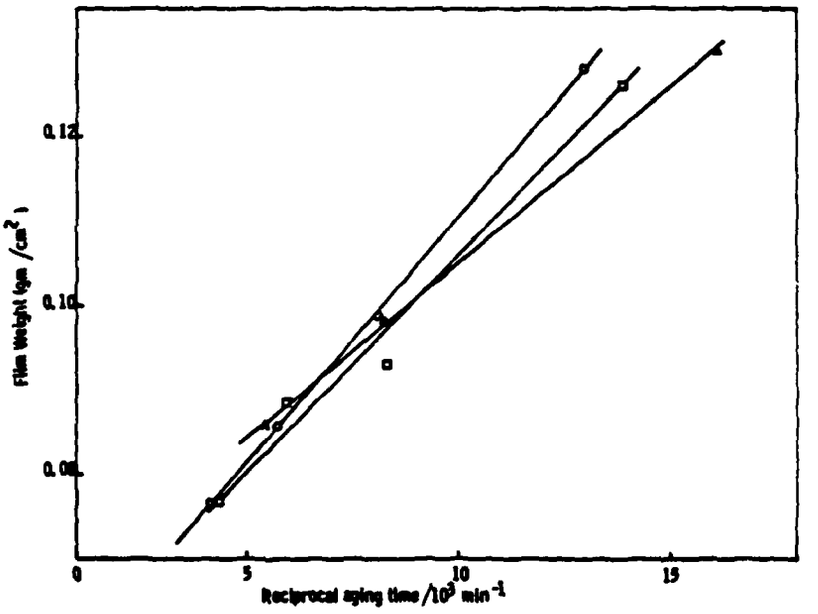

Figure 52. Variation of film weight/cm^2 with reciprocal aging time. Weight ratio of Epon 1001:Emerez 1511 at (□) 2:1; (o) 3:1; and (△) 4:1. Mixtures deposited at 280 v.

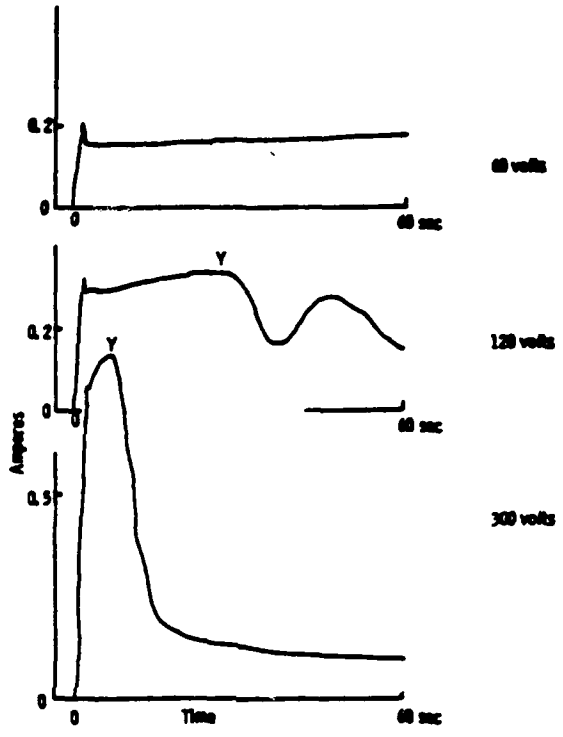

Figure 53. Current-time curves for stoichiometric mixtures of Epon 1001: Emerez 1511 aged for 2 1/4 hr at room temperature before deposition at various voltages.

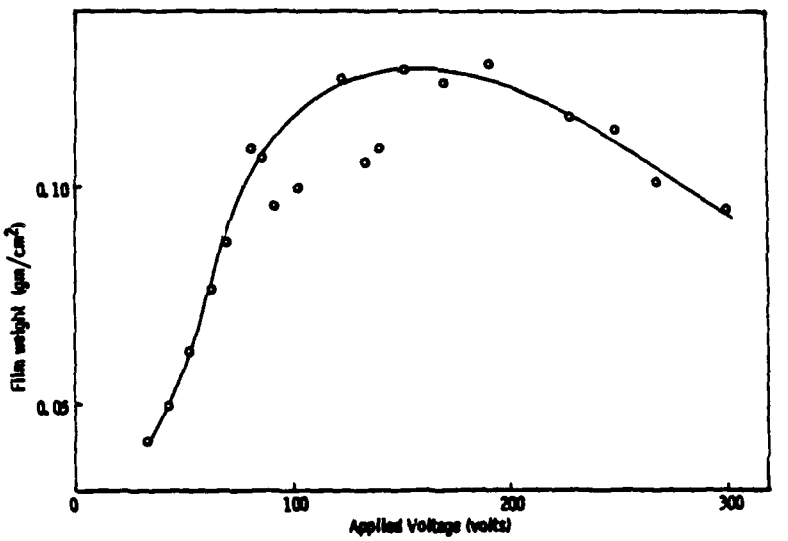

Figure 54. The effect of applied voltage on the film weight for stoichiometric mixtures of Epon 1001:Emerez 1511 aged for 2 hr at room temperature before deposition.

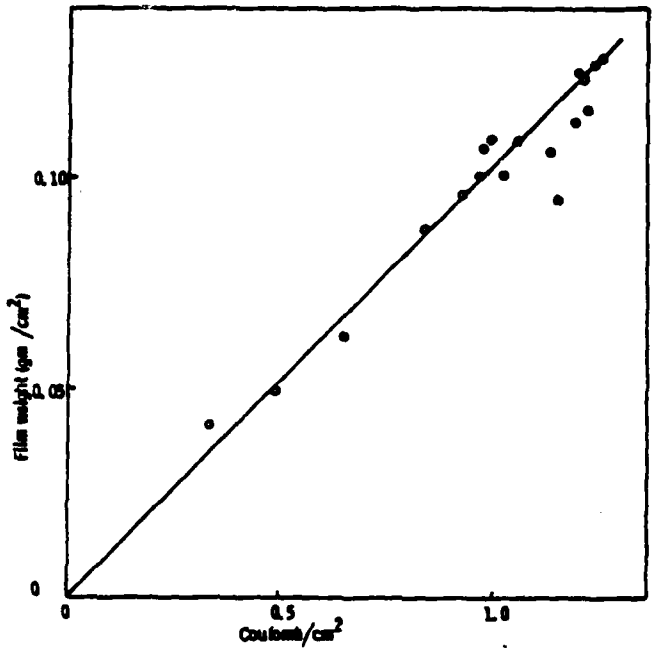

Figure 55. The variation of film weight with coulomb/cm^2 for stoichiometric mixtures of Epon 1001:Emerez 1511 aged for 2 1/4 hr at room temperature before deposition.

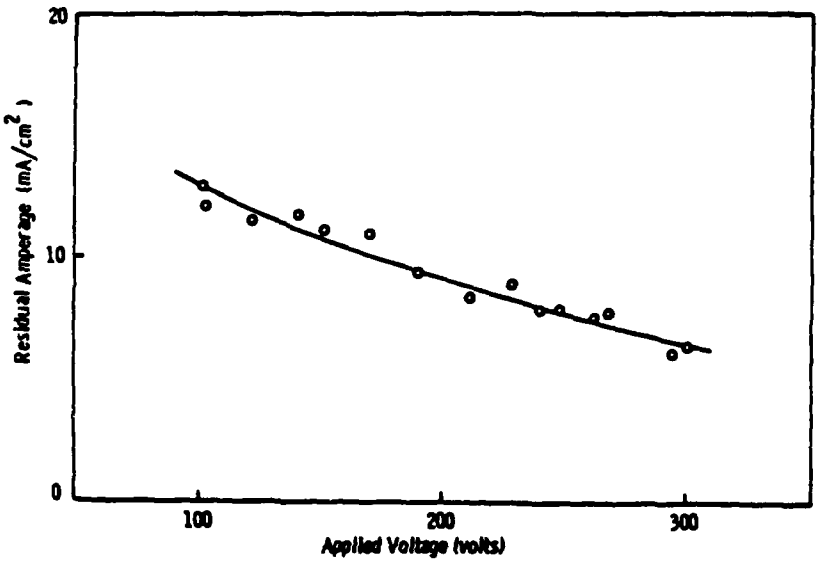

Figure 56. Effect of applied voltage on residual amperage for stoichiometric mixtures of Epon 1001:Emerez 1511 aged 2 1/4 hr before deposition.

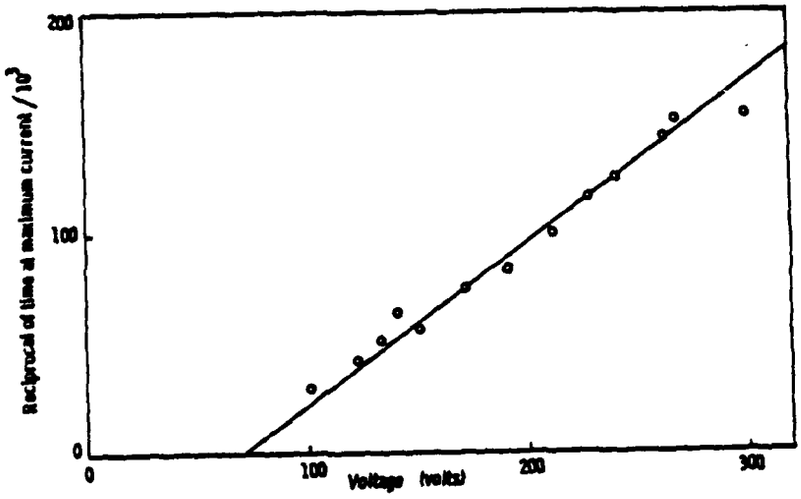

Figure 57. Reciprocal of time at maximum current (Y) vs applied voltage for stoichiometric mixtures of Epon 1001:Emerez 1511 aged 2 1/4 hr before deposition.

Nature and Morphology of Coating Films

Single-Component System: Epoxy Resin Latex

The unbaked films were white in color, opaque, bubbly, and rough in appearance. The water content of the wet film was about 20 to 30%. The deposited film was thick (ca 28 mil max) at high voltage. These thicker films showed smooth surface regions along the edges of the plate. Electron microscopy revealed a high degree of coalescence and fusion of the latex particles into a smooth film at these regions resembling the original bulk epoxy solids. The scanning electron micrographs of these are shown in Figure 58. In contrast, discrete aggregates in which individual latex particles are still discernible were observed in films deposited at low voltage (Figure 59). All deposited films cracked upon air-drying at room temperature. Some cracked right through the deposit, revealing the metal substrate underneath. Latex films are known to crack at low humidity and low temperature below the film formation temperature of the latex polymer. The melting temperature of Epon 1001 is 65-75°C according to specifications of the manufacturer whereas the deposition and air-drying were done at room temperature. Partial melting of the latex polymer did take place, however, at the very high voltage (e.g. 268 v) where film rupture occurred. The top layer of the deposit was physically blown off leaving behind a fused layer adhered to the substrate with the badly torn surface clearly visible (Figure 60). The temperature of the water vapor within the deposit could easily have exceeded 100°C, causing partial melting of the epoxy and better adhesion to substrate.

The interior of the deposit (Figure 61) as observed through the cracked region revealed that it still contained aggregates similar to those shown in Figure 59, but the contours of the aggregates were less sharp, indicating that a certain degree of coalescence and fusion had occurred. The coating-substrate (polymer-metal) interface revealed that a high degree of coalescence and fusion of the latex particles had already taken place, giving a smooth, flat interface; nevertheless, some embedded individual latex particles in the continuous film could still be seen (Figure 62). The adhesion of the film to the substrate was, however, poor.

The baked films were transparent and smooth on the surface, resembling the bulk resin (Figure 63), and the adhesion of coating to the substrate was considerably better than the unbaked films.

Two-Component Systems: Epoxy Resin-Curing Agent Latex Mixtures

For the stoichiometric 2:1 Epon 1001-Emerez 1511 mixture,

a)

b)

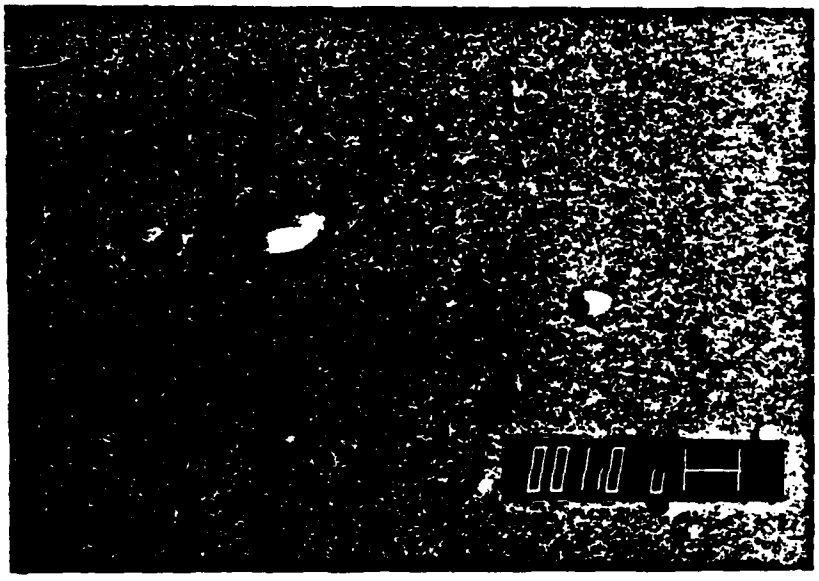

Figure 58. Scanning electron micrographs of:
a) Electrodeposited coating of Epon 1001 latex showing smooth surface regions along edge of plate. Electrocoated at 200 v.
b) Solid Epon 1001 epoxy resin.

Figure 59. Scanning electron micrograph of electrodeposited coating of Epon 1001 latex at 80 v.

Figure 60. Scanning electron micrograph of electrodeposited coating of Epon 1001 latex at 268 v showing film rupture phenomenon.

Figure 61. Scanning electron micrograph of electrodeposited coating of Epon 1001 latex showing interior of coating. Applied voltage was 173 v.

Figure 62. Scanning electron micrograph of electrodeposit of Epon 1001 latex showing surface of deposit that was originally in contact with the substrate. Deposited at 140 v.

Figure 63. Scanning electron micrograph of baked electrocoating of Epon 1001 latex. Deposited at 173 v.

the deposits at short aging times (e.g. 1 hr) were extremely thick, white in color, smooth and paste-like in appearance. They did not adhere well: upon withdrawal from the bath, some tended to slide down and drop off from the plate, leaving behind an underlayer. Upon air-drying, the surface became wrinkled at the edges. In general, the water content of the wet coatings was very high, ranging from 60 to 75%. When the aging time was increased to 2 hr, the deposits became creamy in color, more firm and very smooth in appearance. At 3 hr aging time, crater-like depressions began to form over the surface, presumably as a result of gassing and the deposit was also thinner and more compact. Upon air-drying, no wrinkling was observed, but the film was vitreous in appearance. On increasing the aging time to 4 hr, many more crater-like depressions were formed. On increasing the Epon 1001-Emerez 1511 weight ratio to 3:1 and 4:1, shallow cracks began to form over the surface of the deposits at 3 hr and 4 hr aging times.

For the stoichiometric Epon 1001-Emerez 1511 mixtures aged at room temperature for 2 1/4 hr before deposition as a function of applied voltage, the coating was relatively thin and smooth at low voltage. The coating became thicker, and crater-like depressions began to form as the applied voltage was increased to beyond 210 v. Thus, in terms of appearance, the coatings deposited at low voltage were thin and when baked gave uniform vitreous coatings with good adhesion to substrate; however, in terms of electrical properties, they were conducting films (see Figure 53).

Scanning electron microscopy revealed that coalescence was considerable and extended over the entire surface of the coating (Figure 64). The degree of coalescence was much more extensive compared with the single-component system. This greater coalescence is to be expected since, in the presence of the curing agent, the tendency for film formation is greatly enhanced. The interior of the coating also exhibited similar behavior in that the latex particle contours were obliterated to give a smooth appearance. Similar film morphology had been observed previously (32) on thin films cast from epoxy resin-curing agent latex mixtures and aged at room temperature for various periods of time. The phenomenon of 'further gradual coalescence' (33) was used to explain such observations. It would seem from the above that such explanation could also be applied to the thicker electrodeposited films of the Epon 1001-Emerez 1511 latex mixtures.

Conclusions

Cathodic electrodeposition of the Epon 1001 latex gave the best insulating coating with a residual amperage of 3 mamp/cm^2 over a voltage range of 150-216 v. Below 90 v, only conducting

Figure 64. Scanning electron micrograph of electrodeposit from stoichiometric mixture of Epon 1001:Emerez 1511 aged for one hr before deposition at 280 v.

coatings were formed. Above 216 v, film rupture occurred. The coulombic efficiency of the electrodeposition was essentially independent of the applied voltage and had a value of ca 66.5 mg per coulomb.

In contrast, cathodic electrodeposition from a two-component reactive latex system is much more complex compared with that from epoxy resin latex alone, because of the concurrent heterogeneous flocculation of the mixed latex particles and the chemical reaction of the epoxide groups with the amine groups. The rate of agglomeration of the smaller Emerez 1511 particles with the larger Epon 1001 particles depends on the reactivity of the particles. Chemical reaction begins at the interface of the reactive particles in the agglomerates. Both these factors strongly influence the surface properties of the migrating latex particles and, hence, indirectly the electrodeposition behavior. The experimental results for the latex mixtures showed distinct differences from the single-component system. Thicker, smooth films were formed which did not crack on drying and adhered much better to the substrate. A higher coulombic efficiency was also obtained.

Kinetic Studies of Film Growth

Introduction

The mechanism of the electrodeposition of polymers on metallic substrates is complex involving electrolysis, electrophoresis, electroosmosis, coalescence of colloidal particles, and oxidation of metal. Various explanations have been offered for the deposition process. Thus Fink and Feinleib (34) established that the rate controlling step is the migration of cations through the film to coagulate the incoming emulsion particles. On the other hand, Olsen (35) showed that beyond the first few sec of deposition time, film growth is a diffusion-controlled process. Beck (36) had investigated several factors affecting the deposition, including boundary layer reactions and charge migration within the deposited film. More recently, Pierce et al (37) have applied the theory of oxide film growth to the studies of the electrodeposition process and found that the growth kinetics of electrodeposited organic coatings and oxide films bear a strong similarity. All these studies were carried out on solubilized polymer resin systems electrodeposited anodically, except that of Fink and Feinleib who worked on synthetic latex dispersions. In contrast, information on the kinetics of cathodic electrodeposition of polymer latexes is practically non-existent. Wessling et al(28) have reported work on the cathodic electrodeposition of quaternary ammonium ions stabilized latexes; however, the kinetic aspect of the process was not dealt with.

The purpose of this investigation was to find out how the electrodeposition of latex particles on the cathode begins and the factors that influence the kinetics of film growth.

II. Experimental

Details of the experimental set-up and procedure were given above. Plates were electrocoated for various periods of time at a constant applied voltage. The experiment was repeated for 5 different applied voltages. After deposition, the plates were treated in the same manner described previously.

Results and Discussion

Deposited Mass-Time Dependencies for Epon 1001

The deposition kinetics were followed by observing current flow and extent of coating deposition as a function of deposition time at constant applied voltage. Five different voltages were used in all, viz 80, 120, 175, 215 and 250 v. The electrodeposition of organic coatings on metal substrates has been likened to the growth of inorganic films on metals previously by Pierce et al (37). According to Uhlig (38), the thickness or mass of oxide films can increase with time in three ways: linearly, parabolically or in a logarithmic relationship. Linear relationship indicates that the presence of the film does not affect continued film growth. A parabolic relationship suggests that continued film growth is limited by diffusion through the film. A logarithmic relationship results when the oxidation rate of the metal is controlled by transfer of electrons to the film. The latter relationship only occurs with thin oxide films.

Figures 65-67 illustrate some typical data obtained for deposition at 80, 175 and 250 v plotted in these three ways. It was found that for depositions at 120, 175 and 215 v, the mass deposited could be represented equally well by all three relationships with time. The best insulating films were obtained in this range and were characterized by rapid current cutoff and low residual amperage in their current-time behavior as described earlier. All the plots show two linear portions, i.e., an initial rapid film build-up followed by a much less gradual increase at the later stage of deposition. The transition from the faster rate to the slower one was distinct and was represented by the intersection of the two linear portions of the plot. At 80 and 250 v, the linear time relationship appeared to give the best fit. Some scattering of data points was noted for the square-root time plot but the shape of the plot was the same for both relationships. However, a straight line without any change in shape was obtained when the data were plotted as a

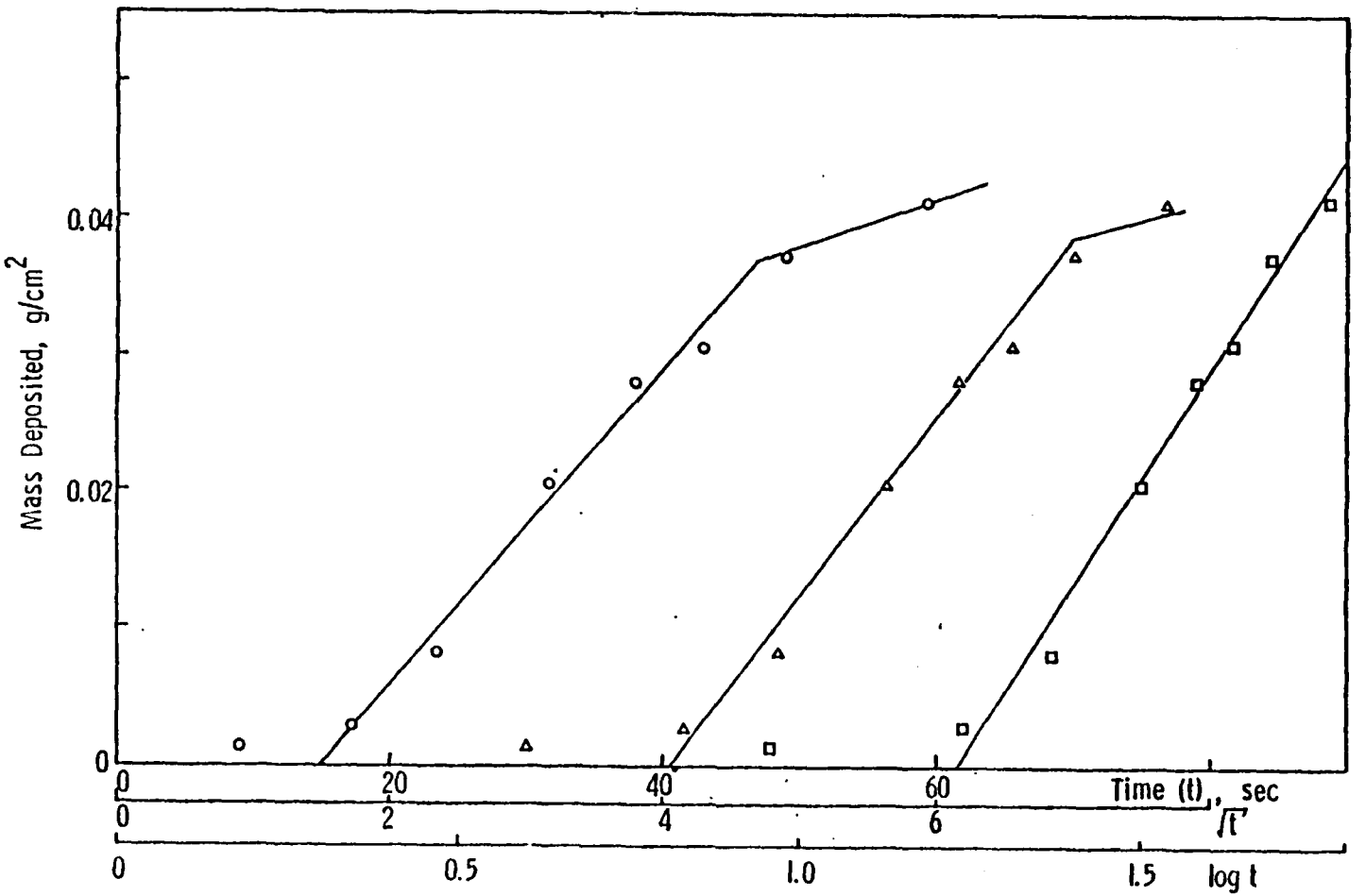

Figure 65. Mass deposited plotted as a linear (-o-), square-root (-Δ-), and logarithmic (-□-) function of deposition time. Deposition voltage was 80 v.

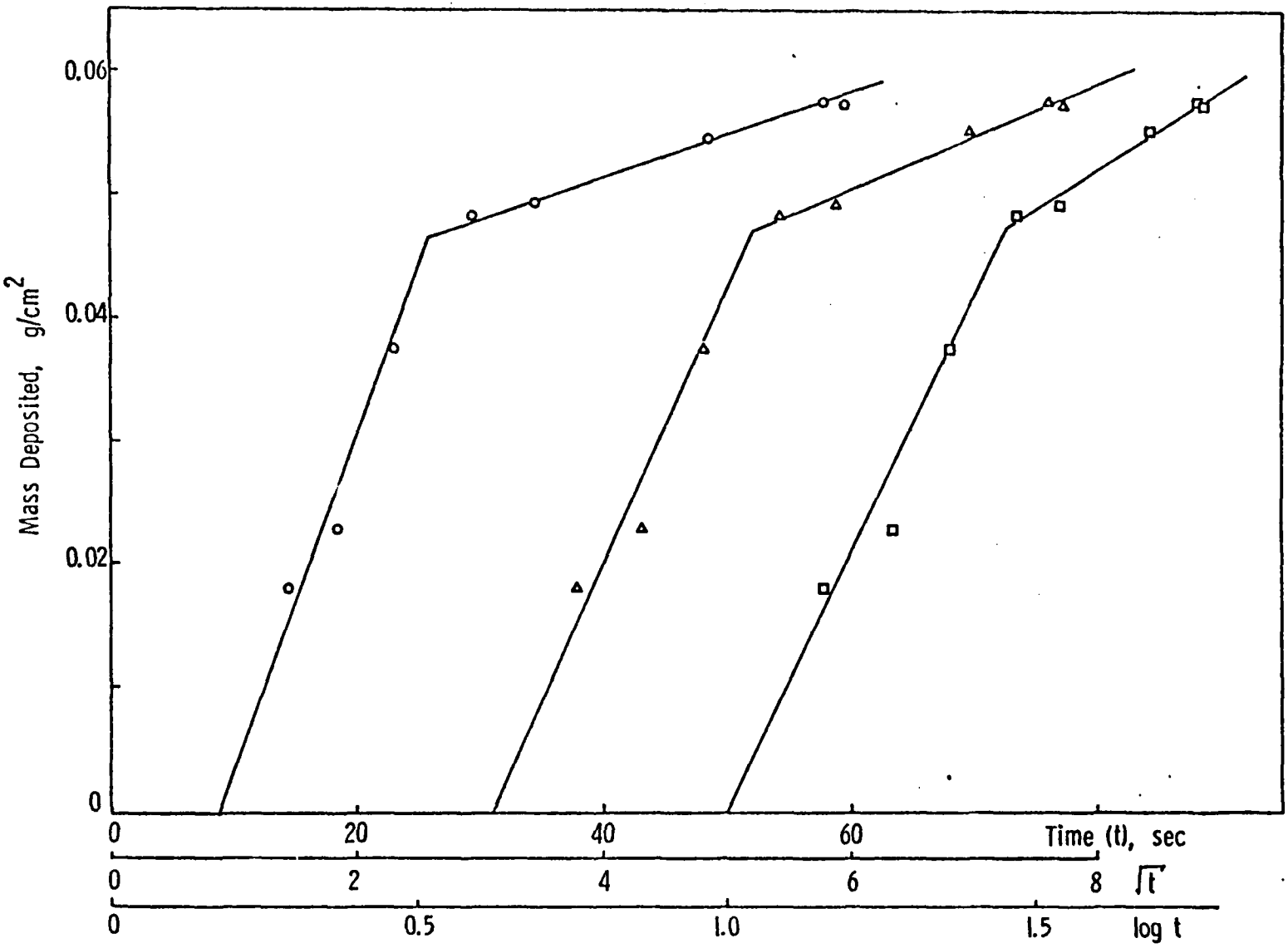

Figure 66. Mass deposited plotted as a linear (-o-), square-root (-$_\Delta$-), and logarithmic (-□-) function of deposition time. Deposition voltage was 175 v.

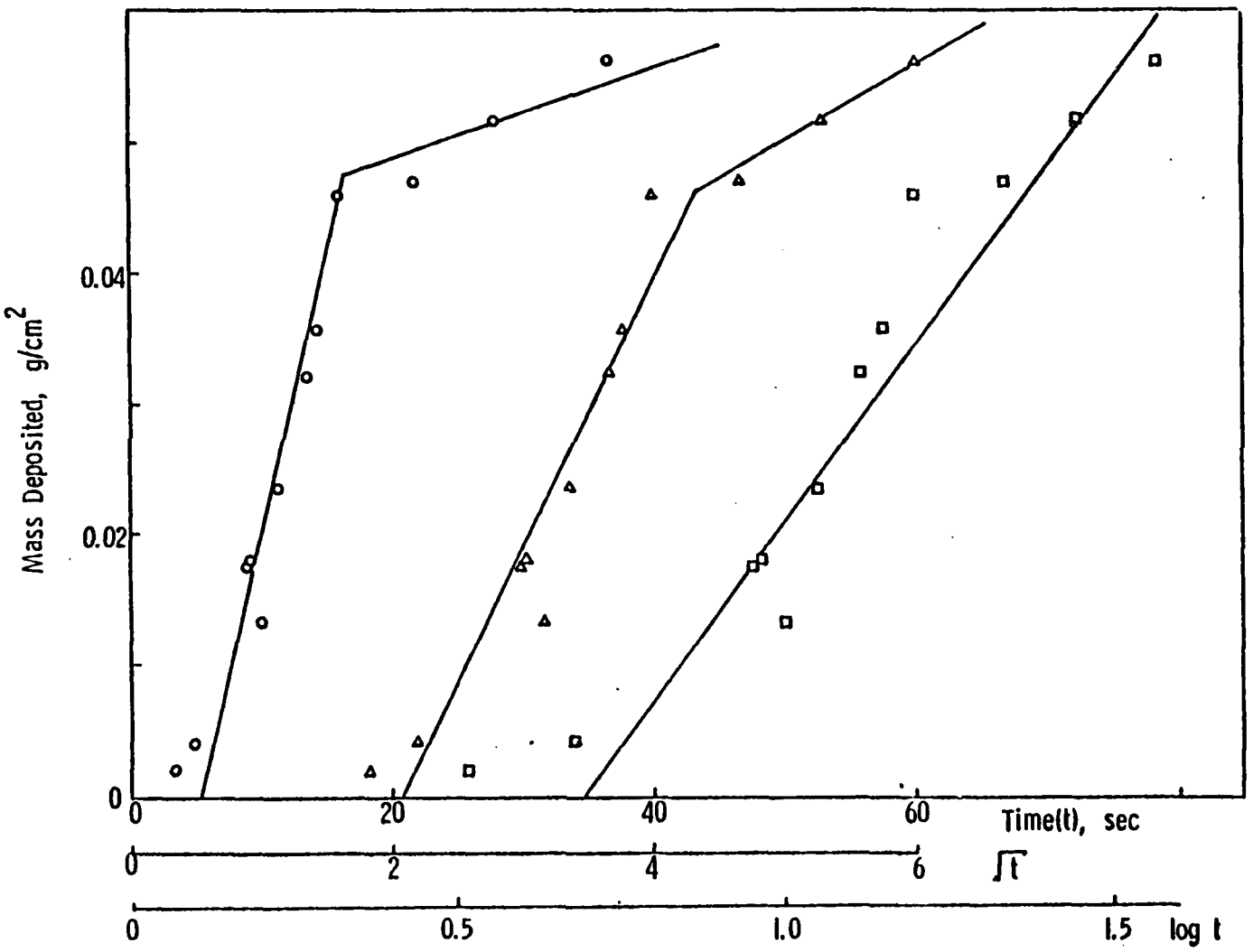

Figure 67. Mass deposited plotted as a linear (-o-), square-root (-Δ-), and logarithmic (-□-) function of deposition time. Deposition voltage was 250 v.

function of logarithm of time. Data for deposition at 80 v seem to give a better fit to the logarithmic relationship than those deposited at 250 v.

Thus it would seem from the above analysis that the linear mass versus time relationship gives the best fit to our experimental data over the entire range of applied voltage used. The straight line obtained for the logarithmic time plot for deposition at 80 v was probably fortuitous. It has been found previously by Olsen (35) working on anodic electrodeposition of some polycarboxylic acid resins that a linear graph of film thickness vs logarithm of time could also fit a square root relationship upon replotting the data. However, the logarithmic time law had been found to be obeyed by an oil-modified polyester resin deposited anodically but only at the very beginning of the electrodeposition (<2 sec) under high applied voltage (>250 v) conditions (39).

Henceforth, it is taken that our data conformed to the linear time relationship and will be analyzed accordingly. A linear dependency on deposition time would indicate an unimpeded growth mechanism at the cathode. It can be seen from Figure 68 that all plots consisted of two linear portions intersecting at a point as mentioned earlier. The initial slope increased with increasing applied voltage. However, the second linear portion at longer deposition time remained essentially constant (3.4×10^{-4} g/cm^2/sec) when the voltage was varied from 80 to 250 v. It is also seen that the initial growth rate was strongly dependent upon the applied voltage, the higher the applied voltage, the faster the rate of deposition (Table XIII). The transition to a slower rate at longer deposition time could signify compaction of the coating after a certain coating mass (or thickness) was reached thereby slowing down further deposition rate. The time at which this transition occurred for each applied voltage is shown in Column 3 in Table XIII. This transition time is closely related to the current-time behavior of the deposition process as will be discussed later. A very similar behavior has also been noted by Rheineck et al (40) on anodic electrodeposition of acrylic copolymer resins on zinc substrate at 125 v. A change in slope of the deposited mass vs time plot was observed after 45 sec of deposition. These investigators found that their data could also be represented by a parabolic time plot but there was a change in the intercept (not slope) after 45 sec.

From Figure 68, it is further noted that the initial linear portion of each deposited mass vs time plot on extrapolation intersected the time axis at a finite value; the higher the applied voltage, the shorter the time at the intersection point. There is the appearance of an induction time. This delay in deposition is at variance with the usual notion on anodic deposition of polymer resins that film deposition starts almost instantaneously under constant voltage condition. The anode is completely covered with a film within a fraction of a second. In contrast, an induction time of a few

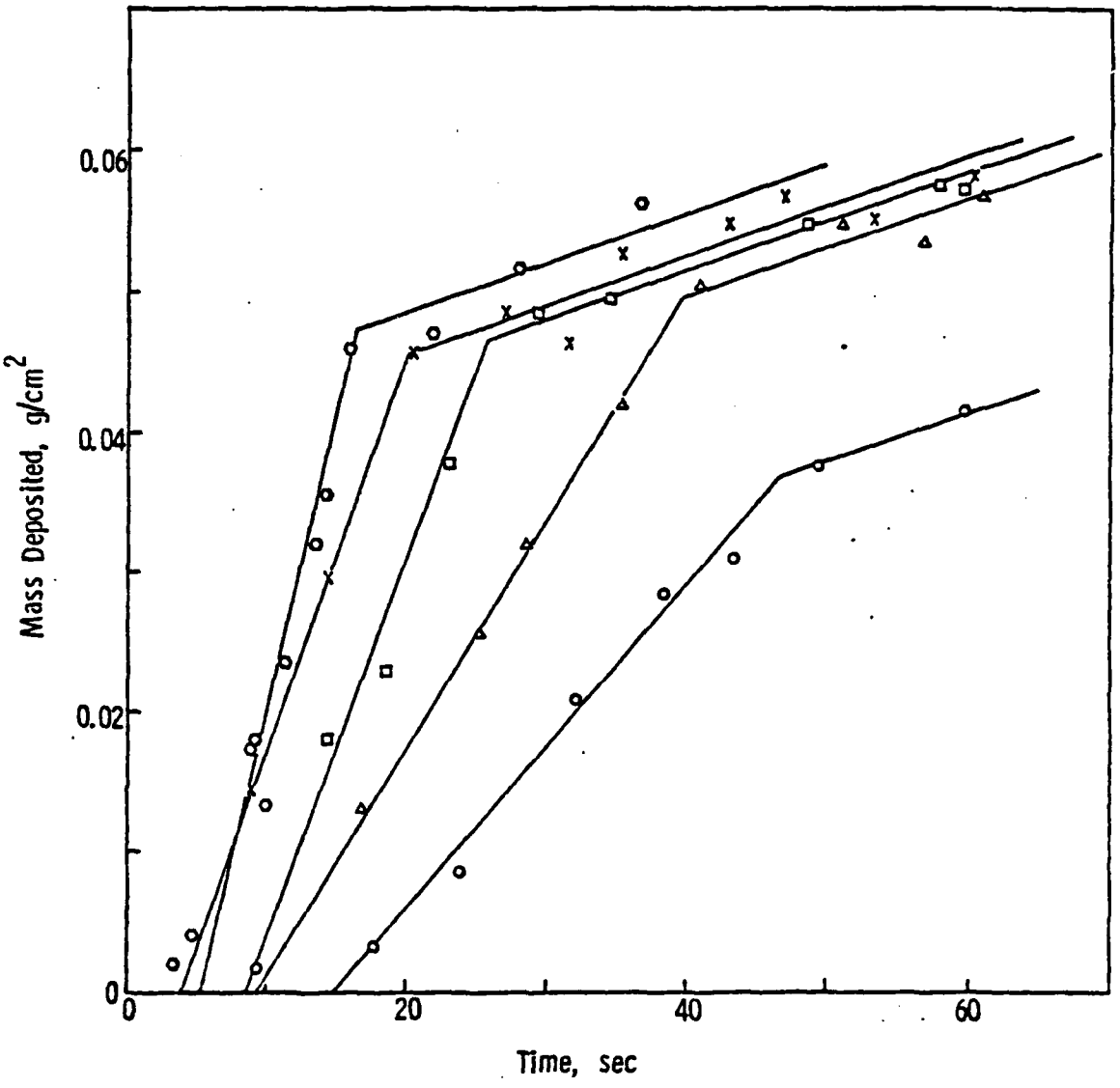

Figure 68. Mass deposited as a function of deposition time. Deposition voltages: 80 v (-o-), 120 v (-Δ-), 175 v (-□-), 215 v (-x-), and 250 v (-O-).

Table XIII

Applied Voltage (v)	Rate of Film Growth [a] ($g/cm^2/sec$)	Transition of film growth [b] rate (sec)	Time to attain maximum g/cou [c] (sec)	Time to attain maximum current [d] (sec)	Value of maximum current [e] (mA)	Coulombic efficiency [f] (mg/cou)
80	1.16×10^{-3}	47.0	48	49.0	180	63.5
120	1.63×10^{-3}	40.0	37	38.0	260	75.5
175	2.75×10^{-3}	26.0	26	25.5	354	78.3
215	2.83×10^{-3}	20.0	20	18.5	440	80.3
250	4.27×10^{-3}	16.5	16	15.5	520	85.2

a) From initial slope of g/cm^2 vs time plot

b) From the intersection of linear portions of the g/cm^2 vs time plot

c) From g/cou vs time plot

d),e) Corresponding to the point Y in the current-time curve (see e.g. Figure 42, Part A)

f) From gradient of g/cm^2 vs cou/cm^2 plot

seconds or longer is usually required before formation of an adherent film occurred under constant current conditions. This phenomenon of induction time is well documented (1) for constant current depositions and is thought to be related to the time taken for the accumulation of protons up to a critical concentration required for electrocoagulation and deposition. In the present system of deposition at the cathode of latex particles stabilized with quaternary ammonium ions, an electric discharge of the latex particles via acid-base reactions by the hydroxyl ions in the alkaline boundary layer of the cathode is most unlikely. It would seem a non-ionic type of mechanism is more important in this instance and one such possible mechanism is by way of "concentration coagulation": accumulation of latex particles at the cathode by electrophoresis, leading to a stronger interaction and thus stimulating coagulation. This process would be unimpeded and dependent only on the applied voltage as the driving force. The velocity of migration of the particles towards the cathode would be faster at higher voltage. The induction time could then be explained by the time taken to establish a moving (particles) boundary before deposition begins. The higher the voltage, the sooner the establishment of this moving boundary and the shorter the induction time. In fact, it was observed during deposition that the dispersion immediately next to the anodes appeared to become less and less turbid as deposition proceeded. At high voltage (250 v) an almost clear layer of liquid became discernible next to the anodes not long after deposition began. It would seem that most of the latex particles moved out of this layer and formed a type of moving boundary. This phenomenon was, however, less obvious when deposition was done at 80 v.

When the deposited mass/cm^2 was converted into thickness of coating using a value of 1.186 g/cm^3 for the density of Epon 1001, and the data plotted as a function of time, a set of graphs similar to those given in Figure 69 for deposited mass vs time was obtained. The same linear function on deposition time was observed as expected.

Coulombic Efficiency

The mass deposited per coulomb of charge passed for different deposition times at fixed applied voltage is shown in Figure 70 for two typical voltages of 250 and 80 v. Some scattering of data points was noted especially at low applied voltage and low charge passed (i.e., at short deposition times). The data seemed to fit a straight line plot passing through the origin, with the deposition at 80 v having a slightly smaller coulombic efficiency (gradient of line) than that at 250 v. The data for depositions at 215, 175 and 120 v fell between these two lines and the gradients for these plots were such that they increased with increasing voltage as shown in Table XIII. The

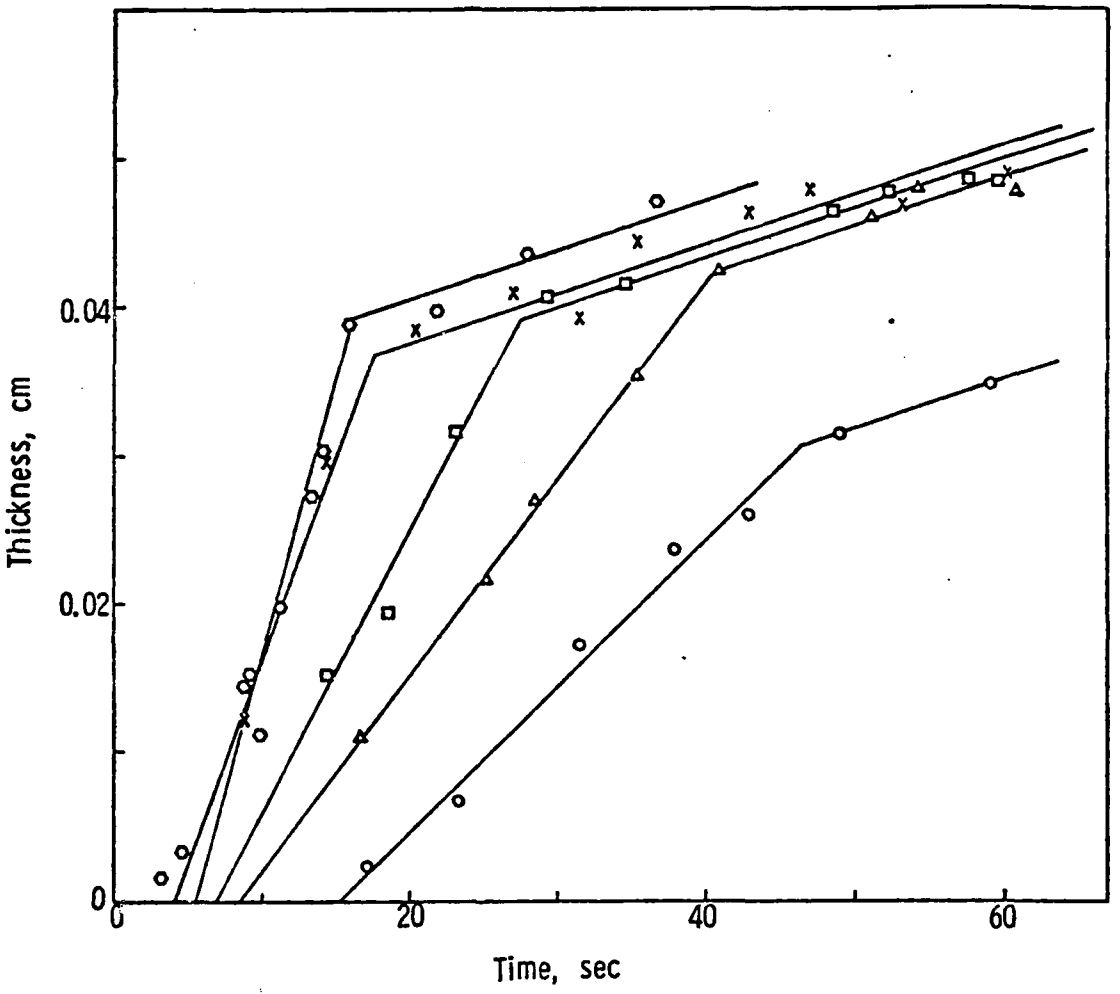

Figure 69. Thickness of coating as a function of deposition voltages: 80 v (-o-), 120 v (-Δ-), 175 v (-□-), 215 v (-x-), and 250 v (-o-).

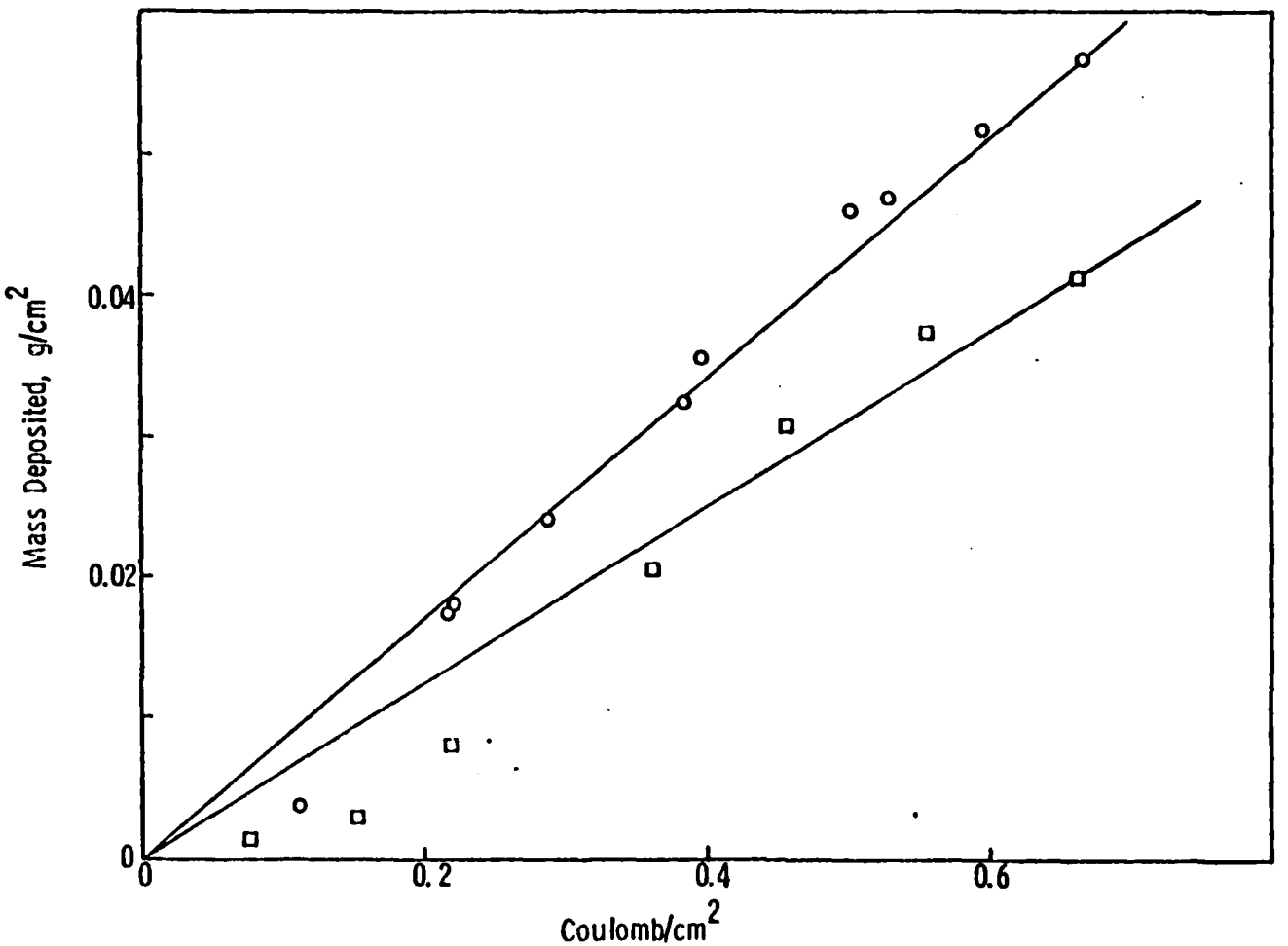

Figure 70. Mass deposited vs coulomb/cm^2 deposited for various time. Deposition voltages: 80 v (-□-) and 250 v (-o-).

indication from such plots is that the coulombic efficiency was independent of deposition time but increased with increasing applied voltage. However, if the coulombic efficiency was calculated for each deposition at different times but at the same applied voltage, it became obvious that the coulombic efficiency was in fact strongly time-dependent as shown in Figure 71. The coulombic efficiency increased steeply with deposition time, until a maximum was reached, it then decreased more gradually with time. The maximum value of the coulombic efficiency attained at each applied voltage was, however, a function of the applied voltage. The higher the applied voltage, the larger the maximum coulombic efficiency obtained. Also, the higher the applied voltage, the earlier the maximum coulombic efficiency was reached. The time to attain maximum coulombic efficiency for each voltage is shown in Table XIII. A discussion of this time will be given later.

The work by Bushey (41) on anodic deposition of a modified acrylic resin on aluminum at deposition times of 2, 4 and 8 sec has shown that the deposition efficiency was indeed dependent upon both deposition time and applied voltage. Figure 72 shows the results plotted in the manner of Bushey for three different deposition times (i.e. 16, 19 and 25 sec). The points were interpolated from data presented in Figures 68 and 70. Fairly straight lines were obtained. Furthermore, these lines were parallel and the slope equalled 86 mg per coulomb, which was about the same as the coulombic efficiency obtained for the highest voltage used in this work (i.e., 250 v). Kovac-Kalko also found a variation of coulombic efficiency with applied voltage on the anodic deposition of oil-modified polyester resins (39).

Effect of Current and Applied Voltage

From the current-time curves on the longest deposition time for each voltage, the current density at various time intervals was calculated and plotted against time in Figure 73. Only the descending portion of the current-time curve after the maximum current Y was considered (refer to Figure 42). It shows the current density for all the curves decayed towards a common residual value of ca 3 mamp/cm^2. This value agrees with the residual amperage value obtained by a different procedure given in Part A. Deposition at 250 v showed the sharpest decrease in current density with time, indicating a very large film resistance leading to a rapid current cut-off. The steepest part of the current density curve tended towards the maximum current Y value as was in the current-time curves. The time at which the maximum current Y was attained and the corresponding value of the maximum current Y for each applied voltage are shown in Table XIII.

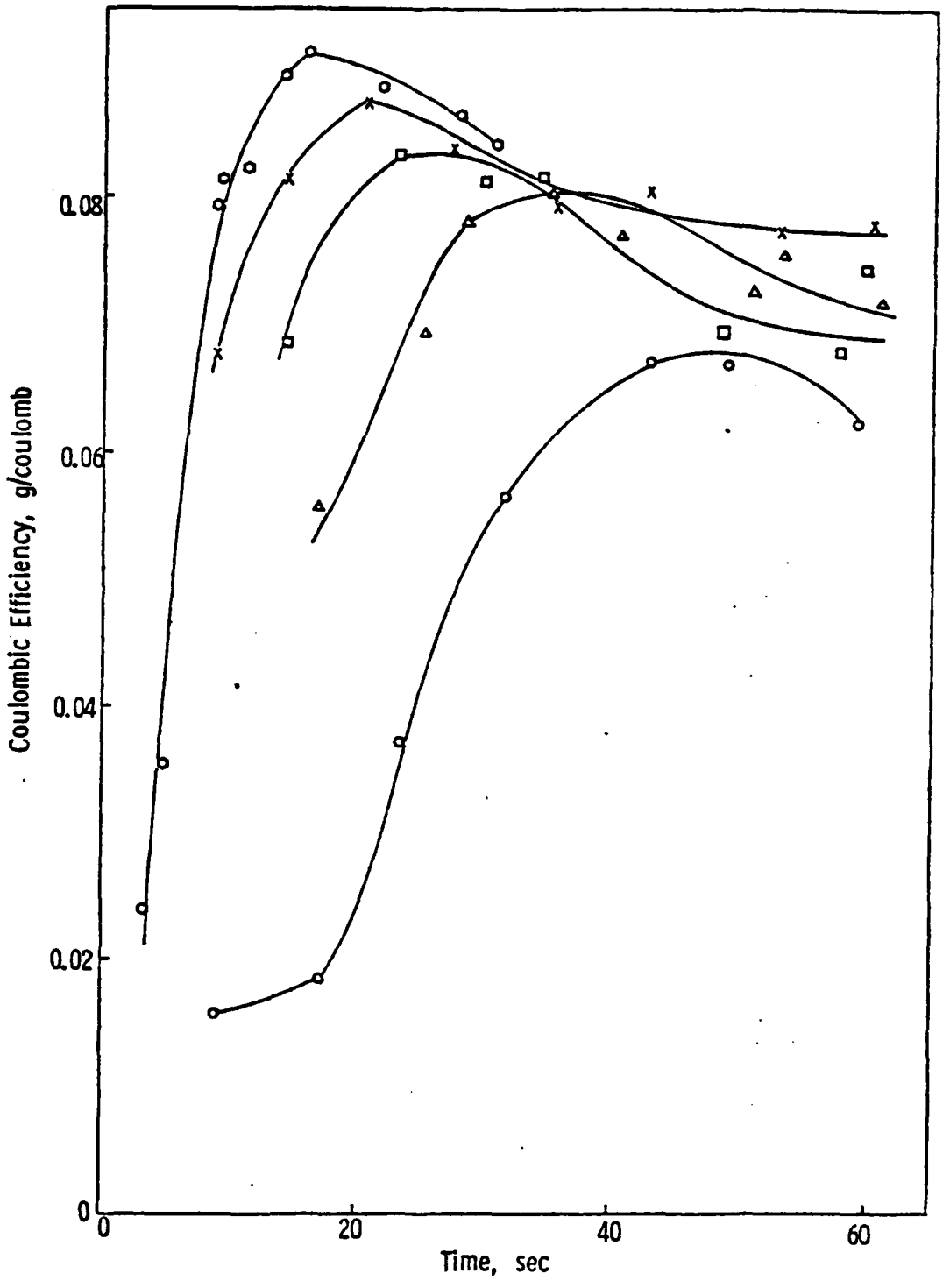

Figure 71. Variation of coulombic efficiency with deposition time. Applied voltages: 80 v (-o-), 120 v (-△-), 175 v (-□-), 215 v (-x-), and 250 v (-○-).

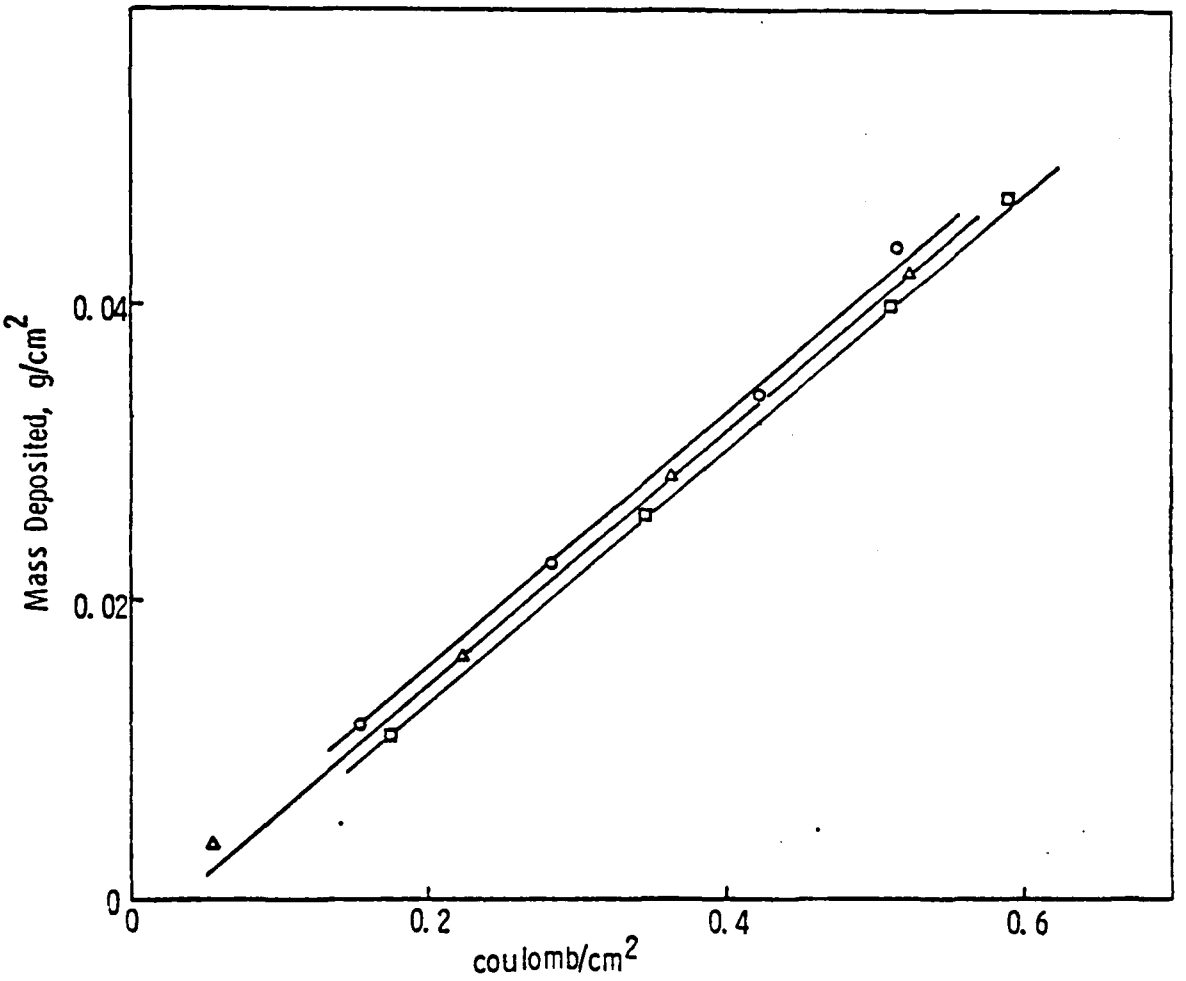

Figure 72. Mass deposited vs coulomb/cm^2. Deposition time: 16 sec (-o-), 19 sec (-Δ-), and 25 sec (—□—).

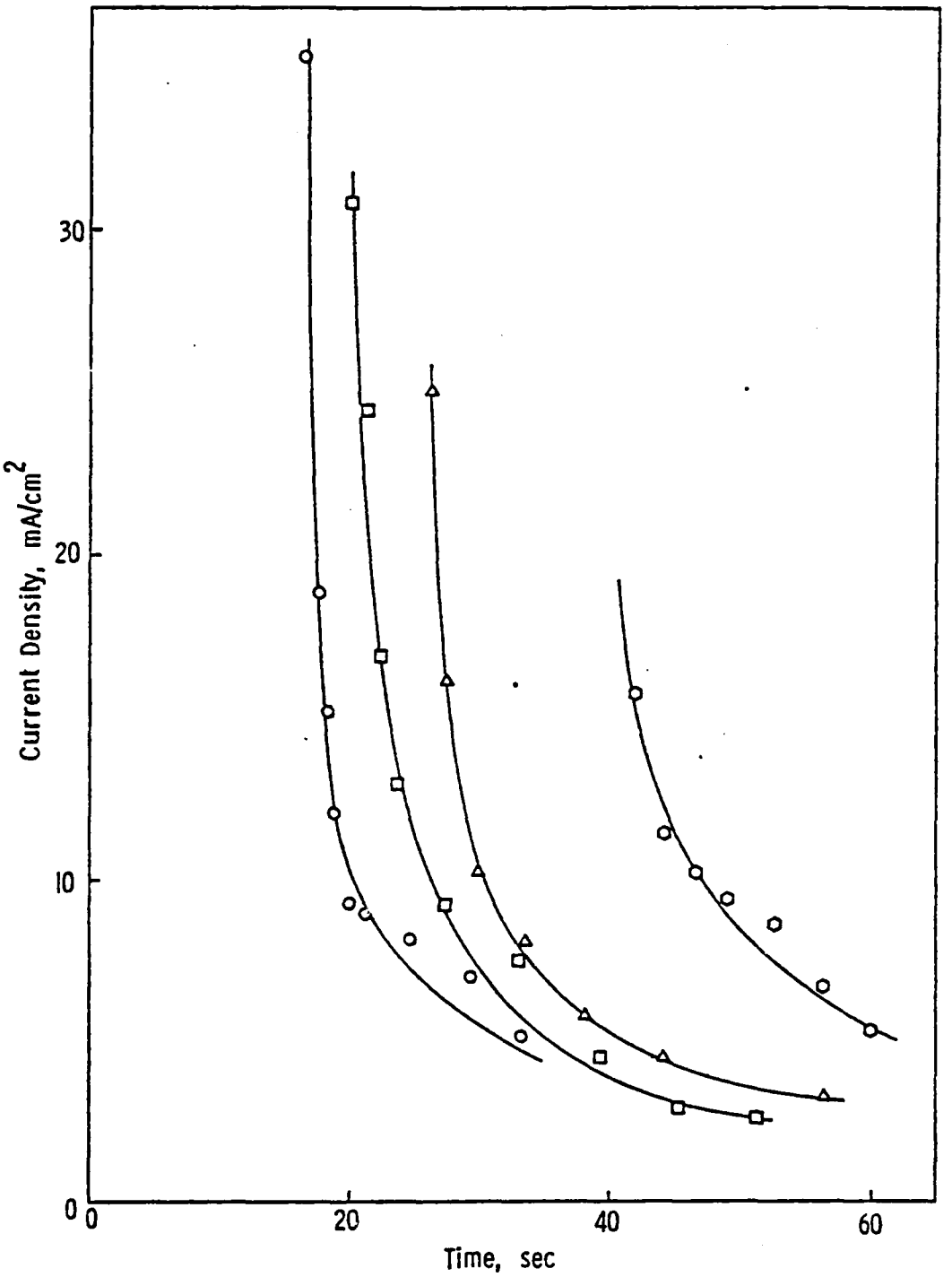

Figure 73. Variation of current density with deposition time. 120 v (-o-), 175 v (-Δ-), 215 v (-□-), and 250 v (-o-).

A quantitative interpretation of the current (density)-time curves has been given by Finn and Hasnip (42). The reciprocal of the square of current should give a linear curve when plotted against deposition time if it is assumed that the specific resistance of the film remains constant during the entire deposition period. It is clear from Figure 74 that the present data did not follow this relationship at all. It may be possible that the specific resistance did not remain constant during the deposition period and that some compaction of the deposit had taken place concurrently with deposition.

The potential profile in an electrodeposition cell is rather nonuniform when deposition begins and its thickness is increasing. Most of the voltage drop occurs within the film from that time on (27). The voltage drop in the electrochemical double layer, in the diffuse double layer and in the bath are small in comparison. The electric field strength in the film normally exceeds that in the bath by 4-5 orders of magnitude. An attempt was made to calculate the field strength within the film during deposition for the present system. The field strength is assumed to be equal to the applied voltage divided by the instantaneous thickness of the coating. The field strength was found to be of the order of ca (2-6) x 10^3 v/cm depending on the applied voltage. This range is about two orders of magnitude smaller than those reported for solubilized polymer resins deposited anodically (i.e., ca 10^5 v/cm). Figure 75 shows the logarithm of the current density vs field strength plots at various applied voltages for the present system. As the thickness increased, the current density and the field strength both decreased. A non-linear current density-field strength relationship was obtained except for deposition at 120 v which seemed to give a non-linear but exponential relationship. For depositions at 175, 215 and 250 v, it can only be said that the relationship was at least non-ohmic. It is conceivable that a field strength of the order of 10^3 v/cm was still too high for the conductance of the film to obey Ohm's law.

It has been pointed out by Beck (27) that severe deviations from ohmic behavior of the current-voltage relationship on electrodeposited film are to be expected especially at high voltages and high current densities. However, a non-linear exponential current density-field strength relationship would closely parallel the oxide film growth theory where the current transport mechanism is pure ionic conduction (43). Such relationship was first observed by Pierce and co-workers on an anodic system recently (37). It should be noted that this relationship also predicts that film growth will cease or approach a limiting value when the current density becomes equal to the value required to prevent dissolution of the film in the electrodeposition bath. Neither of these seems to be applicable to the present system. The film continued to grow at a slow but constant rate of 3.4×10^{-4} g/cm^2/sec.

Examination of Table XIII shows that the time of transition

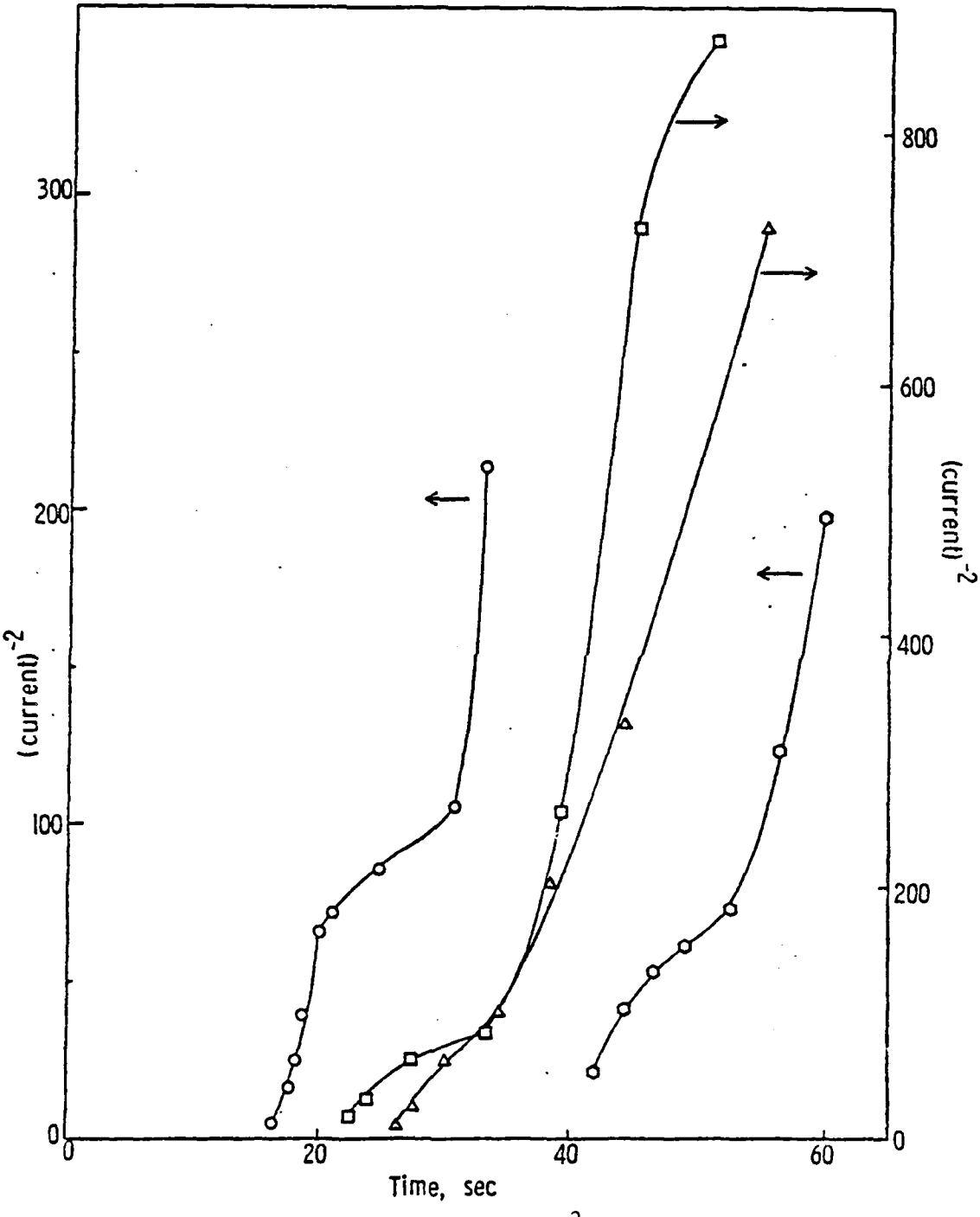

Figure 74. Reciprocal of (current)^2 as a function of deposition time. 120 v (-○-), 175 v (-△-), 215 v (-□-), and 250 v (-o-).

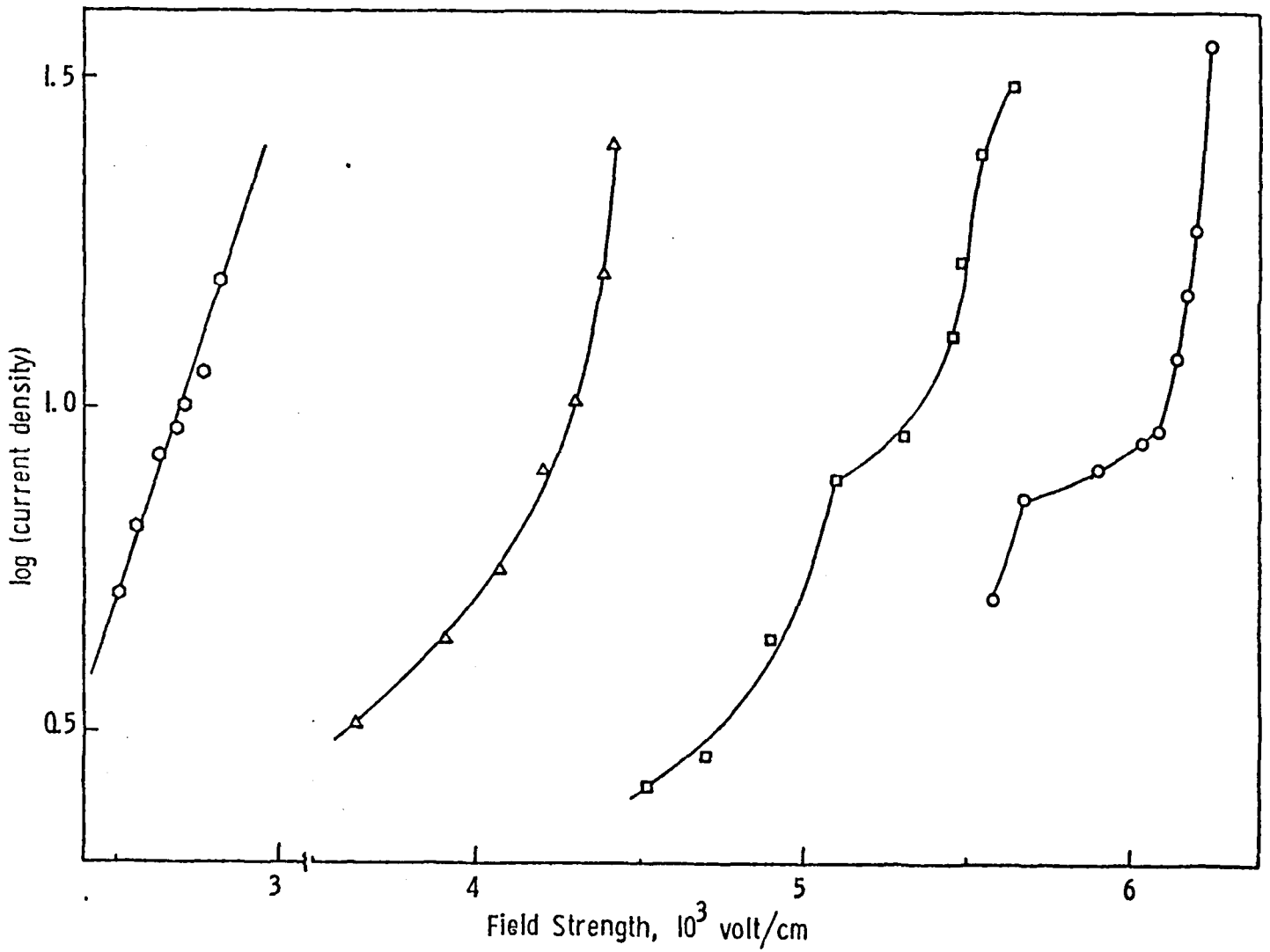

Figure 75. Current density vs field strength for deposition at 120 v (-O-), 175 v (-Δ-), 215 v (-□-), and 250 v (-o-).

from a fast initial rate of film growth to a slower rate (Column 3) agreed well with the time to attain maximum g/coulomb (Column 4) and maximum current (Column 5) for all the applied voltages used. All these three parameters are closely related and will be considered together in the following deliberation. The electrodeposition process for the present system seems to occur in two stages: 1) Before point Y in the current-time curve, the rate of film growth was fast and strongly dependent on the voltage: the higher the voltage, the faster the rate. This process is unimpeded and therefore the film mass increased linearly with time. Also in this region, both the current and the deposition efficiency (g/coulomb) increased rapidly with time of deposition. The film was conducting in nature at this stage. 2) After a certain mass (or thickness) was attained for each applied voltage, point Y was reached. Compaction of the film began and film growth slowed down to a constant rate for all applied voltages. The deposition efficiency therefore decreased. Film resistance would accordingly increase; therefore, current (density) should drop, rapidly or more slowly depending on the applied voltage, and tend towards a common residual amperage. The film became insulating and the electric field strength within the film was very high. Under these conditions, Ohm's law was not obeyed.

Conclusions

The electrodeposition of epoxy latex at constant voltage occurred in two stages. Film growth at the beginning was fast, unimpeded and strongly dependent on the applied voltage. At the second stage, consolidation and compaction set in and film growth slowed down to a common rate for all voltages. The film resistance increased and the film became more insulating. However, the current density-field strength relationship was non-ohmic in behavior. The film mass (or thickness) increased linearly with time for both stages. Even though the oxide film growth theory for pure ionic conductors had been shown to model closely the anodic electrodeposition kinetics of an organic carboxylic resin as outlined by Pierce et al (37), the electric discharge mechanism for the present system does not lend itself to an ionic consideration. A "concentration coagulation" mechanism seems more favorable.

The conclusion arrived at above is in essence qualitative in nature. Further mathematical analysis of the present data in respect to concentration coagulation under an electric field force as analogous to, say, sedimentation under a gravitational or centrifugual field could perhaps yield a more quantitative explanation of the effect of applied voltage, duration of deposition and current-time curves of the electrodeposition process under investigations here.

Part B. Drying and Curing of Epoxy Films

Introduction

Aqueous-based polymer latexes are widely used in the formulation of paints, adhesives, and various other forms of surface coating materials. With the introduction of stringent anti-pollution regulations coupled with rising cost of petroleum-based solvents, these water-borne systems are becoming more attractive to the coating industry as alternatives to the existing solvent-based coating technologies.

A coating with up to 50% or more water initially appears to have many advantages. However, the evaporation rate of water in the coating is strongly influenced by high surface tension, unusual solubility behavior and variable humidity. These factors have created significant technical problems not normally encountered in the solvent-based systems.

Therefore, the purpose of this investigation is to obtain drying curves of epoxy resin—curing agent systems for i) organic solvent-based systems, ii) aqueous-based latexes and iii) modified aqueous-based systems. Such curves, generated under different conditions, are expected to provide information on the initial, intermediate and final evaporation rates, each of which has influence on drying time, streaking, cratering and other properties of coating materials. It is hoped that such study will yield an insight into the mechanism of drying and film formation of epoxy latex systems in general.

Experimental Results

Accurate measurements of the changes in the film-weight and the reduction of fluctuations in the specified parameters during the process of drying are critical to any meaningful interpretation of data. This is of particular importance because of the small size of the film under consideration. Consequently, a considerable effort had been put into providing a suitable environment for the experiment. Figure 76 shows the newly constructed mini-wind tunnel in which the studies of film drying of epoxy-curing agent systems were carried out. Essentially, it consists of three parts, mainly:

1) 32x40x40cm plywood control section where the drying air was maintained at desired conditions before entering the test section.

2) 55x20x20cm Plexiglass test section where the sample was placed, and

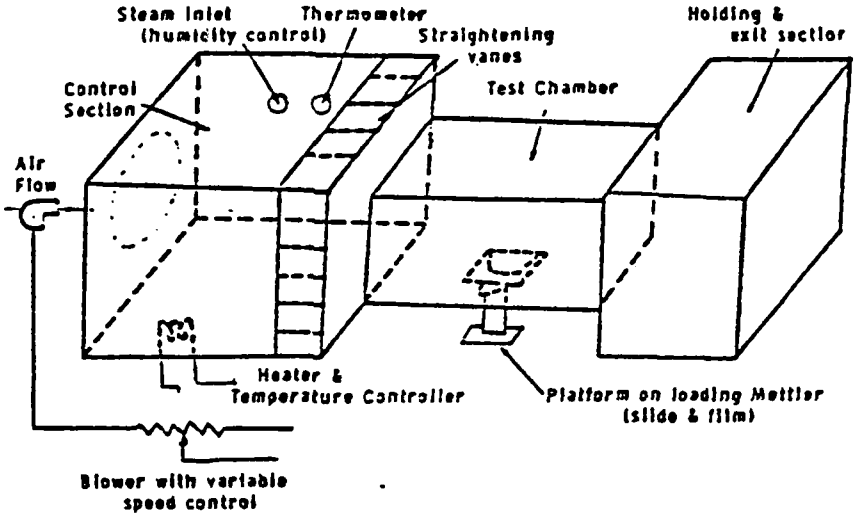

Figure 76. Apparatus for latex film drying

3) 32x40x40cm plywood "holding and exit" section constructed to hold the out-flowing air for a while and reduce disturbances from the ambient conditions.

The upper limit for air velocity in this wind tunnel was approximately 89 cm/sec (2 mph). Excessive fluctuations in film weight measurements occurred at higher air flow rates. The air velocity was measured at sample level with an anemometer wind speed indicator (Davis Instrument Co.).

Figure 77 is the schematic illustration of a new big wind tunnel also to be used for the above work. It had an air velocity upper limit (before fluctuations set in) of ca 4.5 m/sec (10 mph). A better control of the humidity within the tunnel should thus be provided. This big tunnel is still being tested and is not fully operational yet.

The kinetics of film drying on films cast from the following mixtures were carried out in the mini-wind tunnel under controlled conditions:

i) Solvent-based Epon 1001 and Emerez 1511

ii) Aqueous-based Epon 1001 and Emerez 1511 latex mixtures (a)

iii) Aqueous-based modified Epon 1001 and Emerez 1511 latex mixtures

(a) With 10% by weight of Epi-Rez 5018 added.

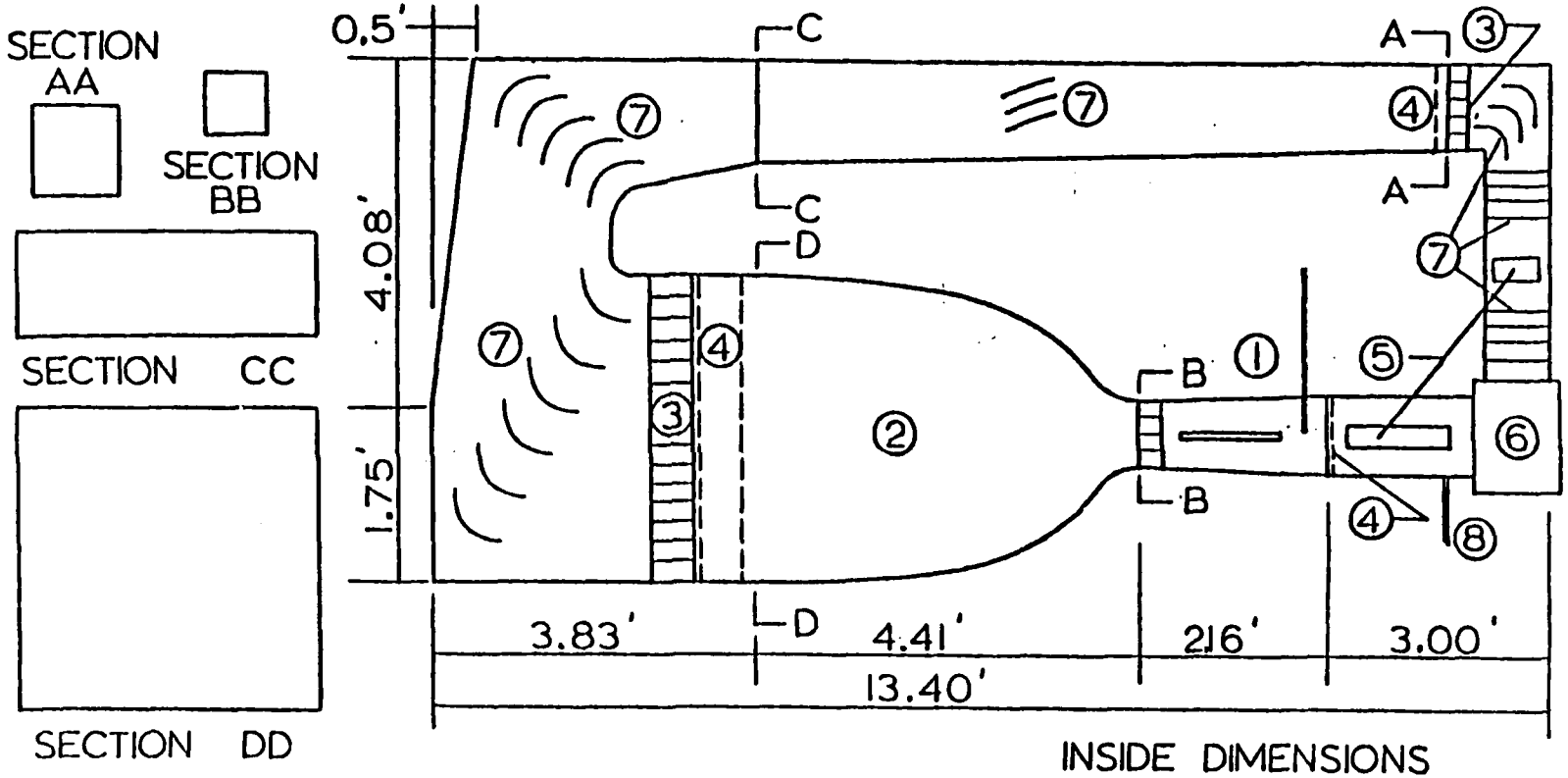

Figure 77. Schematic drawing of new larger wind tunnel to be used in drying studies.

iv) Modified water soluble Epi-Rez 510 liquid epoxy resin and Epi-cure W-50-8535 [Celanese formula 24-174], and

v) Modified water soluble Epi-Rez 510 liquid epoxy resin and Epi-cure WC-60-8537 [Celanese formula 24-180]

Approximately 1-2 g of mixture was evenly coated on a 14x6 cm glass plate by means of a 10 mil-gap draw-down film applicator after allowing to cure for exactly 15 min. Formula 24-174 was cured for 1 1/2 hr before casting. The plate was immediately placed on a level Plexiglass platform in the test-section of the wind tunnel. The platform was mounted on top of a top-loading Mettler PI6ON balance and the weight change during drying was recorded at 1 min intervals until the weight change attributable to evaporation was negligible. The wet area (used in calculation of evaporation flux) was measured from a graph paper placed below the plate.

Results and Discussion

Table XIV shows a typical set of drying data obtained at dry bulb temperature of 40.5°C, 24% relative humidity (calculated from wet and dry bulb temperature readings) and at ca 150 ft/min (76 cm/sec). Drying curves (cumulative weight loss per g solids content vs time plots) under constant temperature and relative humidity conditions but at varying air velocities of 150, 125, 100 and 75 ft/min, respectively, are shown in Figures 78-81 for the five different systems mentioned above. Figures 82-85 show the corresponding plots of the flux (g/cm^2-sec) vs the moisture content (g moisture/g solids) of these systems. Figures 86-95 show regrouping of these drying curves into individual coating systems at different air velocities.

It can be seen from Figures 86-90 that the solvent-based system required the shortest time (ca 600 sec) to reach a constant film weight, whereas the W-50-8535 and WC-60-8537 systems which were essentially aqueous-based solubilized polymer resin systems, took a slightly longer time (ca 900 sec) to attain constant film weight. For the latex systems at least 1200 sec were required before a constant film weight was attained for the Epon 1001: Emerez 1511 latex mixture. The approach to constant film weight was slow and gradual in the case of the latex mixture containing a reactive diluent (Epon 1001 + Epi Rez 5018 + Emerez 1511).

Figures 91-95 show that the drying rates for all the systems seemed to be the same at ca 1.1×10^{-5} g/cm^2-sec. The air velocity

Table XIV

Drying Data Showing Flux as a Function of Time

Time (min)	Epon 1001 : Emerez 1511 Aqueous-based latex	solvent-based	modified latex	Formula 24-174	Formula 24-180
1.0	1.88×10^{-5}	1.75×10^{-5}	1.76×10^{-5}	2.74×10^{-5}	2.20×10^{-5}
2.0	2.26	1.65	2.25	2.40	2.02
3.0	2.09	1.45	1.57	1.68	1.73
4.0	1.72	1.26	1.78	1.50	2.08
5.0	1.74	1.36	1.71	1.50	2.02
6.0	1.75	1.26	–	1.97	–
7.0	1.65	–	1.41	1.99	1.68
8.0	1.65	1.02×10^{-5}	–	1.82	1.63
9.0	1.65	–	1.25	1.69	–
10.0	1.69	8.55×10^{-6}	1.20	1.58	1.34
12.0	1.83×10^{-5}	–	1.50	1.37	1.27
15.0	1.04×10^{-4}	5.83	1.31		
17.0	9.24×10^{-5}	–	1.36		
20.0	–	5.34	1.34		
25.0	–	–	1.13		
30.0	–	–	1.17		

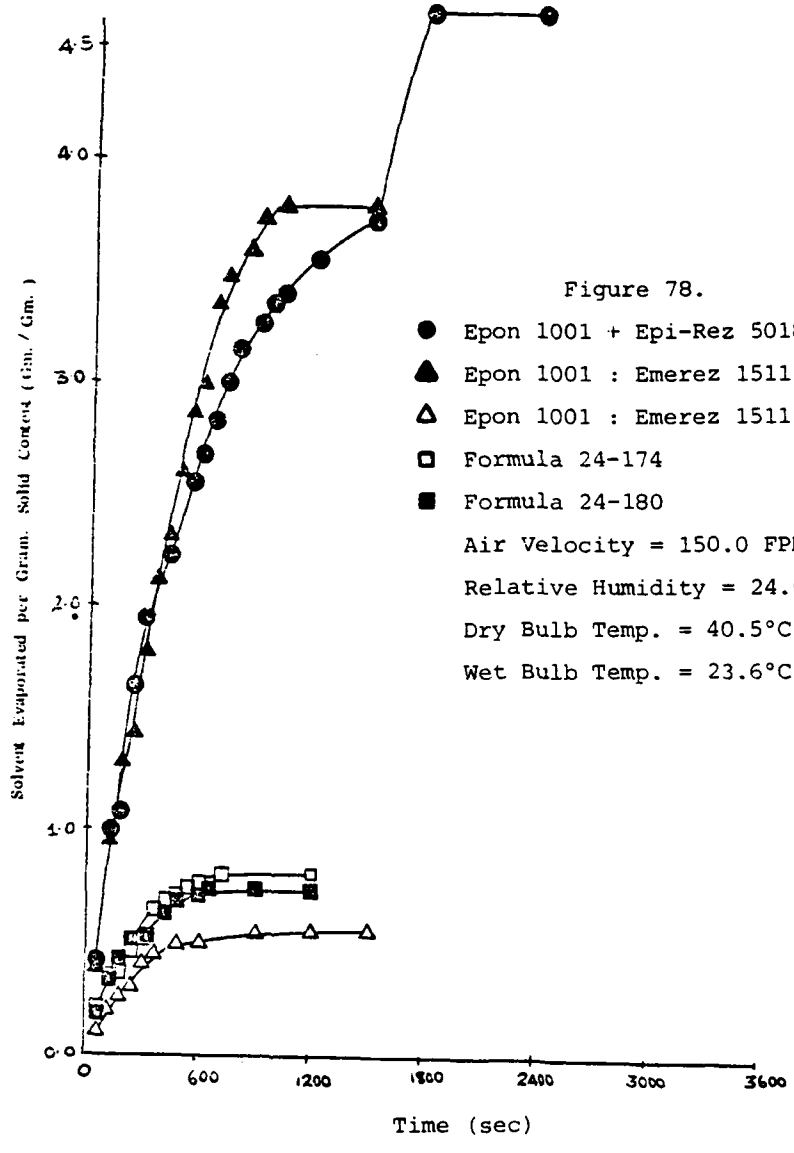

Figure 78.

- ● Epon 1001 + Epi-Rez 5018 : Emerez 1511
- ▲ Epon 1001 : Emerez 1511 (Latex)
- △ Epon 1001 : Emerez 1511 (Solvent)
- □ Formula 24-174
- ■ Formula 24-180

Air Velocity = 150.0 FPM

Relative Humidity = 24.0%

Dry Bulb Temp. = 40.5°C

Wet Bulb Temp. = 23.6°C

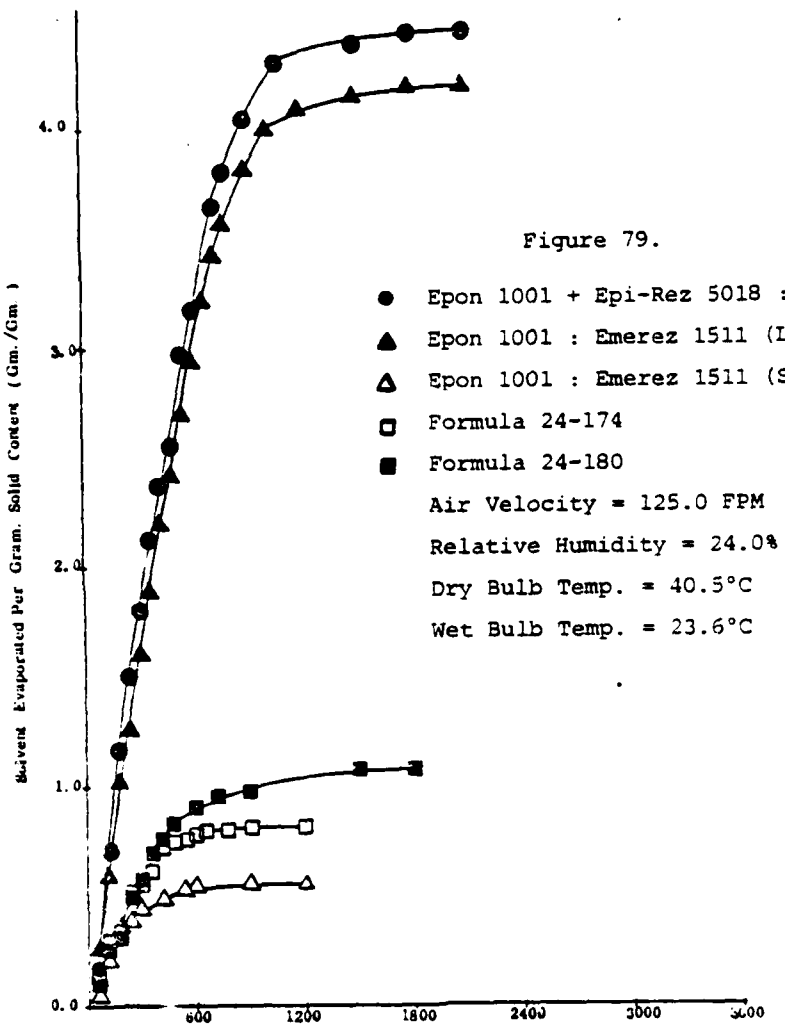

Figure 79.

- ● Epon 1001 + Epi-Rez 5018 : Emerez 1511
- ▲ Epon 1001 : Emerez 1511 (Latex)
- △ Epon 1001 : Emerez 1511 (Solvent)
- □ Formula 24-174
- ■ Formula 24-180

Air Velocity = 125.0 FPM

Relative Humidity = 24.0%

Dry Bulb Temp. = 40.5°C

Wet Bulb Temp. = 23.6°C

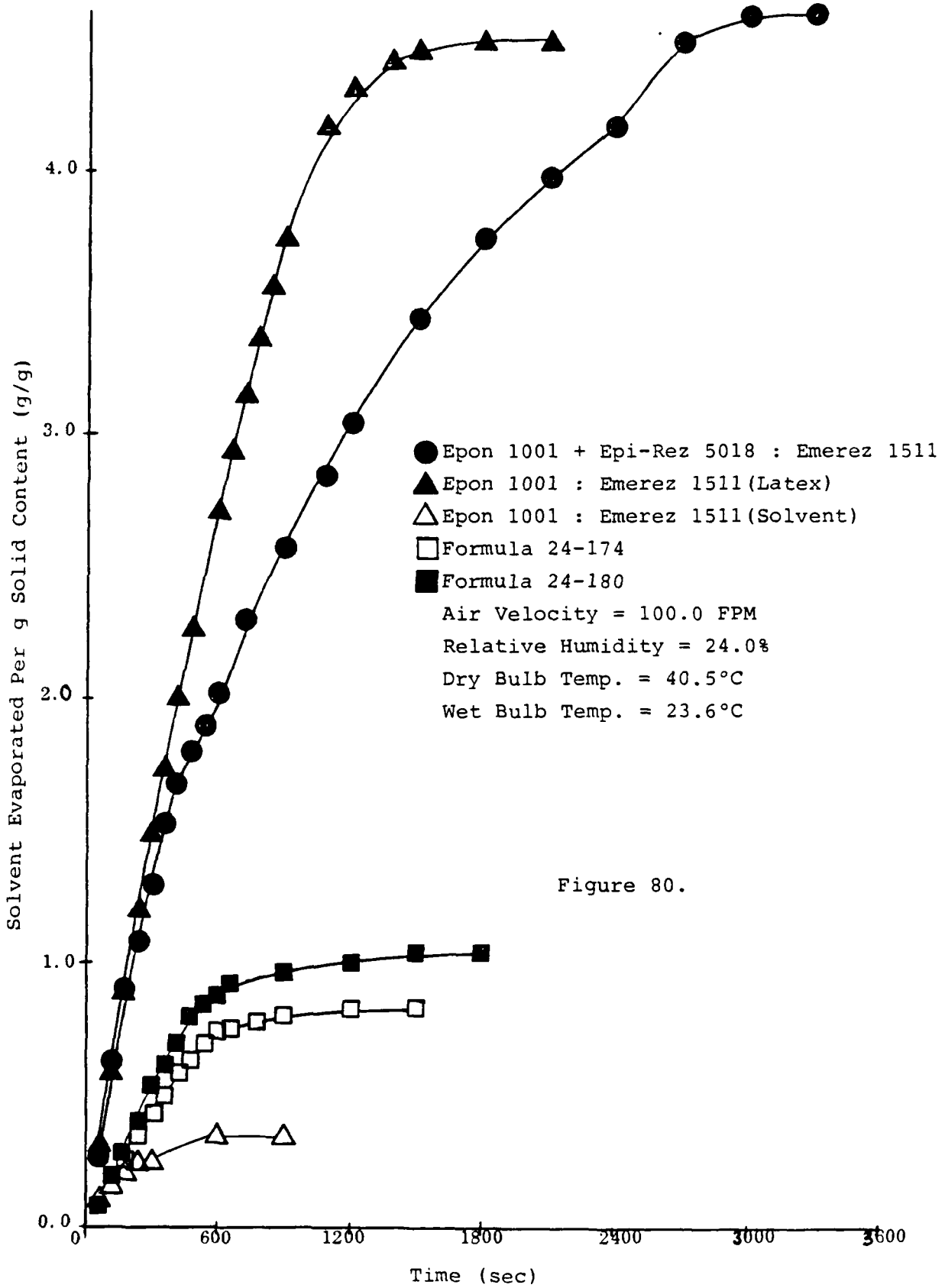
Solvent Evaporated Per g Solid Content (g/g)
4.0
3.0
2.0
1.0
0.0
0
600
1200
1800
2400
3000
3600
Time (sec)
Epon 1001 + Epi-Rez 5018 : Emerez 1511
Epon 1001 : Emerez 1511(Latex)
Epon 1001 : Emerez 1511(Solvent)
Formula 24-174
Formula 24-180
Air Velocity = 100.0 FPM
Relative Humidity = 24.0%
Dry Bulb Temp. = 40.5°C
Wet Bulb Temp. = 23.6°C

Figure 80.

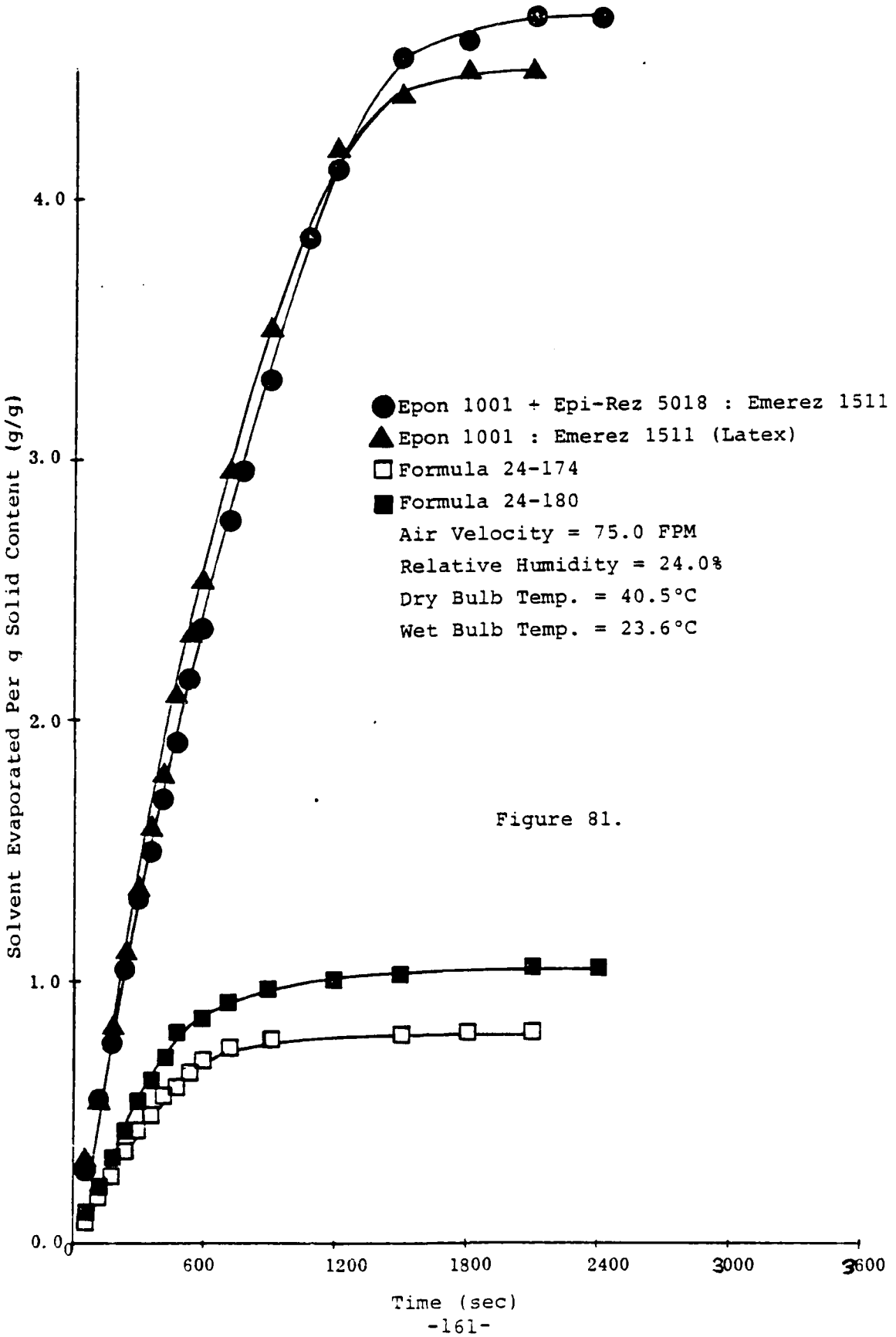
Solvent Evaporated Per g Solid Content (g/g)
4.0
3.0
2.0
1.0
0.0
600
1200
1800
2400
3000
3600
Time (sec)
Epon 1001 + Epi-Rez 5018 : Emerez 1511
Epon 1001 : Emerez 1511 (Latex)
Formula 24-174
Formula 24-180
Air Velocity = 75.0 FPM
Relative Humidity = 24.0%
Dry Bulb Temp. = 40.5°C
Wet Bulb Temp. = 23.6°C

Figure 81.

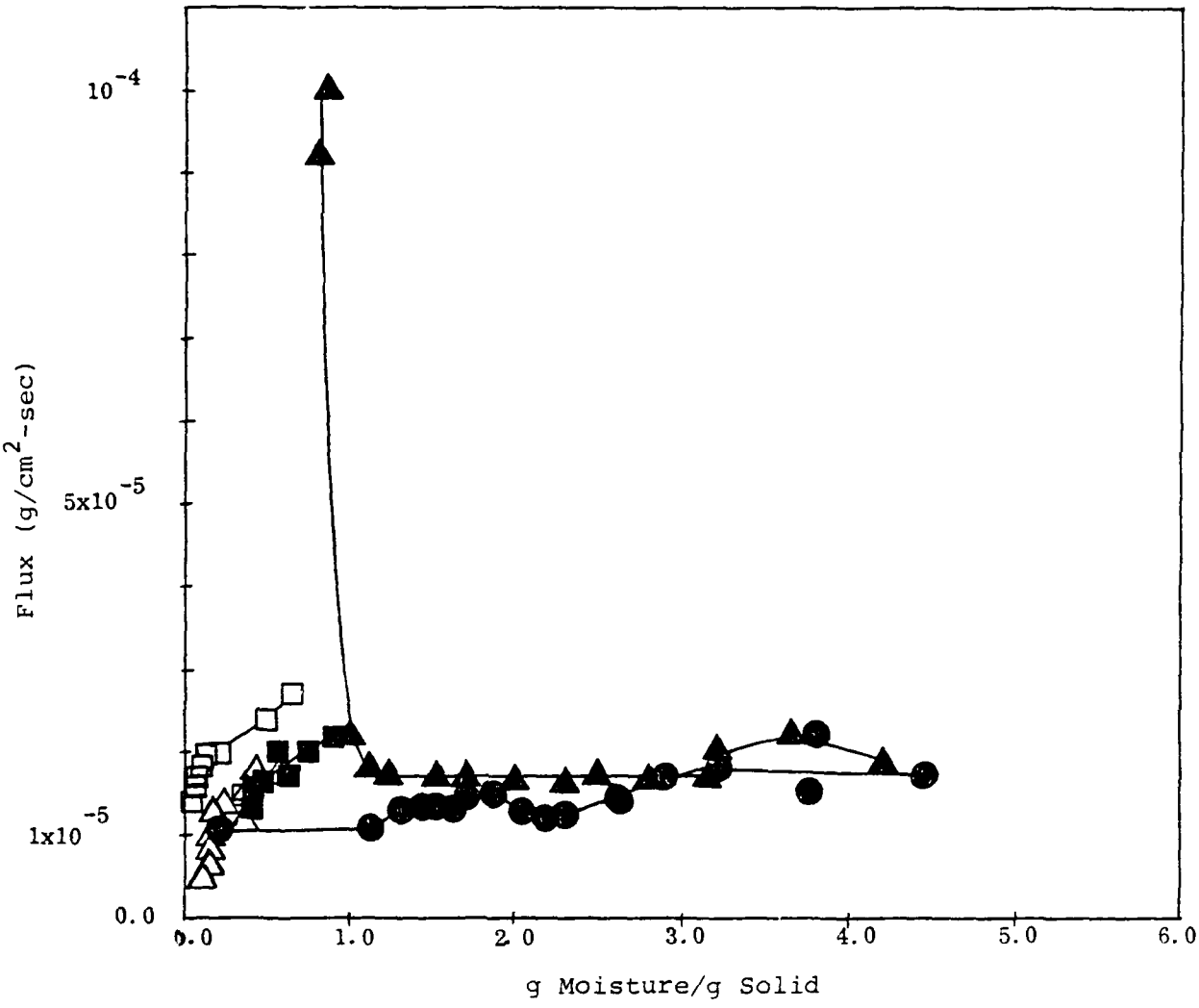

● Epon 1001 + Epi-Rez 5018 : Emerez 1511
▲ Epon 1001 : Emerez 1511 (Latex)
△ Epon 1001 : Emerez 1511 (Solvent)
□ Formula 24-174
■ Formula 24-180
Air Velocity = 150.0 FPM
Relative Humidity = 24.0%
Dry Bulb Temp. = 40.5°C

Figure 82.

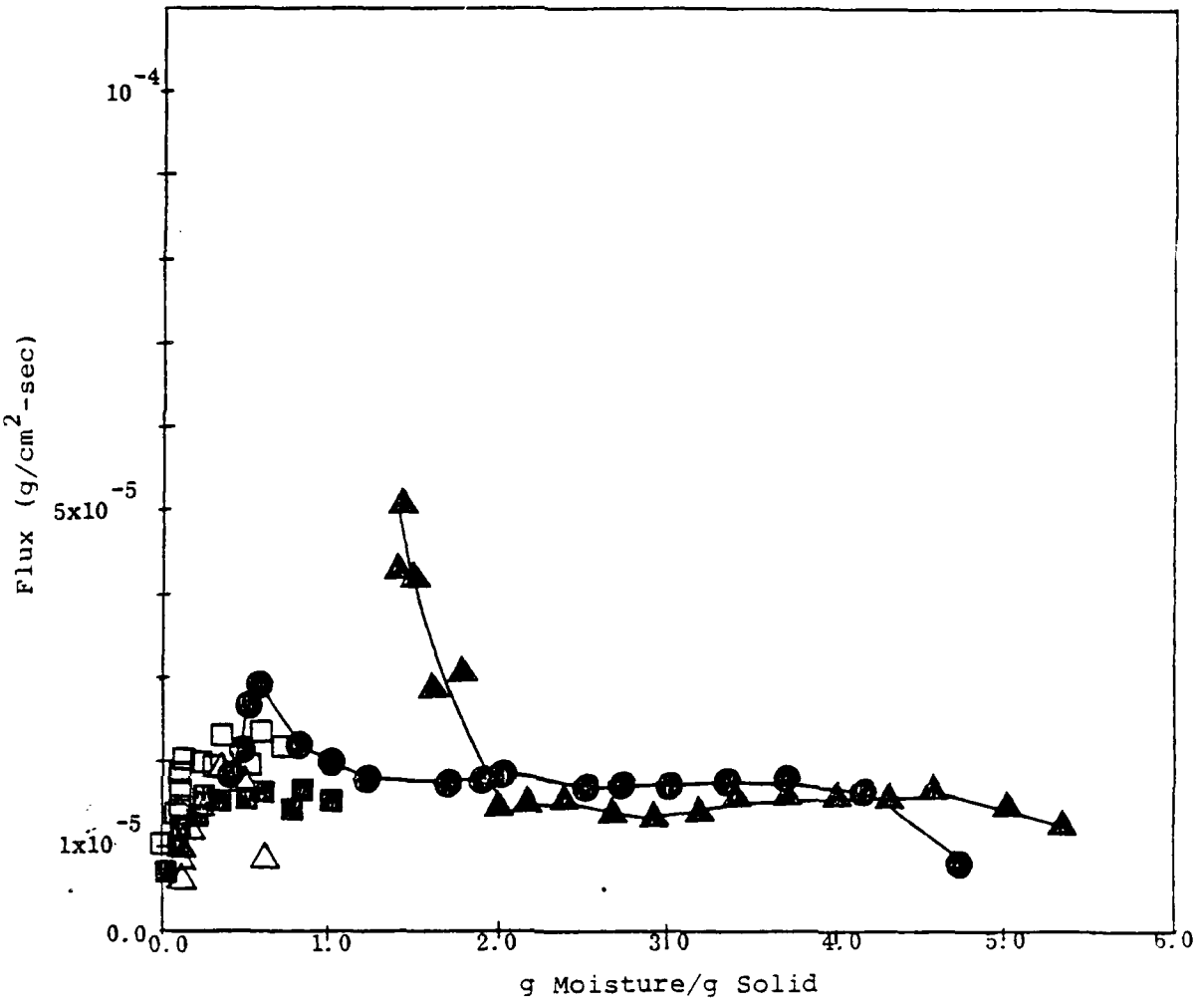

● Epon 1001 + Epi-Rez 5018 : Emerez 1511
▲ Epon 1001 : Emerez 1511 (Latex)
△ Epon 1001 : Emerez 1511 (Solvent)
□ Formula 24-174
■ Formula 24-180
Air Velocity = 125.0 FPM
Relative Humidity = 24.0%
Dry Bulb Temp. = 40.5°C

Figure 83.

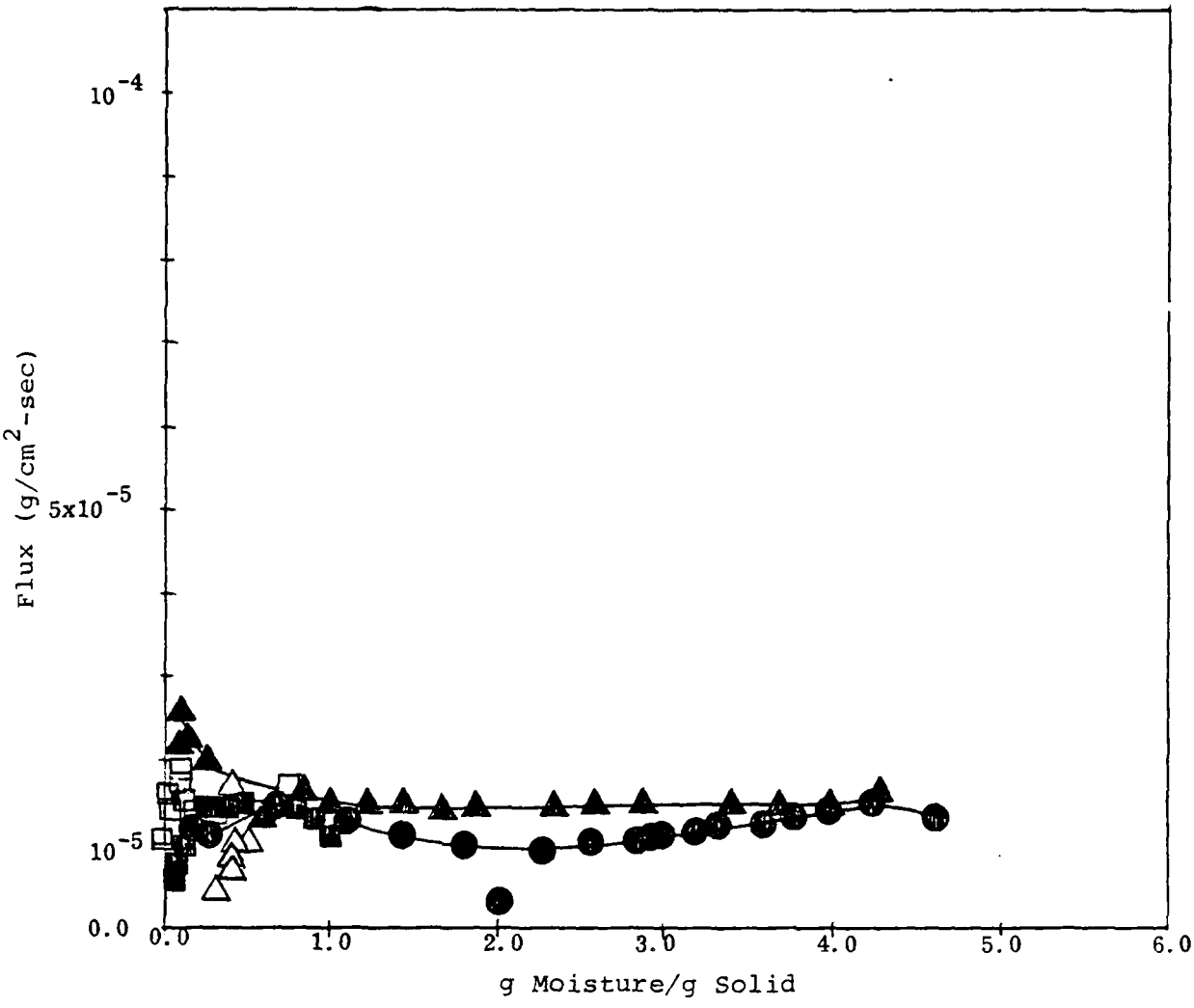

● Epon 1001 + Epi-Rez 5018 : Emerez 1511
▲ Epon 1001 : Emerez 1511 (Latex)
△ Epon 1001 : Emerez 1511 (Solvent)
□ Formula 24-174
■ Formula 24-180
Air Velocity = 100.0 FPM
Relative Humidity = 24.0%
Dry Bulb Temp. = 40.5°C

Figure 84.

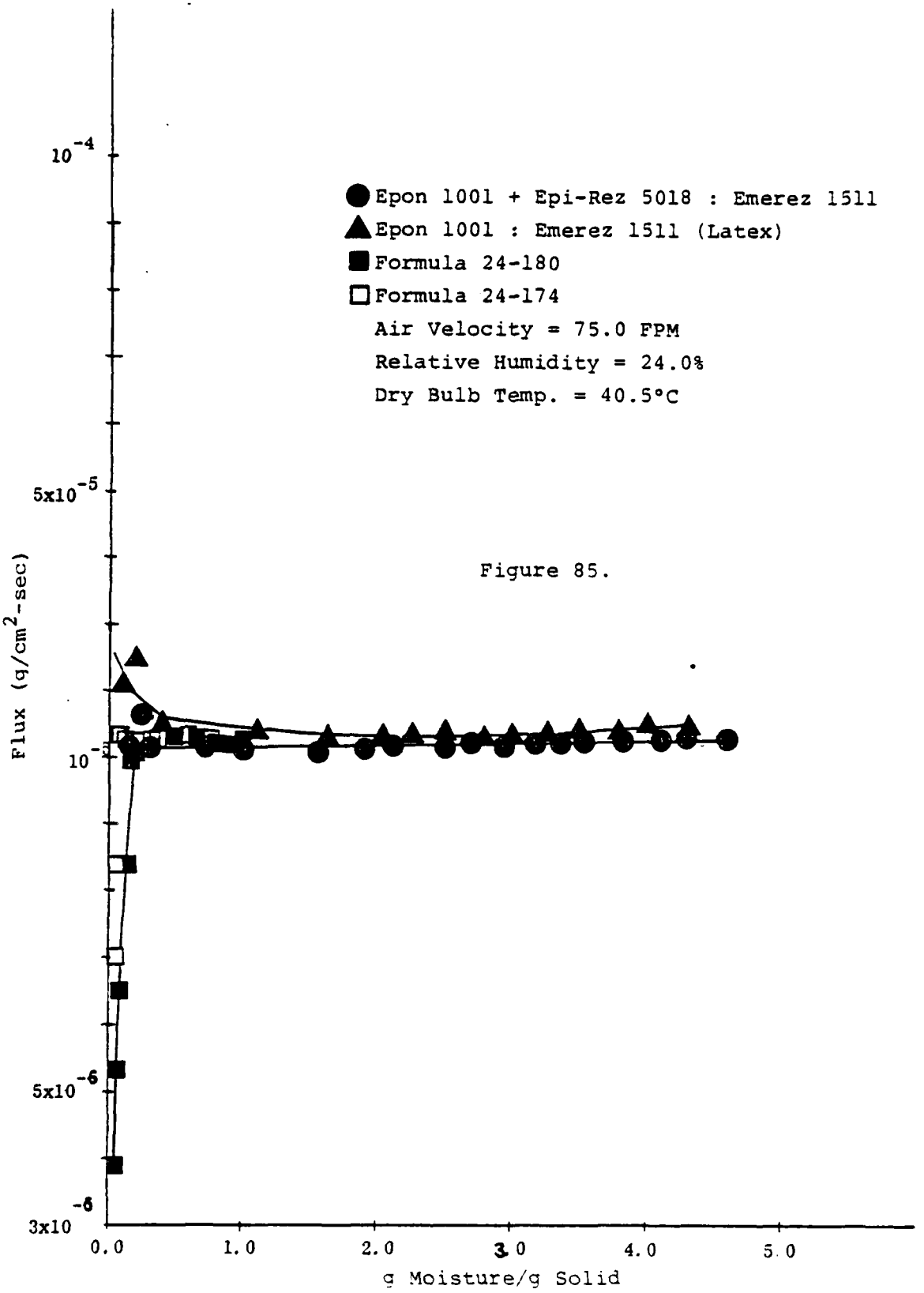
Epon 1001 + Epi-Rez 5018 : Emerez 1511
Epon 1001 : Emerez 1511 (Latex)
Formula 24-180
Formula 24-174
Air Velocity = 75.0 FPM
Relative Humidity = 24.0%
Dry Bulb Temp. = 40.5°C
Flux (g/cm2-sec)
10-4
5x10-5
10-5
5x10-6
3x10-6
0.0
1.0
2.0
3.0
4.0
5.0
g Moisture/g Solid

Figure 85.

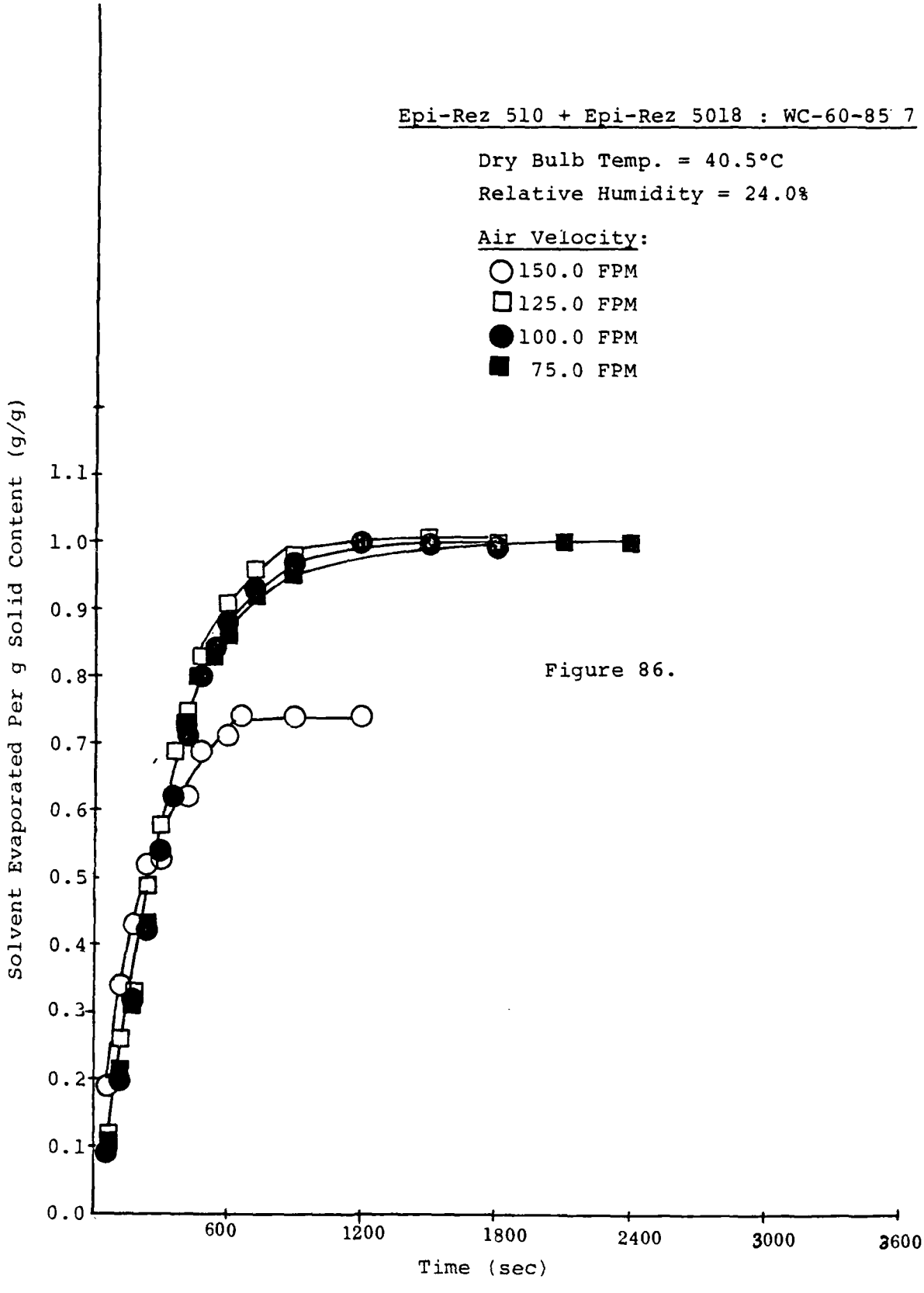
Epi-Rez 510 + Epi-Rez 5018 : WC-60-85 7
Dry Bulb Temp. = 40.5°C
Relative Humidity = 24.0%
Air Velocity:
150.0 FPM
125.0 FPM
100.0 FPM
75.0 FPM
Solvent Evaporated Per g Solid Content (g/g)
0.0
0.1
0.2
0.3
0.4
0.5
0.6
0.7
0.8
0.9
1.0
1.1
600
1200
1800
2400
3000
3600
Time (sec)

Figure 86.

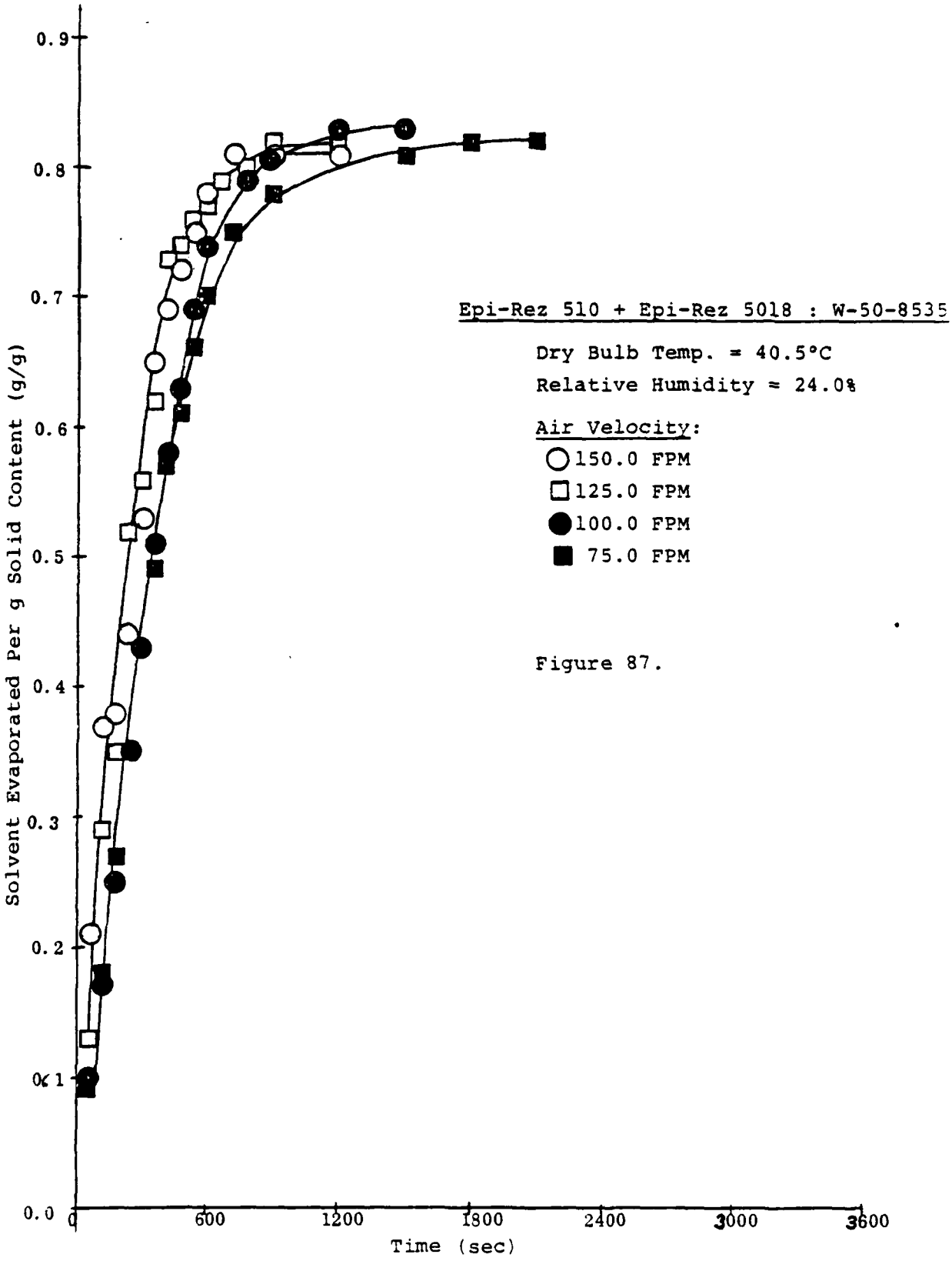

Epi-Rez 510 + Epi-Rez 5018 : W-50-8535

Dry Bulb Temp. = 40.5°C

Relative Humidity = 24.0%

Air Velocity:

○ 150.0 FPM

□ 125.0 FPM

● 100.0 FPM

■ 75.0 FPM

Figure 87.

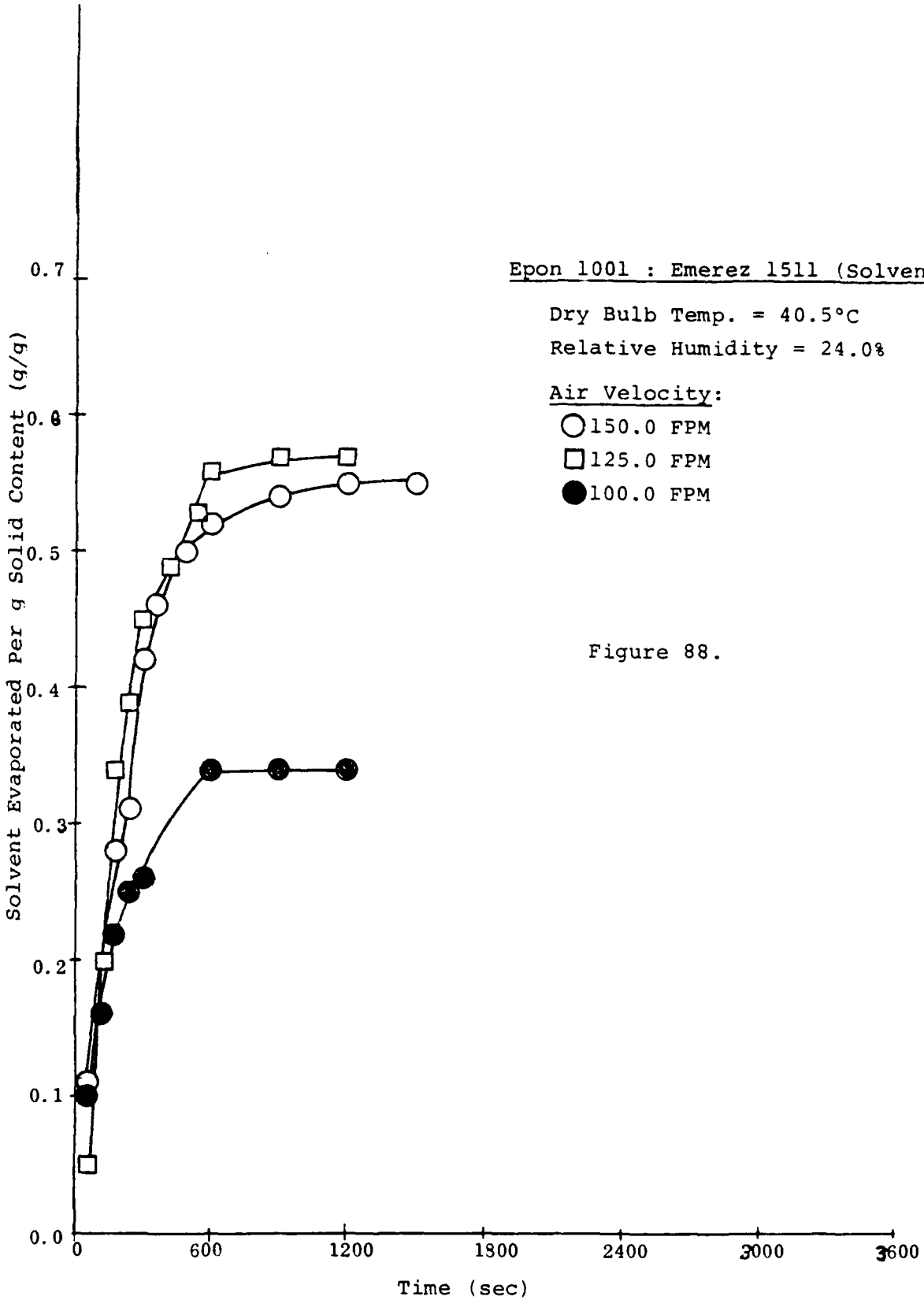
Epon 1001 : Emerez 1511 (Solvent)
Dry Bulb Temp. = 40.5°C
Relative Humidity = 24.0%
Air Velocity:
150.0 FPM
125.0 FPM
100.0 FPM
Solvent Evaporated Per g Solid Content (g/g)
0.0
0.1
0.2
0.3
0.4
0.5
0.6
0.7
0
600
1200
1800
2400
3000
3600
Time (sec)

Figure 88.

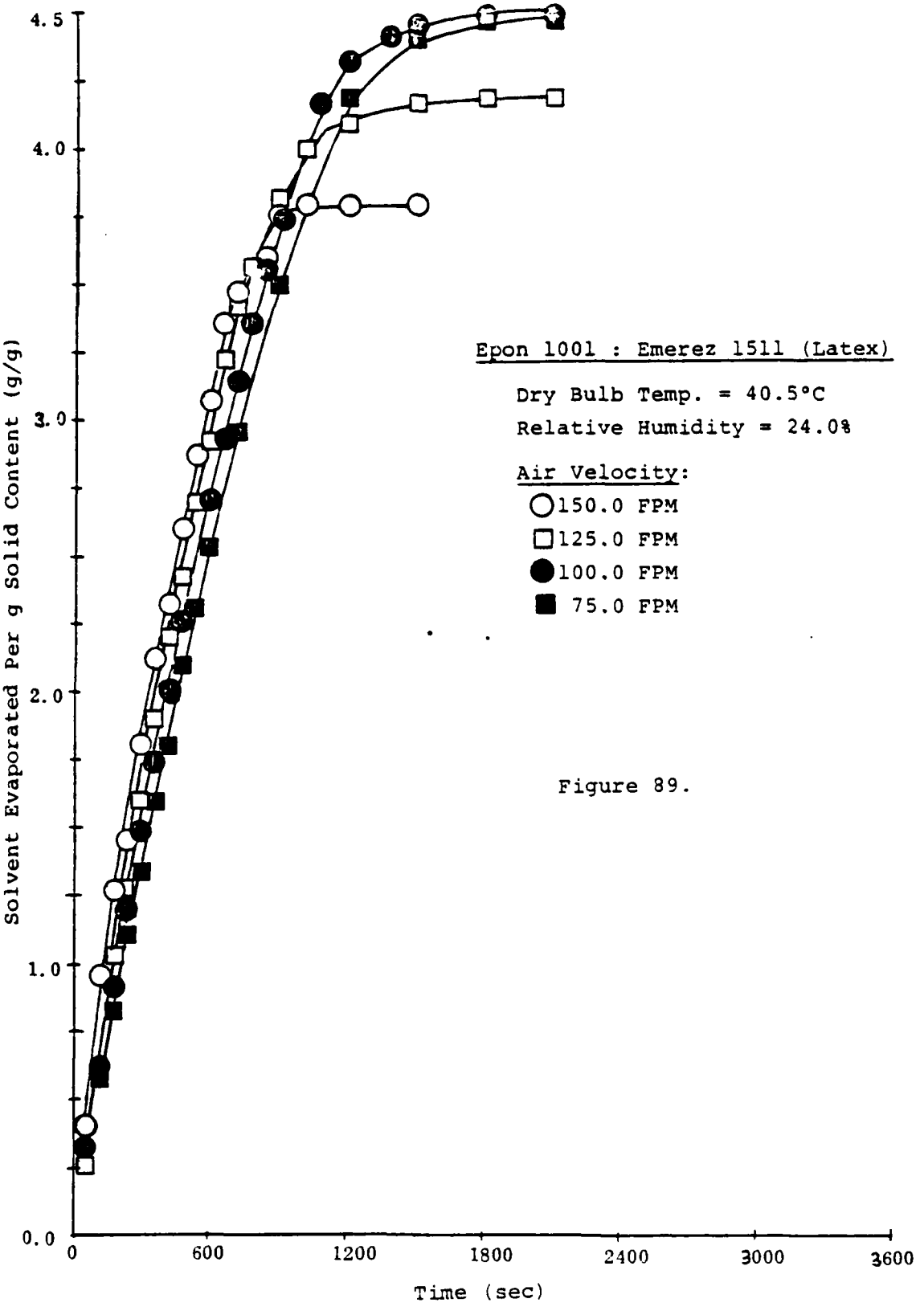
4.5
4.0
3.0
2.0
1.0
0.0
Solvent Evaporated Per g Solid Content (g/g)
0
600
1200
1800
2400
3000
3600
Time (sec)
Epon 1001 : Emerez 1511 (Latex)
Dry Bulb Temp. = 40.5°C
Relative Humidity = 24.0%
Air Velocity:
150.0 FPM
125.0 FPM
100.0 FPM
75.0 FPM

Figure 89.

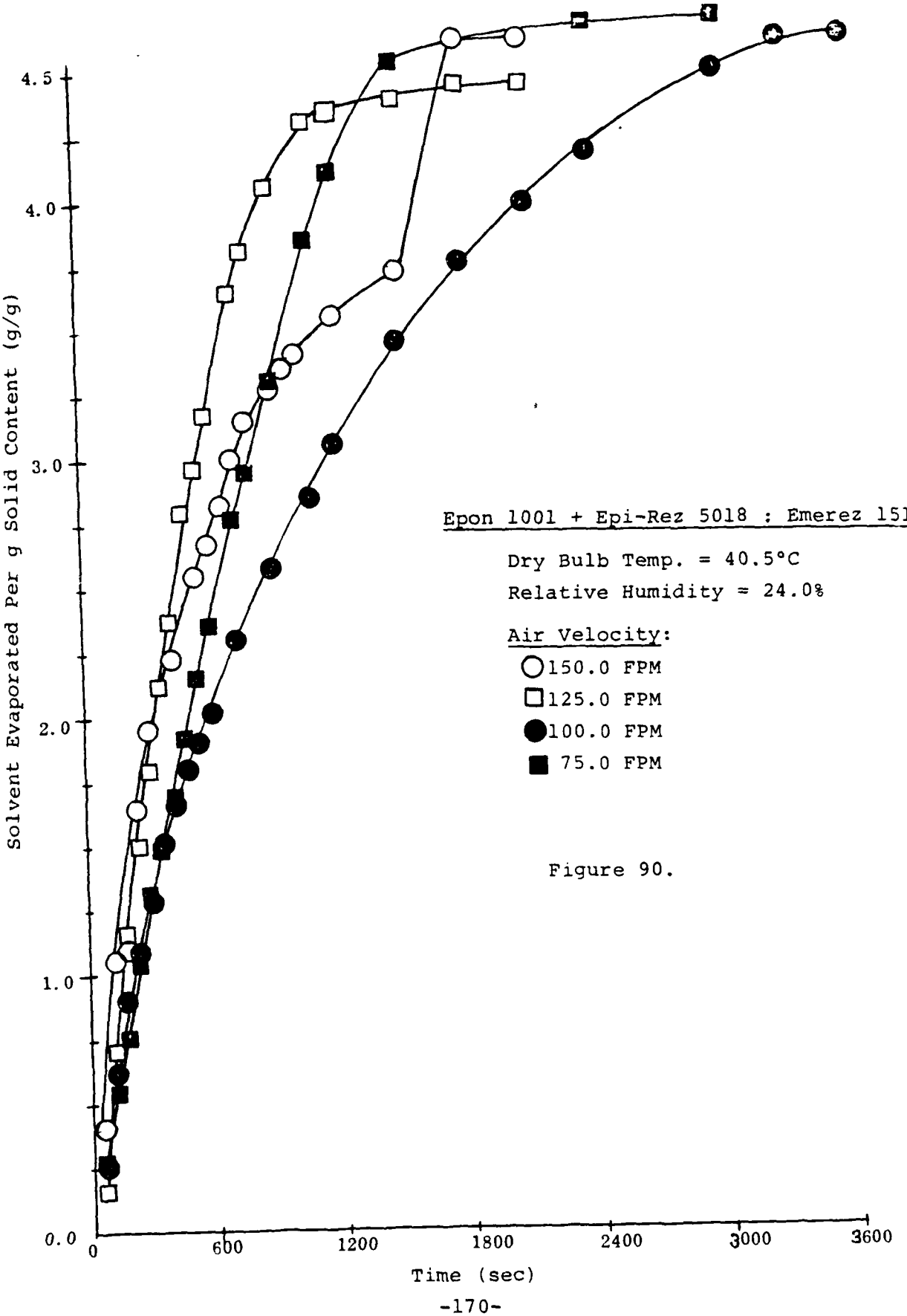

Epon 1001 + Epi-Rez 5018 : Emerez 1511

Dry Bulb Temp. = 40.5°C

Relative Humidity = 24.0%

Air Velocity:

○ 150.0 FPM

□ 125.0 FPM

● 100.0 FPM

■ 75.0 FPM

Figure 90.

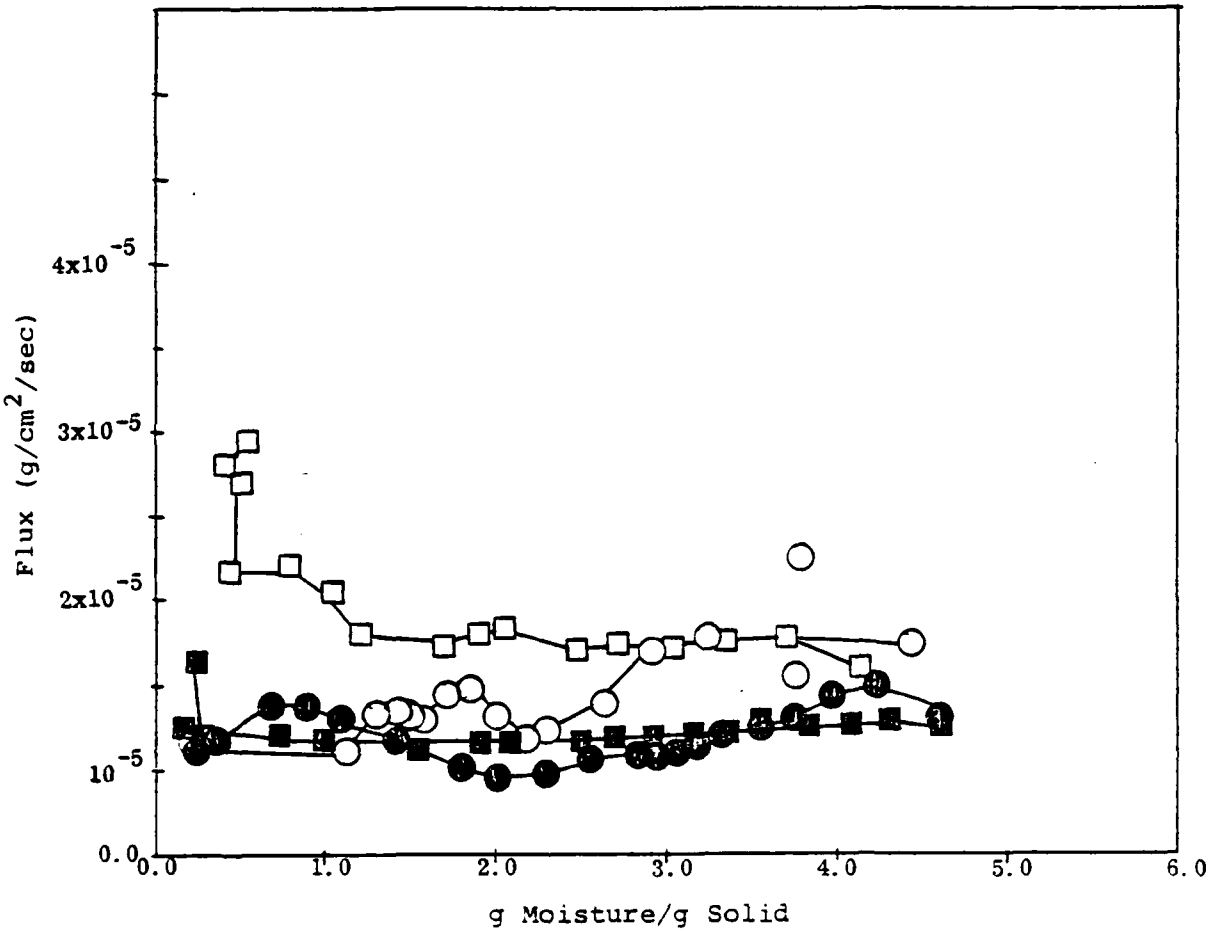

Epon 1001 + Epi-Rez 5018 : Emerez 1511 (Latex)

Dry Bulb Temp. = 40.5°C

Relative Humidity = 24.0%

Air Velocity:

○ 150.0 FPM

□ 125.0 FPM

● 100.0 FPM

■ 75.0 FPM

Figure 91.

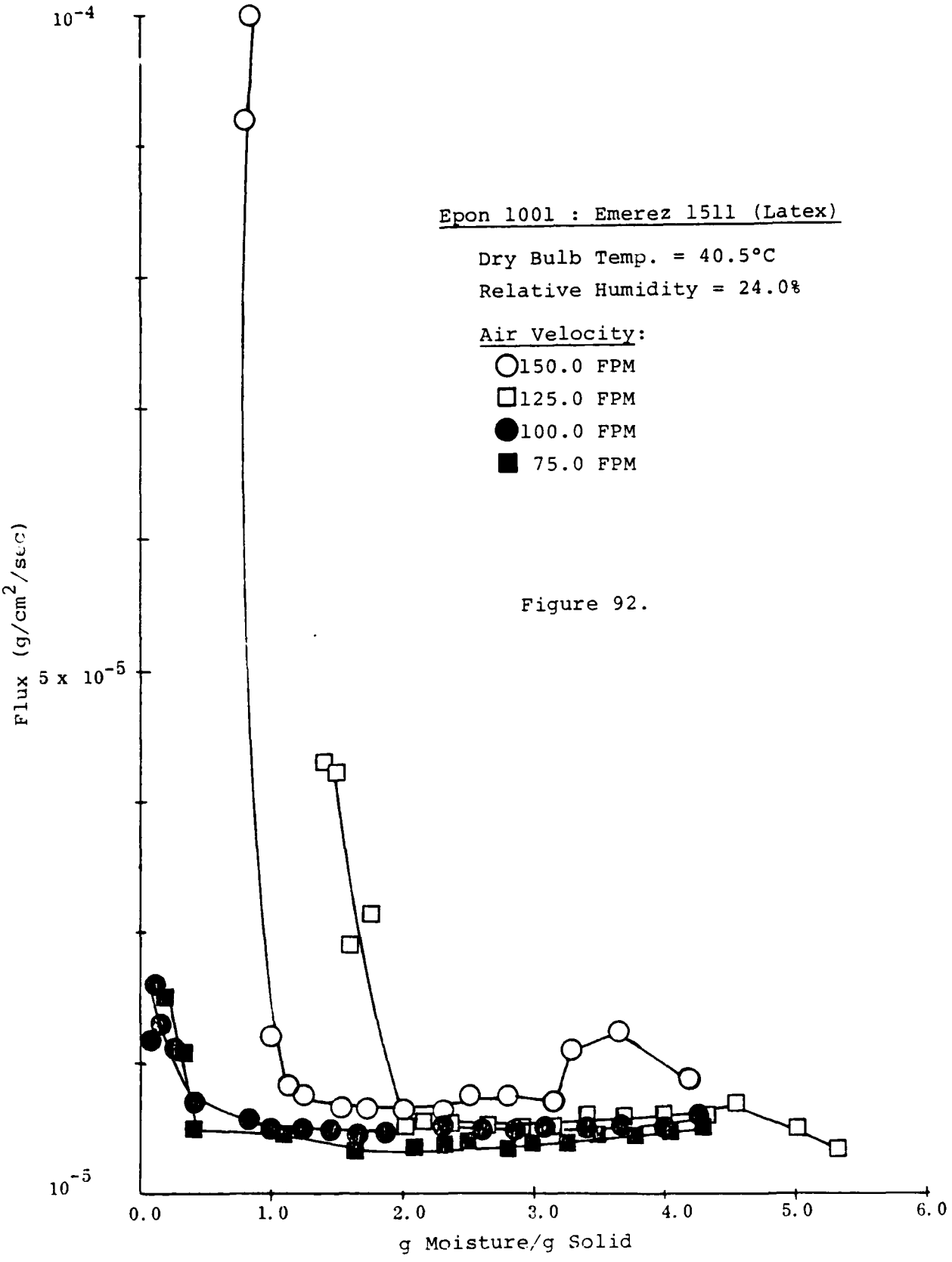
Epon 1001 : Emerez 1511 (Latex)
Dry Bulb Temp. = 40.5°C
Relative Humidity = 24.0%
Air Velocity:
150.0 FPM
125.0 FPM
100.0 FPM
75.0 FPM
Flux (g/cm²/sec)
10⁻⁴
5 x 10⁻⁵
10⁻⁵
0.0
1.0
2.0
3.0
4.0
5.0
6.0
g Moisture/g Solid

Figure 92.

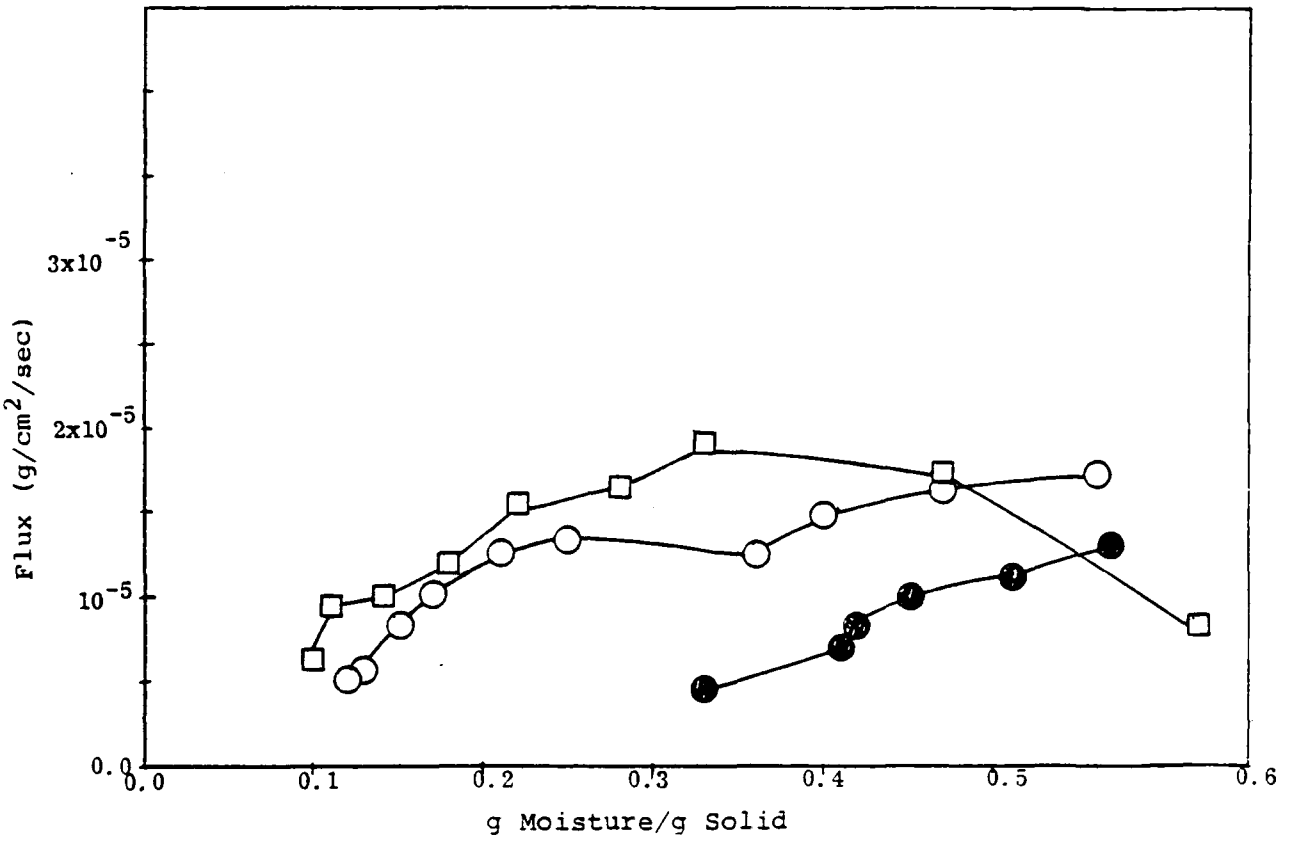

Epon 1001 : Emerez 1511 (Solvent)

Dry Bulb Temp. = 40.5°C

Relative Humidity = 24.0%

Air Velocity:

○ 150.0 FPM

□ 125.0 FPM

● 100.0 FPM

Figure 93.

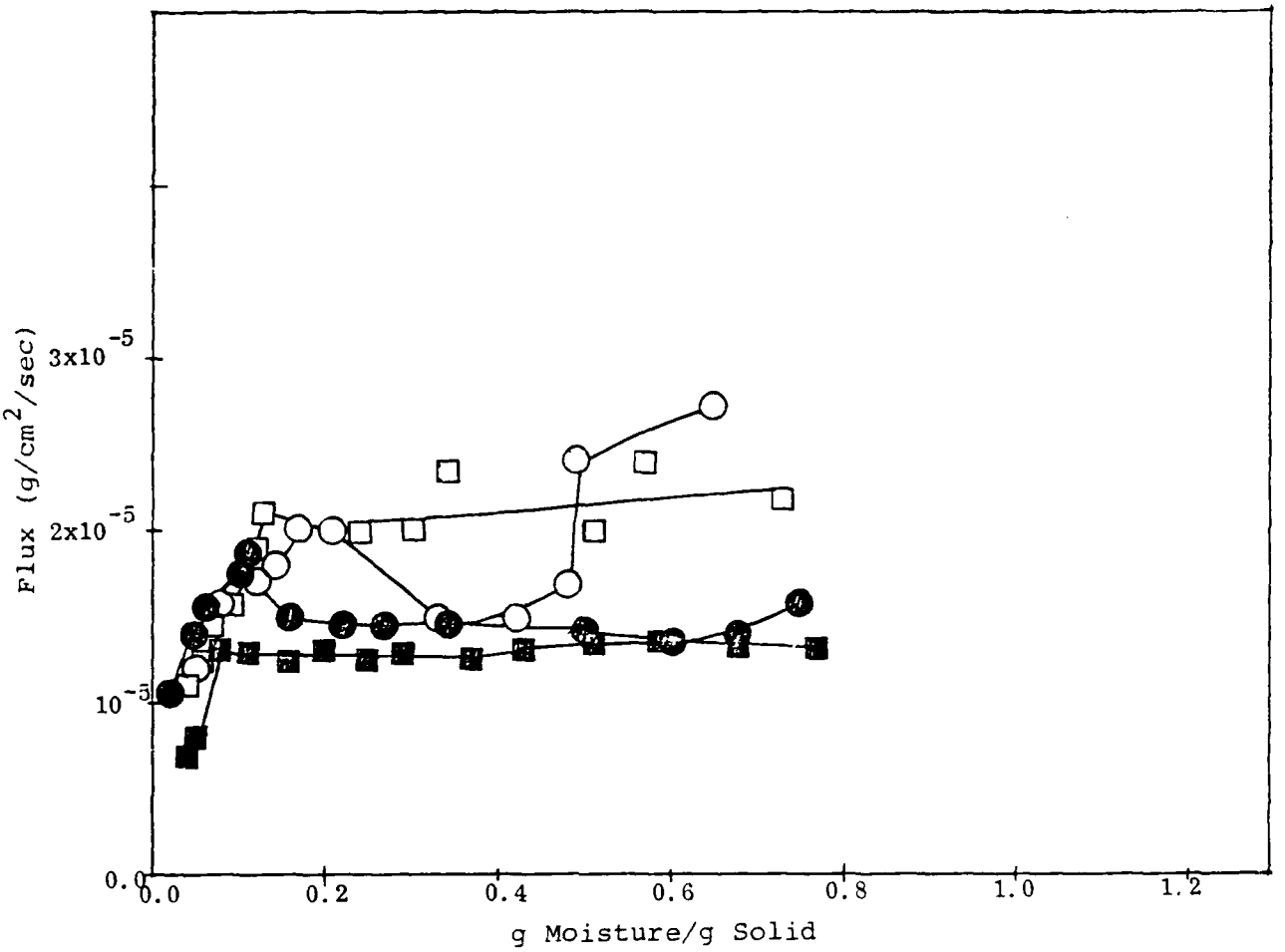

Epi-Rez 510 + Epi-Rez 5018 : W-50-8535

Dry Bulb Temp. = 40.5°C

Relative Humidity = 24.0%

Air Velocity:

○ 150.0 FPM

□ 125.0 FPM

● 100.0 FPM

■ 75.0 FPM

Figure 94.

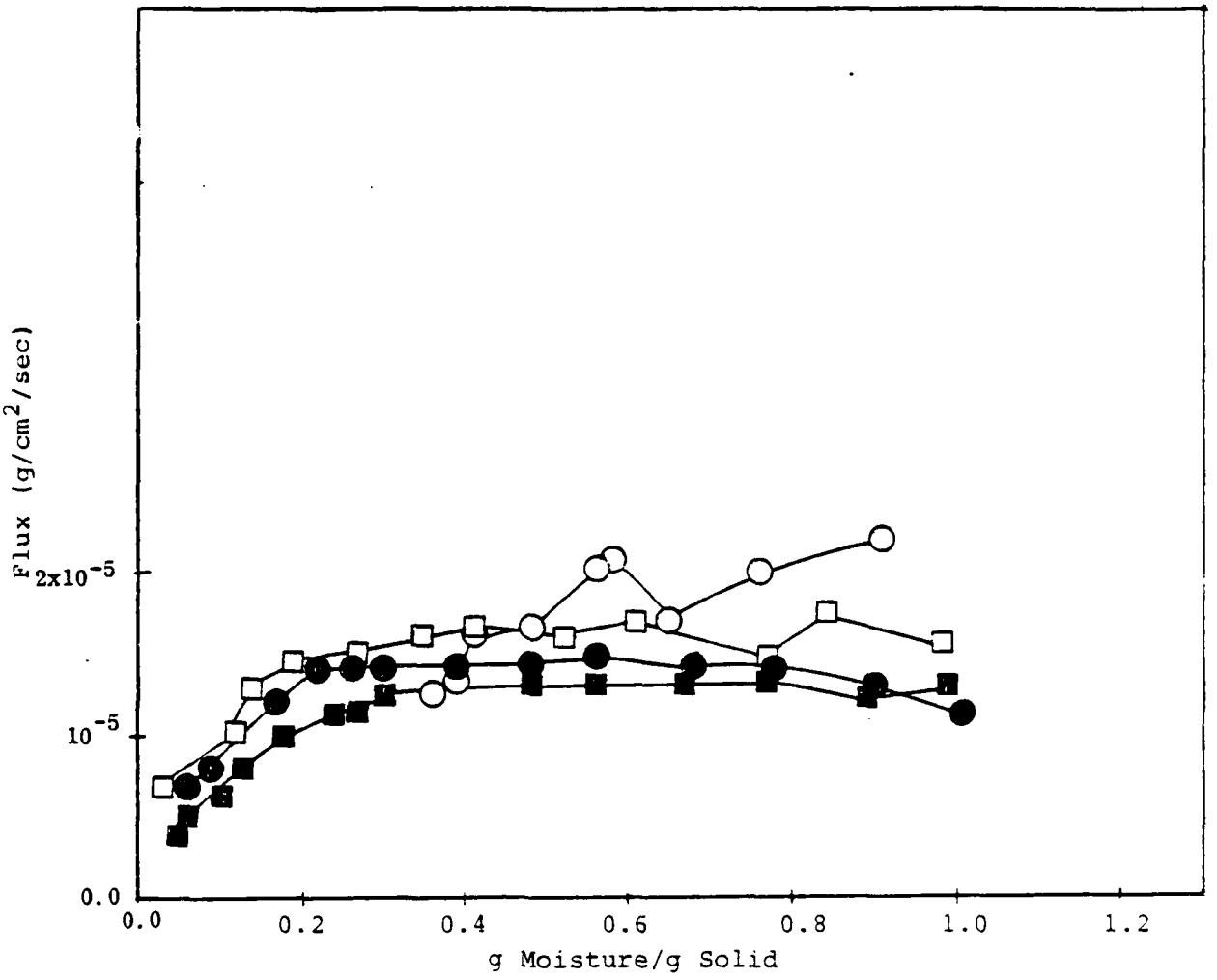

Epi-Rez 510 + Epi-Rez 5018 : WC-60-8537

Dry Bulb Temp. = 40.5°C

Relative Humidity = 24.0%

Air Velocity:

○ 150.0 FPM

□ 125.0 FPM

● 100.0 FPM

■ 75.0 FPM

Figure 95.

appeared to have the effect of increasing the drying rate for all the systems. However, the increase was only marginal over the constant drying rate region when the velocity was varied from 75 ft/min to 150 ft/min. All the drying curves were characterized by a two-stage drying behavior. All exhibited an initial constant drying rate followed by either a falling rate or a rising rate depending on the system. A falling rate was observed for the solvent-based, W-50-8535 and WC-60-8537 systems. However, the two latex mixtures seemed to give a rising rate instead. The rate rose fairly steeply under higher air velocities conditions. The effect was especially pronounced for the Epon 1001: Emerez 1511 latex mixtures.

Conclusion

From the results obtained so far, it is clear that distinct drying behavior exists between a latex system and the conventional solvent-based system. The usual falling drying rate was observed after the constant rate region for the solvent-based system. However, a rising rate was noted for the latex systems. The aqueous-based solubilized polymer resin systems seem to have drying behavior intermediate between these two extreme cases.

Appendix

Description and Specifications of the Epoxy Resins Used in This Report Along with Two Clear Coating Formulations Using Them

Epon 1001 is one of Shell Chemical Company's solid epoxy resins prepared from Bis-Phenol A and epichlorohydrin. It is one of the lowest molecular weight and melting point grades of "solid" epoxy resins. The specifications are:

Melting Point	65-75°C (Durrans' mercury method)
Color	4 max (40% in Butyl Carbitol)
Viscosity (Gardner Holdt)	D-G (40% in Butyl Carbitol)
Viscosity (Stokes)	1-1.65 (40% in Butyl Carbitol)
Epoxide Equivalent	450-550*

* g of resin with one epoxide equivalent

Note: Shell has changed their manufacturing processes to make all solid epoxy resins from the liquid Epoxy Resin 828. (185-192 Epoxide equivalent) and Bis-Phenol A. Their new nomenclature for Epon 1001 is now 1001-F; Shell has provided Lehigh with a 5-gallon sample for our research.

Emerez 1511 is a proprietary, Polyamide manufactured by Emery Industries. It is prepared from dimer acids and a diamine (probably ethylene diamine) in proportions so as to give the following properties which are equivalent to General Mills' (Henkel's) Versamid 115:

$HClO_4$ Amine Value	230-246
Calculated Equivalent Wt.	244-228 (235.7 midpoint)
Viscosity	31-38 Poise
Color-Gardner (ASTM)	9 max
% Solids	100

Epi-Rez 510 is the Celanese equivalent of Shell's liquid epoxy resin Epon 828. Its specifications are as follows:

Weight per Epoxide	180-195 (190 nominal)
Viscosity	10,000-16,000 cps

Epi-Rez 510 Cont'd.

Wt/gal	9.57-9.73 lbs
Color (Gardner)	3 max
Hydrolyzable chlorine	0.1 max

Epi-Rez 5018 (Celanese Plastics & Specialties Co.)

Is a low viscosity reactive diluent used in conjunction with Epi-Rez 510. It is described as a monoglycidyl ether containing alkyl chains which are predominantly C12-C14 in length; the wt per Epoxide is 286.

Epi-Cure W-50-8535 (Celanese P.&S. Co.)

Is a modified polyamido-amine curing agent supplied at 50% solids. It is used along with a volume ratio of 75:25 Epi-Rez 510 & Epi-Rez 5018 in a suggested formula (24-174) for a clear epoxy coating. Its properties are as follows:

Viscosity (Gardner-Holdt)	Z_5-Z_6
Viscosity (Stokes)	100-160
% Solids	50
Wt/gal	8.74
Wt/gal (Solids)	9.19
Color ASTM	12
Volatile Portion	Water
Equivalent weight (solids)	102

Epi-Cure WC-60-8537 (Celanese P.&S. Co.)

In an epoxy resin-amine adduct supplied at 60% solids in 49% H_2O, 38% ethylene glycol monoethyl ether and 13% glacial acetic acid. Like Epi-Cure W-50-8535, it is also recommended for use along with a 70:30 volume ratio of Epi-Rez 510 and Epi-Rez 5018 in a suggested clear coating formula (24-180). Its properties are as follows:

Viscosity (Gardner-Holdt)	Z_2-Z_3	
Viscosity (Stokes)	35-48	
% Solids	60%	49% H_2O 38% Cellosolve (EGMEE) 13% Acetic Acid
% Solvent	40%	
Wt/gal	9.04	

Epi-Cure WC-60-8537 Cont'd.

Wt/gal (Solids)	9.75
Equivalent Wt.	174

SECTION 8

Objective: To Obtain Morphological Information about Polymer Coatings to Complement Electrical and Physical Property Data

Title: Electron Optical Studies of Polymeric Coatings

Senior Investigator: David A. Thomas

Associate: Yale West
Graduate Student

Introduction

Indications exist that there is a relationship between inhomogeneities of a polymer film and the quality of corrosion control. It is believed that inhomogeneities in the structure may serve as paths for the permeation of corrodents in the initiation and continuation of corrosion.

Considerable evidence exists that epoxies, of initial interest in this program, have a primary morphology consisting of particles or microgels on the order of 10 nm in size. These particles are formed during the initial stages of polymerization and interconnect later to form larger network entities. Eventually they aggregate to form macrogel particles exceeding 10 μm in size. Two types of network structure have been observed or inferred: regions of high crosslink density embedded in a low crosslink density matrix, or low crosslink density regions embedded in a high crosslink density matrix. These are some of the inhomogeneities that may play a role in corrosion but others may occur as well, extending to the holes or defects known to coatings practitioners as "holidays".

Experimental

Epoxy samples were prepared from Epon 1001-F (solid, Shell Chemical) and Versamid 115 polyamide (General Mills). The ratio of epoxy to polyamide varied from .8 to 2.0. The epoxy was dissolved in methyl isobutyl ketone (MIBK), and the polyamide was dissolved in xylenes. Methanol was the mutual solvent. Non-filled, zinc-filled (8 μm av. diameter, prepared by M. Heffelfinger), and glass-bead-filled (40 μm av. diameter) systems were prepared.

The filled systems were observed under the Scanning Electron Microscope (SEM), and it was found that the fillers were evenly dispersed throughout the epoxy. Also the fracture surfaces showed that the epoxy encased the filler particles but was not bonded to the surface. This was true for both the zinc and glass-bead-filled system (see Figures 96 and 97).

For the glass-bead-filled system, the glass beads were added at various times relative to the curing of the epoxy. At four or more hr after mixing, the SEM showed that there were regions where the filler was excluded. There are factors to be considered in order to understand this observation. First, an increase in viscosity due to the loss of solvents through evaporation may have led to an inability of the epoxy-polyamide solution to wet the filler particles, thus excluding them from the epoxy matrix. Second, the onset of polymerization may have contributed to the exclusion of the glass beads, due to the development of cross-

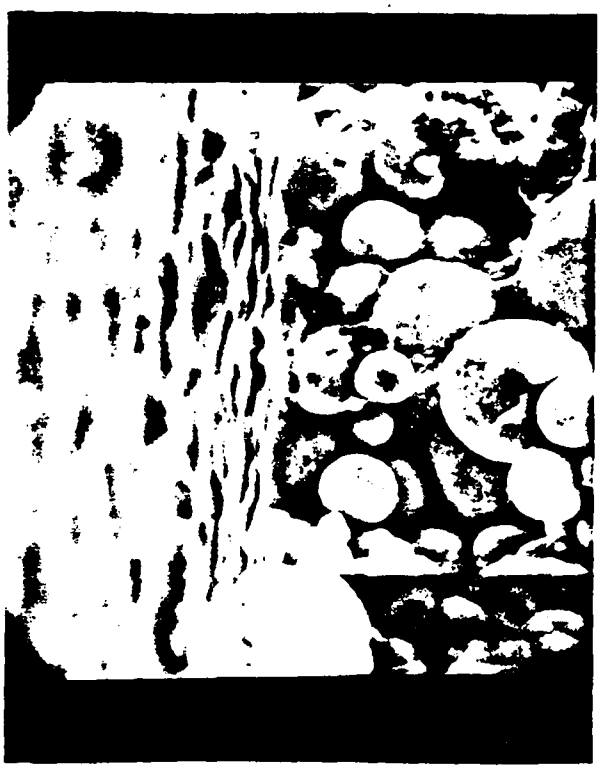

Figure 96. Zinc particles (93% by weight) dispersed in epoxy. X3000

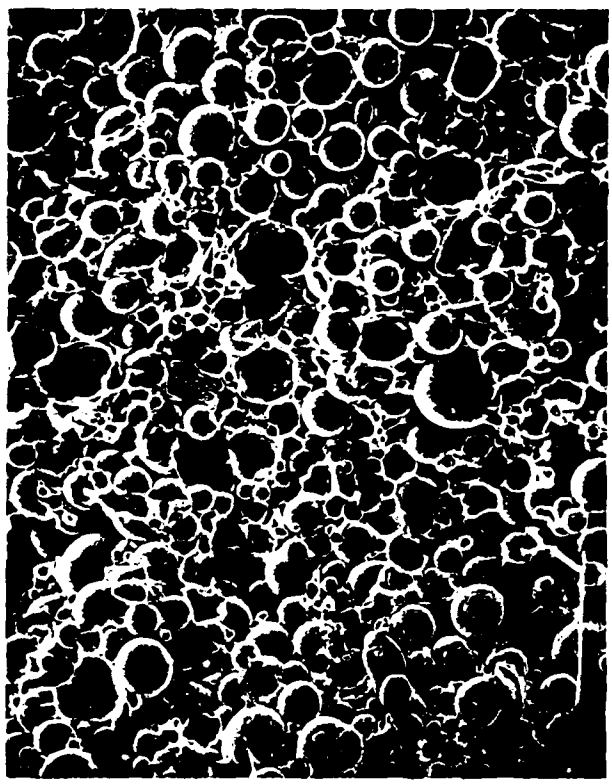

Figure 97. Glass beads (82% by weight) dispersed in epoxy. X800

linked regions. These regions may have served as physical barriers for the filler particles.

The above systems were etched using 1M aqueous solution of H_2CrO_4. In addition to the filled systems, non-filled systems were also etched. The samples were placed in the chromate solution for 24 and 48 hr at room temperature, and for 7 hr at 70°C. This solution preferentially attacks regions of low crosslink density. The SEM showed no appreciable attack by the etching solution on the non-filled system. The surface showed some erosion, but it did not extend into the interior of the bulk epoxy. The zinc and glass-bead-filled systems on the other hand, showed considerable erosion on the surface and in the interior of the sample. It was concluded that there are two possibilities for this observable difference. There may be a difference between the morphology of microstructure of the epoxy in the filled and non-filled systems. Also, there may be a physical difference on the macroscopic level between the filled and non-filled systems. These differences may include channels in the filled systems which may allow transport of the etching solution into the interior of the bulk epoxy. The SEM micrographs showed the epoxy encased the filler particles, but was not bonded to it (see Figures 98 and 99).

Chemically modified systems were also prepared. In one procedure sodium oleate, an eighteen carbon chain with a double bond at the ninth carbon, was added to the epoxy during curing. It was hoped that this long chain sodium salt of oleic acid would aggregate in higher concentrations in low crosslinked regions. Subsequent staining with OsO_4 reveal these high concentration areas. Due to the brittleness which developed as a result of the staining, it has not been possible to make thin sections consistently by ultramichrotomy for Transmission Electron Microscopy (TEM). There were sections which seemed thin enough (less than 1000 Å) for TEM observation. At 100,000X magnification there appeared in samples, where the sodium oleate was added four hr after the onset of cure, the existence of nodular regions. For the samples where the sodium oleate was added immediately, these nodular regions were not observed. Due to the inconsistency of the thin sections, no conclusion can yet be drawn.

In another procedure, sodium perchlorate was added at different times relative to the curing of the epoxy. The samples were then studied under the SEM-EDS (Energy Dispersive Spectrometry, for the detection and analysis of X-rays). An attempt was made to determine the presence of Na or Cl throughout the sample, possibly in varying degrees of concentration, as an indication of differences in crosslink density, a higher concentration of Na or Cl to be found in the regions of lower crosslink density. To date we have obtained X-ray signals for both Na and Cl, and it appears that there are concentration differences.

Collaborative work with Prof. Leidheiser concerning ion permeation into the polymer film has been initiated. It has been

Figure 98. Non-filled epoxy after etching at 70°C for 7 hr. X300

Figure 99a. Zinc-filled epoxy, etched for 7 hr at 70°C. X600

Figure 99b. Glass-bead-filled epoxy, etched for 7 hr at 70°C. X600

shown in cathodic delamination experiments of epoxy on steel, that CsCl solutions give the most rapid delamination. Samples of epoxy were immersed in 1M aqueous solution of CsCl. Using SEM-EDS analysis, CsCl was observed not to permeate into the epoxy in any significant concentration.

At this time samples of delaminated film, which were prepared by Wendy Wang, have been subjected to SEM-EDS analysis. These samples have been delaminated in solutions of LiCl, NaCl, KCl, and CsCl. The concentration of Cl ion has been found to be considerably higher than that of the metal ion in the KCl and CsCl samples. Li and Na were not detectable due to the limitations of the instrument. The concentration of Cl is much too low to determine any regional variations in concentrations.

The suitability of electron optical methods in support of other parts of the program has been shown. The determination of epoxy morphology and its relationship to the corrosion process has been difficult. This effort will continue, but some of the emphasis will be shifted to locating inhomogeneities in the polymer film by chemical or electrochemical corrosion. Detailed characterization by electron optical and microanalytical methods will be carried out.

SECTION 9

Objective: To Relate the Mechanical and Transport Properties of a Zinc-Filled Epoxy-Polyamide Coating in Terms of Structure, Composition and Morphology

Title: The Properties of Zinc-Filled Epoxy-Polyamide Coatings

Senior Investigator: John Manson

Associate: Michael Heffelfinger, Graduate Student

Introduction

It is well known that many properties of polymers are significantly changed by the incorporation of a second phase such as a filler or pigment (44,45). The value of a property such as modulus, tensile strength, ultimate elongation, or permeability depends not only on the values of the constituents (and on their volume fractions) but also on the degree of interfacial adhesion.

Often the observed mechanical properties fall between bounds defined for the limiting cases of good and poor adhesion. With a typical case of good adhesion, Young's modulus of a polymer containing high-modulus fillers is invariably increased but the ultimate elongation and strength tend to be decreased (46). With poor adhesion, Young's modulus and tensile strength are usually decreased significantly; the impact strength and ultimate elongation also decrease, though less than with good adhesion. Thus one must consider the balancing of effects due to the presence of high-modulus inclusions (44-46).

Although the precise mechanisms are not always known, it is often possible to alter the balance of properties just mentioned and to improve the tensile and impact strengths. Indeed many coupling agents have been developed to enhance the overall behavior of composite systems. In some cases, it is possible to get high modulus and high strength simultaneously (45). A key factor may well be the development of a tough or ductile interface or "interphase" (47), which can delay the onset of fracture.

One recent approach to the improvement of properties in filled systems has been to encourage acid-base interactions at the interface (48,49). (A limiting case is exemplified by the family of ionomers, in which toughness is conferred by the dissipation of high levels of energy during the deformation of ionic groups.) This approach also is consistent with many experimental findings. For example, the acid treatment of aluminum has long been known to enhance the bonding to base-catalyzed epoxies, and acidic and basic fillers in plastics and elastomers have been found to give optimum mechanical properties when coupled with basic and acidic polymers, respectively (48-50). Indeed, the quality of protective coatings (in terms of gloss and dispersion) has been shown to be quantitatively related to the acid-base interaction between the pigment and the binder (51). Finally, some of the earlier evidence for the beneficial effects of coupling agents has been successfully interpreted in similar terms (52).

The effects of inclusions such as fillers and pigments on mechanical behavior can be characterized conveniently by the use of stress-strain and dynamic mechanical spectra (DMS) measurements (44-46,52-54). The former yields directly values of

elongation at break tensile strength, modulus, and also evidence of debonding at the particle-matrix interfaces. The latter yields values of storage and loss modulus as a function of temperature and frequency, and values of the glass transition temperature (and other transitions as well), which is important in defining the state of a coating (52-54). The loss modulus (or damping) is also often sensitive to the nature of the interface (44,45). Both stress-strain and DMS measurements are sensitive to changes induced by water absorption or degradation during service. Fracture modes are also important in determining serviceability, and are similarly sensitive to environmental conditions (45,55).

It is important to know and understand the nature of the surface of zinc dust. Namely, dynamic properties, electron microscopy, and permeation are all directly related to the effectiveness of surface polymer attraction forces. Thus, the acidic or basic nature of the surface of zinc and the extent of adsorption are informative parameters essential for basic understanding of some of the unique forces involved in this chosen system. The polymers and solvent chosen were based on research done by Fowkes and Mostafa (4). The basis for the specific interactions mentioned are that dipole-dipole interactions between polar polymers and polar adsorbents appear to be negligibly small compared to dispersion forces and acid-base interactions. In other words, when two polar acidic compounds or two polar basic compounds are mixed, there is little interaction in excess of the dispersion force interaction. The Drago correlation is used since it treats interactions as due only to dispersion forces and acid-base interactions. It was found that negligible adsorption occurs unless there is an acid-base interaction between the polymer and filler surface. Acidic or basic solvents tend to compete for polymer or the filler and if the solvents are acidic or basic enough, no adsorption will occur. The effects on corrosion problems is also important. Namely, enhanced adhesion of the polymer matrix to pigment particles can insure complete coating and separation of particles, thus eliminating particle-to-particle pathways for diffusion of corrosive media or of electric current carriers through the paint or enamel. Enhanced adhesion of polymer coatings to the oxide surface of metals can minimize access of corrosive media to the metal surfaces.

It is under these situations that the following system was chosen to determine if zinc dust is acidic. The filler is zinc dust, poly(methylmethacrylate) PMMA was the polymer chosen with basic ester groups, and a neutral solvent of CCl_4 was used. This is a neutral solvent for this polymer because the heat of acid-base interactions is zero. This system produces the strongest adsorption onto an acidic filler. The system chosen to determine if the filler is basic is the filler (zinc dust), acidic electron acceptor capabilities of post-chlorinated PVC, and the weakly acidic solvent such as CH_2Cl_2. This solvent was chosen because it will allow stronger adsorption of Cl-PVC into basic fillers.

AD-A095 420 LEHIGH UNIV BETHLEHEM PA CENTER FOR SURFACE AND COA--ETC F/G 11/3
CORROSION CONTROL THROUGH A BETTER UNDERSTANDING OF THE METALLI--ETC(U)
DEC 80 H LEIDHEISER, M S EL-AASSER N00014-79-C-0731

UNCLASSIFIED NL

3 OF 3
AD A095 420

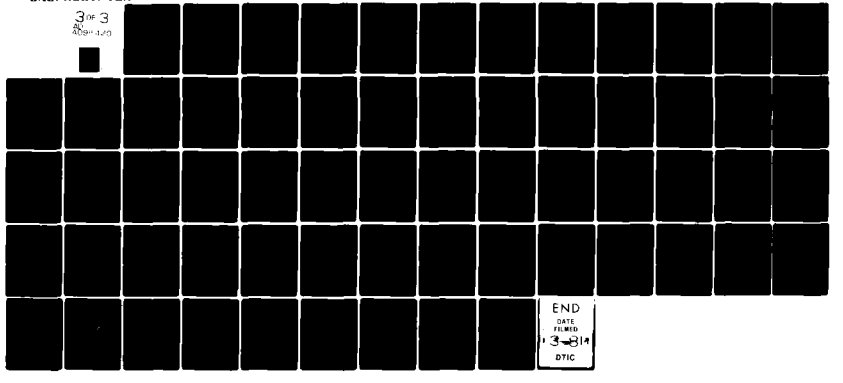

END
DATE FILMED
3-81
DTIC

Table XV

Results from Adsorption Study of PMMA/CCl_4/Zinc Dust

Concentration (g/dl)	Adsorption (mg/g)
0.520	0.9845
1.78	0.6906
2.15	1.434
2.79	1.675

Table XVI

Results from Adsorption Study of Cl-PVC/CH_2Cl_2/Zinc Dust

Concentration (g/dl)	Adsorption (mg/g)
0.494	0
1.852	0
1.930	0
2.70	0

Further research in this area was completed by Williams and Manson (55a).

As a first step in this long range program, measurements have been made to characterize the surface properties of zinc powder and the properties of zinc-filled epoxy-polyamide coatings.

Adsorption of Model Polymers

Zinc Dust (Horse Head) Standard #22 New Jersey Zinc

Cl-PVC (High Temp. Geon) B. F. Goodrich

PMMA DuPont Lucite 4F

A weight of approximately 15 g of zinc dust was used for all cases. This weight corresponds to values used by Fowkes and Mostafa (4). Specific surface area was estimated at 1.05×10^{5} m^2/g. A weight of only approximately 0.0054 g is necessary. Thus enough filler is used to completely adsorb all polymer if possible. Solution concentration of PMMA/CCl_4 of 0.52, 1.78, 2.15 and 2.79 g/dl were made and verified using blank solution techniques. Also, solution concentrations of Cl-PVC/CH_2 Cl_2 of 0.494, 1.852, 1.930, and 2.70 g/dl were made and verified. A weighed amount of solution was then added and allowed to equilibrate with a known amount of zinc dust for approximately 15 min. This time was sufficient for existence on the level portion of the isotherm.

Case Study of Adsorption on Zinc

Since we are using a Versamid and an Epon with a selected solvent system with zinc, it is also interesting to see if this system has significant adsorption onto zinc while in a solvent suspension before solvent incorporation. It was found that Epon only went into solution with xylene in the presence of 0.21%(V/V) methyl isobutyl ketone. The Versamid went into solution easily with pure xylene.

Procedure: A weight of approximately 15 g of zinc dust was used for all cases as before. Solution concentrations of Epon/Xylene (MIBK) of 0.5, 0.948, 1.82 and 2.15 g/dl were made. Also, solution concentrations of Versamid/Xylene of 0.54, 0.936, 1.796, and 2.258 g/dl were made and verified. A weighed amount of solution was then added to a known amount of zinc dust for approximately 15 min.

It is evident that Zinc Dust #22 has clearly an acidic surface since PMMA adsorbed onto the surface from a neutral solvent (see Table XV). Also, there are not any appreciable basic sites (see Table XVI). It is worth noting that PMMA adsorbed onto

Fe_2O_3 with a value of ≈80 mg/g for the same polymer solvent system (56). Thus, the surface although acidic is probably well classified as a weak acidic surface since the same value of zinc is ≈ 1.7 mg/g. It is also worth noting that there is no significant adsorption of Versamid or Epon from solution onto zinc (Tables XVII and XVIII). It is important from the point of view that there is definite solvent competition for the acid sites on zinc. A good mixture of Versamid and Epon is available for reaction. The final dried coating results in some residual solvent, some unbonded zinc spheres, and some well attached polymer around the spheres. This polymer is either unreacted Versamid or reacted Epon and Versamid around the spheres. Finally, these results of solvent competition while the polymer is suspended are also pointed out in Lipatov (57).

Drying Versus Time Study on Solvent Loss from Samples

Problems of solvent retention in coating films has been experienced in many applications. It is of fundamental importance to understand how far each sample film approaches the theoretical solvent content at different temperatures and pressures. As each film was prepared, some of the mix was added to at least three pans for drying studies and the rest was cast for further studies.

Solvent retention may cause some adverse effects on film properties such as hardness and water resistance. Furthermore, two-dimensional stresses are produced as a result of the volume shrinkage as the coating is drying (58). It has furthermore been seen for years that in certain cases 15% of the original solvents used still remain in the coating even when dry to the touch. However, it is reasonable to expect that different polymers retain solvents to different extents with different multicomponent mixtures of solvent systems (59).

It has been possible to interpret or even qualitatively predict the extent of solvent retention. The theory is a two-stage solvent release mechanism theory originally proposed by Hansen (60-64). The escape of solvent molecules from polymeric films occurs in two successive stages. When a polymer solution is applied as a film, solvent is at first lost rapidly, but when its concentration in the polymer has decreased to a certain level, the rate of release is dramatically reduced. The escape of solvent appears to occur in two distinct stages denoted by the "wet" and "dry" stages. The "wet" stage is mostly governed by the rate of escape of the solvent molecules from the surface of the applied film. As the evaporation proceeds, the remaining polymer film becomes less flexible, a solvent concentration gradient is set up within the film, and at a certain residual solvent content, the rate of release of solvent is governed by the rate of transport of the solvent molecules to the surface. The rate governing mechanism thus changes from a boundary-layer phenomenon to a diffusion process. This phenomenon is described further by Yoshida (65).

Table XVII

Results from Adsorption Study of Epon/Xylene(MIBK)/Zinc Dust

Concentration (g/dl)	Adsorption (mg/g)
0.50	0.5600
0.948	0.7796
1.82	0
2.15	0

Table XVIII

Results from Adsorption Study of Versamid/Xylene/Zinc Dust

Concentration (g/dl)	Adsorption (mg/g)
0.54	0
0.963	0
1.796	0
2.258	0

It is of future significance to study the effects of different solvent systems. It is known that defects within the films can occur when the solvent is lost rapidly from a film. The particular defect is called cellular convection. These can cause pigment separation. It is during this stage that physical forces between pigment and matrix can be altered (66).

It is of interest to comment that another mechanism may be in effect here using an epoxy system of Versamid 115 and Epon 1001. Namely, the mechanism of curing will certainly affect the rate of solvent loss from the coating film. There is a "wet" stage where the polymer is well suspended in solution. It is during this stage that reaction occurs and solvent loss occurs. As the reaction proceeds and solvent loss occurs, the film becomes more rigid. If curing proceeds faster than solvent loss, it is possible to conceptualize the notion of trapped solvent and hence some more residual solvent remains. This is compared to a slow cure process at a different temperature where solvent is easily lost. Finally, it is worth mentioning that in cases where solvent is trapped, a dynamic test will certainly produce voids for solvent release and hence there will be solvent release and some additional curing as the test proceeds.

The formulations used are described in a General Mills publication (67).

Emery Liquid Polyamide (EMEREZ 1511) 12/19/79

Shell Epon 1001-F 12/19/79

Ferrophos Enhancer (Hooker Chemicals & Plastics Corp.)

Four pans are filled with a film composition as specified and allowed to set for approximately two days. This is necessary when using vacuum since the samples will boil otherwise. The samples are placed in the appropriate controlled atmosphere at a certain constant temperature and removed to weigh at select times. Experimental results are summarized in Figures 97-104 and in Table XIX.

It is evident that there are some interesting conclusions regarding the drying rate curves vs film type study. It is logical to think that a 25°C sample should dry slower than a 90°C sample. However, there was a strange reproducible inversion of this trend in one case. When the Epon/Versamid was 1.30, the following conclusions are possible (Table XIX).

1. The 93% FILLER (50/50 (Zn/Ferrophos) experienced a more rapid solvent loss compared to the 93% zinc-filled system.

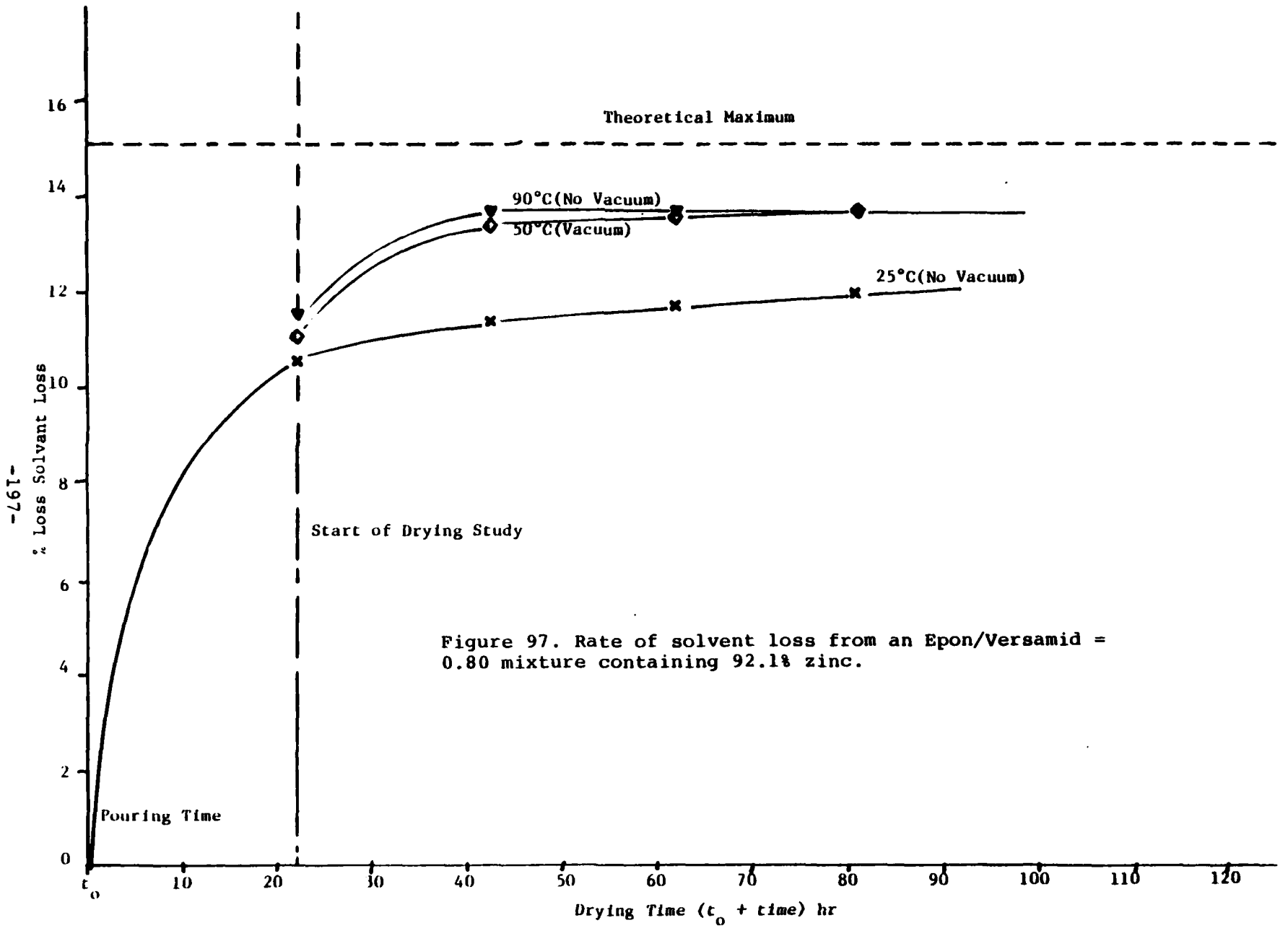

Figure 97. Rate of solvent loss from an Epon/Versamid = 0.80 mixture containing 92.1% zinc.

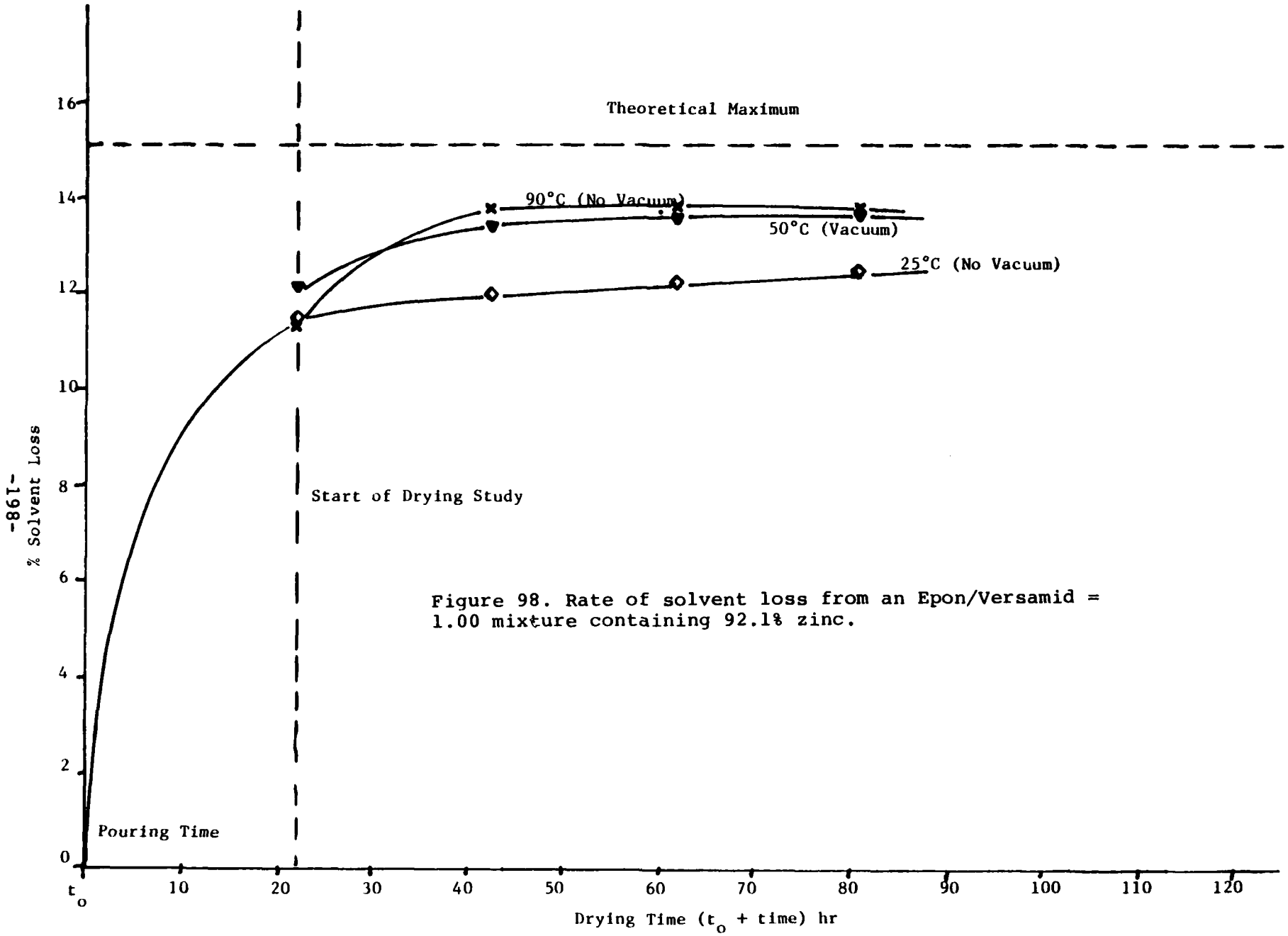

Figure 98. Rate of solvent loss from an Epon/Versamid = 1.00 mixture containing 92.1% zinc.

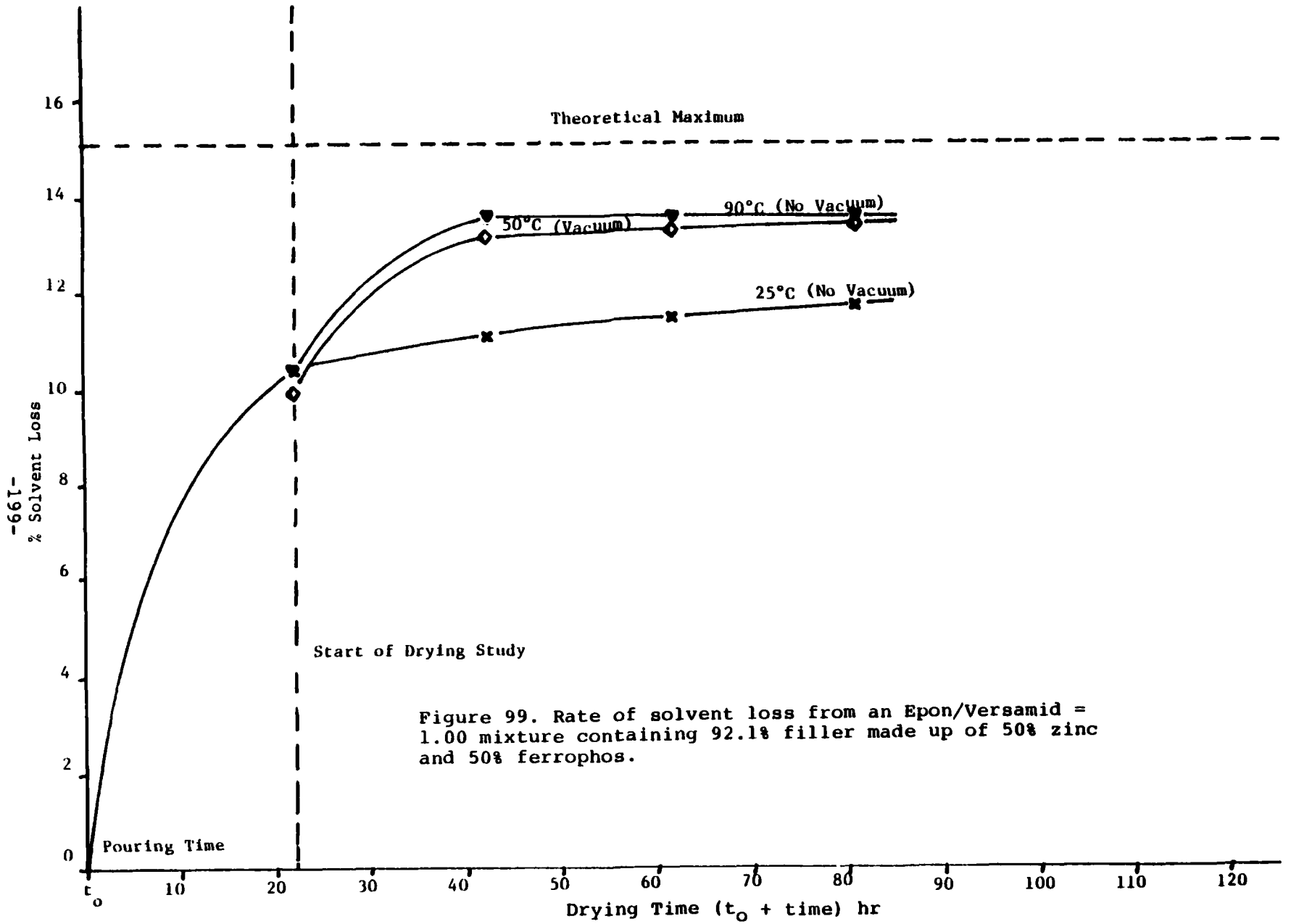

Figure 99. Rate of solvent loss from an Epon/Versamid = 1.00 mixture containing 92.1% filler made up of 50% zinc and 50% ferrophos.

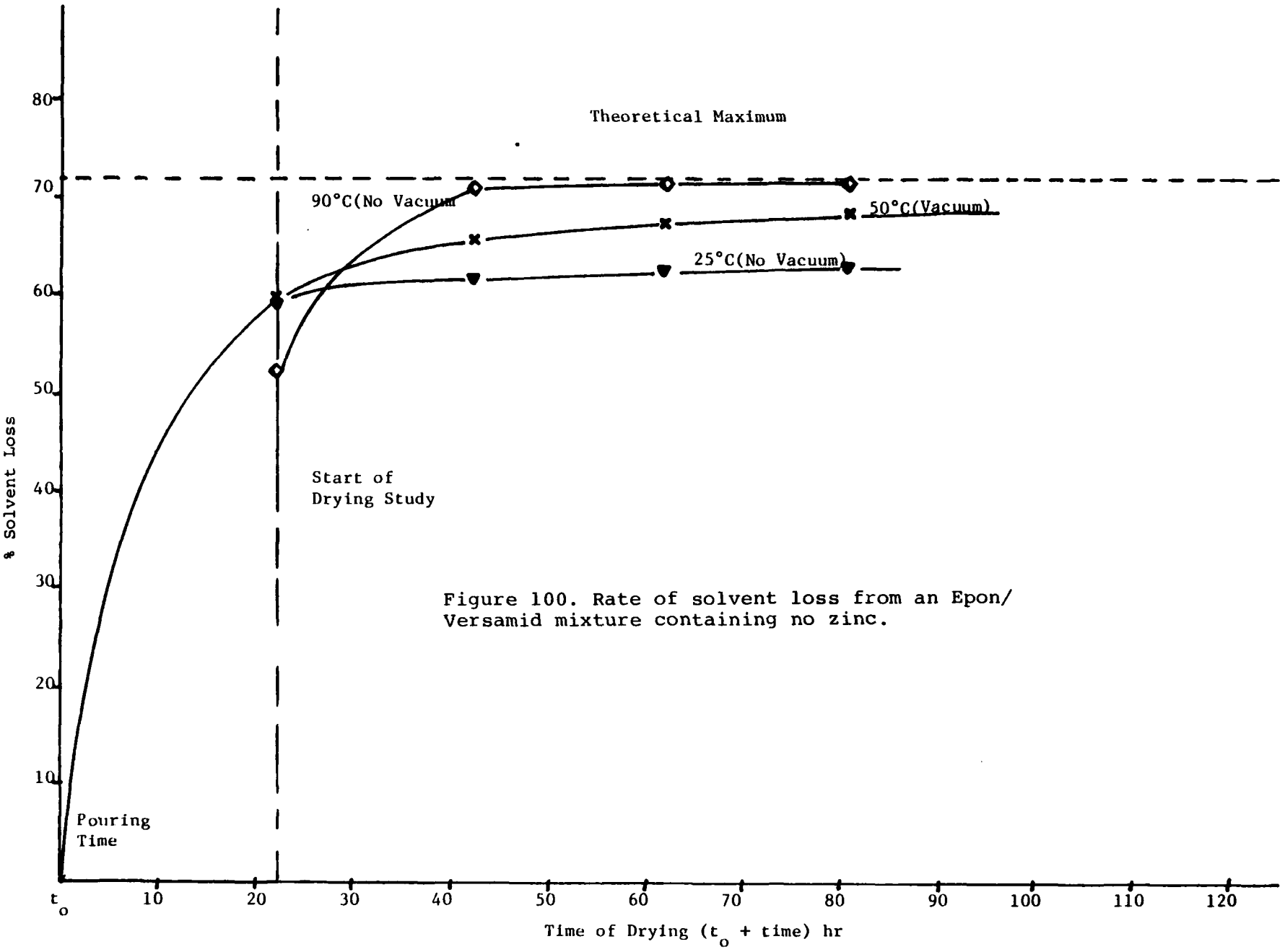

Figure 100. Rate of solvent loss from an Epon/ Versamid mixture containing no zinc.

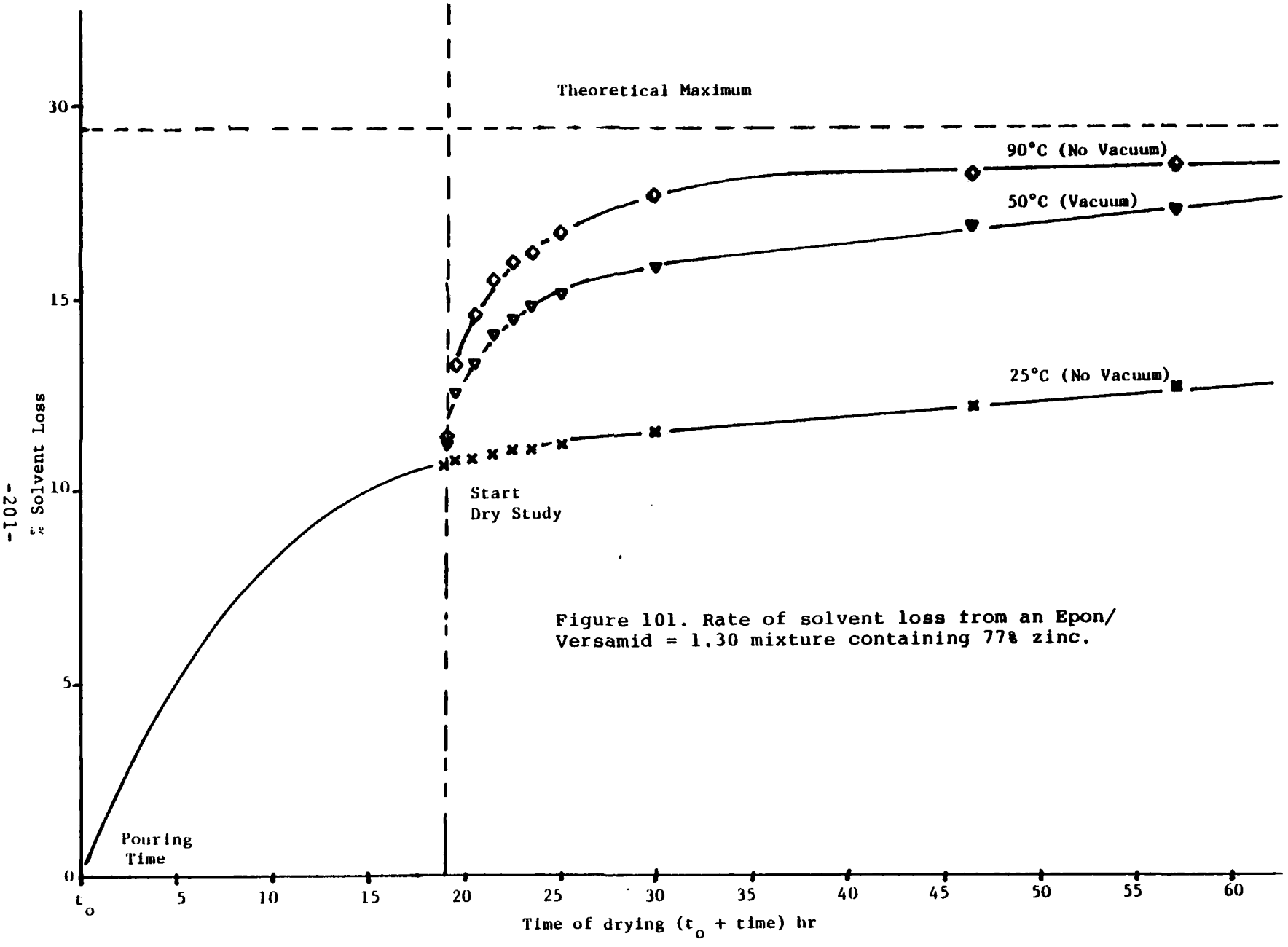

Figure 101. Rate of solvent loss from an Epon/ Versamid = 1.30 mixture containing 77% zinc.

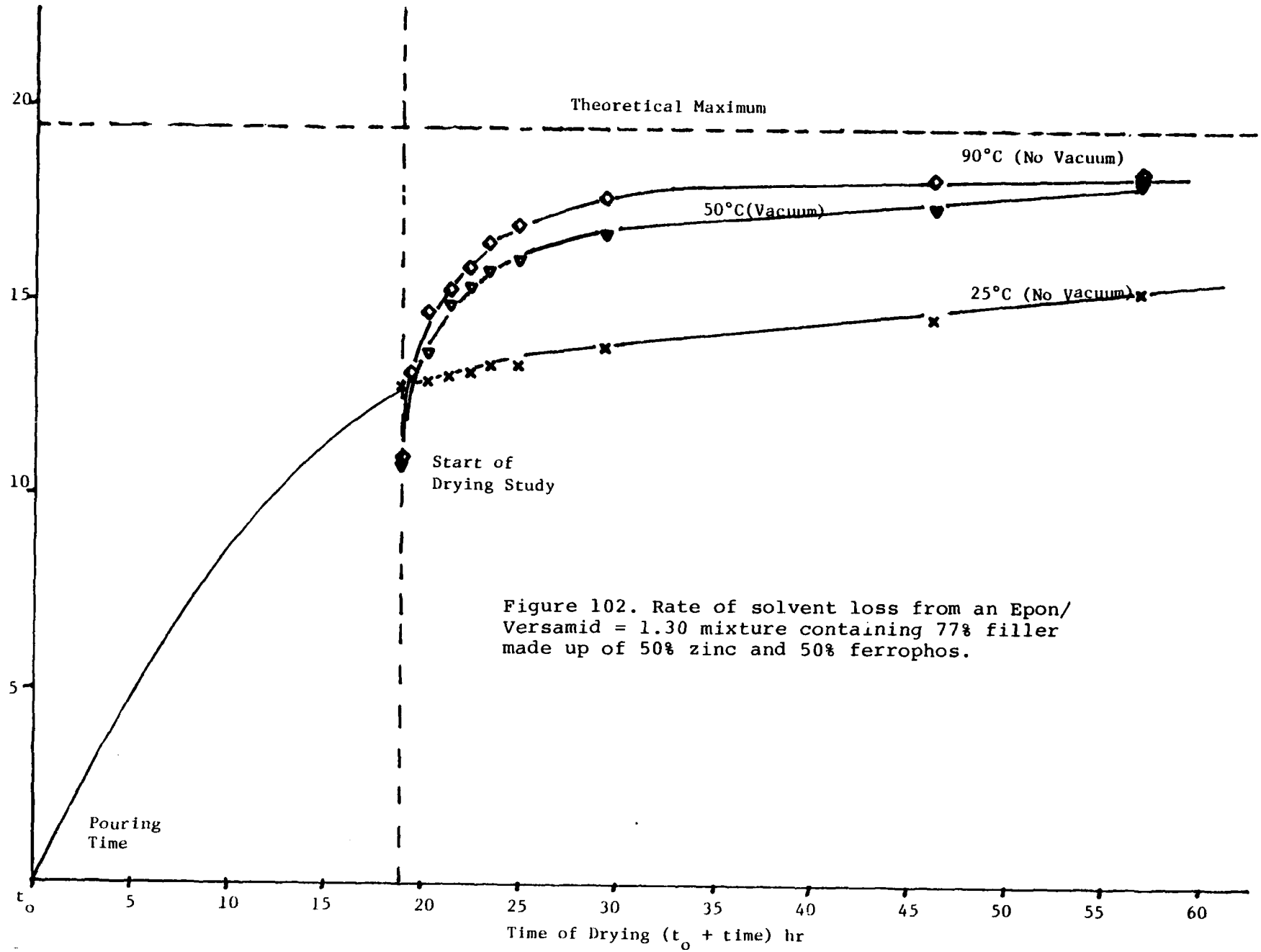

Figure 102. Rate of solvent loss from an Epon/ Versamid = 1.30 mixture containing 77% filler made up of 50% zinc and 50% ferrophos.

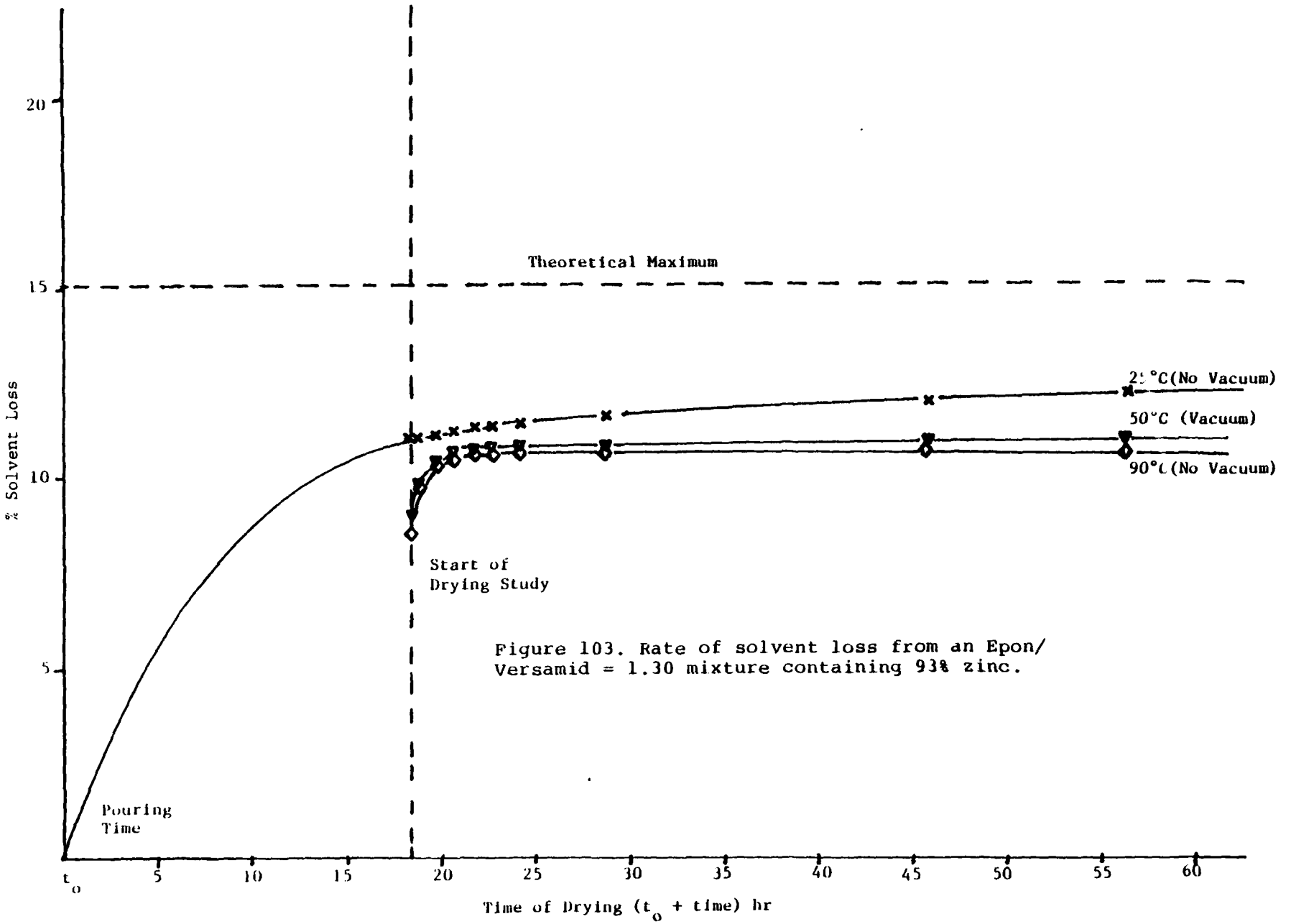

Figure 103. Rate of solvent loss from an Epon/ Versamid = 1.30 mixture containing 93% zinc.

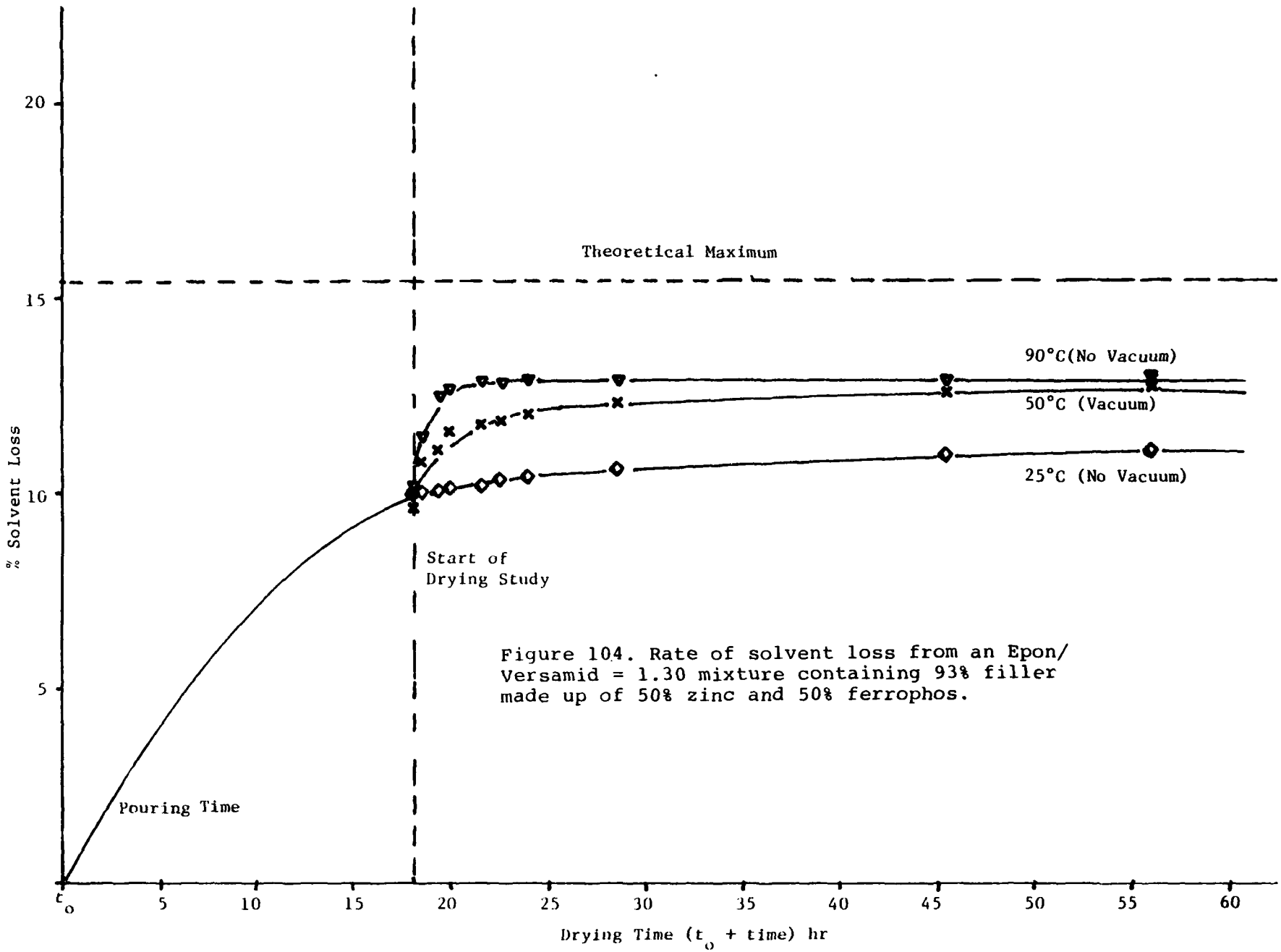

Figure 104. Rate of solvent loss from an Epon/ Versamid = 1.30 mixture containing 93% filler made up of 50% zinc and 50% ferrophos.

Table XIX

Drying of Coatings: Weight % Loss vs Time

Film	Vacuum[a]	Temp°C	Order of Thresholds & Comments
A-2	Yes	25	1st Theoretical (more solvent)
A-2	Yes	40	2nd Theoretical @ 10 hrs
A-2	No	90	3rd Level below theoretical
A-2	No	50	4th Slow rise to theoretical
A-3	No	40	1st Theoretical @ 35 hrs.
A-3	No	90	2nd Level below Theoretical
A-3	No	50	3rd Slow rise to theoretical
A-3	Yes	25	4th Slow rise to theoretical
A-4	No	25	1st Slow rise to theoretical
A-4	Yes	50	2nd Level below theoretical
A-4	No	90	3rd Level below theoretical
A-5	No	90	1st Level below theoretical
A-5	Yes	50	2nd Slow rise to theoretical
A-5	No	25	3rd Slow rise to theoretical
B-1	No	90	1st Level below theoretical
B-1	Yes	50	2nd Level below theoretical
B-1	Yes	40	3rd Level below theoretical
B-1	No	25	4th Slow rise
B-2	No	90	1st Theoretical @70 hr.
B-2	No	50	2nd rise to theoretical
B-2	Yes	25	3rd rise to theoretical
B-4	No	90	1st slow rise to theoretical
B-4	Yes	50	2nd more repid rise to theoretical
B-4	No	25	3rd slow rise to theoretical
B-5	No	90	1st level below theoretical

Table XIX (Cont'd.)

Drying of Coatings: Weight % Loss vs Time

Film	Vacuum	Temp°C	Order of Thresholds & Comments
B-5	Yes	50	2nd rapid rise to theoretical
B-5	No	25	3rd rapid rise to theoretical
C-1	No	90	1st Theoretical @ 100 hrs.
C-1	Yes	50	2nd rapid rise to theoretical
C-1	No	25	3rd slow rise to theoretical
D-1	No	90	1st level below theoretical
D-1	Yes	50	2nd level below theoretical
D-1	No	25	3rd slow rise to theoretical
D-2	No	90	1st level below theoretical
D-2	Yes	50	2nd level below theoretical
D-2	No	25	3rd slow rise to theoretical
D-3	No	90	1st level below theoretical
D-3	Yes	50	2nd level below theoretical
D-3	No	25	3rd slow rise to theoretical

a 30 mm Hg

2. A strange inversion of normal situations is experienced for the 93% zinc-filled sample. It is seen that the 25°C sample rises faster to the theoretical value of solvent loss while the 90°C and 50°C samples level off below the theoretical value.

3. It is seen in the 77% filled samples that vacuum @ 50°C causes a faster rise to the theoretical value than 50°C no vacuum. This is also true for the 25°C sample.

4. In most cases the rise to the theoretical value of solvent loss is very slow, or in certain cases a level below the theoretical value is reached. This result might be explained for example in the 93% filled system, on the basis that the sample has cured around pockets of solvent and has essentially prevented further evaporation in the 90°C sample. While the 25°C and 50°C samples will slowly and eventually exceed the 90°C sample, these samples are not fully cured and will still allow solvent loss.

Conclusions for Film C - D

1. No strange inversion is seen for E/V = 1.00 for the 93% Zinc sample as has occurred for E/V = 1.30 for the 93% Zinc sample. Furthermore, evaporation is quicker for film D-2 compared to film A-4. This result might possibly be explained on the basis of curing. Film D-2 is off stoichiometry and curing might be worse than film A-4. Thus, solvent loss would be faster for the less cured sample. The inversion for film A-4 might be due to perfect conditions of fast, trapped solvent, cure at 90°C compared to 25°C.

2. The 93% filled (50/50) sample is lower in evaporation rate compared to a 93% Zinc filled system when E/V = 1.00.

3. Evaporation rates are comparable with 93% Zinc when E/V = 0.8 and E/V = 1.00.

The important conclusion possible is that each sample has its own unique drying response and in many cases the sample never dries fully. The proof is that solvent is evident upon breaking the films. It is important to note that almost no film has ever approached the theoretical maximum.

Differential Scanning Calorimetry

Differential Scanning Calorimetry (DSC) gives a measure of the difference in the rates of heat adsorption by a sample with respect to an inert reference as the temperature is raised at a constant rate. In the absence of chemical reaction, a second-order transition is shown as a discontinuity in the thermogram. The second-order transition associated with the softening point in crosslinked networks has been shown by Gordan (68), using dynamic mechanical methods, to increase with the extent of cure. It is of much importance to characterize the epoxy system in terms of its glass transition as the temperature is varied.

Detailed studies by Fava (69) have shown that partially cured samples show a residual curing exotherm while subsequent scans show that the T_g shifts to higher temperatures as the resin becomes more and more cured. Thus the position of the transition region can be used as a sensitive cure index during the later stages of cure where the DSC is not sensitive enough to detect any residual exotherm in the sample. It was further found that the glass transition occurs at the cure temperature, indicating that as soon as the resin becomes glassy further reaction is very slight and not detectable. Further, only slight changes in the state of cure are detectable indicating that the glassy state provides a large barrier to continued polymerization. The mechanisms leading to a glass transition in crosslinked systems have not been treated in detail but the transition in thermoplastics is described in terms of a supercooled liquid state. The liquid state is supposed to contain holes which are characterized by a molar volume and a molar excess energy over the "no-hole" situation. It is of further importance that annealed epoxy resins show a characteristic endothermic peak in thermograms as predicted by the "hole" theory. The endothermic peak is due to the higher degree of order in the glassy state for the annealed sample. Many articles have also developed these ideas of curing and thermal history (70-73).

One final review of epoxy thermal history has been found in Wilkes (74). After aging a sample for 36 days at 23°C, the first scan results in a sharp endothermic peak and the second scan shows only the glass transition. The following conclusions were made:

1. The enthalpy relaxation peak is well below the transition.

2. The phenomenon is reversible, where additional annealing after cooling from above the glass transition creates the relaxation peak again and it grows with time.

3. The glass transition of the annealed sample is somewhat higher than in the quenched state.

4. During the annealing, the relaxation peak is shifting to higher temperatures and grows in magnitude.

5. For a given annealing time, the position of the relaxation peak depends upon the sub-T_g annealing temperature; it shifts upward as the sub-T_g annealing temperature increases.

6. The growth rate of the relaxation peak depends upon the annealing temperature in that an increase in the annealing temperature accelerates the growth of the enthalpy relaxation peak. The important conclusion possible is that there is a physical aging process due to the enthalpy relaxation which is important from the point of view of nonequilibrated states of quenched glassy polymers.

Results and Discussion

The results of the DSC study are presented in Tables XX to XXVII. The search for an exotherm using the DSC was not possible due to the fact that the samples were tested many months after preparation. Most measurable heats of reaction had ceased. However, the glass transition region still can be used as a reliable measure of the degree of cure of the sample. The results are significant on the basis that they are consistant with the dynamic mechanical tests shown in section on Dynamic Mechanical Properties. Namely, these results (Table XXVI) show that the T_g of the 25°C cure sample is approximately equal to the T_g of the 50°C sample. The T_g of the 90°C cure sample is much higher since it is more fully cured. Also a 10° change in scan rate seems to cause an elevation in $T_g \simeq 7$ (Table XXII, XXVI).

The studies on curing effects are summarized in Table XXVIII. It is evident that at a temperature greater than 360°K for the air cured sample, there is increasing degree of cure as evidenced by an increase in T_g. This is important to note, a film is even curing more at 400°K.

The thermal history results are summarized in Table XXIII, XXV. The first time a 90°C sample was run, a large endothermic peak around the T_g of the sample was observed. This result led to a series of runs to determine if this was a reproducible peak. The large endotherm appeared at 318°K on the T_g transition. On a rerun of the same sample, the endotherm decreased to almost nonexistence. There appeared some exothermic peaks around 334°K which are not explainable. A new sample was used and again the endothermic peak appeared at 317°K on the T_g transition. On a rerun the endotherm disappeared and an exotherm was noted at

Table XX

Attempts to Reproduce the Glass Transition on DSC Scan Rate 20°C/min Sample C-1 (Air Cure)

Scan Range (°K)	T_g (°K)	Comments
220-330		276°K Tm water, no T_g
250-305	286	
305-200	252	Small exotherm @ 234°K
200-305	283	
305-200	274	Large exotherm @ 209°K
200-305	283	
305-200	272	
200-305	282	
200-305	285	

Heating T_g = 283.8°K; cooling T_g = 273°K

Table XXI

Study of Effects of Curing on DSC Scan Rate
20°C/min Sample C-1 (Air Cure)

Scan Range (°K)	T_g (°K)	Comments
200-305	285	
200-310	286	Motion @ 243°K
230-320	287	Motion @ 255°K
220-330	286	Motion @ 245°K
320-230	280	
230-340	287	Motion @ 254°K
340-230	280	
230-360	286	Motion @ 250°K, 2nd transition @ 345°K
360-230	280	
230-370	290	Motion @ 250°K, 2nd transition @ 345°K
370-230	281.5	
230-390	290	Motion @ 255°K, 2nd transition Vanishing
390-230	283	
230-400	297	Motion @ 255°K, 2nd transition nearly gone

Table XXII

Studies on Scan Rate on DSC Sample C-1 (Air Cure)

Scan Range (°K)	Scan Rate (°C/min)	T_g (°K)
200-300	10	277.5
230-330	10	282
200-300	10	243
200-300	10	242.5
230-285	10	270
200-330	20	288.5
250-330	20	290.5
200-300	20	273
200-300	20	272.5
170-360	40	315
200-330	40	280
200-330	40	280

Table XXIII

Studies on Thermal History on DSC; Sample C-1 Cured at 90°C and Allowed to Cool to Room Temperature for Two Months

Scan Range (°K)	Scan Rate (°C/min)	T_g (°K)	Comments
290-360	10	313	
290-360	10	313	
230-380	10	313	Exotherm @ 288.5°K Endotherm @ 313°K Endotherm @ 371°K
200-380	20	310	Exotherm @ 319°K
270-370	20	318	
270-370	20	318	
220-350	20	315	
380-220	20	300	

Table XXIV

DSC Run on Sample Cured at 50°C (Sample C-1)

Scan Range (°K)	Scan Rate (°C/min)	T_g (°K)	Comments
	20	281	Endotherm @ 263°K

Table XXV

DSC Studies on Induced Thermal History Sample C-1, Cured at 90°C, Scan Rate 20°C/min

Run	Scan Range (°K)	T_g (°K)	Comments
1st run	230-325	312	Large endotherm @ 318°K endotherm on T_g transition
2nd run	230-365	311	Greatly decreased endotherm @ 318°K, exotherm @ 334°K
1st run	230-370	318	Endotherm @ 317°K on T_g movement at 260°K
2nd run	230-390	311	No endotherm @ 317°K exotherm at 369°K
3rd run (held @25°C for 30 min)	230-390	312	Peat at 317°K increased but not as large as 1st run, no exotherm at 370°K
1st run	230-380		Endothermic Peak @ 318°K T_g not obvious, shoulder at 275°K
2nd run	230-380	316	No evidence of endothermic or exothermic peaks

Table XXVI

Summary of DSC Results on Glass Transition - Sample C-1

Cure Temp (°C)	Scan Rate (°C/min)	T_g (°K)	Cooling (+), Heating (-)
25	10	277.5	-
25	20	283.8	-
25	20	273	+
25	40	291.7	-
50	20	281.0	-
90	10	313	-
90	20	318	-

Table XXVII

Summary of Curing Effects with DSC Sample C-1 (Air Cured), 20°C/min Scan Rate

Scan Range (°K)	T_g (°K)	Comments
230-360	286	2nd Transition @ 345°K
230-370	290	
230-390	290	2nd Transition Vanishing
230-400	297	2nd Transition gone

369°K. The same sample was held at 25°C for 30 minutes. A small peak developed at 317°K but not nearly as large as the original peak. There was also no exotherm at 370°K. These tests were again rerun with the same results. These results suggest some residual stresses in the 90°C cured sample that developed upon cooling to room temperature.

Sea Water Permeation

The penetration of water through the films is an important question from the point of view of corrosion and film stability. It is also of interest to explore further the area of X-ray analysis to coating problems. Along with providing a direct and simple method for pigment analysis, the X-ray diffraction method can be used to determine pigment dispersion and other elemental analysis (25). In the present case, emitted secondary X-rays, after excitation by a suitable source, can be detected by a wavelength instrument. The X-ray detection is also supplemented with scanning electron microscope pictures.

Permeation through polymer films has not been completely and rigorously given exact solutions to the problem. However, the permeation process can be considered with respect to the shape and orientation of filler particles along with the type of particle. It is important to note that the properties of the interface and the effects a filler has on relaxation characteristics of the matrix resin has direct influence on permeation. Furthermore, permeability includes both the effects of solubility and inherent diffusivity. Permeation must be reduced by the presence of an impermeable filler for two related reasons. First, there is an increased path length of the permeating molecules which is like having a thicker membrane. Second, there is a reduced cross section area of matrix available for permeation (76,77).

It is generally concluded that fillers tend to reduce permeation in polymers (78-81). However, there are many exceptions, as for example cases where the filler is not well bonded or uniformly wetted by the resin or cases where the filler or interface absorbs the penetrant.

The mechanism of permeation in polymers is believed to depend upon the ability of segments to move in such a way as to creat a hole which can accommodate a penetrant molecule. Any restriction or enhancement of mobility would be expected to alter the permeability which is similar to effects of glass transition temperature of a polymer (82).

Finally, the effects of permeation of water can be followed by incorporation of chloride ion. An interesting study was done by Fawcette and Stearns (83). It was concluded that the presence of Fe_2P in a weight percent of 50% gave substantial

corrosion protection with zinc as the other component in an epoxy-ester-based primer system. Further, it was found that the zinc efficiency as given by the percent of original zinc remaining after 200 hr is increased by the presence of Fe_2P. Thus Fe_2P has the effect of moderating the rate at which zinc is consumed. The results were believed to be due to the fact that Fe_2P and the steel substrate serve as a co-cathodic site. Since the Fe_2P pigment is finely divided, it has a surface area very much larger than steel and expansion of the cathodic surface area would bring it into approximate balance with the anodic surface area of the zinc and reduce the cathodic current density. It was also noted that permeation is actually increased with the presence of Fe_2P. These results are in contradiction to studies done at Lehigh.

Samples of air cure at 25°C (see Table XXVIII) were exposed to a synthetic sea water compound (Rila Marine Mix). The time of exposure was six (6) months. The zinc and Ferrophos used were exactly as used before along with the epoxy binder system. The following observations summarize the results:

A-1 93% Zinc	Permeation of the Cl^- ion is evident and is concentrated near the surface of exposure. There is a significant amount of Cl^- ion in the middle after breakage. (Reproducible)
A-3 93% Filler (50/50)	Permeation of Cl^- ion is drastically reduced compared to the above sample.

Discussion of Broken Film Surfaces as Observed by SEM

Film A-1 Particles are seen to be well coated with polymer; however, there do exist some voids. There are also more particles since it is 93% filled.

Film B-1 Less amount of zinc particles and greater amount of epoxy matrix. There is evidence of spheres completely pulled from the matrix.

Film B-2 Greater evidence of pot marks where spheres pulled away from the matrix. Upon closer examination the spheres appear to be loosely fitted within the epoxy matrix. There is also an uneven distribution of sizes, 5 μ, 1.5 μ, and 10 μ.

Film A-2 There are more particles and evidence of some uncoated zinc particles; appear to be loosely fitted in the matrix.

Film A-3 Many strange shaped particles due to the Ferrophos; a very brittle looking sample.

Table XXVIII

Description of Samples Used in SEM and Permeation Studies

Film Identification	% Filled (z = Zinc; F = 50/50 Zinc Ferrophos)	Epon Versamid
A-1	93 (z)	1.31
A-2	93 (z)	1.30
A-3	93 (F)	1.30
A-4	93 (z)	1.30
A-5	93 (F)	1.30
B-1	77 (z)	1.30
B-2	77 (z)	1.30
B-3	77 (F)	1.30
B-4	77 (z)	1.30
B-5	77 (F)	1.30
C-1	0	1.30
D-1	92.1 (z)	0.80
D-2	92.1 (z)	1.00
D-3	92.1	1.00

General Results on Hardness Study

77% zinc samples	3B
93% zinc samples	6H

Dynamic Mechanical Tests

Mechanical properties have to be considered as the most important of all the physical and chemical properties of high polymers. There are a great many structural factors which determine the nature of the mechanical behavior of such materials. The following structure factors are considered important, molecular weight, crosslinking and branching, crystallinity and crystal morphology, copolymerization, in addition to the chemical composition, plasticization, orientation and fillers. The following environmental or external variables are important in determining mechanical behavior, temperature, time, pressure, stress and strain, amplitude, type of deformation (shear, tensile, biaxial), heat treatment or thermal history and the nature of the surrounding atmosphere. There is a strong dependence on temperature and time of the properties of polymers compared to those of other materials such as metals. This strong dependence of properties on temperature and on how fast the material is deformed is a result of the viscoelastic nature of polymers (84).

The glass transition is the most important material characteristic of a polymer as far as mechanical properties are concerned. This is the region where the elastic modulus may decrease by a factor of over 1000 times as the temperature is raised through the glass transition region. The glass transition temperature is generally measured by experiments which correspond to a time scale of seconds. If the experiments are done more rapidly so that the time scale is shortened, the apparent T_g is lowered. As generally measured, T_g is not a true constant but shifts with time. Changing the time scale by a factor of ten times will shift the apparent T_g by roughtly 7°C for a typical polymer (84).

The mechanical properties of filled polymers have been discussed very extensively in the literature (84-89). Fillers are used to reduce the cost of the product, to improve the mechanical properties and to impart special characteristics such as color and corrosion resistance. There are special effects due to filler incorporation which are classified as filler reinforcement. The following properties are important concerning the filler itself. The size of the particle, the shape of the particle and the surface characteristics are all important aspects of reinforcement. In general, a filler blended with a polymer will increase the modulus because of the restrained nature of the polymer chain when in the presence of the filler.

Finally, when studying a system such as an epoxy-versamid

system, there is an ultimate cure time and temperature for desired properties such as modulus. In a dynamic test, the curing reaction can be seen to occur as evidenced by an increase in T_g as the temperature of cure is increased.

Gehman Test (ASTM Designation D1053-73)

Rheovibron (DDV-III-C)

The high-filled zinc films proved to be difficult to run on the Rheovibron due to their brittle nature. To prevent breakage, the films had to be mounted first in the gribs of the Rheovibron using some Mylar film to prevent grip breakage. This procedure was not totally effective.

The Gehman results given in Table XXIX show that the sample with the lowest T_g is that of pure epoxy. The next highest is the 77% filled epoxy system. The next highest is the 93% filled system of (50/50) zinc and Ferrophos. The final highest T_g was that of zinc filled samples. This result is interesting in that the 93% sample of (50/50) zinc and Ferrophos showed a reduction in permeation. Thus this new system might be worth exploring further from the point of view of having a comparably equal strength compared to 93% pure zinc, reduced permeation, and a T_g comparable to a 77% pure zinc sample and finally good corrosion resistance (75).

The Rheovibron test results show definite curing effects. There is also a high probability of solvent loss during the test. The results in Table XXX show curing trends. As the temperature is raised from an air cured sample to 50°C and held for at least 24 hr in an isotherm oven, the glass transaction temperature is raised. These results are similar to those obtained using DSC. It seems to be apparent that 90°C is the limiting threshold for final curing. This is because a sample film at 95°C for the same amount of time did not drastically change its glass transition. Similarly the modulus is increasing as the curing proceeds.

The 77% zinc film system proved to be able to be tested on the Rheovibron. It is seen (Table XXXI) that the modulus is not drastically affected by the degree of cure. However, the glass transition is shifted about 20 degrees. Also, as predicted above, the modulus of the filled system is higher along with glass transition at the same temperature of cure, 90°C.

Table XXIX

Relative Gehman Mechanical Test Results
for Samples Cured at 25°C

Film	36 (dynes/cm^2 at -150°C	T_g (°C) at log 36 = 10
A-1	3.16 x 10"	70
B-1	7.96 x 10^{10}	32
A-3	1.26 x 10"	45
C-1	3.16 x 10^{10}	19

Table XXX

Relative Rheovibron Mechanical Test Results to Study
Curing of Samples (Film C-1)

Cure Temp °C	E'(dynes/cm^2) at -150°C	T_g(°C) at log E' = 10.0
25	2.0 x 10^{10}	12
50	3.16 x 10^{10}	21
50 to 70	2.23 x 10^{10}	37
70 to 95	2.82 x 10^{10}	53
90	1.78 x 10^{10}	52

Table XXXI

Relative Rheovibron Mechanical Test Results
for Filled and Unfilled Samples

Film	Cure Temp (°C)	E'(dynes/cm^2) at -150°C	T_g(°C) at log E = 10.0
B-1	25	7.94×10^{10}	52
B-1	90	7.94×10^{10}	72
B-1	25	6.31×10^{10}	53
C-1	25	2.0×10^{10}	12
C-1	90	1.78×10^{10}	52

SECTION 10

Objective: To Develop an Improved Technique for Studying Corrosion under Organic Films on a Localized Scale

Title: Localized Electrical Properties of Epoxy-Polyamide Coatings on Metallic Substrates

Senior Investigator: Michael C. Hughes

Associates: Jeffrey Parks, Graduate Student

Introduction

The corrosion of polymer-coated metals exposed to electrolytes often occurs in a highly localized manner. Mayne and Mills (90) correlated the areas in which corrosion occurred with those areas of a film which had low DC electrical resistance measured after the separation of the film from the substrate. Others have shown that the resistance of a coating decreases with increasing exposure time to an electrolyte. Kendig and Leidheiser (91) have shown that a polybutadiene/steel system experiencing localized corrosion exhibits a characteristic electrical behavior. The prevailing evidence is that in many cases, reduced electrical resistance of a coating can be correlated with the susceptibility of the coating/substrate system to corrosion.

A method recently developed by Isaacs and Kendig (92) and expanded by Standish and Leidheiser (93) provides a means for studying localized corrosion beneath an organic coating and for studying coatings on a local scale prior to the onset of corrosion. This work has the goal of expanding on the probe techniques used previously (92, 93).

Experimental and Results

An AC probe has been designed which is similar to that reported by Isaacs and Kendig (Figure 105); a major difference is that our probe contains a true reference electrode (Ag/AgCl, saturated NaCl). It is expected that this design will produce more consistent probe response, and at the same time will allow for the interpretation of the probe response in terms of the standard theory of the AC response of electrochemical systems (94-96).

Electronic instrumentation has been constructed using commercially available equipment (Figure 106). The potentiostat is a Princeton Applied Research Corporation (PARC) Model 173/176; the lock-in amplifier is a PARC Model 5204/90 Dual Vector Lock-In Amplifier; the signal generator is a Wavetek Model 185; the X-Y recorder is a Hewlett-Packard Model 7047A. Hewlett-Packard digital voltmeters and frequency meters are used to monitor the instrument response. The configuration of the instrumentation is a three-electrode alternating current potentiostat with dual vector readout. The probe contains two of the electrodes: the probe wire is the counter electrode and the reference electrode is contained in the body of the probe (see Figure 105): the metal substrate of the sample is the working electrode (virtual ground). The instrument has an effective working frequency range of 10 Hz to 90 kHz. For most experiments a 10 mV (RMS) AC potential was applied. Varying DC bias potentials were applied to the samples to keep the steel substrate in its passive region.

For all work reported here, the sample was held on a machinist's table which could be moved in the X and Y directions by hand wheels calibrated in thousandths of an inch (0.0025 cm). A ten-turn potentiometer powered by flashlight batteries was connected to the X-axis drive of the stage and this signal drove the X-axis of the X-Y recorder. Movement of the stage in both axes was made manually.

At the time that this report is being written, an automated stage using servo motors, controllers and ranging switches to provide automatic scanning over a pre-set area at a selected scan rate is being constructed. A prototype of the stage has been made and tested, and a local machine shop has been engaged to manufacture the moving parts of the system. A micrometer head has been designed to hold the probe in the automated stage; this head will permit adjustment of the probe position above the surface of the substrate, and will also maintain the probe exactly vertical to the sample.

Metal and coated metal samples were normally 5x7.5 cm or 7.5x10 cm. An insulated ring 3.4 cm in diameter and about 2.5 cm high was glued to the sample to provide a container for the electrolyte. The electrolyte used for all experiments reported here was 3.5% NaCl. Steel samples were conventional cold-rolled mild steel and galvanized steel obtained from Armco; analyzed lot samples of Type 304 and 316 stainless steel and Monel 400 were obtained from Schrader Stainless Steel Corp., Quakertown, Pa. Cold-rolled steel

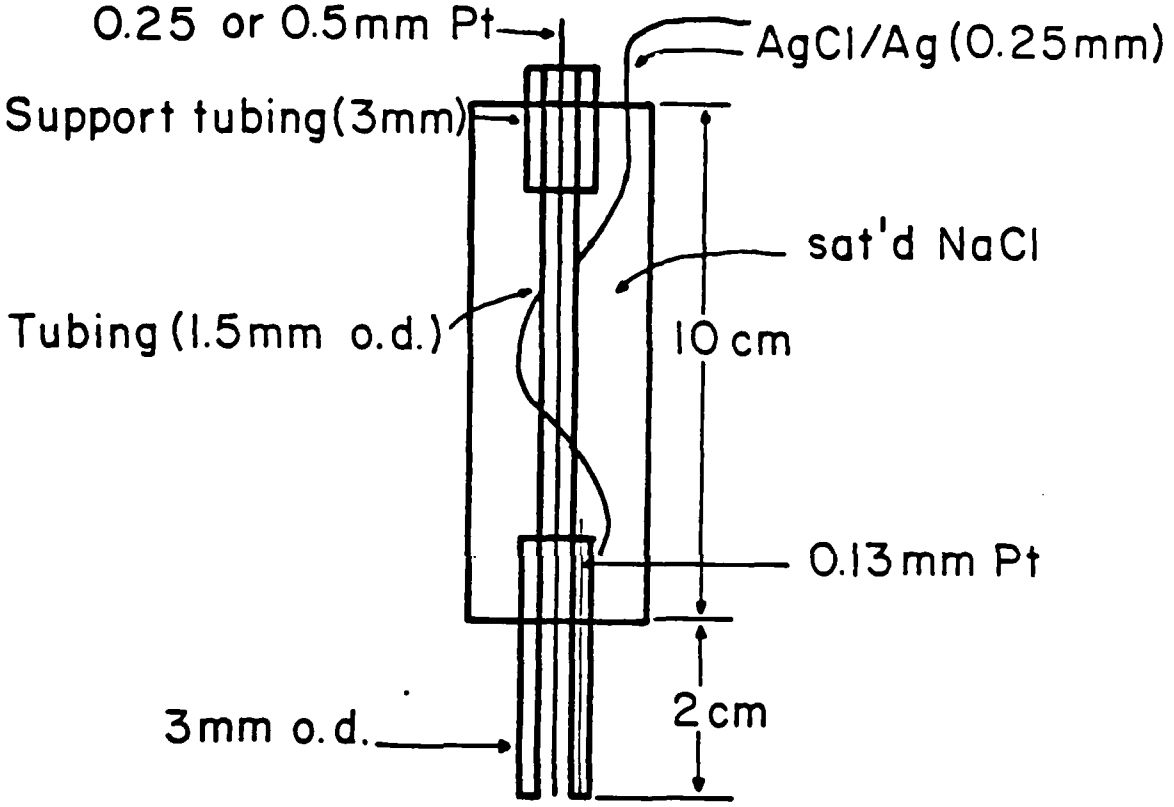

Figure 105. Detailed Drawing of Probe Construction.

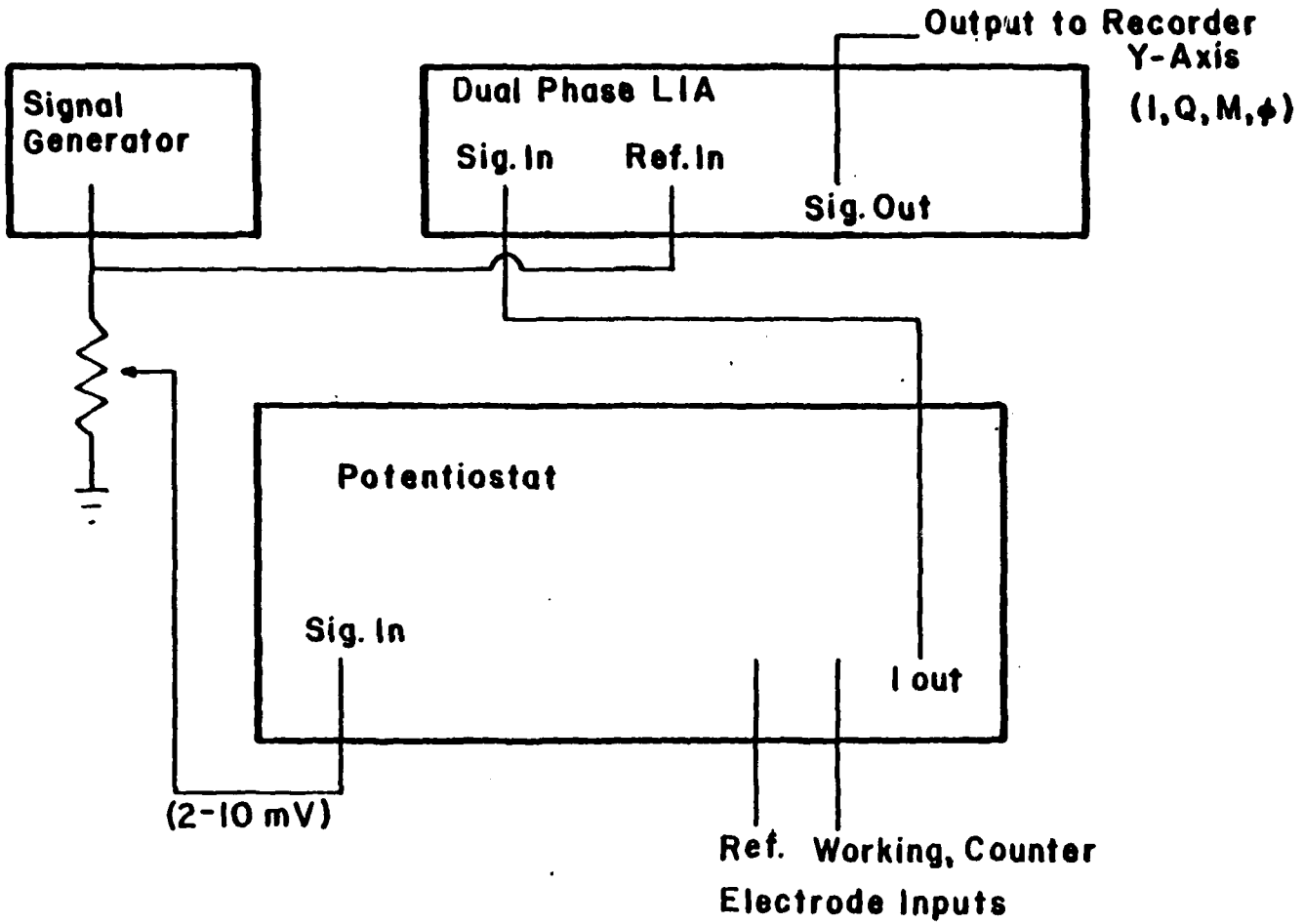

Figure 106. Block Diagram of Probe Electronic Circuit.

was phosphated by immersion in a solution of 50 ml Granodine phosphating agent per liter at a temperature of 70-80°C, followed by rinsing the steel in chromic acid (1.5 g/L).

Two types of polymer coatings were used. For the first coating, ten g of Epon 828 (Shell) were mixed with 8.28 g Versamide polyamide in toluene solvent. The second coating was 5.00 g Epon 1010F (Shell) mixed with 2.36 g Emerez 1511 polyamide in toluene solvent. In both cases the coating was applied with a draw bar apparatus to give a coating thickness in the 50-75 μm range. The coating samples were baked for 20 min at 100°C after application.

Figures 107, 108, and 109 show the types of response which may be obtained from the probe. The sample was a phosphated cold-rolled steel coated with the Epon 828/Versamid epoxy. A DC bias potential of -0.56V (vs Ag/AgCl, sat. NaCl) was applied to the probe and the applied AC potential was 10mV at 6.49 kHz. The DC bias potential was determined by monitoring the DC current flowing at the substrate as the probe potential was made increasingly negative (biasing the substrate—the working electrode—positive) until the DC current was less than 1 μA. This procedure was used to prevent damage to the sample which usually occurred when the DC potential was not in the passive region. The X-axis and Y-axis resolution, in Figures 107-109, are typical of the probe resolution, although much finer resolution may be obtained (vide infra).

The defect was a deliberate one made by cutting the polymer surface gently with a razor blade. The shape of the defect is shown in the inset in Figure 107. Figures 107 and 108, taken immediately after the defect was produced and the 3.5% NaCl electrolyte added, show that the I and Q responses essentially parallel each other in both distribution and magnitude. When contrasting this behavior with that reported for some other systems below, it should be kept in mind that the defect was fresh and showed no visible signs of corrosion or delamination. Figure 109 shows the relative phase angle response for the same defect. The phase angle measured is the angle between the applied alternating potential and the total current vector, measured directly by the lock-in amplifier; it does not correspond to the phase angle of the faradaic current usually encountered in AC electrochemistry. Also, the measured values are not corrected for the complex response function of the probe itself. Nonetheless, Figure 109 does show the phase angle decreases as the probe passes over the defect region, the expected behavior if the complex AC impedance of the system becomes more resistive and less capacitive in the region where the polymer is cut.

Figures 110 and 111 illustrate the sensitivity of the probe, and also the utility of the phase-sensitive detection. The sample is Epon 1001/Emerez 1511 epoxy coated on a galvanized steel substrate. The scans were run at a DC bias potential of 0 V (potentiostated, not open circuit) vs Ag/AgCl (saturated NaCl) with an applied AC potential of 10 mV at 10.9 kHz. The defect consists of

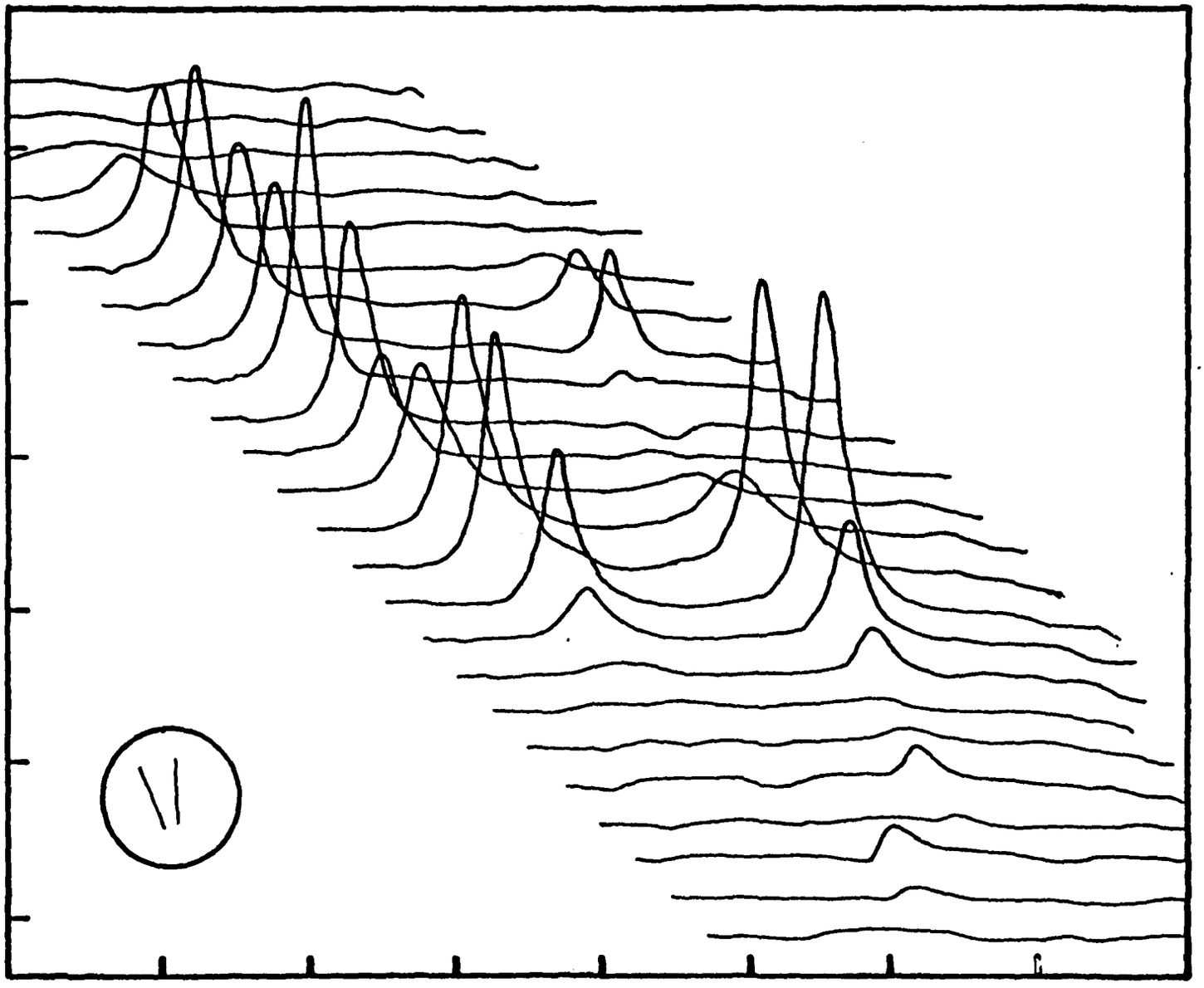

Figure 107.

I component response of a defect in Epon 828/Versamid epoxy coating in phosphorated cold rolled steel. DC bias potential = -0.56V. Applied AC potential = 10mV. Frequency = 6.49 kHz. X-axis scale: 1 division = 0.254 cm (0.100 inch). Y-axis scale: 0.0635 cm (0.025 inch) between scans. Current sensitivity = 5μA/division. Inset shows the shape of the defect.

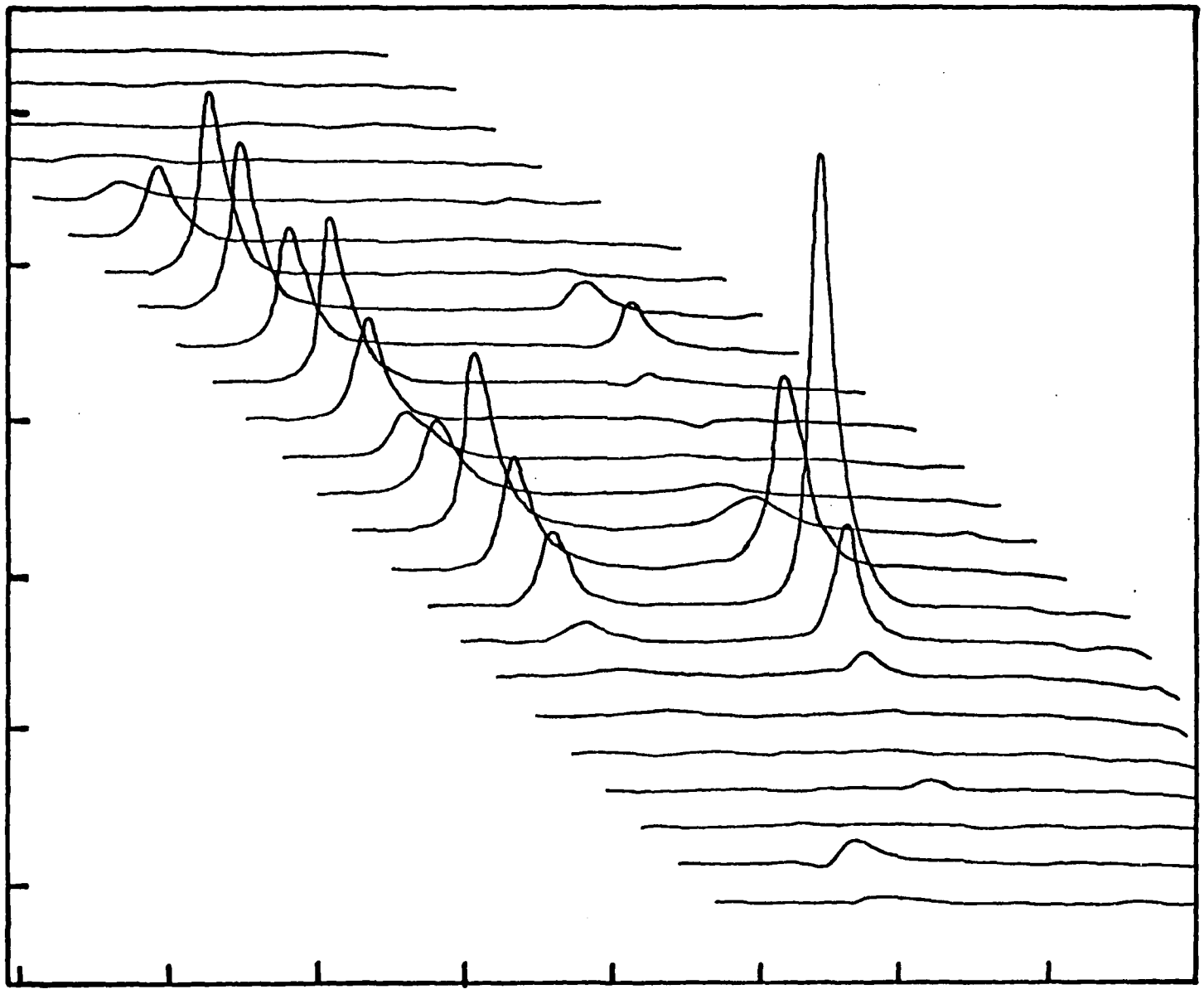

Figure 108.

Q component response for the defect shown in Figure 107. All parameters are

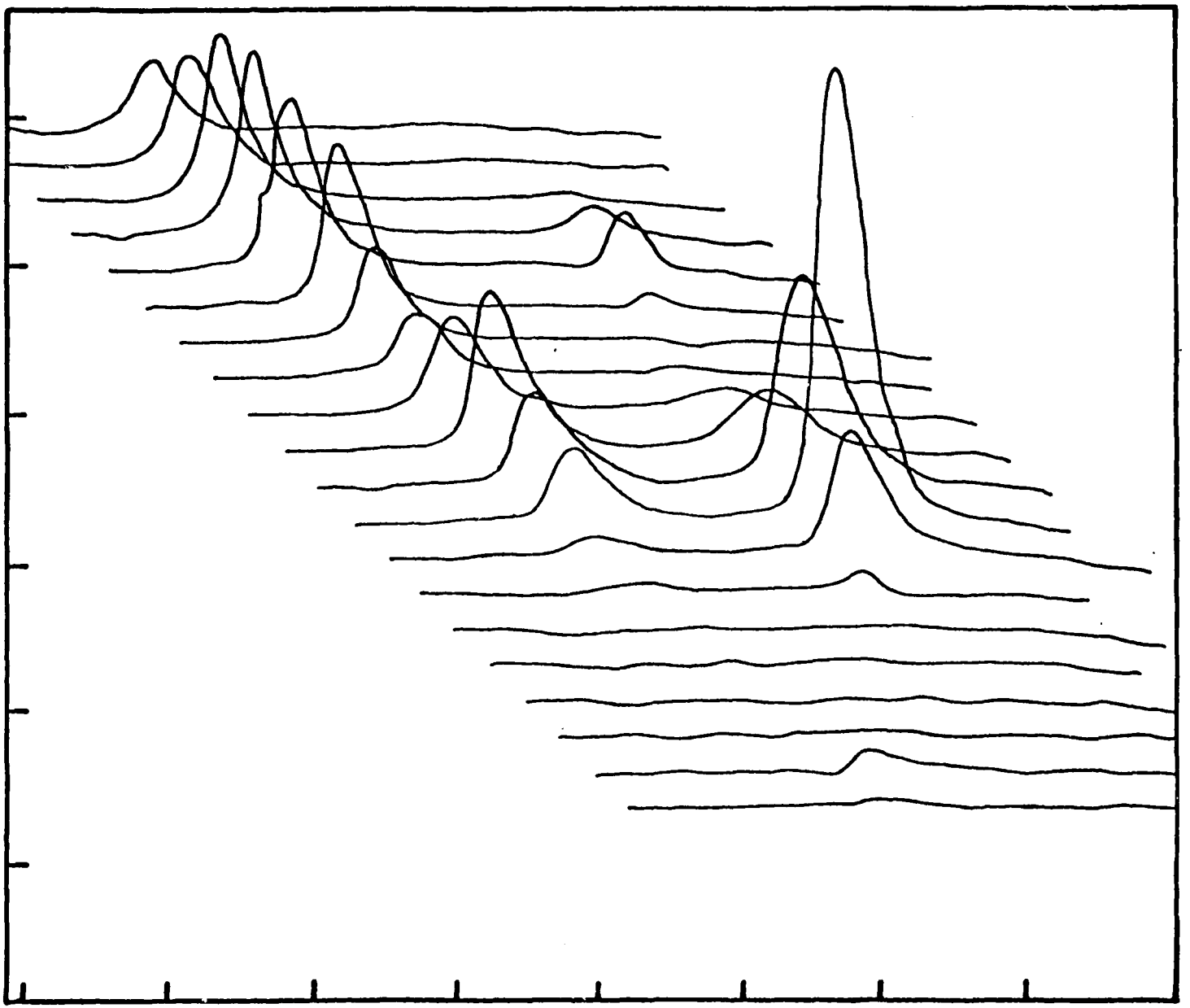

Figure 109.

Relative phase angle response for the defect shown in Figure 107. Initial value of ϕ = 76° for all scans, with ϕ decreasing with increasing response on the vertical axis. All other parameters the same as for Figure 107.

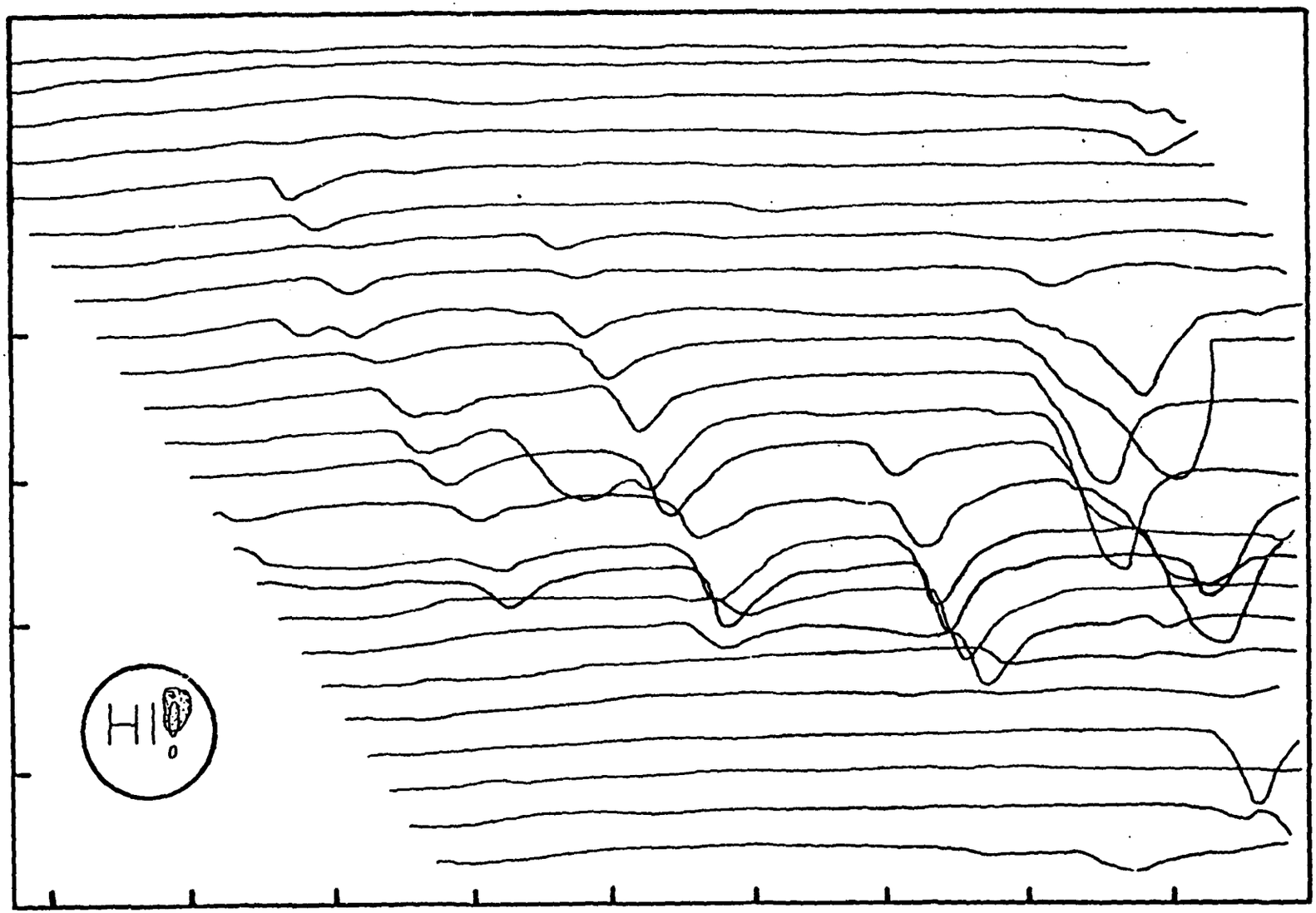

Figure 110.
Q component response of a defect on galvanized steel underneath Epon 1001/-Emerez 1511 epoxy. DC bias potential = 0.0V. Applied AC potential = 10mV, frequency = 10.9 kHz. X-axis scale: 1 division = 0.254 cm (0.100 inch). Y-axis scale: 0.0635 cm (0.025 inch) between scans. Current sensitivity = 125nA/division. Inset shows the shape of the defect and the delamination

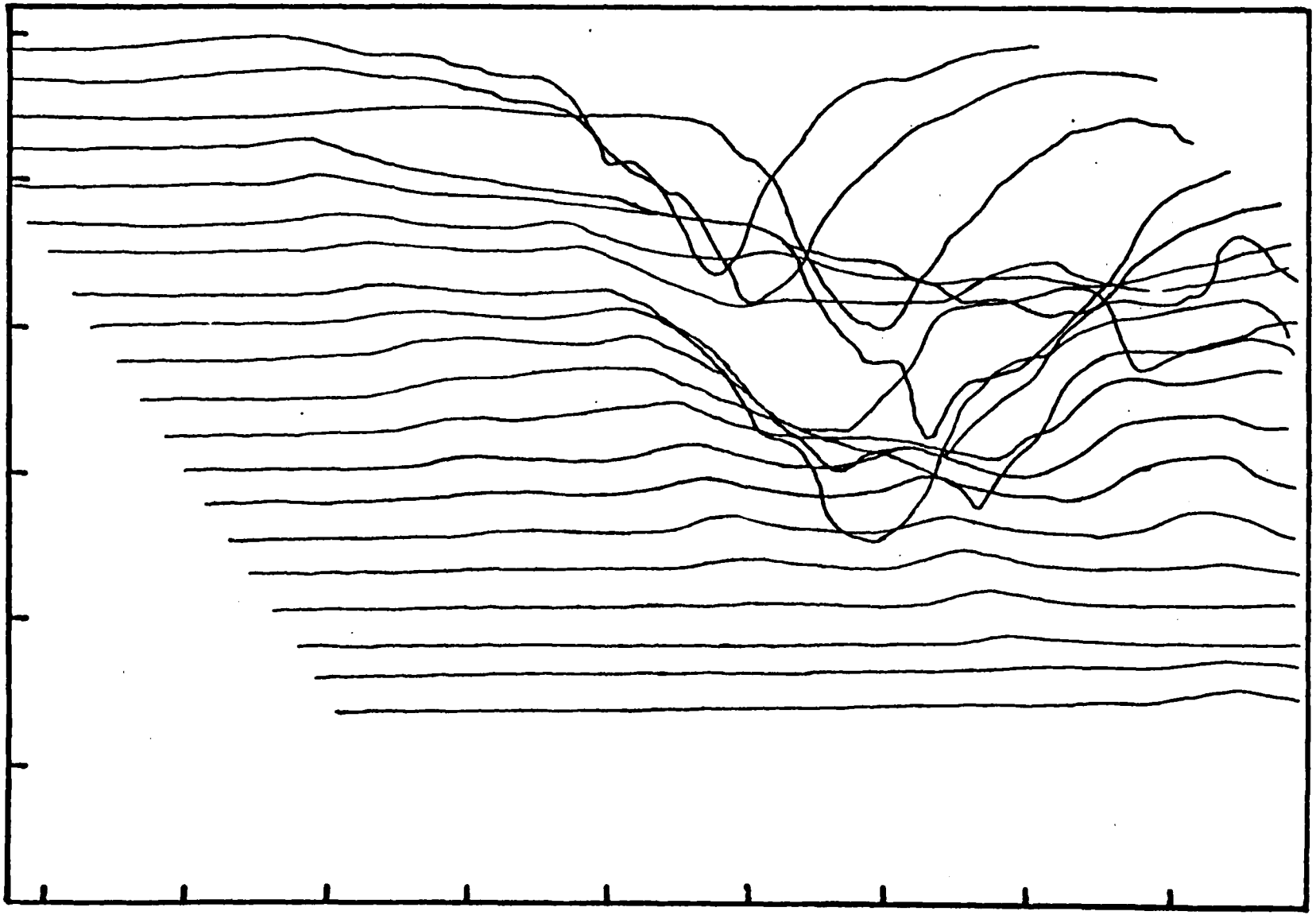

Figure 111.
I component response for the defect shown in Figure 110. Current sensitivity = 10μA/division. All other parameters the same as in Figure 110.

scratches made on the galvanized steel surface immediately before the application of the coating. The inset in Figure 110 shows the shape of the defect and the location of the regions of corrosion and delamination which developed after the sample remained in contact with the 3.5% NaCl solution overnight. The coating was completely intact when the measurements were made. Figure 110 is the Q component response. The pattern of the scratches underneath the coating is quite obvious, even in the areas where delamination has occurred. In contrast, the I component response (Figure 111) shows essentially no signal except in the delamination region, where a massive response is obtained.

Figures 112-116 further illustrate the use of the phase sensitive detection. The sample was the Epon 1001/Emerez 1511 epoxy coated on a cold-rolled steel substrate. The defect was a scratch made in the coating with a razor blade. The shape is shown in the inset in Figure 112. A DC bias potential of -0.39V vs Ag/AgCl (saturated NaCl) was applied to the probe, and the applied AC potential was 10mV at 6.48 kHz. Figure 112 is the I component response run approximately 1 hr after immersion of the defect region in 3.5% NaCl. The shape of the defect is clearly delineated.

After 48 hr of immersion in the 3.5% NaCl, the entire defect had become covered with brown iron oxide corrosion. Figures 113 and 114 are the I and Q component response, respectively, run at this point. The defect area appears to be passivated and virtually no I component signal is observed. The Q component does still show the defect clearly enough that its general shape can be readily discerned.

After the scans in Figures 113 and 114 were run, the corrosion coating covering the defect was deliberately broken up, the entire system stirred and allowed to sit for about one hr. At the end of this time, massive corrosion was present on the defect and the product was distributed in the electrolyte. Delamination was visible in the region indicated in the inset in Figure 115, as well as along both edges of the defect. Figure 115 shows the Q response. The signal intensity has greatly increased with the onset of active corrosion and the outline of the defect is again clearly visible. The cause of the change in polarity of the Q component relative to the earlier measurements is not understood at this time. This behavior was observed for a number of other experimental runs, and may be an artifact of the response function of the probe itself. Figure 116 shows the I response. As in the example cited previously (Figure 111), an especially strong I response quite clearly outlines the region of delamination. The remainder of the defect shows a complex response of multiple peaks in the I component compared to the Q component. This apparently reflects the delamination which was visibly beginning to occur all along the defect.

The magnification of a defect which is possible with the probe is illustrated in Figure 117. The sample was phosphated cold rolled

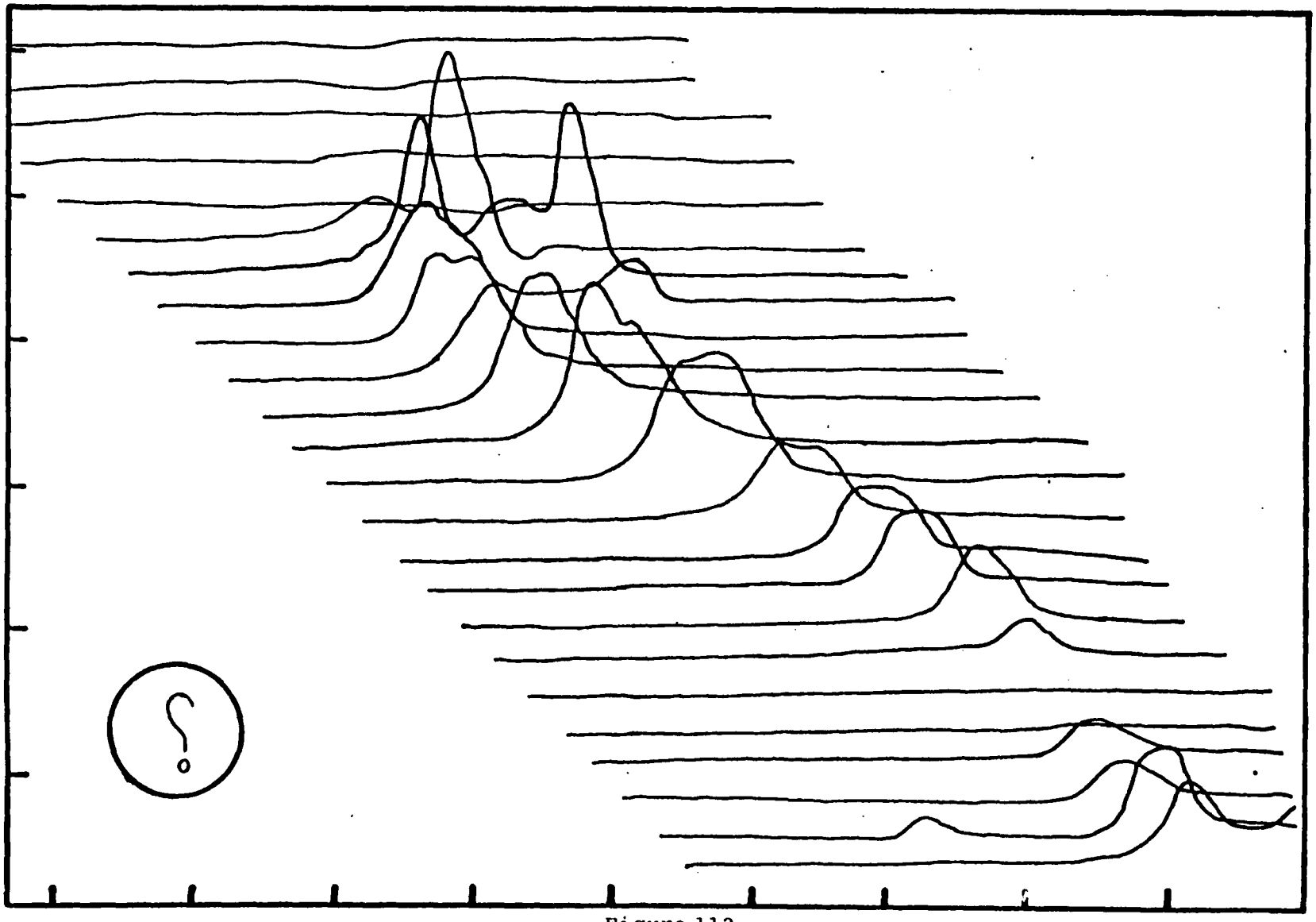

Figure 112.
I component response of a defect in Epon 1001/Emerez 1511 epoxy coating on cold rolled steel. DC bias potential = -0.39V. Applied AC potential = 10mV. Frequency = 6.48 kHz. X-axis scale: 1 division = 0.254 cm (0.100 inch). Y-axis scale: 1 division = 0.0635 cm (0.025 inch) between scans. Current sensitivity = 10μA/division. Inset shows the shape of the defect.

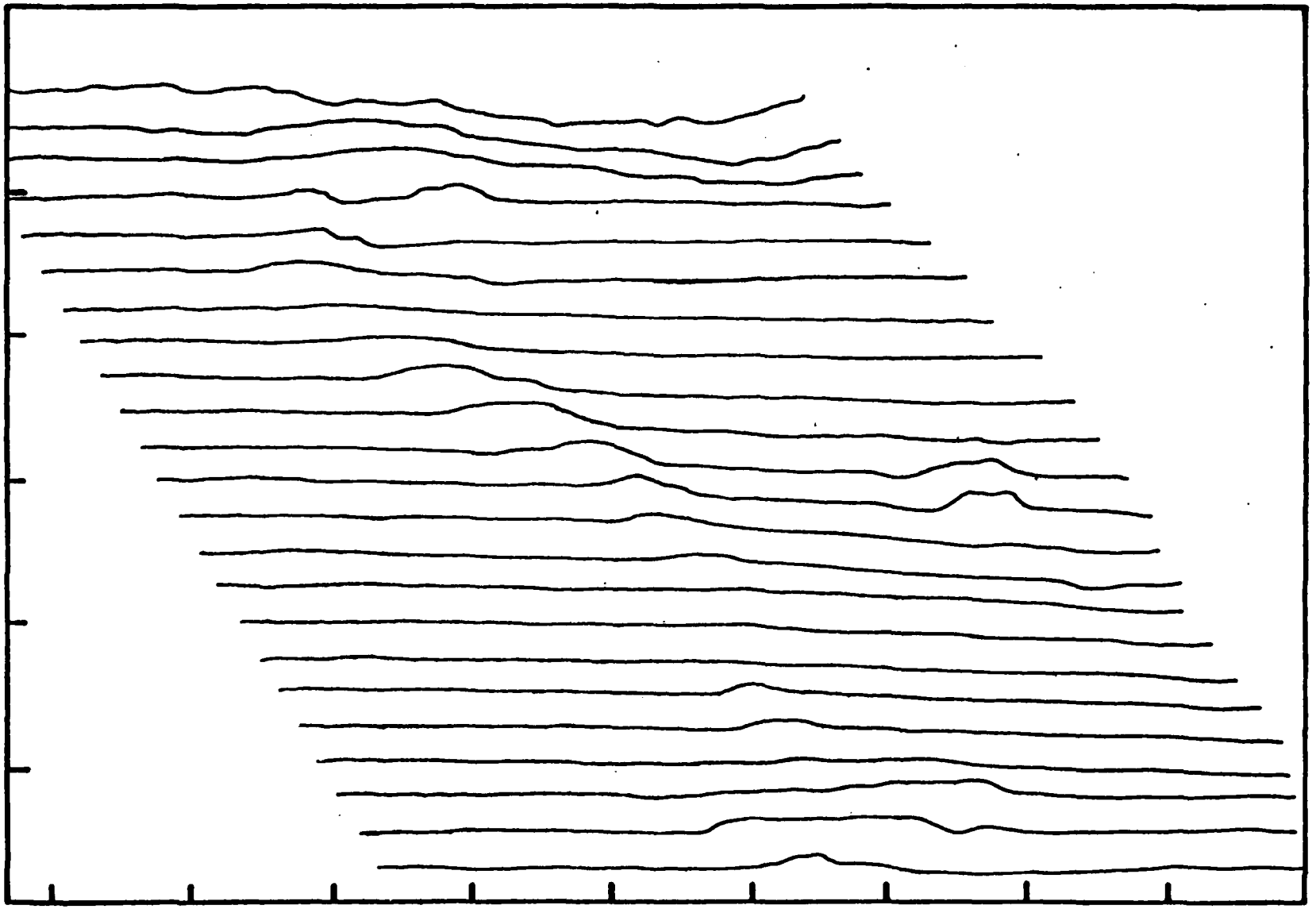

Figure 113.

I component response of defect shown in Figure 112 after 48 hours exposure to 3.5% NaCl. All parameters the same as in Figure 112.

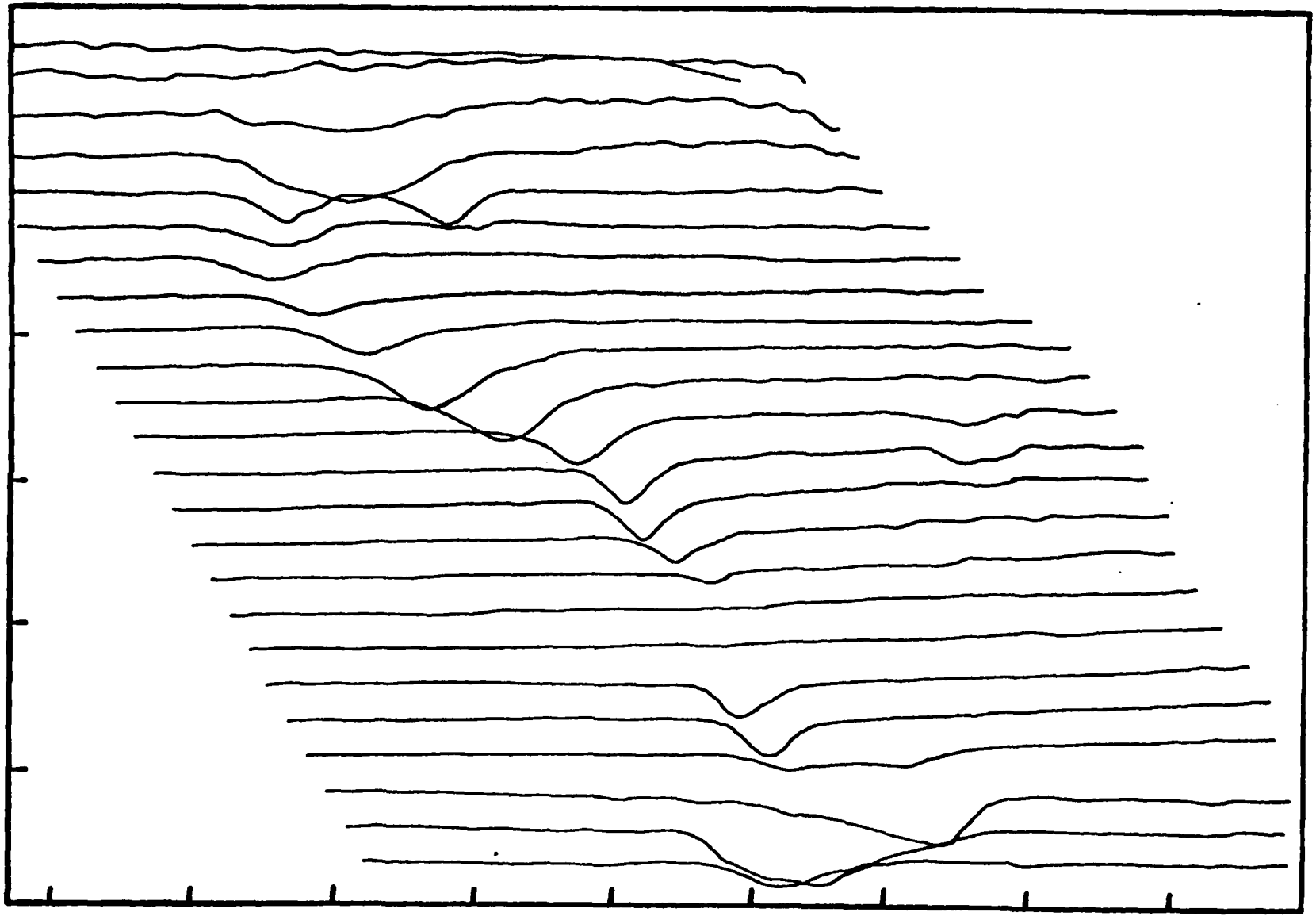

Figure 114.

Q component response of defect shown in Figure 113.
All parameters the same as Figure 113.

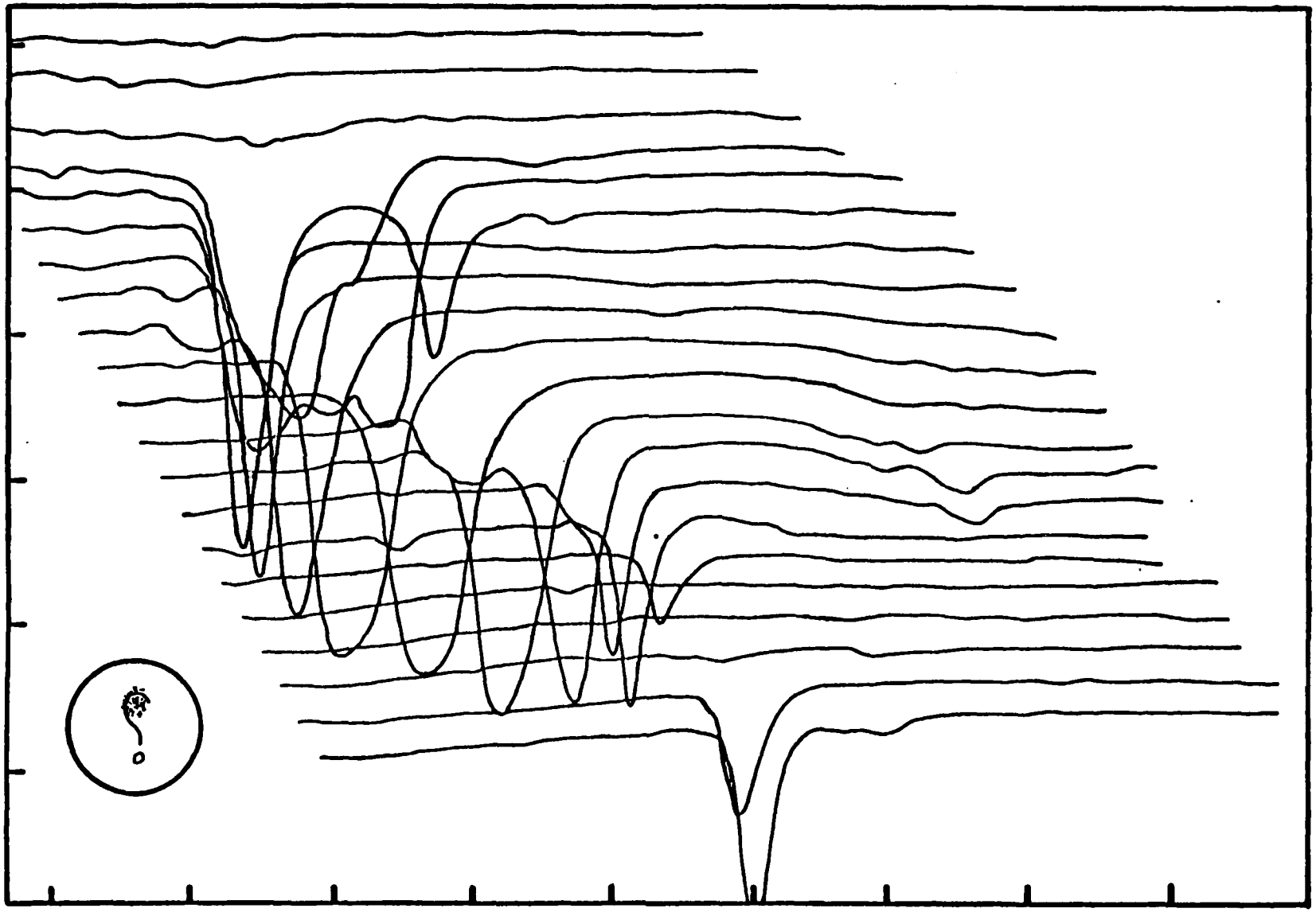

Figure 115.
Q component response of defect shown in Figures 113 and 114 after disturbance (see text for details). All parameters the same as for Figure 112. Inset shows the location of delamination (stippled area).

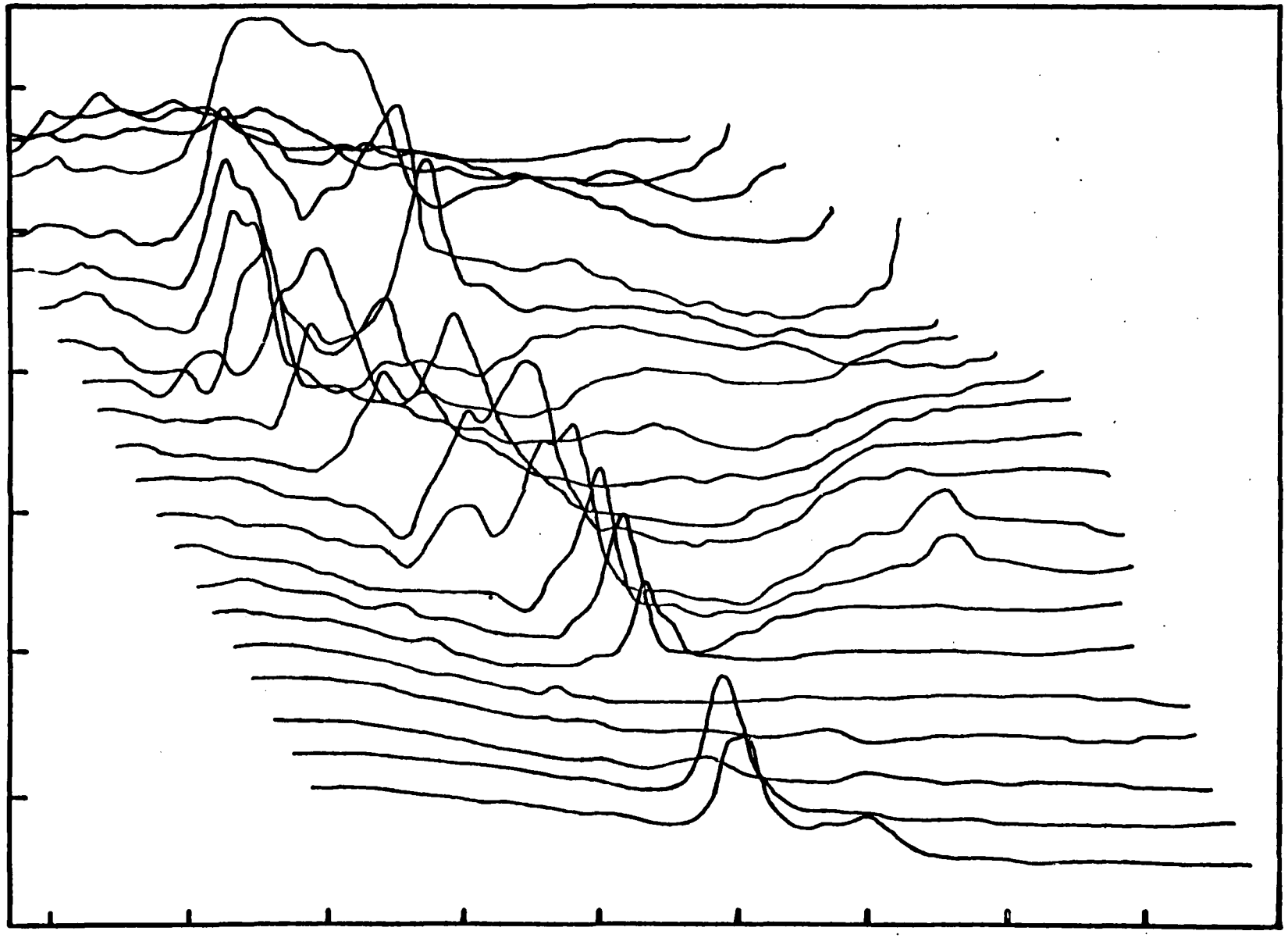

Figure 116.
I component response of defect shown in Figure 115.
All parameters the same as for Figure 112.

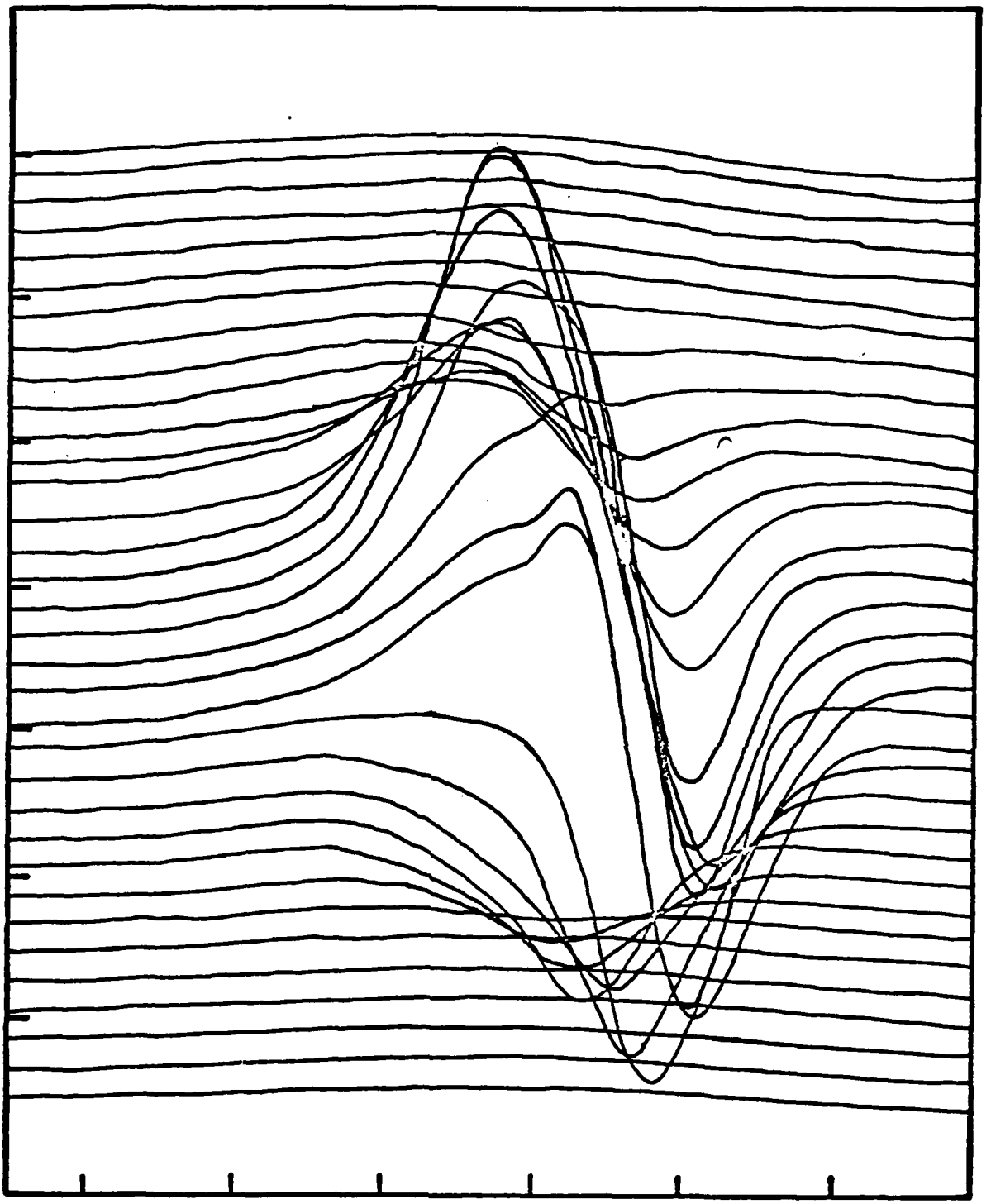

Figure 117.

I component response for a point defect in Epon 828/Versamid epoxy coating on phosphorated cold rolled steel. DC bias potential = -0.57V. Applied AC potential = 10mV. Frequency = 22.2 kHz. X-axis scale: 1 division = 0.082 cm (0.0323 inch). Y-axis scale: 0.013 cm (0.0005 inch) between scans. Current sensitivity = 1μA/-division.

steel coated with Epon 828/Versamid epoxy. The DC bias to the probe was -0.57V vs Ag/AgCl (saturated NaCl), and the applied AC potential was 10mV at 22.2 kHz. The defect was a spot defect produced by piercing the coating with the tip of a needle. The sodium chloride electrolyte was added and the defect region was scanned immediately. Figure 117 shows the I component response; the Q component was essentially identical. Resolution is better than 250 μm (0.01") on both the X and Y axes.

Figures 118 and 119 illustrate how the variable magnification effect of the probe can be used to follow the progress of corrosion and delamination in a somewhat complex defect, the outline of which is shown in the inset in Figure 118. The system was Epon 1001/Emerez 1511 epoxy on cold rolled steel. The DC bias potential on the probe was -0.45V vs Ag/AgCl (saturated NaCl), and the applied AC potential was 10mV at 2.07 kHz. Figure 118 shows the I component of the entire defect region immediately after the electrolyte was added. After 48 hr of exposure to the electrolyte, delamination had begun in a portion of the defect region (see inset in Figure 119). Figure 119 shows I component scans run at a higher resolution than in Figure 118 and covering only the delamination region, so that the pattern in that region can be seen more clearly. The shape of the defect is well defined and in agreement with other results shown, the magnitude of the I component response increased considerably relative to the fresh defect (Figure 118).

The results reported above indicate that the AC potential probe is capable of providing a great deal of information regarding the location of defects in or under a polymer coating on a metal surface. Further, definite qualitative distinctions between some types of defects can be seen, and the progress of corrosion and delamination can be followed. The resolution of the probe is great enough so that quite detailed "impedance maps" of a defect region can be made. Thus, the probe can and is being used at the present time to locate and follow the changes in small defects in polymer coated steels.

Characterization of the AC Impedance of the Probe

As was indicated earlier in this report, some characteristics of the probe response, particularly the appearance of negative-going quadrature currents in the defect regions, appear to be anomalous with respect to the expected AC impedance behavior. In order to determine whether this behavior was due to a characteristic response of the probe, second measurements were made to determine the AC impedance of the probe and its effect on basic impedance measurements. Components of the complex impedance, Z', the real component, and Z", the imaginary component, were determined by standard procedures (94).

From the measured current components Figure 120 shows the characteristics of the probe as a reference/counter electrode vs

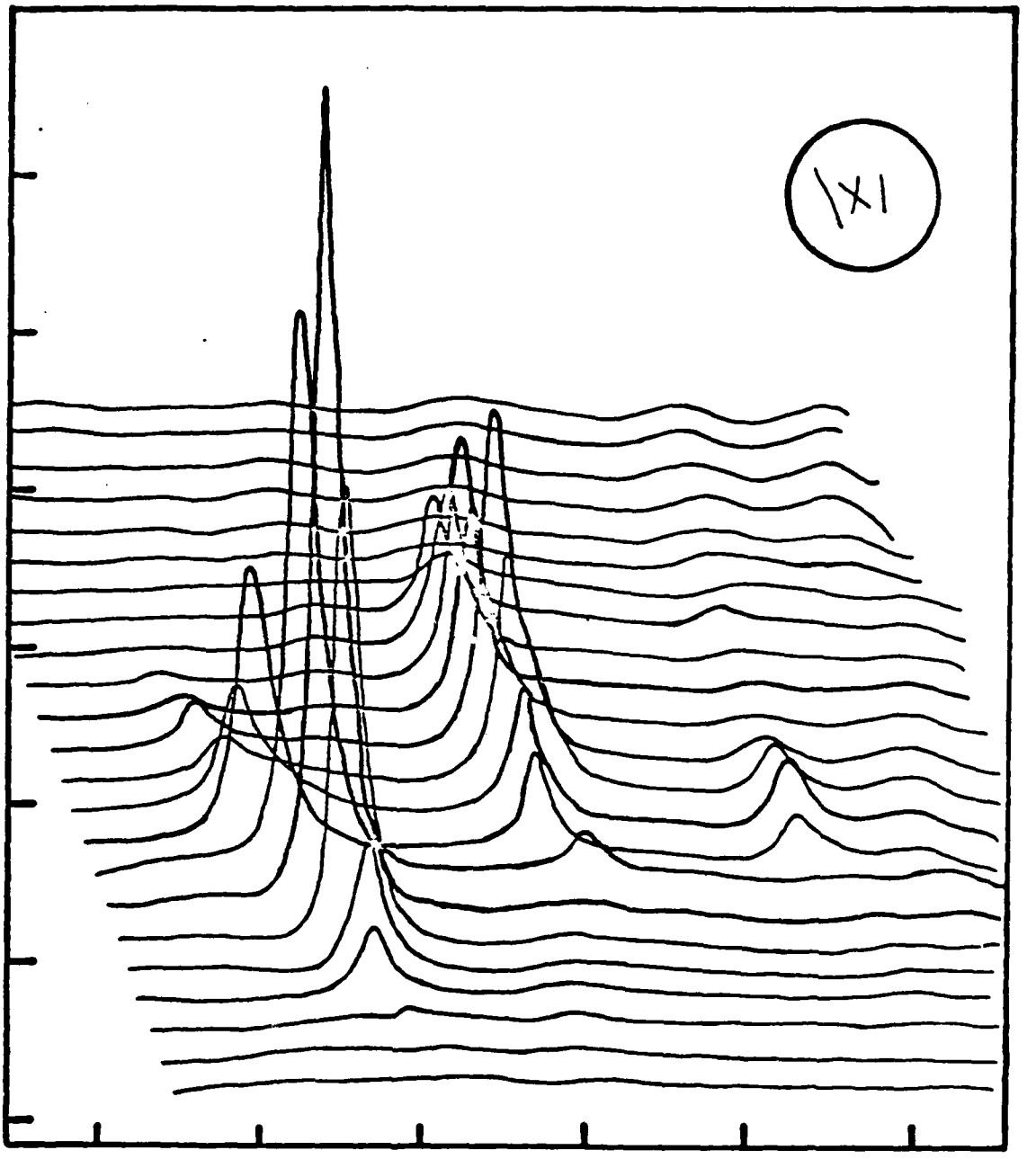

Figure 118.

I component response of a defect in Epon 1001/Emerez 1511 epoxy coated on cold rolled steel. DC bias potential = -0.54V. Applied AC potential = 10mV. Frequency = 2.07 kHz. X-axis scale: 1 division = 0.410 cm (0.161 inch). Y-axis scale: 0.051 cm (0.020 inch) between scans. Current sensitivity: 10μA/division. Inset shows the shape of the defect.

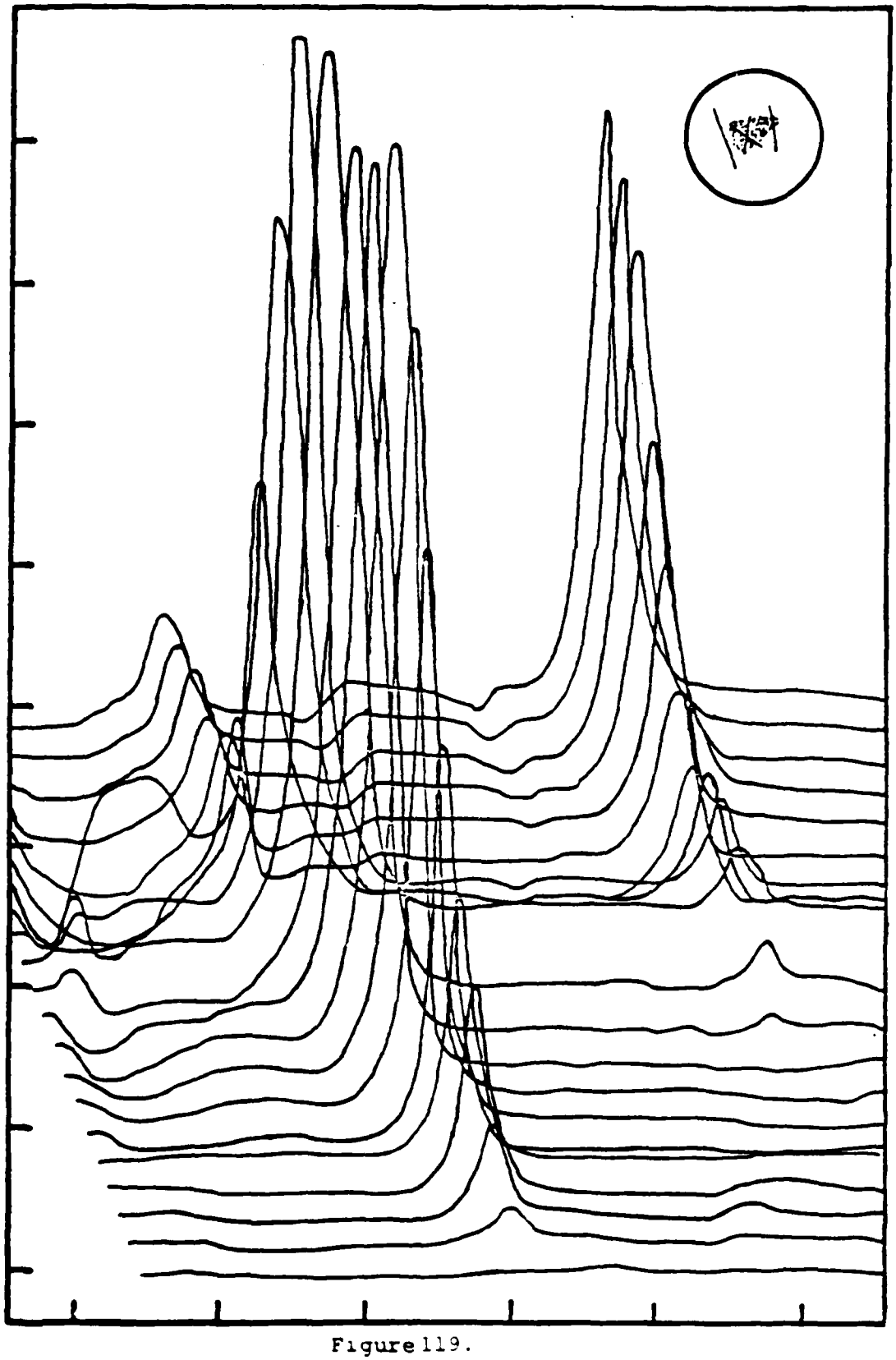

Figure 119.

Magnified scan of delamination region (see inset) in the defect shown in Figure 118 after 48 hours of exposure to NaCl electrolyte. X-axis scale: 1 division = 0.254 cm (0.100 inch). Y-axis scale: 0.025 cm (0.010 inch) between scans. Current sensitivity: [illegible]

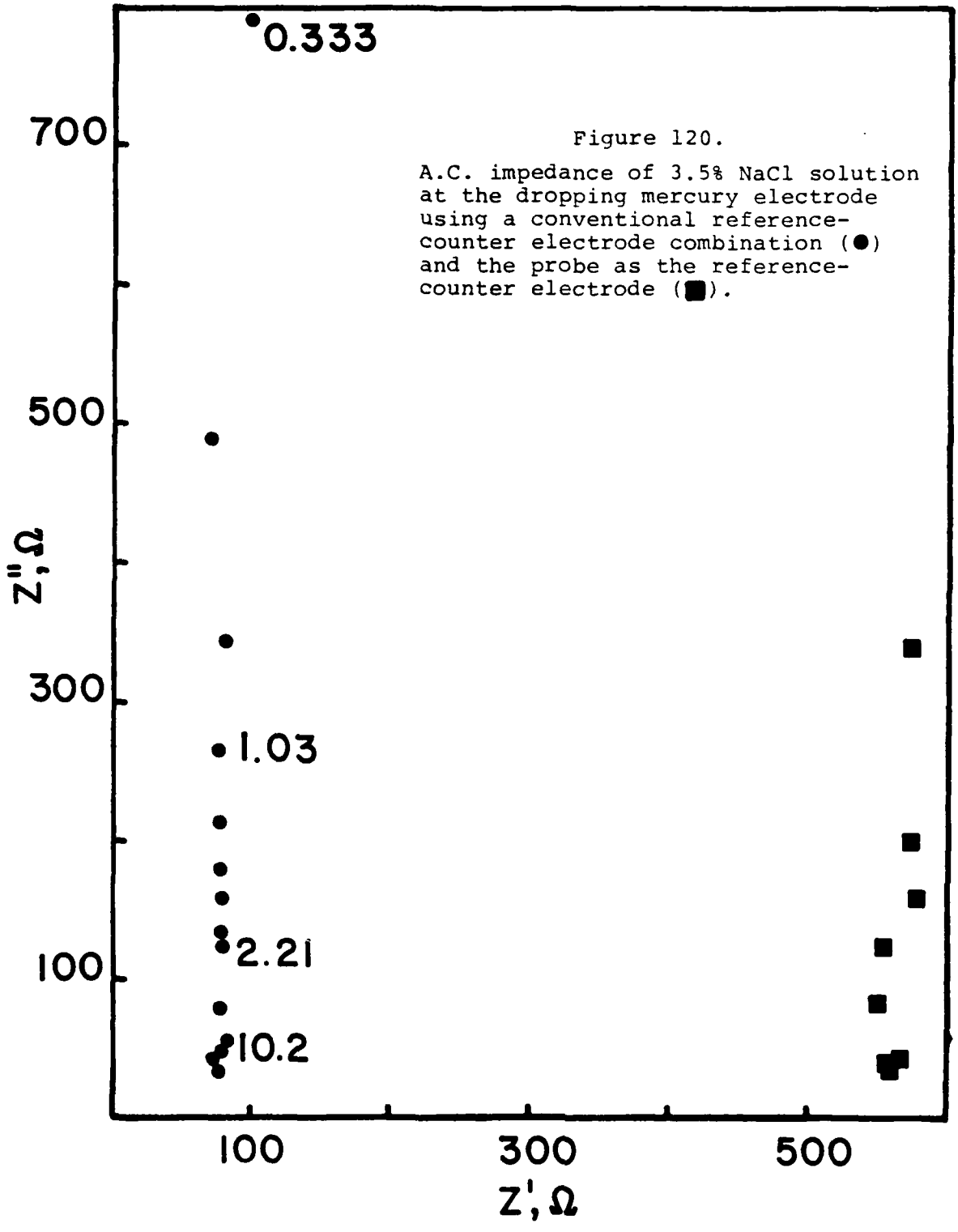

Figure 120.

A.C. impedance of 3.5% NaCl solution at the dropping mercury electrode using a conventional reference-counter electrode combination (●) and the probe as the reference-counter electrode (■).

a dropping mercury electrode (AC polarography). The applied DC potential was -1V vs the probe reference electrode (Ag/AgCl, saturated NaCl) and the applied AC potential was 2.0 mV. The electrolyte was the same 3.5% NaCl used in all of the probe measurements. The plot indicates that the probe forms a conventional electrode system with the DME for AC polarography, giving a somewhat higher resistance (about 550 Ω) than a conventional reference/counter electrode system (about 80 Ω).

Figures 121 and 122 show a very different aspect of the probe impedance response. Here the probe was employed in the same configuration used to map defects in samples. The probe was mounted approximately 0.5 cm above the surface of uncoated metal samples (Figure 121) and epoxy-coated metal samples (Figure 122). From Figure 121 it can be seen that the stainless steels and Monel metal give impedance plots which appear normal at low frequencies but go to negative values of Z" at high frequencies. Since Z" is derived from the Q component of the AC current, this behavior reflects that observed with many of the defect samples. When the metals are coated with epoxy, the impedance plots no longer go to negative Z" values at high frequency (Figure 122). The addition of the coating represents, naively, the insertion of an extra series capacitance into the equivalent circuit of the system. The negative values of Z" observed with bare metal samples would normally be attributed to the presence of a pseudo-inductance in the circuit, and the fact that the capacitance of the coating raises the Z" value by several orders of magnitude appears to reinforce this interpretation. Since the impedances measured are for the entire system including the probe, and the chemical system contains no elements which would be expected to produce a pseudo-inductance, we propose tentatively that the probe itself, possibly because of restricted diffusion into the sensor electrode (counter electrode) wire of the probe, is introducing a pseudo-inductive element into the system.

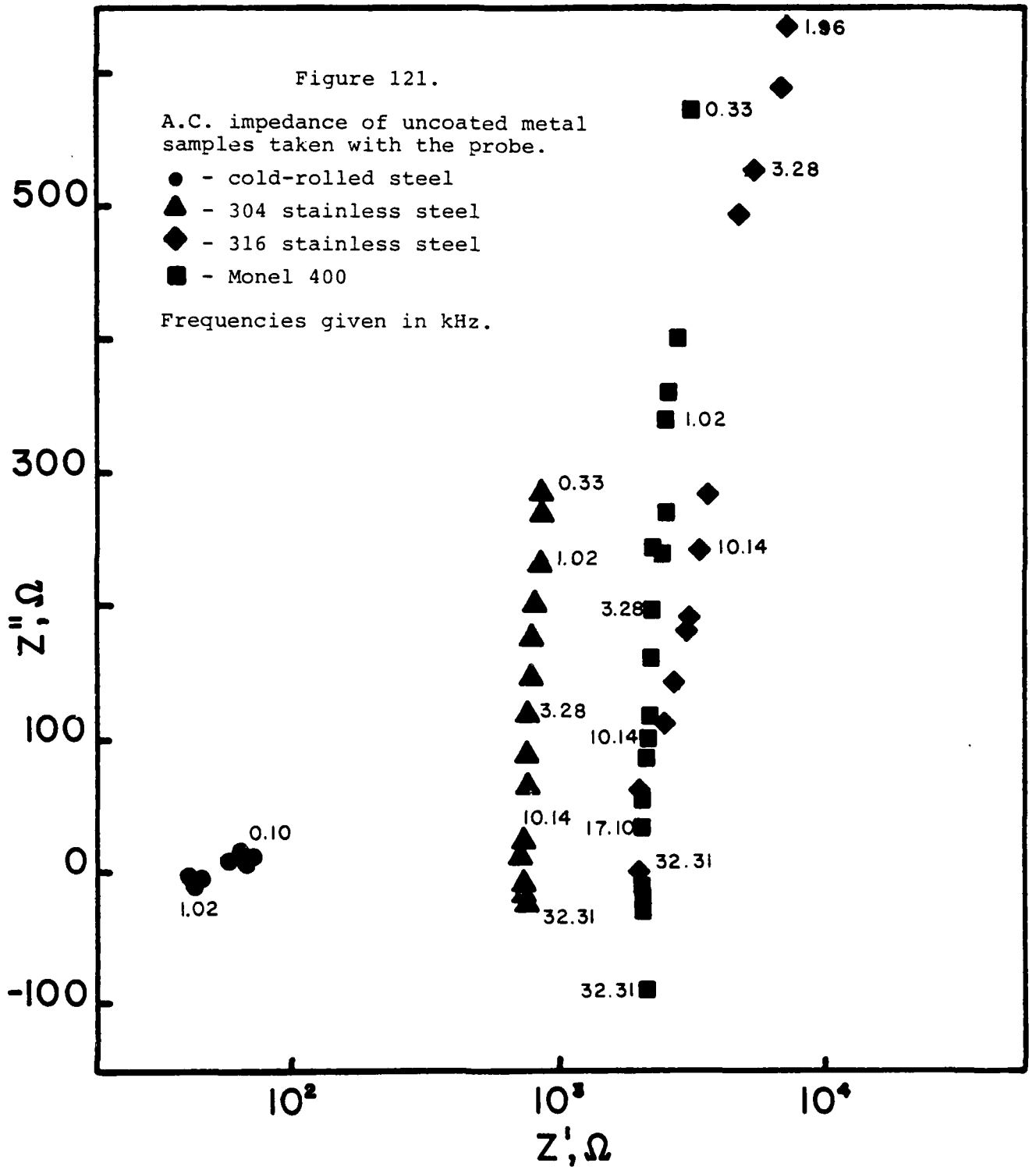
Figure 121.
A.C. impedance of uncoated metal samples taken with the probe.
● - cold-rolled steel
▲ - 304 stainless steel
◆ - 316 stainless steel
■ - Monel 400
Frequencies given in kHz.
500
300
100
0
-100
Z'', Ω
10²
10³
10⁴
Z', Ω
1.96
0.33
3.28
1.02
0.33
1.02
10.14
3.28
3.28
10.14
10.14
17.10
32.31
0.10
1.02
32.31
32.31

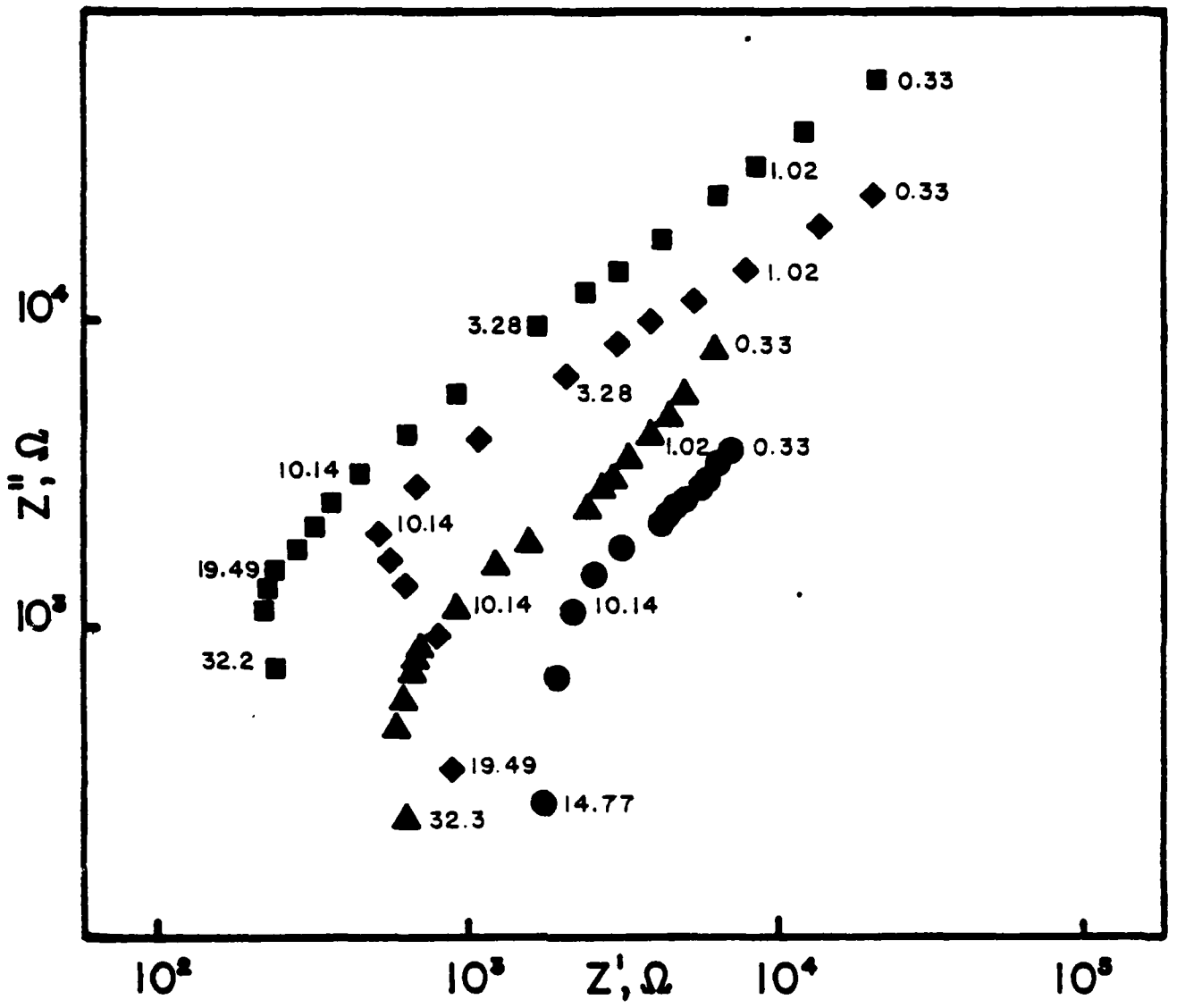

Figure 122.

A.C. impedance of coated metal samples taken with the probe. Symbols the same as in Figure 121.

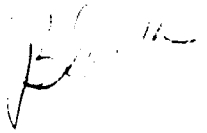

REFERENCES

(1) M. J. Graham and M. Cohen, Corrosion 32, 432 (1976).

(2) S. M. Ahmed, M. S. El-Aasser, G. H. Pauli, G. W. Poehlein, and J. W. Vanderhoff, J. Colloid Interface Sci. 73, 388 (1980).

(3) M. J. Marmo, M. A. Mostafa, H. Jinnal, F. M. Fowkes, and J. A. Manson, Ind. Eng. Chem., Prod. Res. Dev. 15, 206 (1976).

(4) F. M. Fowkes and M. A. Mostafa, Ind. Eng. Chem., Prod. Res. Dev. 17, 3 (1978).

(5) R. S. Drago, G. C. Vogel, and T. E. Needham, J. Amer. Chem. Soc. 93, 6014 (1971).

(6) E. Matijević and P. Scheiner, J. Colloid Interface Sci. 63, 509 (1978).

(7) Joint Committee on Powder Diffraction Standards, 1972,

	Card File Number
α-Fe_2O_3	4-0755
α-FeOOH	17-536
β-FeOOH	13-157
γ-Fe_2O_3	24-81
Fe_3O_4	19-629

(8) L. A. Welo and O. Baudisch, Phil. Mag. 3, 396 (1927).

(9) T. Sugimoto and E. Matijević, J. Colloid Interface Sci. 74, 227 (1980).

(10) R. A. Dickie and A. G. Smith, Chem. Tech. 1980, No. 1, 31.

(11) H. Leidheiser, Jr. and W. Wang, J. Soc. Coatings Technol., in press, December 1980 issue.

(12) H. Leidheiser, Jr. and M. W. Kendig, Corrosion 32, 69 (1976).

(13) Polymer Handbook, J. Brandrup and E. H. Immergut, Editors, Interscience (1966).

(14) A. Seidell and W. F. Linie, "Solubilities of Inorganic and Metal Organic Compounds", 4th Edition, Am. Chem. Soc., vol. 2, pp. 1228-32 (1965).

(15) H. Leidheiser, Jr. and I. Suzuki, Corrosion, in press, November 1980 issue.

(16) R. E. Touhsaent and H. Leidheiser, Jr., Corrosion 28, 435 (1972).

(17) John Standish, Ph.D. Thesis, Lehigh University, October 1980.

(18) H. Leidheiser, Jr. and I. Suzuki, J. Electrochem. Soc., in press.

(19) J. S. Hammond, J. W. Holubka, and R. A. Dickie, J. Coatings Technol. 51, 45 (1979).

(20) R. S. Drago, G. C. Vogel, and T. E. Needham, J. Amer. Chem. Soc. 93, 6014 (1971); R. S. Drago, L. B. Parr, and C. S. Chamberlain, J. Amer. Chem. Soc. 99, 3203 (1977).

(21) F. M. Fowkes and M. A. Mostafa, Ind. Eng. Chem., Prod. Res. Dev. 17, 3 (1978); F. M. Fowkes, Adhesion and Adsorption of Polymers A. pp. 43-52 (Plenum, 1980) ed. L. H. Lee.

(22) E. McCafferty and A. C. Zettlemoyer, Discussions, Faraday Soc. 52, 239 (1971).

(23) Yung=Fang Yu Yao, J. Phys. Chem. 67, 2055 (1963).

(24) T. L. Barr, J. Phys. Chem. 82, 1801 (1978).

(25) J. K. Gimzearski, B. D. Padalia, S. Affrossman, R. M. Watson, and D. J. Fabian, Surface Sci. 62, 386 (1977).

(26) A. Freeuwsma and J. Lyklema, Discussions, Faraday Soc. 52, 324 (1971).

(27) F. Beck, Prog. Org. Coatings 4, 1 (1976).

(28) R. A. Wessling, D. S. Gibbs, W. J. Settineri, and E. H. Wagener, in "Electrodeposition of Coatings", G. E. F. Brewer, ed. (1973), p.110.

(29) J. W. Vanderhoff, M. S. El-Aasser, and J. Ugelstad, U.S. 4,177,177, Dec. 4, 1979.

(30) S. Mercouris and W. F. Graydon, J. Electrochem. Soc. 117, 717 (1970).

(31) A. E. Rheineck and A. M. Usmani, J. Paint Tech. 41 (538), 597 (1969).

(32) M. S. El-Aasser, J. W. Vanderhoff, S. C. Misra, and J. A. Manson, J. Coatings Tech. 49 (635), 71 (1977).

(33) E. B. Bradford and J. W. Vanderhoff, J. Macromol. Chem. 1, 335 (1966).

(34) C. G. Fink and M. Feinleib, Trans. Electrochem. Soc. 94, 309 (1948).

(35) D. A. Olsen, J. Paint Tech. 38 (499), 429 (1966).

(36) F. Beck, Farbe Lack. 72, 218 (1966).

(37) P. E. Pierce, Z. Kovac and C. Higginbotham, Ind. Eng. Chem. Prod. Res. Dev. 17 (4), 317 (1978).

(38) H. H. Uhlig, "Corrosion and Corrosion Control", p. 156, John Wiley (1963).

(39) Z. Kovac-Kalko, "Electrodeposition of Coatings", G. E. F. Brewer, ed., p. 149 (1973).

(40) A. E. Rheineck and A. M. Usmani, "Electrodeposition of Coatings", G. E. F. Brewer, ed., p. 130 (1973).

(41) A. H. Bushey, J. Coatings Tech. 48 (619), 51 (1976).

(42) S. R. Finn and J. A. Hasnip, J. Oil Color Chem. Assoc. 48, 1121 (1965).

(43) K. J. Vetter, "Electrochemical Kinetics", p. 759-771, Academic Press, N.Y. (1967).

(44) L. E. Nielsen, Mechanical Properties of Polymers and Composites, Dekker, N.Y., 1974, 2 vols.

(45) J. A. Manson and L. H. Sperling, Polymer Blends and Composites, Plenum, N.Y. 1976, Ch. 12.

(46) L. E. Nielsen, J. Appl. Polym. Sci. 10, 97 (1966).

(47) L. H. Sharpe, Org. Plast. Coatings Prepr. 31 (2), 201 (1971).

(48) M. J. Marmo, M. A. Mostafa, H. Jinnai, J. A. Manson, and F. M. Fowkes, Ind. Eng. Chem. Prod. Res. Dev. 15, 206 (1976).

(49) M. A. Mostafa and F. M. Fowkes, Ind. Eng. Chem. Prod. Res. Dev. 17, 3 (1978).

(50) T. P. Abbott, C. James, and F. H. Otey, J. Appl. Polym. Sci. 23, 1223 (1979).

(51) P. Sorenson, J. Coatings Technol. 47 (602), 31 (1975).

(52) P. Nylen and E. Sunderland, Modern Surface Coatings, Interscience, N.Y., 1965, Ch. 15.

(53) P. E. Pierce, in Treatise on Coatings, vol. 2, part 1, ed. by R. R. Myers and J. S. Long, Dekker, N.Y., 1969, Ch. 4.

(54) E. H. Plueddemann, Org. Plast. Coatings Prepr. 38 (1), (1978).

(55) R. M. Evans and J. Fogel, J. Coatings Technol. 49 (634), (1977).

(55a) J. Williams and J. Manson, "Organic Coatings and Plastic Chemistry", vol. 42, p. 175 (2980).

(56) M. Heffelfinger, "Adsorption Characteristics for Fe_2O_3 Using PMMA/CCl_4 and Cl-PVC", Term Paper.

(57) Y. Lipatov, L.M. Sergeeva, Adsorption of Polymers, John Wiley & Sons, N.Y.-Toronto (1974).

(58) K. Sato, Prog. in Org. Coatings 8, 143 (1980).

(59) D. J. Newman and C. J. Nunn, Prog. in Org. Coatings 3, 221 (1975).

(60) C. M. Hansen, Off. Dig. 37, 57 (1965).

(61) C. M. Hansen, Teknisk Licentiat Thesis, Tech. Univ. of Denmark, 1964.

(62) C. M. Hansen, Doctoral Thesis, Tech. Univ. of Denmark, Danish Technical Press, Copenhagen, 1967.

(63) C. M. Hansen, Ind. Eng. Chem. Prod. Res. Dev. 9, 282 (1970).

(64) C. M. Hansen, J. Oil Colour Chem. Assoc. 51, 27 (1968).

(65) T. Yoshida, Prog. Org. Coatings 1, 72 (1972).

(66) J. Ramshutham, Prog. Org. Coatings 81, 113 (1980).

(67) Technical Bulletin 11-D-3, "Protective and Decorating Coatings Based on Versamid Polyamide Resins", General Mills (1963).

(68) M. Gordan and W. Simpson, Polymer Lond. 2, 383 (1961).

(69) R. A. Fava, Polymer 9, 137 (1968).

(70) K. Hovie, H. Hivra, M. Sawada, I. Mita, and H. Kambe, J. of Polymer Sci., Part A, vol. 8, 1357 (1970).

(71) A. Shimazaki, J. Applied Poly. Sci., vol. 1,w, p. 2013 (1968).

(72) A. F. Lewis and J. K. Gillham, J. of Applied Poly. Sci., Vol. VI, 422 (1967).

(73) Polymeric Materials, Relationship Between Structure and Mechanical Behavior, American Society for Metals, 1975.

(74) Z. Ophic, J. Emerson, and G. Wilkes, J. of Applied Phys. 10, vol. 49, 5032 (1978).

(75) P. Kamarchik and G. Cunningham, Prog. Org. Coatings 8, 81 (1980).

(76) L. E. Nielsen, J. Macrmol. Sci. A1, 929 (1969).

(77) J. Manson and L. Sperling, Polymer Blends and Composites, Plenum Press, N.Y. and London (1976).

(78) J. Bardelebov, Kinststoffe 53, 162 (1963).

(79) W. Funke, U. Zorel and B. K. G. Murthy, J. Paint Technol. 41, 210 (1969).

(80) A. S. Michaels, Off. Digest 37, 638 (1965).

(81) D. Y. Perera and P. M. Heerties, J. Oil Colour Chem. Assoc. 54, 313, 774 (1971).

(82) G. S. Crank and W. R. Park, Diffusion in Polymers, London, Academic (1969).

(83) N. Fawcett and C. Stearns, Organic Coatings and Plastics Chemistry, vol. 43, 599 (1980).

(84) L. Nielsen, Mechanical Properties of Polymers and Composites, vol. 1 & vol. 2, Marcel Dekker, N.Y. (1974).

(85) L. Nielsen and T. Lewis, J. Polym. Sci. A-2 7, 1705 (1969).

(86) T. Lewis and L. Nielsen, J. Appl. Polymer Sci. 14, 1449 (1970).

(87) J. C. and J. L. Kordes, J. Appl. Phys. 43, 2235 (1972).

(88) T. Murayama and J. P. Bell, J. Poly. Sci. A-2, 8, 437 (1970).

(89) K. Sato. Prog. Org. Coatings 4, 271 (1976).

(90) J. E. O. Mayne and D. J. Mills, J. Oil Colour Chemists Assocn. 58, 155 (1975).

(91) M. W. Kendig and H. Leidheiser, Jr., J. Electrochem. Soc. 123, 982 (1976).

(92) H. S. Isaacs and M. W. Kendig, Corrosion 36, 269 (1980).

(93) J. V. Standish and H. Leidheiser, Jr., Corrosion 36, 390 (1980).

(94) P. Smith, in "Electroanalytical Chemistry", vol. 1, 1966, A. Bard, ed., Marcel Dekker, N.Y.

(95) M. Reybach-Sluyters and J. Sluyters, in "Electroanalytical Chemistry", vol. 4, 1970, A. Bard, ed., Marcel Dekker, N.Y.

(96) A. Bard and L. Faulkner, "Electrochemical Methods", 1980, John Wiley, N.Y.

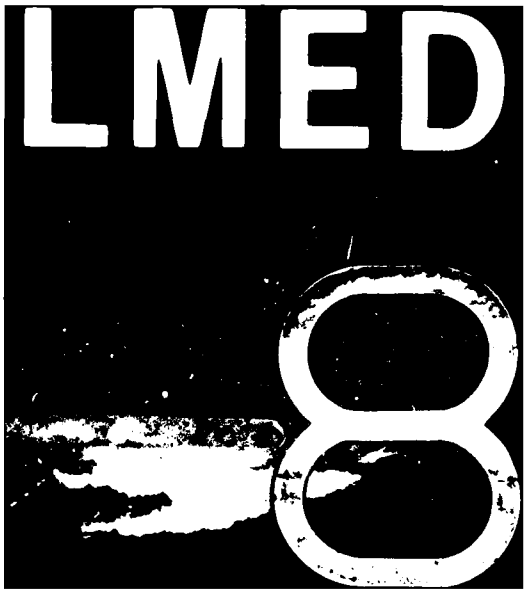
LMED
8